Dynamics of topological defects in exciton-polariton quantum fluids

Sergei Koniakhin

▶ **To cite this version:**

Sergei Koniakhin. Dynamics of topological defects in exciton-polariton quantum fluids. Quantum Physics [quant-ph]. Université Clermont Auvergne [2017-2020], 2020. English. NNT : 2020CLFAC068 . tel-03442356

HAL Id: tel-03442356
https://theses.hal.science/tel-03442356v1

Submitted on 23 Nov 2021

HAL is a multi-disciplinary open access archive for the deposit and dissemination of scientific research documents, whether they are published or not. The documents may come from teaching and research institutions in France or abroad, or from public or private research centers.

L'archive ouverte pluridisciplinaire **HAL**, est destinée au dépôt et à la diffusion de documents scientifiques de niveau recherche, publiés ou non, émanant des établissements d'enseignement et de recherche français ou étrangers, des laboratoires publics ou privés.

INSTITUT PASCAL - UNIVERSITÉ CLERMONT AUVERGNE - CLERMONT FERRAND

ECOLE DOCTORALE DES SCIENCES FONDAMANTALES

UFR SCIENCES ET TECHNOLOGIES

THESE DE DOCTORAT

Pour accéder au grade de

Docteur d'université en sciences

de l'Université Clermont Auvergne

Specialité : Physique, Milieux denses et Matériaux

Défendue par

Sergei V. KONIAKHIN

Dynamics of topological defects in exciton-polariton quantum fluids

Préparée à l'Institut Pascal, Clermont-Ferrand,
au sein de l'équipe:
Optoélectronique Quantique et Nanophotonique

Soutenue publiquement le 09/07/2020

Commission d'examen:

Rapporteurs :	Prof. Léonie Canet
	Prof. Ivan Savenko
Examinateurs :	Prof. Jacqueline Bloch
	Prof. Ivan Shelykh
Directeur de thèse :	Dr. Guillaume Malpuech
	Prof. Dmitry Solnyshkov

Remerciements

D'abord et sans autres mots d'introduction je veux chaleureusement remercier mes parents pour leur patience. Car pour eux mon travail et mon séjour en France étaient une épreuve beaucoup plus sévère que pour moi-même. Je leur ai manqué et ils me manquent, et ils subissent mon absence très fortement, sans aucun doute. Et en même temps je sens à quel degré ils sont fiers de moi, du fait que j'ai décidé de prendre ce défi et de tout changer dans ma vie : le pays, l'institut, les collègues, le sujet de la recherche. Presque chaque soir nous nous voyons par Skype et nous nous soutenons mutuellement selon ce que peut permettre ce moyen de communication. Et maintenant je suis très heureux d'avoir la possibilité de les rendre fiers car je suis très près de mon but principal des trois ans précédents, notamment, d'obtenir en France le degré de docteur de physique.

Ce but ne pourrait point être approché sans mes encadrants, Guillaume et Dima. Avec eux j'ai rencontré le mode de travail très diffèrent par rapport à ce que je pratiquais auparavant. Il s'agit de l'interaction en échange permanent des idées et des résultats. Cette méthode s'est éminemment manifestée durant le mois d'avril 2020 pendant notre télétravail et ses visioconférences quotidiennes. Avant que je sois venu ici, à Clermont-Ferrand, mes habitudes de travail étaient très différentes. Je travaillais presque indépendamment, libre, mais sans appui. Par conséquent, c'était très difficile pour moi d'apprendre de nouveaux sujets de la recherche. J'ai aussi appris comment communiquer avec les collègues. Et je sens nettement, a quel degré c'était parfois difficile pour eux d'interagir avec moi. Pour cela, pour les fructueuses discussions scientifiques, pour leur aide et leurs encouragements, dans les moments où j'estimais sceptiquement et lamentablement les résultats que j'ai obtenus, je leur exprime cordialement ma profonde gratitude.

Je voudrais témoigner ma reconnaissance à Françoise et Vanessa, qui étaient toujours très gentilles et qui m'aidaient communiquer avec le monde extérieur au labo, par exemple pour organiser les missions. Je voudrais remercier madame Hernandez pour son aide à la préparation de documents pour la soutenance. Je suis chanceux d'avoir passé quelques semestres de cours au centre linguistique FLEURA pour étudier le français et je remercie tous les professeurs et toutes les professeures qui m'enseignaient.

J'exprime ma gratitude à tous mes collègues. À Charly et Ismael, qui ont rejoint le Labo en 2019 et qui lui ont fourni un nouveau sang. Et aussi à mes collègues (et en même temps des amis) qui travaillent à Saint-Pétersbourg et avec qui j'ai fait très bonnes recherches collaboratives. Ils sont Oleg Utesov, Daniil Stupin, Stas Shmakov, Ivan Shishkin. Parmi les autres, je témoigne ma spéciale gratitude à Olivier Bleu, qui, en étant toujours gentil et souriant, a soulagé mon acclimatement dans le nouveau pays et ainsi que pour ses

cadeaux. Merci à Anton Nalitov, sans qui je ne me serais jamais trouvé ici. Je voudrais remercier Prof. Bramati, le chef du labo à l'Université Sorbonne, où j'ai passé la mémorable par tous les évènements mission en Avril 2019. Merci à tous ses collègues, Anne Maître, Ferdinand Claude, Simon Pigeon, Giovanni Lerario, Quentin Glorieux, qui m'ont montré comment exciter et détecter ces légendaires polaritons en expérience réel. Je me sens obligé à jury, dont les membres ont accepté y participer dans le moment tant peu ordinaire. Enfin, merci beaucoup à Eugeny Eidelman, mon moniteur ancien, qui a contribué à mon établissement comme le chercheur physicien ainsi qu'à Misha Glazov pour son attitude toujours gentille et pour les discussions constructives.

Ce n'est pas possible de ne pas remercier mes voisins et mes amis Ghislaine et Bernard. Sans eux je me sentirais en quelque sorte perdu et seul, surtout dans le début de mon séjour en France. Parmi beaucoup d'autres bienfaits, ils m'ont montré les petites belles villes d'Auvergne telles que Thiers, Salers, Riom es Montagne. Grâce à eux j'ai commencé à découvrir notre belle région. Curieusement, Olivier n'est pas le seul membre de la famille Bleu, à qui je dois beaucoup. Ses parents, Odile et Jean-Paul, m'accueillaient très gentiment chez eux pendant des visites amicales. Je vais à jamais me souvenir les promenades avec eux dans les prés et les forêts autour de Laschamps.

Pour finir, sans moindre hésitation, je dis que la décision d'aller travailler à l'Institut Pascal a été la meilleure décision dans ma vie. C'était une expérience incroyable! Dans l'avenir je serais très heureux de retourner à Clermont-Ferrand pour participer dans la conférence, pour la mission ou le travail.

Résumé

Le condensat de Bose-Einstein (CBE) est un nouvel état de la matière qui donne la possibilité étonnante d'observation de phénomènes quantiques, comme l'existence de la fonction d'onde sur des échelles macroscopiques. Cette recherche porte sur le type particulier de CBEs, en l'occurence celui qui est basé sur les excitons-polaritons dans des microcavités optiques de semi-conducteurs. Grâce aux interactions non-linéaires, le comportement des condensats de Bose-Einstein ressemble à celui de fluides classiques. Une meilleure compréhension de ces similarités est le but principal du projet d'ANR "Fluides quantique de lumière", dans le cadre duquel cette recherche a été réalisée. Les deux premiers chapitres du manuscrit sont introducteurs et décrivent la physique des exciton-polaritons dans des nanostructures de semi-conducteurs,les propriétés des condensats de polaritons, les propriétés des défauts topologiques des fluids quantiques que sont les tourbillons quantiques et les solitons.

Le chapitre 3 présente l'étude du phénomène de turbulence quantique basé sur la résolution numérique de l'équation de Gross-Pitaevskii. Nous avons étudié différentes stratégies d'agitation et démontré le transfert d'énergie depuis les petites échelles spatiales vers les grandes échelles. La présence de structures fractales formées de clusters de tourbillons a été démontré numériquement. Le domaine d'échelle spatiale, où la loi de Kolmogorov pour la dépendance de la densité d'énergie cinétique incompressible est réalisée, coïncide avec celle où on observe ces structures fractales caractérisées par une dimension de Minkowski fractionnelle. Toutefois, ces régions deviennent visibles uniquement lorsque la contribution des tourbillons isolés et des dipôle est éliminée. Par conséquent, les signatures de la présence de ces structures fractales ne peuvent être obtenues expérimentalement qu'à travers une mesure complète de la fonction d'onde du fluide quantique en fonction du temps, notamment son amplitude et sa phase. Cette difficulté peut etre résolue par l'utilisation de plateforme polaritonique qui se caractérise par une accessibilité unique à la mesure de la dynamique des fonctions d'onde et qui est donc une plateforme attractive pour l'étude de la turbulence quantique.

Dans les fluides classiques les solitons sont des ondes solitaires se propageant sur de longues distances sans se déformer. Les solitons sont des excitations stables des fluides quantiques 1D. Cependant, en 2D, ils subissent la fameuse instabilité modulationnelle en se désintégrant en chaines de paires de tourbillon/anti-tourbillon qui s'éloigne les unes des autres. Ce type de phénomène dynamique peut difficilement être observé expérimentalement sous pompage optique continu. Dans le Chapitre 4, nous introduisons une configuration facile à réaliser expérimentalement et qui permet de résoudre cette difficulté. Nous proposons de réaliser un couloir de potentiel unidi-

mensionel en utilisant une modulation spatiale de l'intensité de pompage et le caractère bistable du système polaritonique. Les zones fortement pompés occupe la branche haute de bistabilité optique et forment des murs de potentiel abrupt par rapport à la zone faiblement pompée qui est sur la branche basse de bistabilité. Nous avons démontré des solitons sombres se forment dans ces couloirs. Leur nombre et leur parité (1-3 ou 2-4) sont contrôlés par la différence de phase et l'écartement entre les murs. Les équations de Bogoliubov-de Gennes montre que ces solitons sont instables et évoluent vers une chaine stationnaires de tourbillon/anti-tourbillon. Ces chaînes dont l'évolution temporelle est bloquée par la présence des murs de potentiel peuvent être symétriques ou antisymétriques selon la distribution d'intensité du laser. Lorsque l'intensité du laser augmente fortement les chaines de tourbillons disparaissent à partir des extrémités fermés des couloir, alors que les chaînes restent stables au niveau des extrémités ouvertes. Ce phénomène permet à la chaine de tourbillon de connecter uniquement son entrée et sa sortie et d'ainsi réaliser un algorithme de résolution "tout optique".

Abstract

The Bose-Einstein condensate is a new state of matter which gives the astonishing possibility of observation of quantum phenomena, like the existence of the wave function on macroscopic scales. Present research is devoted to the particular type of BECs based on excitons-polaritons in semiconductor microcavities. Due to non-linear interactions, the behavior of Bose-Einstein condensates, and more general of polaritons at high densities, resembles that of classical fluids. Better comprehension of these similarities is one of the goals of ANR "Quantum fluids of light" project, within which present research was conducted. The first two chapters of the manuscript provide the necessary introduction to the physics of excitons-polaritons and properties of polariton condensates (including the topological defects: vortices and solitons), respectively.

In classical fluids, the solitons are solitary waves propagating over long distances without deformation and similar situation is actual for 1D quantum fluids. However, in 2D case the solitons undergo the so-called "snake instability" and transform to the chains of vortex-antivortex pairs, which is a principal obstacle to study this phenomenon in polariton quantum fluids especially in CW experiments. In the next chapter, the simple to implement by the means of spatial light modulator configuration that allows avoiding this restriction was proposed and extensively studied. The configuration is a narrow 1D channel with the walls of high condensate density at upper bistability branch created by intensive laser radiation. It was shown that in such channels dark solitons appear parallel to the channel axis by odd (1-3) or even (2-4) number in order to accommodate the phase constraint induced between the walls. According to the Bogoliubov-de Gennes analysis, these soliton molecules are typically unstable and trigged by the disorder evolve toward stationary symmetric or anti-symmetric arrays of vortex streets. Also the soliton head repulsion from the corridor dead-end was demonstrated, giving a straight possibility to experimentally implement maze solving procedure by dead-end stroking algorithm.

As for quantum turbulence, the possibility of observing the energy transfer from small spatial scales to large ones (reverse energy cascade) and the formation of fractal structures composed of quantum vortices in polaritonic condensates were demonstrated. The region of Kolmogorov -5/3 power law in the spectrum of incompressible kinetic energy coincides with the region of fractional Minkowski dimension of the structures of clustered vortices. However, for various condensate stirring methods, this power law becomes visible only after eliminating the contribution of single vortices and vortex dipoles. Thus, the experimental observation of the spectrum of such shape will be possible after full wave function reconstruction including both amplitude and phase, which justifies that polaritons are the promising platform for studying quantum turbulence.

Contents

Chapter 1

Introduction to cavity exciton-polaritons

Contents

The semiconductor technology contributed dramatically to the progress in science and technology of the mankind in the second half of XX century. The examples of these technological breakthroughs are transistors [1] and other electronic components essential for computers, digital and analog electronic devices of other types: light sensors, high power components, solar cells *etc.* The important examples are also the light sources, including diodes and semiconductor lasers. In the beginning of his Nobel lecture in the year 2001 [2], Zhores Alferov writes:

It is impossible to imagine now modern solid-state physics without semiconductor heterostructures. Semiconductor heterostructures and, particularly, double heterostructures, including quantum wells, wires, and dots, are today the subject of research of two-thirds of the semiconductor physics community.

Present chapter gives the necessary review presenting the topic of semiconductor microcavity exciton polaritons. The chapter is organized as follows. In the section 1 we introduce the excitons as the electron-hole composite quasiparticles in semiconductors, discuss their properties in quantum wells, describe the mechanisms of their decay and the exciton-exciton interactions. The Section 2 is devoted to the description of semiconductor microcavities, including the cavity photon dispersion. In Section 3 we will write the Hamiltonian for the system of interacting quantum well exciton and cavity photon. We will discuss the weak coupling regime and the strong coupling regime and show that the realization of the latter will lead to the formation of a new unique quasiparticle, the exciton-polariton, sharing the properties of matter and light. The chapter will be finished with a description of the Gross-Pitaevskii equation for cavity exciton polaritons, the regime of quasi-resonant pumping, and the phenomenon of bistability.

1.1 Excitons in semiconductors

1.1.1 Exciton as a quasiparticle

One of the most famous and actively studied quasiparticles in physics of semiconductors and an essential ingredient to form the polaritons are the excitons, the composite eletron-hole hydrogen atom-like quasiparticles. The wave function of an electron in the periodic potential of a semiconductor writes in the terms of the Bloch wave function [3]:

$$\psi_{n\mathbf{k}} = e^{i\mathbf{kr}} u_{n\mathbf{k}}(\mathbf{r}), \tag{1.1}$$

where the function $u_{n\mathbf{k}}(\mathbf{r}+\mathbf{R}) = u_{n\mathbf{k}}(\mathbf{r})$ reflects the periodicity of a crystal lattice. n is an index of a band and $\mathbf{R}$ is a translation vector. The bands n are closely related with the atomic orbitals and inherit their symmetry. They also exhibit a complex interplay between spin and angular momentum. Due to the translational invariance, the actual wave vector in the crystals $\mathbf{k}$ becomes restricted to the Brillouin zone of a crystal, approximately from 0 to π/a_0, where a_0 is a lattice constant. The energy dispersion relation for the electrons

in the periodic potential of a crystal reads

$$E_n(\mathbf{k}) = E_{0n} + \frac{\hbar^2 k^2}{2m_n}, \tag{1.2}$$

where m_n is an effective mass of an electron in corresponding band n. The value of the effective mass can be obtained from the overlap integrals γ in the Tight-Binding Model [4] with the following general proportionality:

$$m_{\text{effective}} \propto \frac{\hbar^2 a_0^2}{\gamma}. \tag{1.3}$$

In the semiconductors, the n-th band lying below the Fermi level (an energy necessary to place one new electron to the crystal) is nearly filled with electrons and the next $n+1$-th band is nearly vacant. These bands correspond to valence and conduction bands, respectively. Electron density in the upper (conduction) band increases with temperature and also can be also increased by irradiation by light or application of electric bias. The doping also allows the control of electron density in the bands. Within this formalism, the absence of an electron in the band n can be considered as new quasiparticle with a negative mass (and thus a negative energy) and a positive electric charge, called a hole.

The typical values of electron and hole effective masses are comparable at least by the order of magnitude with the mass of a free electron m_0. For the particular semiconductor studied in this thesis, GaAs, the values are $m_e = 0.067m_0$, $m_h = 0.51m_0$ and $m_l = 0.082m_0$ [5]. In fact, due to the anisotropy of crystals, the masses are tensor quantities depending on the wave vector direction with respect to crystallographic axes. Also the masses, being the derivative of the overlap integral, are thus sensitive to the pressure (up to $\approx 1\%$ per kilobar for GaAs) and to the temperature with the electron-phonon interaction contribution up to dozen of percents for various materials, see. Ref. [6]. . Fig. 1.1 shows the electronic structure of GaAs. The heavy holes (h), light holes (l), and a split-off band originate from the mixture of p-symmetry atomic orbitals.

Being oppositely charged, the Bloch electron and the hole experience a mutual Coulomb attraction. Thus the Schrödinger equation for these two interacting particles has a form:

$$\left(\frac{\hat{p}_e^2}{2m_e} + \frac{\hat{p}_h^2}{2m_h} - \frac{e^2}{\varepsilon|\mathbf{r}_e - \mathbf{r}_h|} \right) \Psi = E\Psi, \tag{1.4}$$

with $\hat{p}_{e,h}$ representing the momentum operators for electron and hole, respectively, and the effective masses denoted as $m_{e,h}$. ε is a dielectric constant of a medium, suppressing the electron-hole attraction force. This equation completely resembles the equation for the hydrogen atom and thus the solution is of the same structure. The variables are separated for the center mass and for the relative motion. The energy of such system reads

$$E_\nu^X(k_X) = \frac{\hbar^2 k^2}{2M} - \frac{R_X}{\nu^2} + E_g, \tag{1.5}$$

The first term in the equation above represents the kinetic energy of the electron-hole composite quasiparticle called exciton and the second term is the exciton binding energy. E_g is the energy of the band gap separating the valence and the conduction bands. It is important to write E_g explicitly because it should be accounted for, when tuning the light

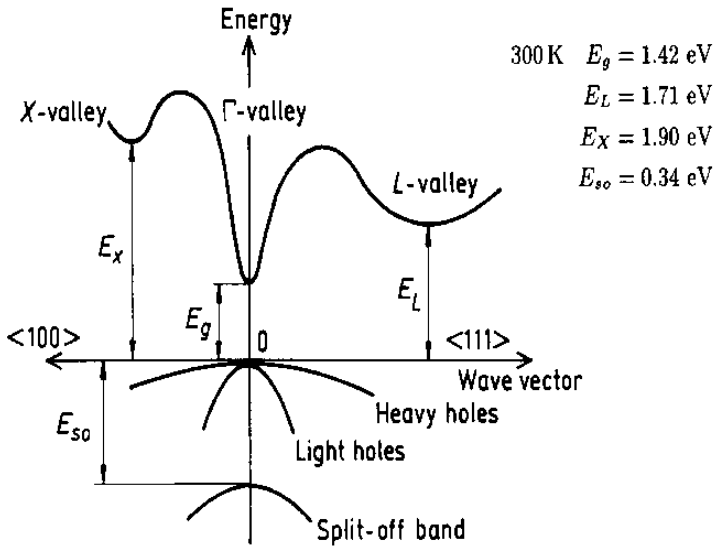

Figure 1.1: Band structure of GaAs for electrons with small wave-vectors. Valence band is of three subbands: light holes (LH), heavy holes (HH), and split-off band (S)). E_g is the size of the band gap. Adopted from Ref. [5].

energy for the creation of the exciton. M is the sum of the masses of an electron and a hole and $R_X = \frac{\mu e^4}{2\hbar^2\varepsilon^2}$ is a Rydberg for the exciton. ν enumerates the principal quantum number and μ is the reduced mass. The Bohr radius of an exciton reads:

$$a_X = \frac{\hbar^2\varepsilon}{\mu e^2}, \tag{1.6}$$

and for GaAs one obtains 11.6 nm for the radius and 4.8 meV for the binding energy. Together with band gap $E_g = 1.519$ eV, one obtains 1.514 eV for the photon energy to be completely in resonance with the exciton of bulk GaAs.

Importantly, optical transitions between the states in the valence and the conduction bands are determined by the momentum conservation law telling that an electron transition accompanied by photon absorption is allowed only when the momentum of the final state of the electron differs from the momentum of the initial state of the electron by the magnitude of the photon momentum. Due to the fact that the latter is small compared to the electron momentum in the crystal, it can be assumed that optical transitions in semiconductors occur if the quasimomenta of the initial and final states are equivalent to each other. This limitation makes optical transitions in a direct-gap semiconductor more probable than in indirect-gap semiconductors. The optical transitions in indirect-gap materials are still possible, but they require the participation of additional particles (such as phonons) to obey the momentum conservation law.

The important case of semiconductor excitons are the confined excitons in the low-dimensional structures. Such confinement takes place when placing the semiconductor in the material with larger band gap or in the dielectric matrix. Particularly efficient is the technology of $Ga_xAl_{1-x}As$ structures. From Fig. 1.2 one sees that this combination of materials allows obtaining significant contrast in electronic properties (band gap width) while the lattice constants for GaAs and AlAs differ weakly, which gives possibility to

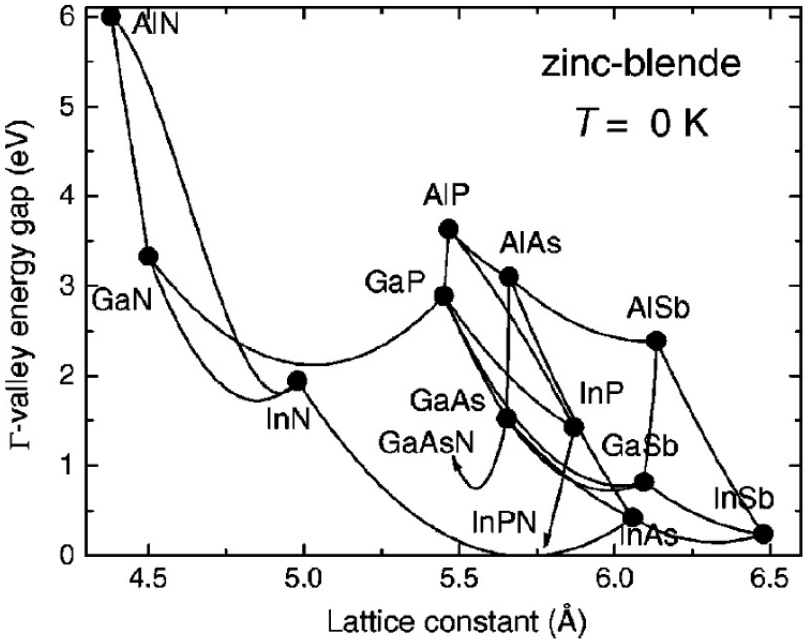

Figure 1.2: Band gaps versus lattice constant for various mixtures of zinc-blend materials at low temperatures. Adopted from Ref. [7]

grow the structures with sufficiently low concentration of defects.

The limit case of quantum confinement is the 0D nanostructure, or a Quantum Dot. The Schröedinger equation for a particle (including the exciton) in cubic QD reads:

$$\left[-\frac{\hbar^2}{2m}\nabla^2 + U(\mathbf{r})\right]\Psi = E\Psi, \tag{1.7}$$

where the potential $U(\mathbf{r})$ is defined as

$$U(x) = \begin{cases} U_0, \ |x| > L_x/2 \text{ or } |y| > L_y/2 \text{ or } |z| > L_z/2 \\ 0, \text{ otherwise} \end{cases}$$

Considering the case of a QD with an infinite barrier U_0 (applying zero boundary conditions for the wave function), one obtains for the electrons and the holes the problem similar to the problem of an electromagnetic wave in a metallic resonator with the same wave function spatial structure and the energy levels writing as:

$$E_{e,h}^{QD} = \frac{\hbar^2\pi^2}{2m_{e,h}}\left(\frac{n_x^2}{L_x^2} + \frac{n_y^2}{L_y^2} + \frac{n_z^2}{L_z^2}\right), \tag{1.8}$$

where n_α are quantum numbers and L_α are the dimensions of a quantum dots. Due to parabolic dispersion of excitons, one has n_α^2 for them, instead of the power 1 in the case of electromagnetic waves in the resonator in the shape of rectangular parallelepiped.

The effect of size quantization also takes place in quantum wires and the quantum wells. The latter case is the most relevant for the present study:

$$E_{e,h}^{QW}(k) = \frac{\hbar^2}{2m_{e,h}}\left(k^2 + \frac{\pi^2 n_z^2}{L_z^2}\right). \tag{1.9}$$

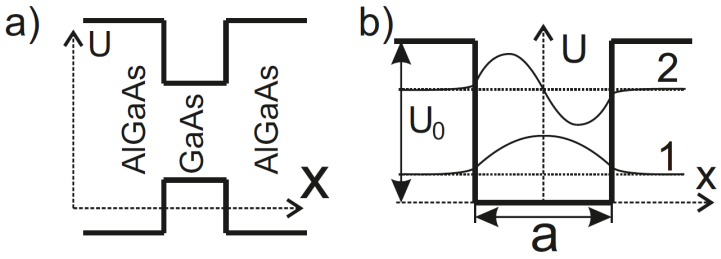

Figure 1.3: a) Energy band diagram of GaAs quantum well. b) Two lower energy levels in quantum well and corresponding symmetric (1) and antisymmetric (2) wave functions. Adopted from Ref. [8].

In the equation above $k = (k_x, k_y)$ is the wave vector in the plane of quantum well, L_z is its thickness and n_z enumerates the z-direction quantized level (see Fig. 1.3). As a result, in the quantum well the exciton energy is shifted by

$$E_{X1}^{QW} = \frac{\hbar^2 \pi^2}{2\mu} \frac{1}{L_z^2}. \tag{1.10}$$

The energy shift induced by the size quantization is visible when irradiating the GaAs quantum well by linearly or circularly polarized light. In most number of semiconductors, the orbital part of the wave function of the electrons in the conduction band originates from the atomic orbitals of s-state symmetry and thus the possible projections of the electron total angular momentum onto the structure growth axis (hereinafter referred to as spin) are equal to $J_e^z = \pm\frac{1}{2}$. On the other hand, the wave functions of a hole in the valence band usually have a an origin the states with p symmetry, and thus the total angular momentum projection (a sum of spin and orbital momentum) is $J_h^z = \pm\frac{1}{2}, \pm\frac{3}{2}$. A similar situation occurs for most semiconductor materials, such as GaAs, Si, Ge, CdTe, etc. The states with the spin projection $J_h^z = \pm\frac{1}{2}$ correspond to light holes and the states with $J_h^z = \pm\frac{3}{2}$ correspond to heavy holes.

The process of creation of an electron-hole pair by a photon should obey the angular momentum conservation law. Fig. 1.4 shows the corresponding selection rules. One sees that in bulk samples, the states of the heavy and light holes at $k = 0$ are degenerate in energy. Thus, regardless of the polarization of light (linear, left circular, or right circular) the energy of such transitions is the same. However, in low-dimensional systems this degeneracy is lifted due to the difference in effective masses of the holes and a non-zero value of the wave vector in the direction(s) of quantum confinement, according to Eq. (1.10). Thus the energy levels of heavy holes are shifted smaller than the levels of light holes. Using the circularly polarized light, one can create spin-polarized distributions of electrons and holes, including both heavy holes and light holes (depending on the light energy). However, the linearly polarized light, being a superposition of σ^+ and σ^-, can not create polarized distributions of holes and electrons. But tuning the energy leaves the possibility to create either heavy holes or light holes.

In the analogy with the electrons and other particles, the quantum value of the total angular momentum can be also introduced for the exciton and in fact it is a sum of electron and hole angular momenta. According to the angular momentum addition theorem [10], the projection of the exciton total angular momentum on the growth axis of the structure

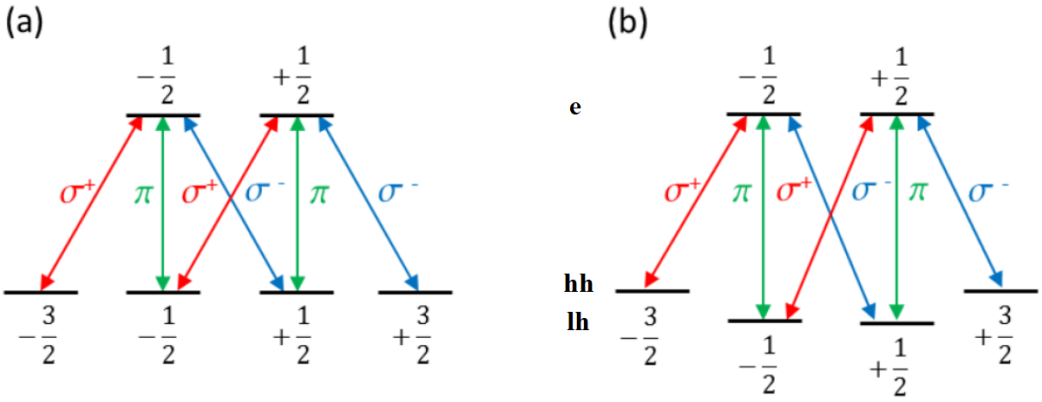

Figure 1.4: Selection rules for bulk semiconductor a) and quantum well b). In the case of quantum wells, one sees the difference in the transition energy due to quantum confinement effect and differing masses of light holes and heavy holes. Red and blue arrows denote right and left circular light polarization, respectively. Green arrow is for linear polarization. Adopted from Ref. [9].

can take the values 0, ±1, or ±2. Again, due to the angular momentum conservation, only the excitons with angular momenta 0, ±1 can interact with light. In the case of ±2 one has the so-called dark excitons. They do not interact with light and lack the possibility to form the polaritons. Meanwhile, the exciton-exciton interactions allow the optical access to the properties of the excitons with extremely low oscillator strength (dark and indirect excitons), see e.g. [11, 12].

The electrons and holes forming the excitons are fermions thus providing the bosonic nature to excitons. However one can not completely avoid the fermionic nature of exciton components and thus, unlike the photon, the phenomenon of exciton-exciton interaction exists basing mostly on the overlap of electron and hole wave functions in the excitons undergoing the scattering process. Despite this, due to bosonic nature, the effect of Bose-Einstein condensation of excitons exists giving a possibility to study the systems of a condensate of a weakly interacting bosons. The phenomenon of Bose-Einstein condensation will be described in more details in Chapter 2.

Depending on the nature of the hosting material, the two limit cases of exciton behavior exist. First, in the materials with low dielectric constants, due to high electron-hole attraction, the radius of exciton is small (of the order of lattice constant) and the energy is high (up to 1 eV). Such exciton has a form of an electron bound to the localized hole (in fact, an ionized atom in the crystal). This situation is also typical for the excitons in molecular crystals, when the exciton is completely localized on the molecule [13, 14]. Such excitons are referred to as Frenkel excitons [15].

Another limit corresponds to the Wannier-Mott excitons typical, for semiconductors [16]. Due to high dielectric constant and small electron mass, the Bohr radius of such excitons exceed drastically the interatomic distance in the crystal up to several orders of magnitude. This limit takes place in the semiconductors considered in present study. Due to the low interaction energy, the energy difference between the states of free electrons and holes and their bound state (exciton) is small, and thus the excitons in such materials

are very sensitive to the temperature. In this sense, the transition metal dichalcogenides (TMD) are perspective due to their high exciton energy, up to several hundreds meV [17, 18].

To conclude the introduction to excitons, it is worth mentioning the so-called Rydberg excitons, corresponding to the states with very high quantum numbers [19, 20, 21], up to $\nu = 25$. Also the biexcitons (an excitonic hydrogen molecule-like quasiparticle) and excitonic ions (trions: two electrons + hole or two holes + electron) can exist [18].

1.1.2 Lifetime of excitons

The very important parameter of excitons, affecting also their possibility to interact with light, is the lifetime. According to Matthiessen rule the expression for the exciton broadening writes [22]:

$$\Gamma_X = \left| \frac{\partial E}{\partial L_z} \langle \delta L_z \rangle \right| + \Gamma_I + \gamma T + \frac{\Gamma_{\mathrm{LO}}}{\exp(\hbar\omega_{\mathrm{LO}}/k_B T) - 1} + \Gamma_0. \tag{1.11}$$

The first term origins from the exciton energy fluctuations (see Eq. (1.9)) due to unavoidable fluctuations of the quantum well width. The second term denotes the scattering by charged impurities and boundary scattering. Next two terms arise from the phonons: third is for acoustic phonons contribution and the fourth for the optical phonons contribution (mainly the longituginal optical phonons). Finally, the intrinsic broadening Γ_0 (according to the terminology used in Ref. [22]) is a combination of multiple processes: radiative decay, exciton-exciton scattering, exciton-carriers scattering etc.

Even in the middle of 90ies, the quantum well technology reached the level where the exciton lifetime overcame hundreds of picoseconds [23]. One sees that in fact the dependencies of broadening of exciton lines on temperature, quantum well width, and carrier concentration are relatively weak (see Fig. 1.5). Thus other intrinsic mechanisms, and importantly, the quality of a structure play the same role. It means that it is difficult to make exciton lifetime sufficiently larger than several nanoseconds and at the same time the exciton lifetime can not be smaller than at least hundreds of picoseconds for all quantum well structures of sufficient quality.

1.1.3 Exciton-exciton interaction in quantum wells

The Hamiltonian of the system of excitons in the presence of exciton-exciton interaction can be written as [24]

$$H = \sum_{\mathbf{k}} E_X(\mathbf{k}) \chi^\dagger_{\mathbf{k}} \chi_{\mathbf{k}} + \sum_{\mathbf{k}} M_{X-X}(\mathbf{k}, \mathbf{k}', \mathbf{q}) \chi^\dagger_{\mathbf{k}+\mathbf{q}} \chi^\dagger_{\mathbf{k}'-\mathbf{q}} \chi_{\mathbf{k}} \chi_{\mathbf{k}'}, \tag{1.12}$$

where $M_{X-X}(\mathbf{k}, \mathbf{k}', \mathbf{q})$ is a matrix element of exciton-exciton interaction. The energy of exciton-exciton interaction consists of the four terms [25]: direct Coulomb interaction, exciton-exciton exchange interaction, electron-electron exchange interaction, and hole-

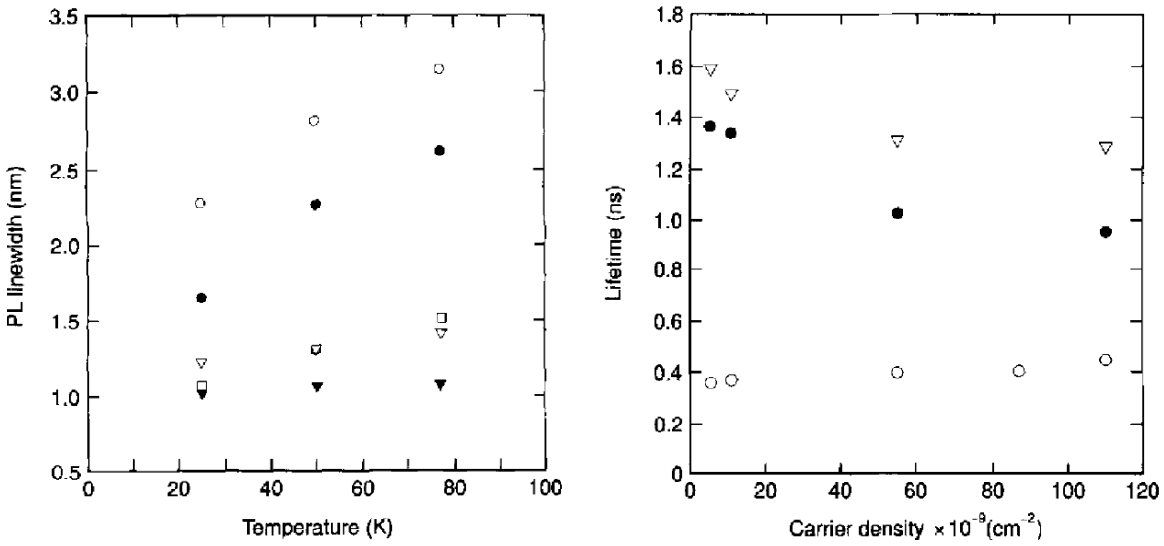

Figure 1.5: Exciton emission broadening and lifetimes in GaAs quantum wells at various temperatures (left panel) and carrier densities (right panel). Adopted from Ref. [23].

hole exchange interaction. The direct Coulomb interaction writes

$$H_{dir}^{X-X}(\mathbf{k},\mathbf{k}',\mathbf{q}) = -\int d\mathbf{r}_e \int d\mathbf{r}_h \int d\mathbf{r}_{e'} \int d\mathbf{r}_{h'}\ \psi_{\mathbf{k}}^{\dagger}(\mathbf{r}_e,\mathbf{r}_h)\psi_{\mathbf{k}'}^{\dagger}(\mathbf{r}_{e'},\mathbf{r}_{h'}) \times V_I(\mathbf{r}_e,\mathbf{r}_h,\mathbf{r}_{e'},\mathbf{r}_{h'})\psi_{\mathbf{k}+\mathbf{q}}(\mathbf{r}_e,\mathbf{r}_h)\psi_{\mathbf{k}'-\mathbf{q}}(\mathbf{r}_{e'},\mathbf{r}_{h'}), \quad (1.13)$$

where V_I is the full energy of the interaction of two excitons being composed of pair-wise contributions for all electrons and holes:

$$V_I(\mathbf{r}_e,\mathbf{r}_h,\mathbf{r}_{e'},\mathbf{r}_{h'}) = V(|\mathbf{r}_e-\mathbf{r}_{e'}|)+V(|\mathbf{r}_h-\mathbf{r}_{h'}|)-V(|\mathbf{r}_e-\mathbf{r}_{h'}|)-V(|\mathbf{r}_h-\mathbf{r}_{e'}|), \quad (1.14)$$

and V is the Coulomb interaction in the medium with the dielectric constant ε

$$V(|\mathbf{r}_e-\mathbf{r}_{e'}|) = \frac{e^2}{\varepsilon r}. \quad (1.15)$$

The exciton-exciton exchange interaction (and also a hole-hole one) writes

$$H_{exch}^{X-X}(\mathbf{k},\mathbf{k}',\mathbf{q}) = -\int d\mathbf{r}_e \int d\mathbf{r}_h \int d\mathbf{r}_{e'} \int d\mathbf{r}_{h'}\ \psi_{\mathbf{k}}^{\dagger}(\mathbf{r}_e,\mathbf{r}_h)\psi_{\mathbf{k}'}^{\dagger}(\mathbf{r}_{e'},\mathbf{r}_{h'}) \times V_I(\mathbf{r}_e,\mathbf{r}_h,\mathbf{r}_{e'},\mathbf{r}_{h'})\psi_{\mathbf{k}+\mathbf{q}}(\mathbf{r}_{e'},\mathbf{r}_{h'})\psi_{\mathbf{k}'-\mathbf{q}}(\mathbf{r}_e,\mathbf{r}_h). \quad (1.16)$$

Finally, the electron-electron exchange interaction has a similar form

$$H_{exch}^{e-e}(\mathbf{k},\mathbf{k}',\mathbf{q}) = -\int d\mathbf{r}_e \int d\mathbf{r}_h \int d\mathbf{r}_{e'} \int d\mathbf{r}_{h'}\ \psi_{\mathbf{k}}^{\dagger}(\mathbf{r}_e,\mathbf{r}_h)\psi_{\mathbf{k}'}^{\dagger}(\mathbf{r}_{e'},\mathbf{r}_{h'}) \times V_I(\mathbf{r}_e,\mathbf{r}_h,\mathbf{r}_{e'},\mathbf{r}_{h'})\psi_{\mathbf{k}+\mathbf{q}}(\mathbf{r}_{e'},\mathbf{r}_h)\psi_{\mathbf{k}'-\mathbf{q}}(\mathbf{r}_e,\mathbf{r}_{h'}). \quad (1.17)$$

The direct Coulomb interaction can be presented in a form

$$H_{dir}(q) = \frac{1}{S}\frac{e^2}{\varepsilon}a_X\left(\frac{2}{\pi}\right)^2 I_{dir}(qa_X), \quad (1.18)$$

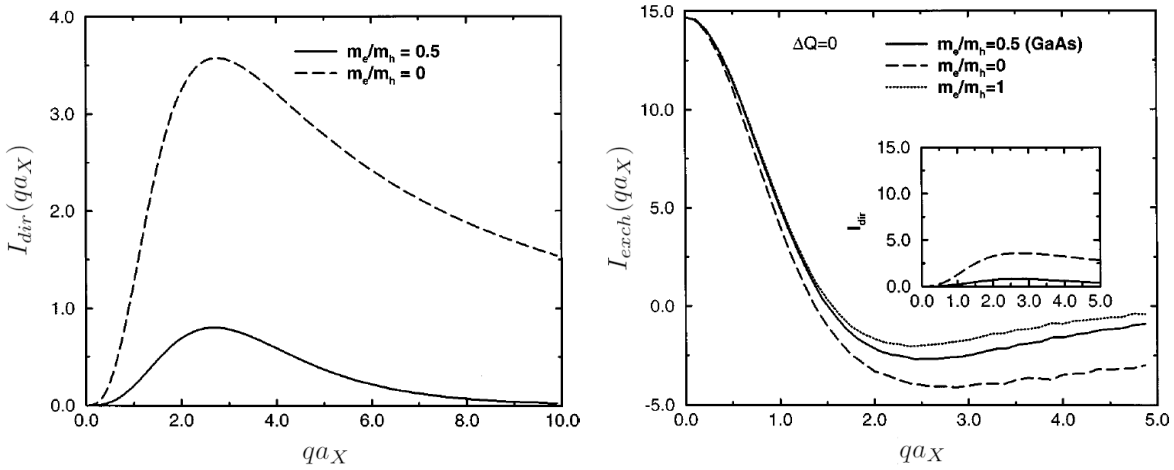

Figure 1.6: Wave vector dependencies of direct Coulomb $I_{dir}(qa_X)$ and electron-electron exchange $I_{exch}(qa_X)$ interactions. Adopted from Ref. [25].

where

$$I_{dir}(qa_X) = \frac{\pi^3}{2qa_X} \cdot f(qa_X). \tag{1.19}$$

and $f(qa_X)$ is a function of the order of unity in magnitude and also depending on the ratio of electron and hole masses m_e/m_h.

In the same manner one writes for the exchange interaction

$$H_{exch}(q) = \frac{1}{S}\frac{e^2}{\varepsilon}a_X \left(\frac{2}{\pi}\right)^2 \cdot I_{exch}(qa_X). \tag{1.20}$$

The direct interaction is a long-range one, but because of its dipole-dipole character it still decays very rapidly. Moreover, the factor I_{dir} stemming from the geometry of the overlapping wave functions is small. It drastically depends on the ratio of the electron and hole masses. For $m_e/m_h \approx 0.5$ this factor is 4 times smaller than for the model case $m_e/m_h = 0$. The exchange interaction regulated by I_{exch} is short range and vanishes nearly at the distances of Bohr radius ($qa_X \approx 4$). Fig. 1.6 shows the wave vector dependencies of the function $I_{dir}(qa_X)$ and $I_{exch}(qa_X)$.

The relevant wave vectors for the physics of polaritons are units of reciprocal microns. It means that $qa_X \ll 1$. In this limit the exciton-exciton interaction is governed by the exchange interaction and one can make the following estimation:

$$M = 6E_X a_X^2. \tag{1.21}$$

For the GaAs excitons, the estimation $M \approx 7$ meV$\cdot\mu$m^2 is actual. To obtain the potential energy shift, which is experienced by the excitons due to interaction with other excitons, one should multiply M by the density of excitons.

1.2 Photons in microcavities

Historically, the development of the lasers has contributed drastically to the semiconductor technology, especially for the heterostructures and microcavities. By the nature, the lasers require a presence of some active medium (i. e. the hetero-structure in the case of semiconductor lasers), to create in it a population inversion, and a high-quality resonator for the photons. The active medium of semiconductor lasers (namely the quantum well) is created with various types of epitaxy processes. The resonators (Fabry-Perot) can be formed by mirrors made of polished heterostructure edges and in this case the light propagation direction is parallel to the heterojunction plane.

However, the resonators can be formed by the epitaxial Bragg mirrors (distributed Bragg reflector, DBR) above and below the active region. Using this geometry, a vertical-cavity surface-emitting laser can be manufactured [26]. The structure of the same type is essential for the fundamental studies of the interaction of light and excitons in the semiconductors and of the formation of a light-matter quasiparticle called exciton-polariton.

The Bragg mirror is a one-dimensional superlattice of alternating layers of semiconductors or dielectrics with different refractive indices n_i. Bragg mirror functions properly when the layer thicknesses d_i are chosen so that the energy of the photonic stopband (photonic band gap) lies in the desired interval, determined by the energy of the exciton transition in the quantum well. This relation reads $d_i = \lambda/4n_i$. The reflection coefficient for a Bragg Mirror reads [27, 28]:

$$R = \left[\frac{\left(\frac{n_2}{n_1}\right)^{2N} - \frac{n_f}{n_0}}{\left(\frac{n_2}{n_1}\right)^{2N} + \frac{n_f}{n_0}} \right]^2, \tag{1.22}$$

where n_0 and n_f are the refractive indices before and after the mirror composed of N layers of materials with the indices n_1 and n_2.

Secondly, the distance between the two DBRs should be proportional to an integer number of half-wavelengths of light in this medium (photon energy should be near the center of photonic stopband). These two conditions provide the longest possible lifetime of a photon in the cavity. The materials for the DBRs are chosen to provide sufficient contrast in refractive indices and also should have close values of lattice constant to obtain defect-free structures, see Fig. 1.7 for the diagram of refractive index versus lattice constants for various materials. Fig. 1.8 shows the typical wavelength dependencies of the reflectivity of the DBR structures of different materials.

The photon dispersion in the planar microcavity differs from the dispersion of a photon in free space. And the confinement effect plays again a crucial role in this. For the energy of a photon in free space one writes

$$E_{ph} = \hbar c^* \sqrt{k_x^2 + k_y^2 + k_z^2}, \tag{1.23}$$

where $c^* = \frac{c}{\sqrt{\varepsilon}}$ is the light velocity in the medium.

In the case of Bragg mirrors lying within (x,y) plane, the wave vector k_z in the direction perpendicular to the mirrors becomes quantized according with the distance between the mirrors: $k_z = n_z \frac{\pi}{L_z}$ (see Fig. 1.9). As a result, using the Taylor expansion, one obtains the photon dispersion in the form

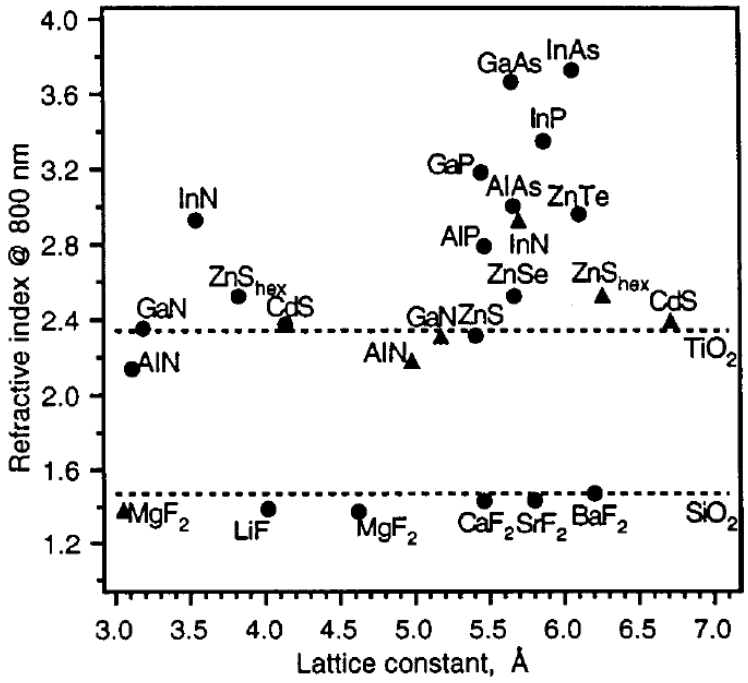

Figure 1.7: The values of refractive indices for various materials. Adopted from [29]

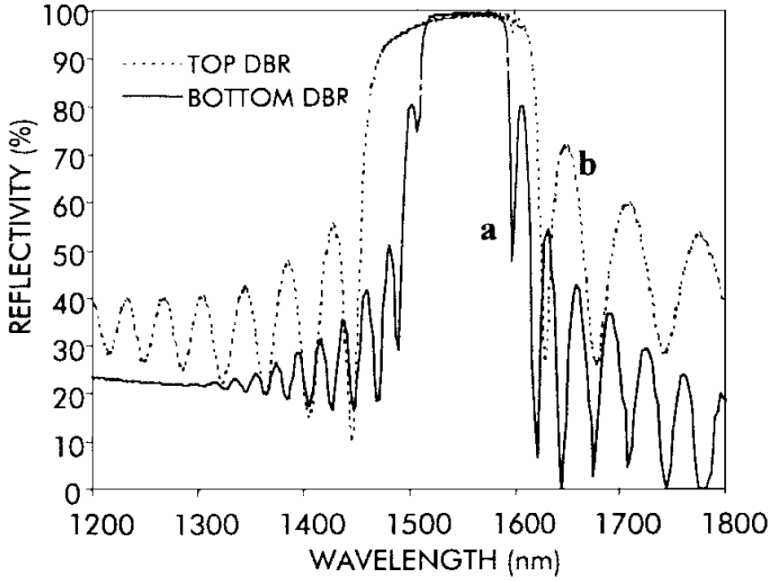

Figure 1.8: Wavelength dependence of reflectivity for (a) InGaAsP–InP DBR structure and (b) GaAs–AlAs DBR structure. Adopted from Ref. [30].

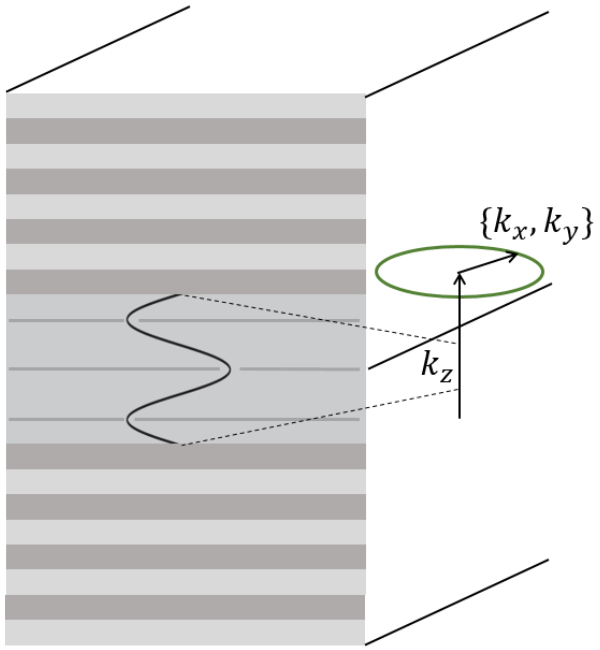

Figure 1.9: Photon wave vector in the microcavity formed of two Distributed Bragg Reflectors.

$$E_{ph} = \hbar c^* \sqrt{k^2 + k_z^2} \approx \hbar c^* k_z + \frac{h^2 k^2}{2m_C}, \tag{1.24}$$

where the cavity photon mass is defined by

$$m_C = \frac{\hbar k_z}{2c^*}. \tag{1.25}$$

The parameter n_z controls a number of nodes of a standing wave in the resonator and one can tune it to control the strength of photon-exciton coupling. Namely, with increasing n_z the number of nodes of electromagnetic field also increases and placing multiple quantum wells (see Fig. 1.10) at the antinodes of the field, one also increases the light-matter interaction which is crucial to obtain the regime of strong light-matter coupling.

1.3 Strong light-matter coupling

1.3.1 Full Hamiltonian

The problem of exciton interaction with light is dating back to the pioneering works of Hopfield [31]. To write the corresponding Hamiltonian, one should firstly write the energy of dipole interaction of a certain material system and the electromagnetic field [32]:

$$U = -\mathbf{d} \cdot \mathbf{E}, \tag{1.26}$$

where $\mathbf{d}$ is the dipole moment of this material system and $\mathbf{E}$ is the electric field. This equation corresponds to the first order term in the magnitudes of electric moments and

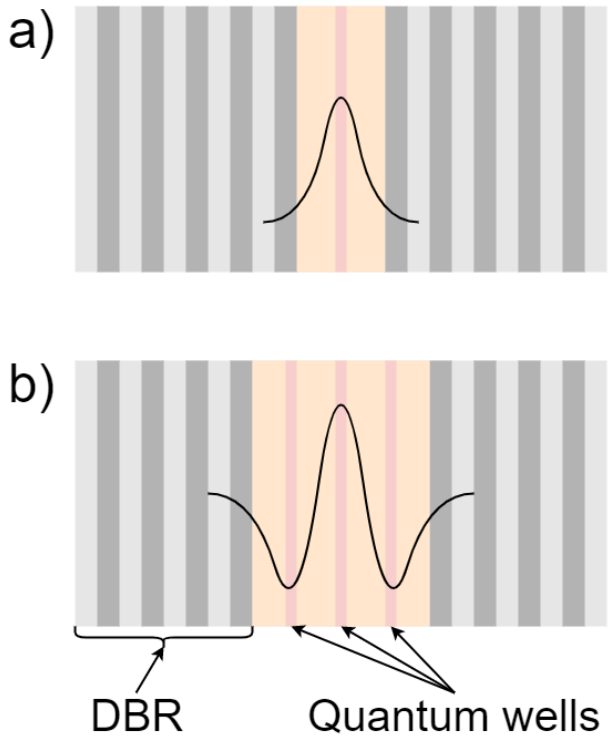

Figure 1.10: Sketch of cavity photon mode. The cases of single QW in the microcavity a) and triple quantum well b). In the latter case the photonic $n_z = 3$ mode is tuned to have the antinodes overlapping with quantum wells.

electric field, while for some cases the higher order electric multipoles play a role. Also a magnetic field integrating with magnetic dipole moment of the system can be of interest in some situations. To rewrite Eq. (1.26) in terms of quantum mechanics, one replaces the classical dipole moment with the dipole moment, which corresponds to transition between two electronic states (initial i and final f):

$$\mathbf{d} \rightarrow \hat{\mathbf{d}}_{if} = e \int d\mathbf{r} \psi_f^*(\mathbf{r}) \mathbf{r} \psi_i(\mathbf{r}). \tag{1.27}$$

In terms of creation and annihilation operators for material excitations corresponding to transitions between these states $\hat{\mathbf{d}} = d_{eg}\mathbf{x}(\sigma + \sigma^\dagger)$, where $\mathbf{x}$ gives the direction of the dipole vector and d_{eg} is a factor of the order of atomic dipole moment. The latter estimation can be straightly understood from the form of integral in Eq. (1.27).

The electric field magnitude can be also expressed via the quantized (ladder) operators in the cavity (3.75, [33]):

$$\mathbf{E} = \mathbf{e}\sqrt{\frac{\hbar\omega}{2V}} \cdot (\phi e^{-i\omega t} + \phi^\dagger e^{i\omega t}), \tag{1.28}$$

where ω is the photon mode frequency, $\phi^\dagger$ and ϕ are creation and annihilation operators for the photons, V is the volume accessible to the photon and $\mathbf{e}$ is the polarization.

1.3.2 Hamiltonian of light matter interaction for the case of polaritons

To describe the light-matter interaction in the microcavities the following Hamiltonian in the second quantization form is used [33]:

$$H = E_C\phi^\dagger\phi + E_X\chi^\dagger\chi + hg(\phi + \phi^\dagger)(\chi + \chi^\dagger), \tag{1.29}$$

where $\phi^\dagger$ and ϕ are creation and annihilation operators for cavity photons. Here we assume that a single cavity photon mode (C) as well as a single exciton (X) mode couple together in the system. First term describes the presence of a photon of the energy E_C in the cavity and the second one is for an exciton with energy E_X. The creation and annihilation operators are renamed to reflect now the excitonic and photonic nature of the particles. The third term describes the exciton-photon interaction.

One sees the presence of the operators combinations $\phi\chi$ and $\phi^\dagger\chi^\dagger$ stemming from the third term of Eq. (1.29). These terms are off-resonant and correspond to presence of both cavity photon and QW exciton or the absence of both (virtual states). Sometimes it is important to take these into account, however, in most cases the Hamiltonian can be simplified by omitting these terms:

$$H = E_C\phi^\dagger\phi + E_X\chi^\dagger\chi + hg(\phi\chi^\dagger + \phi^\dagger\chi), \tag{1.30}$$

Let us also introduce in the Hamiltonian the wave vector $\mathbf{k}$ dependencies for the cavity photons and QW excitons. Accounting for energy dispersion relations is essential for polaritons. After this the Hamiltonian takes a form

$$H_{\mathbf{k}} = E_C\left(\mathbf{k}\right)\phi_{\mathbf{k}}^\dagger\phi_{\mathbf{k}} + E_X\left(\mathbf{k}\right)\chi_{\mathbf{k}}^\dagger\chi_{\mathbf{k}} + \hbar\Omega_R\Big(\phi_{\mathbf{k}}^\dagger\chi_{\mathbf{k}} + \chi_{\mathbf{k}}^\dagger\phi_{\mathbf{k}}\Big), \tag{1.31}$$

where $E_C(k)$ and $E_X(k)$ are the introduced above dispersion relations for cavity photon and exciton, Ω_R is half-Rabi splitting controlling the strength of photon-exciton interaction. $\phi_{\mathbf{k}}^\dagger$ and $\phi_{\mathbf{k}}$ are creation and annihilation operators, respectively, for cavity photon with wave vector $\mathbf{k}$, and $\chi_{\mathbf{k}}^\dagger$ and $\chi_{\mathbf{k}}$ are creation and annihilation operators for quantum well excitons.

In the matrix form this Hamiltonian can be rewritten as

$$M = \begin{pmatrix} E_C\left(\mathbf{k}\right) & \hbar\Omega_R \\ \hbar\Omega_R & E_X\left(\mathbf{k}\right) \end{pmatrix}, \tag{1.32}$$

where the vector $(1,0)^T$ corresponds to the presence of cavity photon and no exciton and $(0,1)^T$ to presence of the exciton and absence of the photon. As mentioned above, the exciton mass is comparable with the effective masses of electrons and holes, and thus to the mass of a free electron. For the cavity photon, one can estimate $m_C \approx 5 \cdot 10^{-5} m_0$. Thus with sufficient accuracy the exciton dispersion can be considered as flat. Let us denote the detuning Δ as a difference between the energies of cavity photon with zero wave vector and exciton energy:

$$\Delta = E_C(0) - E_X. \tag{1.33}$$

Diagonalization of the Hamiltonian leads to the following energies of the two eigenstates, the first corresponding to the lower polariton branch:

$$E_L(\mathbf{k}) = \frac{1}{2}\left(E_\phi(\mathbf{k}) + E_\chi(\mathbf{k}) - \sqrt{\left[E_\phi(\mathbf{k}) - E_\chi(\mathbf{k})\right]^2 + 4\hbar^2\Omega_R^2}\right), \tag{1.34}$$

and the second to the upper polariton branch

$$E_U(\mathbf{k}) = \frac{1}{2}\left(E_\phi(\mathbf{k}) + E_\chi(\mathbf{k}) + \sqrt{\left[E_\phi(\mathbf{k}) - E_\chi(\mathbf{k})\right]^2 + 4\hbar^2\Omega_R^2}\right). \tag{1.35}$$

The polariton dispersions at various values of detuning are plotted in Fig. 1.11. From the first two terms in Eqs. (1.35) and (1.34) it can be seen that the mass of polariton writes (at low wave vectors):

$$\frac{1}{m_{pol}} \approx \frac{1}{2}\left(\frac{1}{m_X} + \frac{1}{m_C}\right). \tag{1.36}$$

Due to the high exciton mass, one directly estimates with very high accuracy $m_{pol} = 2m_X$. In the plot with actual scales, the exciton dispersion is completely flat. Index U corresponds to the upper polariton branch and index L corresponds to the lower polariton branch. In fact, this diagonalization allows rewriting the Hamiltonian (1.31) in the polariton basis:

$$H_\mathbf{k} = E_U(\mathbf{k})\, u_\mathbf{k}^\dagger u_\mathbf{k} + E_L(\mathbf{k})\, l_\mathbf{k}^\dagger l_\mathbf{k}, \tag{1.37}$$

where $u^\dagger$ and u are the creation and annihilation operators for the upper polariton branch and $l^\dagger$ and l are the creation and annihilation operators for the lower polariton branch with the following definition:

$$u_\mathbf{k}, l_\mathbf{k} = X_{U,L}(\mathbf{k})\chi_\mathbf{k} + C_{U,L}(\mathbf{k})\phi_\mathbf{k}, \tag{1.38}$$

where $X_{U,L}(\mathbf{k})$ and $C_{U,L}(\mathbf{k})$ are the Hopfield coefficients whose dispersion is drawn in Fig. 1.12 for various values of detuning.

The Hopfield coefficients are expressed as:

$$C_U(\mathbf{k}) = X_L(\mathbf{k}) = \frac{E_U(\mathbf{k}) - E_X(\mathbf{k})}{\sqrt{\hbar^2\Omega_R^2 + \left(E_U(\mathbf{k}) - E_X(\mathbf{k})\right)^2}}, \tag{1.39}$$

and

$$X_U(\mathbf{k}) = -C_L(\mathbf{k}) = \frac{\hbar^2\Omega_R^2}{\sqrt{\hbar^2\Omega_R^2 + \left(E_U(\mathbf{k}) - E_X(\mathbf{k})\right)^2}}. \tag{1.40}$$

Once the strong coupling regime is achieved (the difference between strong and weak coupling regime implies accounting for the lifetime and it will be explained in the next section), one can use the so-called parabolic approximation to write the Schrödinger equation for polaritons (either from the lower polariton branch or from the upper polariton branch):

$$i\hbar\frac{d}{dt}\psi(\mathbf{r},t) = \left[-\frac{\hbar}{2m}\nabla^2 + U(\mathbf{r})\right]\psi(\mathbf{r},t), \tag{1.41}$$

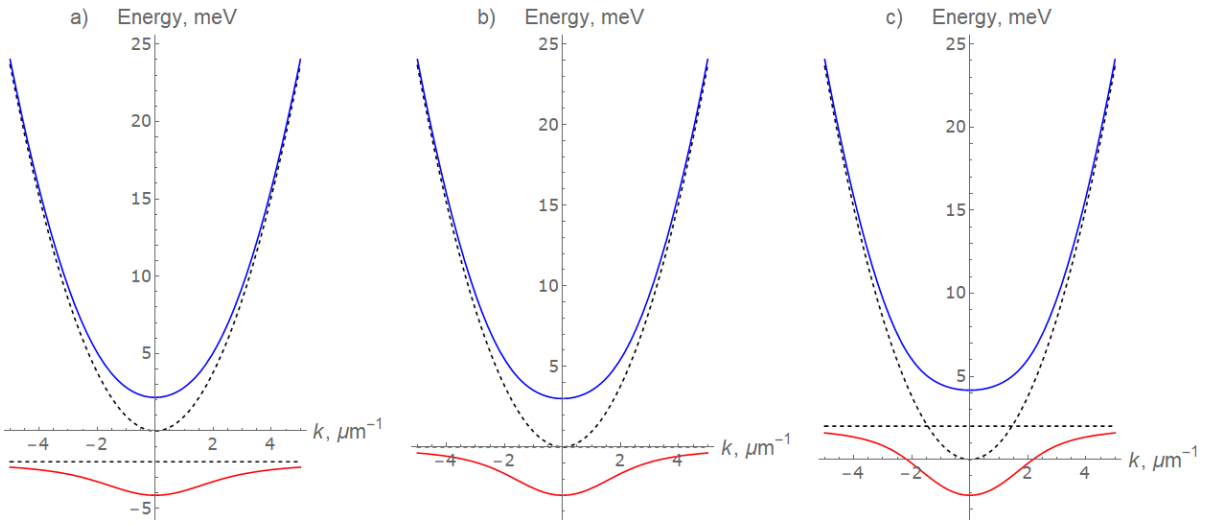

Figure 1.11: Dispersion of polaritons obtained based on the dispersion of exciton (horizontal dashed line) and cavity photon (dashed parabola). The obtained lower polariton branch (LP) is given in red and the upper polariton branch (UP) is given in blue. Panel a) is for positive detuning $\Delta = 2$ meV, panel b) is for zero detuning, and panel c) is for negative detuning $\Delta = -2$ meV. We have used a Rabi splitting of $\hbar\Omega_R = 3$ meV, typical for a single quantum well cavity.

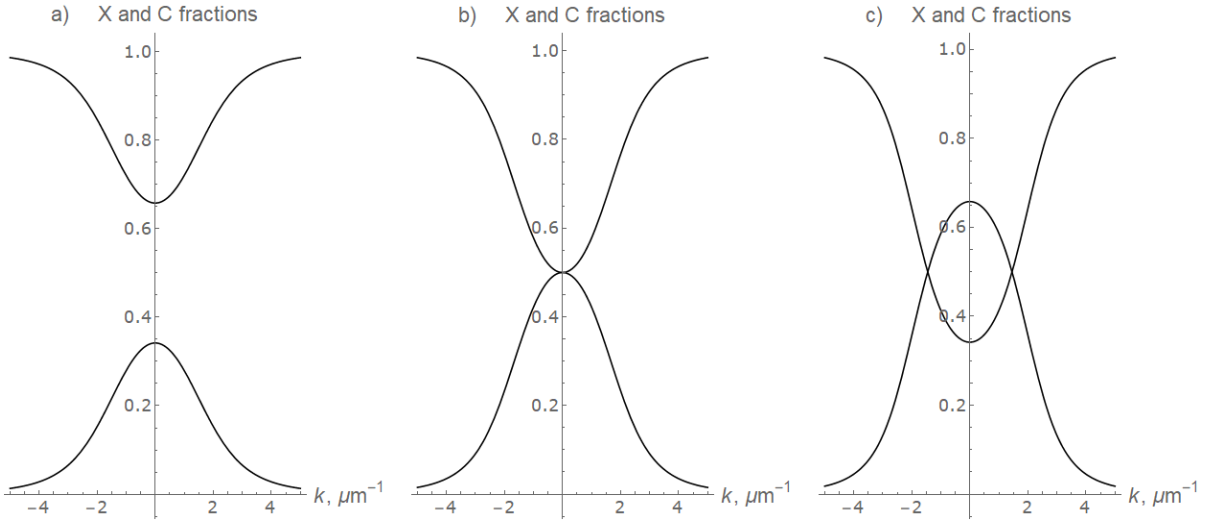

Figure 1.12: Excitonic and photonic fracions in terms of Hopfield coefficients (namely their squares $|X_{U,L}(\mathbf{k})|^2$ and $|C_{U,L}(\mathbf{k})|^2$) for LP branch. Panel a) is for positive detuning $\Delta = 2$ meV, panel b) is for zero detuning, and panel c) is for negative detuning $\Delta = -2$ meV.

where m is polariton mass and $U(\mathbf{r})$ is the potential experienced by the polaritons, engineered in reality by etching the microcavity, spatial modulation of the quantum well thickness, interaction with exciton reservoir *etc.*

Concluding, exciton-polaritons are composite quasiparticles whose wave function is a superposition of exciton and photon wave functions. In this regard, polaritons inherit the properties of light with the properties of material excitations (excitons). So, their effective mass is extremely small and in order of magnitude coincides with the effective mass of the photon mode of the resonator. On the other hand, due to the presence of an exciton component, polaritons retain the ability to effectively interact with each other, acoustic and optical phonons, and free electrons.

The polaritons were obtained as a solutions of the first step of a Jaynes-Cummings/bosons ladder, see Fig. 5.7 from [33].

1.3.3 Lifetime concept in the system of coupled excitons and photons

Despite the description within the Hamiltonian formalism in quantum mechanics is correct for conservative systems only, very important results on exciton-photon coupling can be obtained when introducing the particle (excitons and photons) decay into the Hamiltonian (1.32). In previous subsection, we did not account for cavity photon and exciton lifetimes, the quantities which have a crucial importance for the principal possibility of polariton existence as a composite exction-photon quasiparticle.

Despite the restrictions of the Hamiltonian approach, the lifetime can be straightforwardly be added to the Hamiltonian as an imaginary part of the energies of excitons and photons:

$$M_{\mathbf{k}} = \begin{pmatrix} E_C(\mathbf{k}) - i\hbar\Gamma_C & \hbar\Omega_R \\ \hbar\Omega_R & E_X(\mathbf{k}) - i\hbar\Gamma_X \end{pmatrix}, \tag{1.42}$$

where the decay rates are defined through the lifetimes:

$$\Gamma_C = \frac{1}{2\tau_C},\ \Gamma_X = \frac{1}{2\tau_X}. \tag{1.43}$$

In the case of zero detuning and for the bottom of the dispersions (zero wave vector condition: $E_X(0) = E_C(0) = E_0$), one obtains the following equation for the polariton energies for upper and lower branches:

$$E_{U,L}(0) = E_0 - i\hbar\frac{\Gamma_X + \Gamma_C}{2} \pm \frac{\hbar}{2}\sqrt{-\left[\Gamma_X - \Gamma_C\right]^2 + 4\Omega_R^2}. \tag{1.44}$$

The two possibilities exist:

1. $|\Gamma_X - \Gamma_C| > 2\Omega_R$ corresponds to a *weak coupling regime*, where the real parts of the energies of the eigenstates of a coupled system in resonance are equal to each other (crossing of exciton and cavity photon dispersions). The difference is present in the imaginary parts of the energies corresponding to the line widths and thus the lifetimes of elementary excitations. Thus the exciton-like excitation and photon-like excitation exist and decay separately. In the case of $\Omega_R \ll \Gamma_X, \Gamma_C$ one obtains

$$E_{U,L}(0) \approx E_0 - i\hbar\Gamma_{C,X}, \tag{1.45}$$

which means that exciton and photon do not feel each other, for each of them one observes the specific decay rate. However, in the more realistic case $\Gamma_C > \Omega_R > \Gamma_X \approx 0$, one obtains from Eq. (1.44) the following expressions for the values of line broadening of cavity photon and exciton:

$$\begin{aligned} \Gamma'_C &\approx \Gamma_C, \\ \Gamma'_X &\approx \frac{4\Omega_R^2}{\Gamma_C}, \end{aligned} \tag{1.46}$$

where the values with primes are for the broadenings with accounting for the interaction. One sees the increasing of the exciton broadening (in fact increasing the intensity of emission) due to interaction with the cavity photon mode, or the so called Purcell effect [34].

2. $|\Gamma_X - \Gamma_C| < 2\Omega_R$ corresponds to the *strong coupling regime*, where the anti-crossing of the dispersion branches takes place and an energy splitting between the upper and lower polariton branches, called Rabi splitting ($2\Omega_R$), is observed at the intersection point ($k = 0$). The second term in Eq. (1.44) corresponds to the decay rate of the excitations (exciton-polaritons).

This behavior can be understood in the following way. Inverse Rabi frequency is in fact the time of conversion of the excitation between the excitonic and the photonic states. If the lifetime of the photonic or the excitonic state is lower than the inverse Rabi frequency, it means that the collective excitation does not have enough time to experience the exchange between the photonic and the excitonic states. As a result, these states become completely independent. Fig. 1.13 shows the dispersions of the system of coupled exciton and cavity photon at various photon lifetimes with the transition between the strong and the weak coupling regimes.

This reasoning can be committed by the argument that the Rabi frequency is to be compared with the quantity $|\Gamma_X - \Gamma_C|$. Indeed, if the excitonic and the photonic components decay synchronously, the strong coupling regime will be also achieved. However, in practice, if $\Gamma_{X,C} \gg \Omega_R$, one will not be able to resolve the upper polariton branch and the lower polariton branch because the broadening would be larger than the distance between the modes. Actually, the lifetime of cavity photons is much less than the lifetime of the excitons and therefore it is reasonable to compare the Rabi frequency Ω_R with the reciprocal cavity photon lifetime Γ_C.

The transition between weak and strong coupling regimes is tightly connected with the physics of the PT symmetric systems [35], the systems with the non-Hermitian "Hamiltonian" but possessing real (not complex) eigenvalues. In the terms of two level system with 2x2 Hamiltonian, the time inversion operator $\hat{T}$ is the complex conjugate and the parity operator $\hat{P}$ is a σ_x Pauli matrix. Applying the $\hat{P}\hat{T}$ transformation one obtains [36, 37]:

$$\hat{H}|\psi\rangle = E|\psi\rangle \xrightarrow{\hat{P}\hat{T}} \hat{P}\hat{T}\hat{H}\hat{T}\hat{P}|\psi\rangle = \hat{P}\hat{T}E\hat{T}\hat{P}|\psi\rangle = E^*|\psi\rangle. \tag{1.47}$$

In the case of PT invariance of the Hamiltonian one obtains:

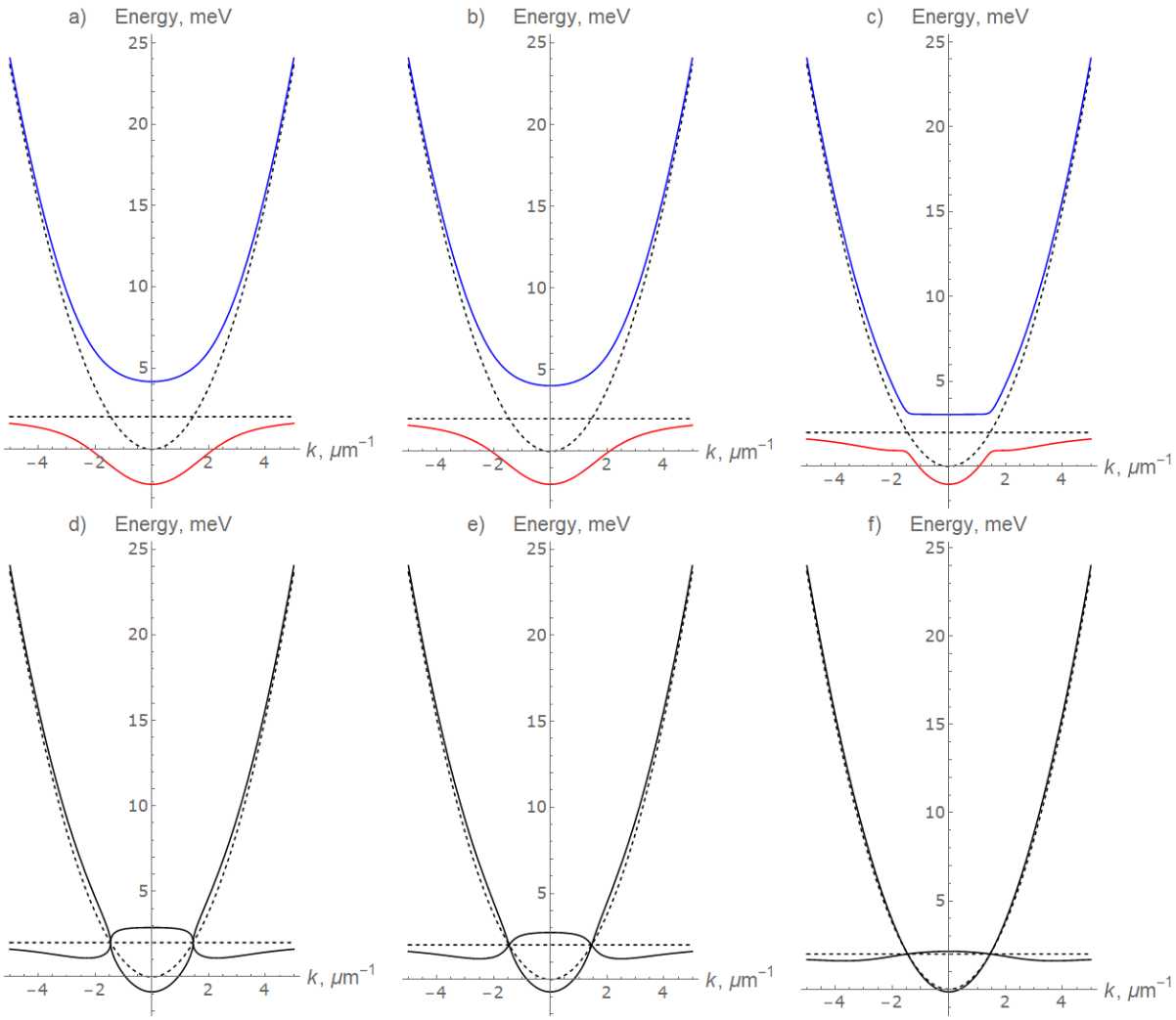

Figure 1.13: Upper row: strong coupling regime. Dispersion of polaritons obtained based on the dispersion of exciton (horizontal dashed line) and cavity photon (dashed parabola), the detuning is negative: $\Delta = -2$ meV and $\hbar\Omega_R = 3$ meV. The obtained lower polariton branch (LP) is given in red and the upper polariton branch (UP) is given in blue. Panel a) is for broadening $\Gamma = 0$ meV, panel b) is for broadening $\Gamma = 2$ meV and panel c) is for broadening $\Gamma = 5.5$ meV. In the lower row broadening reaches $2\Omega_R$ and thus the weak coupling regime is realized and no polariton as a quasiparticle exists. In fact only the perturbed dispersion of the cavity photon and an exciton remain. Panel d) is for broadening $\Gamma = 6$ meV, panel e) is for broadening $\Gamma = 6.5$ meV and panel f) is for broadening $\Gamma = 12$ meV.

$$E^* = E, \tag{1.48}$$

which corresponds to the real eigenvalues. The PT invariant Hamiltonian in its general form writes as [36]

$$H_{\mathrm{PT}} = \begin{pmatrix} re^{i\theta} & s \\ s & re^{-i\theta} \end{pmatrix}, \tag{1.49}$$

with real parameters θ, r, and s.

Obviously the Hamiltonian (1.42) can decomposed into the following sum:

$$M = H_{\mathrm{PT}} + H_{\mathrm{Losses}} + H_{\mathrm{Zeeman}}, \tag{1.50}$$

where

$$H_{\mathrm{Losses}} = \begin{pmatrix} -ig & 0 \\ 0 & -ig \end{pmatrix}, \tag{1.51}$$

and

$$H_{\mathrm{Zeeman}} = \begin{pmatrix} d/2 & 0 \\ 0 & -d/2 \end{pmatrix}. \tag{1.52}$$

The second term defines the common part of the decay of the two components of a wave function and the thid one shows the energy difference between the two states, while namely the first term defines if decay is synchronous (real eigenvalues of H_{PT} and realization of strong coupling regime) or not (weak coupling regime). Obviously, the condition for strong coupling regime expressed in the terms of r, s and θ is the same as for the formulation via Rabi splitting and photon and exciton line widths.

Experimentally, the polariton dispersion is measured by the angle resolved photoluminescence [38, 39]. This experiment is based on the fact that the in-plane wave vector $k = \sqrt{k_x^2 + k_y^2}$ defines the angle at which the light leaves the microcavity (see Fig. 1.9), and this angle is $\arctan(k/k_z)$. Thus collecting light from various directions and sending it to the spectrometer one obtains the dispersion in terms of $E(k)$ or even $E(\mathbf{k})$ if the dispersion is anisotropic in the cavity plane. Fig. 1.14 shows an example of such a dispersion. The sample was a 3.5 μm thick nanowire with a Rabi splitting of 15 meV and a cavity photon lifetime 15 ps. The formation of 1D sub-bands due to the confinement effect is also visible.

Using the same reasoning as for the polariton mass, one can conclude that the lifetime of polaritons is approximately two times larger than the lifetime of photons:

$$\Gamma_{pol} \approx \frac{1}{2}\left(\Gamma_X + \Gamma_C\right), \tag{1.53}$$

and as far as typically $\Gamma_X \ll \Gamma_C$, one indeed concludes that $\tau_{pol} = 2\tau_C$. This picture can be also understood in the following manner. If the Hopfield coefficients are equal (in the case of resonance), for one half of all time polariton exists in the photonic state and another half of time in the excitonic state. And existing in the cavity photon state the polariton experiences the rapid decay as a photon. On the other hand, while being in the excitonic state, there is no significant decay of the polariton.

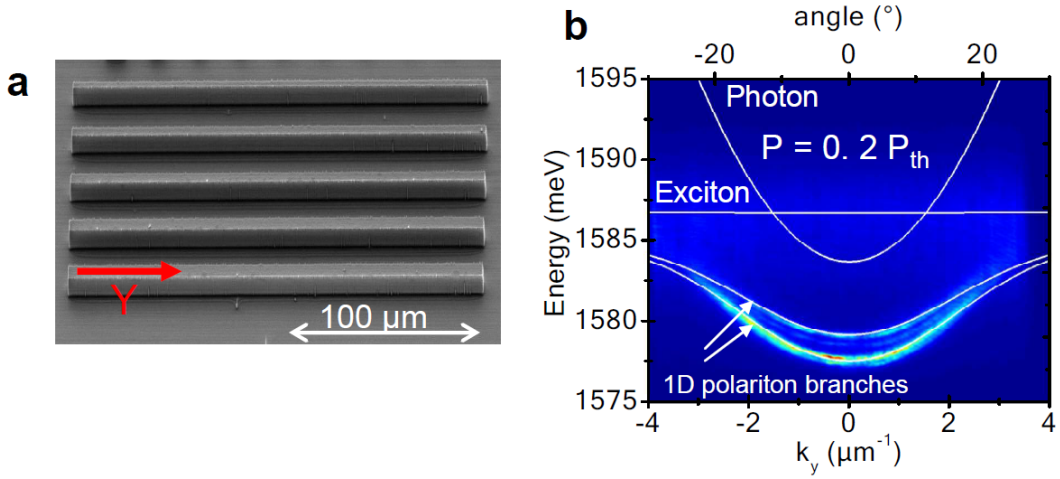

Figure 1.14: Experimentally observed dispersion (b) in a cavity in the shape of a wire (a). The horizontal axis is given both in reciprocal microns and in degrees of the emission angle. Adopted from Ref. [40].

1.3.4 Values of lifetimes and Rabi splitting in modern microcavities

In this subsection we would like to outline the parameters of several real microcavities, which are currently investigated in the context of polariton-based quantum fluids. A significant number of results on the polariton quantum fluids were obtained in the laboratory LKB in Paris by the group of Prof. Alberto Bramati [41, 42, 43, 44, 45] using the cavity introduced in Ref. [46]. We pay a special attention to the parameters of this sample, because these parameters were used to obtain the results of **Chapter 3** on the solitons and vortex chains in polariton quantum fluid. Taking the parameters of a really existing cavity allowed to provide a direct connection of the theoretical predictions with a real experiment and opened up a possibility of very rapid verification of the results. Also, the description of this device allows to explicitly indicate a lot of important cavity parameters, introduced and used in the equations in previous sections. This device was a GaAs/AlGaAs microcavity with 21/24 (front/back) layers of DBR and $In_{0.04}Ga_{0.96}As$ quantum wells at each of the three antinodes of the confined electromagnetic field. The experiments with this cavity should be performed in the cryostat below 10 K (0.86 meV). The exciton energy is 1.485 eV, the cavity exciton-photon detuning is negative (-1.4 meV) and the half Rabi splitting V is 2.55 meV. This yields a polariton mass $\approx 5 \cdot 10^{-5}$ free electron mass. The polariton lifetime in this cavity is ~ 14 ps.

A similar value of the Rabi splitting was observed in a cavity in Ref. [47]. However, the Rabi splitting can be several times larger in semiconductor mircicavities: up to 15 meV [48] for a GaAs active region. In Ref. [40], the Rabi splitting was of the same magnitude (15 meV) and a cavity photon life time was around 15 ps. In wide-bandgap materials (like ZnO) the values of Rabi splitting can reach 100-200 meV [49, 50, 51, 52]. In the sample used in Ref. [53], the lifetime was as large as several hundred ps with a Rabi splitting of 16 meV, which makes this sample one of the most advanced for the present day. This value of polariton lifetimes opens up possibilities to investigate even the outstanding

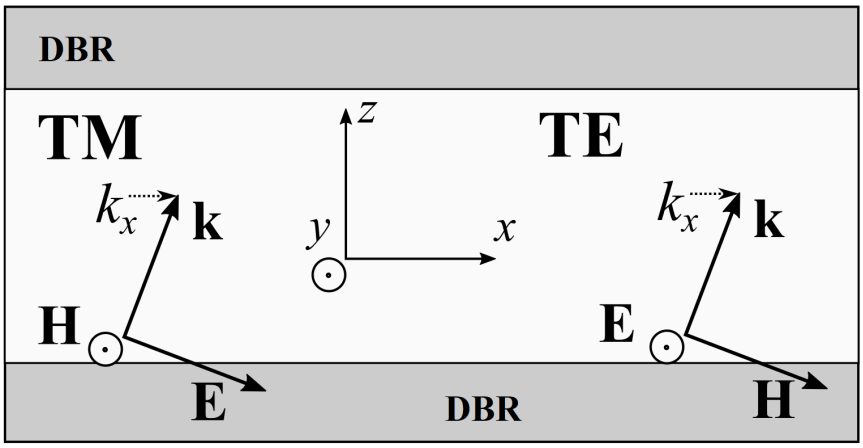

Figure 1.15: Difference in the geometry of TE-TM modes. The growth axis is z axis.

by the complexity behavior in the systems of turbulent quantum fluids. The values of Rabi splitting up to 15 meV can be achieved by the usage of multiple, e.g. 12 quantum wells for the excitons. Concluding, for the most relevant for this research GaAs-based microcavities, typical values of photon lifetimes are 15 ps (0.3 meV) and Rabi splitting reaches 15 meV. In the state-of-the-art one can expect 10 times larger lifetime.

1.3.5 TE-TM splitting

As for other type of waveguides and resonators, in semiconductor microcavities exist TE (transverse-electric) and TM (transverse-magnetic) modes differing in the directions of electrical and magnetic field with respect to the plane of growth. When in-plane wave vector of light differs from 0, the electric and magnetic fields penetrate to the mirrors differently for TE and TM modes see. Fig. 1.15. As a result the energies of such modes also become different, giving an origin for the effect of **k**-dependent TE-TM splitting. Obviously, at zero wave vector, TE and TM modes have the same energy.

Additional contribution comes from the splitting of excitons [54, 55]. The effect of TE-TM splitting can be expressed as a difference between longitudinal and transverse polariton masses. As a result, in a basis of circular polarizations one can write

$$\Delta E_{LT} = \begin{pmatrix} 0 & \beta_{LT}(k_y - ik_x)^2 \\ \beta_{LT}(k_y + ik_x)^2 & 0 \end{pmatrix}, \tag{1.54}$$

where β_{LT} is an effective constant of the TE-TM splitting that can be written via the longitudinal and transverse polariton masses as

$$\beta_{LT} = \frac{\hbar^2}{4}\left(\frac{1}{m_L} - \frac{1}{m_T}\right). \tag{1.55}$$

1.4 Driven-dissipative Gross-Pitaevskii equation for cavity Polaritons

1.4.1 Gross-Pitaevskii equation for cavity Polaritons

The photon-photon interaction in microcavities due to Kerr effect and related phenomena is weak, except the case when the interactions are mediated by material excitations (excitons). Due to their excitonic component, the polaritons can interact with each other. The equation for the polariton wave function accounting for such polariton-polariton interaction reads

$$i\hbar\frac{\partial}{\partial t}\psi(\mathbf{r},t)=\left[-\frac{\hbar^2\nabla^2}{2m_{pol}}+\int\psi^\dagger(\mathbf{r}',t)V(\mathbf{r}-\mathbf{r}')\psi(\mathbf{r}',\mathbf{t})\mathrm{d}\mathbf{r}'+U(\mathbf{r},t)\right]\psi(\mathbf{r},t), \tag{1.56}$$

where m_{pol} is the polariton mass and $V(r)$ is the interaction potential between two polaritons separated by a distance r and $U(\mathbf{r})$ is the external potential for the polaritons. By the structure, the interaction term in this equation is similar to the case of interacting excitons (see Eq. (1.13)).

As it was pointed out above, the polariton-polariton interaction is governed by the repulsion of the excitons in the excitonic components, which is mainly exchange short-range interaction with the characteristic scale comparable with Bohr radius of exciton, see Fig. 1.6. To be precise, to account for the exciton-exciton interaction as for short-range (contact) interaction expressed in term of δ-function, one should require that the exciton-exciton potential decays at the distances much lower than the wave function variations. Mathematically all this leads to the following approximation:

$$V(r)=g\delta(r), \tag{1.57}$$

and as a consequence to

$$i\hbar\frac{\partial}{\partial t}\psi(\mathbf{r},t)=\left[-\frac{\hbar}{2m}\nabla^2+U(\mathbf{r})+g|\psi(\mathbf{r},t)|^2\right]\psi(\mathbf{r},t), \tag{1.58}$$

which means that Eq. (1.56) becomes a mean-field equation where the mean-field potential energy induced by other polaritons is experienced by the polariton due to repulsive interaction controlled by the term $g|\psi|^2$, where g is an interaction constant. This equation is a so called Gross-Pitaevskii equation and it is essential for description of the polariton wave function including the case of Bose-Einstein condensates.

The interaction constant g for the polaritons is obtained straightly from the one of excitons. The interaction constant for polaritons is smaller than one for excitons because part of its life it exists in the form of non-interacting cavity photons. This attenuation is controlled by the Hopfield coefficient X_L. Finally one writes for the more relevant lower polariton dispersion:

$$g=6E_b|X_L|^2a_B^2. \tag{1.59}$$

This equation is directly based on the exciton-exciton matrix element given in Eq. (1.21). Remarkably, for the polaritons it contains the Hoperfield coefficients in the form $|X_L|^2$ (for the lower polariton branch) showing the excitonic fraction.

To end this subsection, it is instructively to mention that the short range interaction is not the only case for the polaritons. The electrically polarized exciton-polaritons ("dipolaritons") are the systems with long range interaction [56, 57], the long-range interaction is also expected in TMDs [58, 59].

1.4.2 Resonant pumping and bistability for cavity exciton-polaritons

In the same manner how the exciton and photon decay were included into the Jaynes-Cummings Hamiltonian, one can add the dissipation and generation of polaritons due to irradiation by a laser to the Gross-Pitaevskii equation (or Schrödinger equation). In this chapter we give GPE as is, because its more gorunded derivation essentially requires discussion the nature of quantum fluids and many-body wave function given in Chapter 2. The driven-dissipative Gross-Pitaevskii equation (DDGPE) takes a form:

$$i\hbar\frac{\partial}{\partial t}\psi(\mathbf{r},t) = \left[-\frac{\hbar}{2m}\nabla^2 + U(\mathbf{r}) + g|\psi(\mathbf{r},t)|^2 - i\Gamma_{pol}\right]\psi(\mathbf{r},t) + P(\mathbf{r})\exp(-i\omega t), \quad (1.60)$$

where ω is laser frequency with respect to the bottom of polariton dispersion and $P(\mathbf{r})$ is a spatial profile of a laser electric field. Such equation is valid even in the case of a slight detuning of the laser energy with respect to the energy of polariton mode. This case is referred as quasi-resonant pumping.

In the case referred as a quasi-resonant pumping and with a positive laser detuning (the laser is above the bare polariton mode), the phenomenon of bistability exists. It corresponds to appearance of a hysteresis loop in the dependence of polariton density versus the laser electric field amplitude. I.e. in some range of lase power the two possible stable in time polariton density values exist and they depend on the history of the system [60, 61, 62, 63]. The bistability can be analyzed as follows. First, we neglect the potential energy $U(\mathbf{r})$. Second, we consider a homogeneous system and thus we omit the kinetic energy term. These two conditions lead to zero-dimensional DDGPE:

$$i\hbar\frac{\partial\psi}{\partial t} = \left[g|\psi|^2 - i\Gamma_{pol}\right]\psi + P\exp(-i\omega t). \quad (1.61)$$

Fig. 1.16 shows the typical curves of polariton density $|\psi|^2$ versus laser field amplitude P obtained for various polariton lifetimes by the means of numerical solution of Eq. (1.61) in `Matlab`. The parameter $g = 3$ meV. Each curve corresponds to a single simulation where the laser amplitude is slowly increased and then slowly decreased.

The behavior of the system can be described as follows. When one starts from the zero density and zero laser power, the polariton density slowly increases with increasing the laser power (field amplitude). The bistability loop is passed by the *lower bistability branch* and at the right border of the bistability loop the abrupt jump to the high density takes place. It happens because of the blue shift of the polariton energy due to the increase of the interactions, bringing the mode in resonance with the laser. During the further increase of the laser power, the system saturates and density goes up relatively slowly. If one now starts decreasing the laser power, the bistability loop will be passed at the *upper bistability branch*. It means that the system is sensitive to its history. The similar behavior takes place for the magnetization of ferromagnetic materials and the bistability loop is

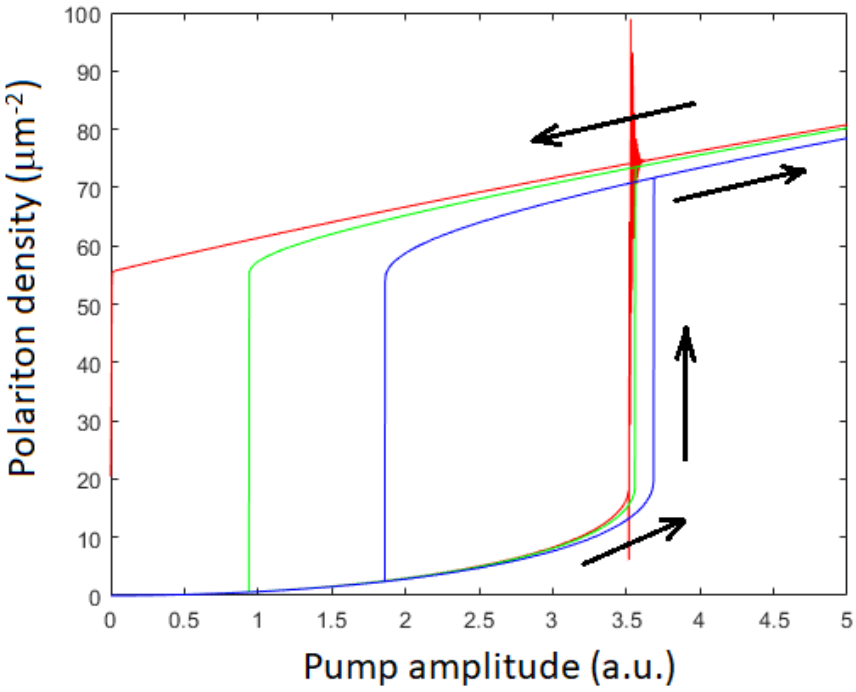

Figure 1.16: Bistability for polaritons in the regime of quasi-resonant pumping obtained in the real-time solution of zero dimensional DDGPE. Dependence of polariton density as a function of electromagnetic wave amplitude. Red color is for $\Gamma = 0.01\Gamma_0$, green color is for $\Gamma = 1.01\Gamma_0$, blue color is for $\Gamma = 2.01\Gamma_0$, where $\Gamma_0 = \hbar/(2 \cdot 15\text{ps})$.

in fact a hysteresis loop. Despite the slowness of laser power rising in the simulations (2 μs for the path there and back again for these simulations) , the red curve exhibits the visible spike at the moment of the rapid switching from lower to upper bistability branch.

To analyze the features of the DDGPE leading to the bistability, one can also solve (1.61) in the stationary case. In this case, there is no time dependencies except the common multiplier $\exp(-i\omega t)$, which gives rise to the term with $\hbar\omega$ in the following stationary reduced GPE:

$$P = -\left[-\hbar\omega + g|\psi|^2 - i\Gamma_{pol}\right]\psi. \tag{1.62}$$

Without losing the generality, one can assume P to be real and positive. This equation is not simple to be straightforwardly solved in terms of $\psi(P)$, but it is a simple function $P(\psi)$. Obtained in this sense P has both real and imaginary parts, and thus for returning to real and positive value, one should use the rotation in the complex plane $P' = PP^*/|P|$, where star is for complex conjugation. The same aligning of the argument is to be done for the wave function: $\psi' = \psi P^*/|P|$. Fig. 1.17 shows the dependence of $|\psi|^2$ and the relative phase of P and ψ versus P from the numerical solution of Eq. (1.62).

One sees that at lower bistability branch the polariton wave function has the phase close to the phase of the pump P (approximately, $P = \hbar\omega\psi$). On the contrary at the upper bistability branch, the polaritons are in the antiphase with the laser. One sees that the wave function phase remains pinned (or locked) to the phase of laser, and at the upper bistability branch this pinning is also very strong. This phenomenon is important in the context of observation of topological defects in polariton quantum fluids and will be discussed in the corresponding chapters. Noteworthy, at large Γ the polariton phases at upper and lower branches becomes closer to each other. Having a parallel with the case of Van der Waals isotherm, the part of a curve with negative slope is unstable, which can be shown using the Bogoliubov-de Gennes approach, see the next chapter for the details.

The minimal pumping required for being at the upper bistability branch is

$$P_{min} = \Gamma\sqrt{\frac{\hbar\omega}{g}}, \tag{1.63}$$

which is well illustrated in Figs. 1.16 and 1.17. At the upper bistability branch the polariton density is approximately estimated from the relation $\hbar\omega = g|\psi|^2$. Bistability for polaritons was observed numerous times in the system of quasi-resonantly pumped cavities [64] : typical experimental curves are presented in Fig. 1.18. The situation is more complex and demonstrates rich behavior when takes place the competition between the polaritons with different polarizations due to the usage of circularly polarized light [65].

1.4.3 Non-resonant pumping

In the case of quasi-resonant pumping, light excites directly the polaritons having the energy the same or close to the energy at which the detection will take place. The corresponding term in GPE was introduced in previous section.

Non-resonant pumping corresponds to the case where the difference of the laser energy and polariton modes is much larger than the broadening. More precisely, the laser energy

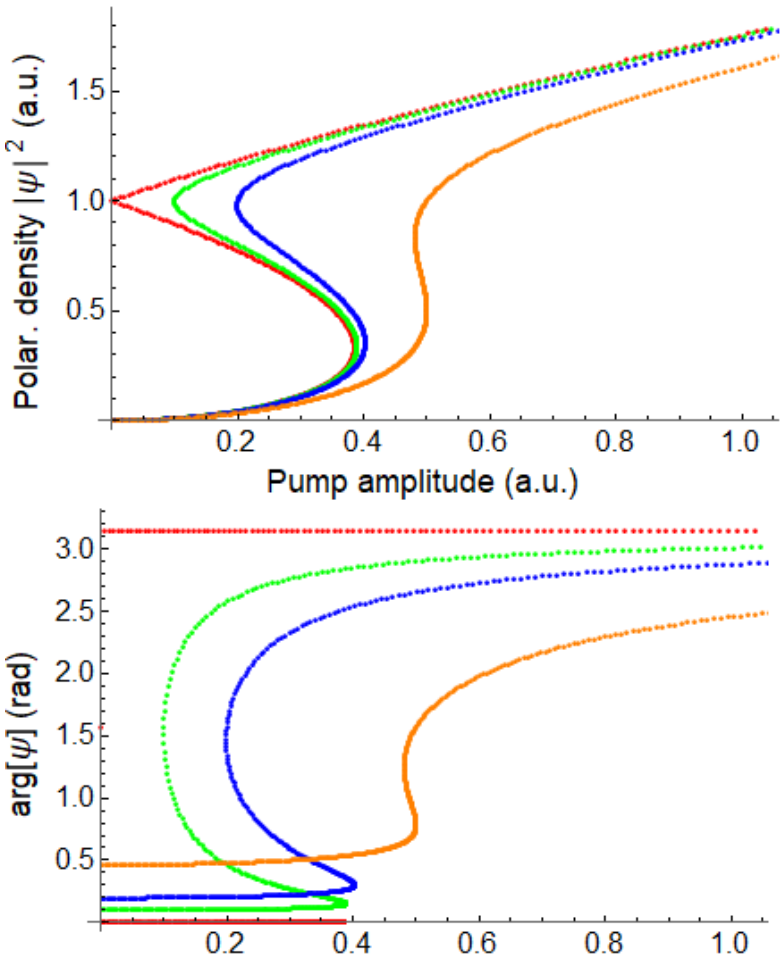

Figure 1.17: Analytical bistability curve in the dimensionless equation ($\hbar\omega = 1$, $g = 1$). Upper panel is for polariton density $|\psi|^2$ and lower is for arg[ψ]. Red color is for $\Gamma = 0.0001$, green color is for $\Gamma = 0.1001$, blue color is for $\Gamma = 0.2001$, and orange color is for $\Gamma = 0.5001$. Here Γ is given in arbitrary units natural for the dimensionless Eq. (1.62).

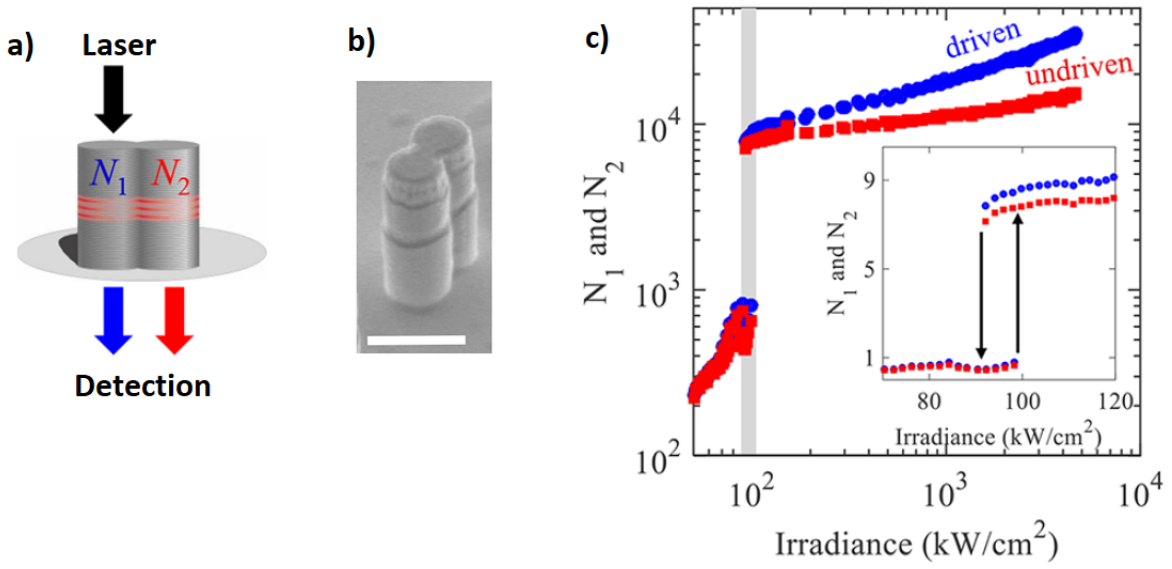

Figure 1.18: Experimentally observed bistability for polaritons in the cavity etched in the shape of a diatomic molecule of pillars. a) Scheme of experiment b) SEM image of a cavity c) Bistability curves for the same pillar N_1 and neighboring pillar N_2. Adopted from Ref. [64].

much is higher than on of the "target" polaritons near the LP branch bottom to be excited. Non-resonant pumping implies the processes of the irradiation-induced creation of plasma of electron and holes, then to formation of excitons and polaritons with dominating excitonic fraction and finally to the phonon-mediated relaxation of such polaritons to the bottom of lower polariton branch where they will be detected, see Fig. 1.19. All these scattering processes are complicated but can be described phenomenologically. The very important concept is the so called *reservoir*, a pool of a polaritons with dominating excitonic component at a flat part of lower polariton branch dispersion. From this reservoir the polaritons can be scattered in *stimulated* regime to the bottom of lower polariton branch. During this process the polaritons should unavoidably pass the "bottleneck", a region where it is difficult to obey the energy and momentum conservation laws. In case of very high pumping level, the polariton density can reach some threshold and the Bose-Einstein condensation will occur.

To reflect the mentioned above stimulated regime and presence of the reservoir, the following modification of GPE was proposed in the *Diffusive Gross-Pitaevskii model* [67]:

$$i\hbar\frac{\partial}{\partial t}\psi(\mathbf{r},t) = \left[-\frac{\hbar^2}{2m}\nabla^2 + U(\mathbf{r}) + g|\psi(\mathbf{r},t)|^2 + 2g_R n_R - i\Gamma_{pol} + \frac{i}{2}f_R(n_R(\mathbf{r},t))\right]\psi(\mathbf{r},t), \tag{1.64}$$

where $f_R(x)$ some monotonically growing function of the local density of the polariton reservoir $n_R(\mathbf{r},t)$ in the bottleneck region, obeying the following kinetic equation:

$$\frac{\partial}{\partial t}n_R(\mathbf{r},t) = P_R(\mathbf{r},t) - f_R(n_R(\mathbf{r},t))|\psi(\mathbf{r},t)|^2 - \gamma_R n_R(\mathbf{r},t), \tag{1.65}$$

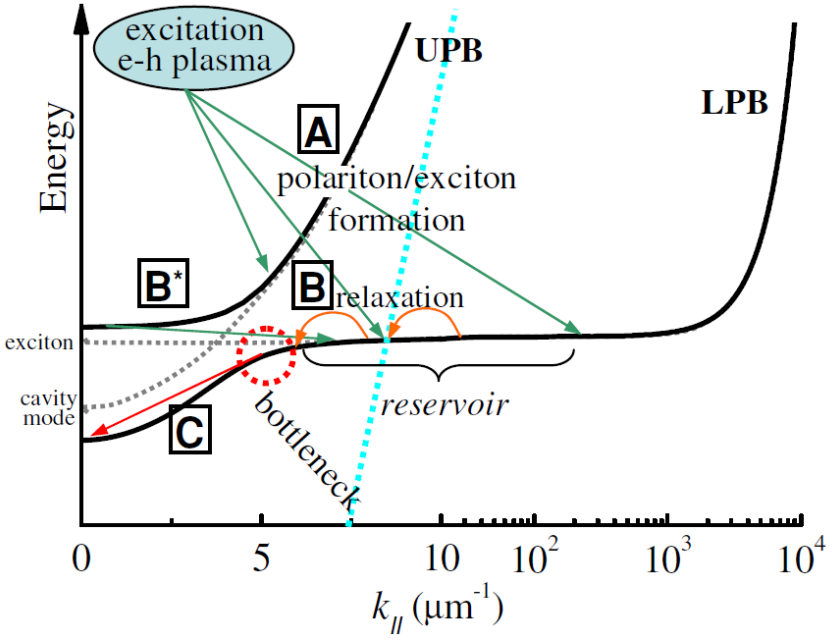

Figure 1.19: The processes of polariton relaxation taking place when off-resonant excitation. Adopted from Ref. [66].

where P_R is pumping power and $\gamma_R = 1/2\tau_R$ is the inverse mean lifetime of polaritons in the reservoir. For linear function $f_R(x) = Rx$ these equations can be rewritten as

$$i\hbar\frac{\partial}{\partial t}\psi(\mathbf{r},t) = \left[-\frac{\hbar^2}{2m}\nabla^2 + U(\mathbf{r}) + g|\psi(\mathbf{r},t)|^2 + 2g_R n_R \right. \\ \left. -i\Gamma_{pol} + \frac{1}{2}\frac{i\hbar R P_R(\mathbf{r},t)}{\gamma_R + R|\psi(\mathbf{r},t)|^2}\right]\psi(\mathbf{r},t). \quad (1.66)$$

In the stationary and homogeneous case, the two last terms (dissipative and driven) in square brackets can be put equal with taking $|\psi|^2 \equiv n_0$, where n_0 is homogeneous density of polaritons: $\Gamma_{pol} = \frac{1}{2}\frac{\hbar R P_R(\mathbf{r},t)}{\gamma_R + R n_0}$. Making this substitution for Γ_{pol} in Eq. (1.66) and then using the Taylor expansion of the last term (assuming $R|n_0 - |\psi(\mathbf{r},t)|^2| \ll \gamma_R + Rn_0$, which is satisfied e.g. when $\gamma_R \gg Rn_0$ and $\Gamma_R \gg R|\psi(\mathbf{r},t)|^2$), previous equation can be rewritten as

$$i\hbar\frac{\partial}{\partial t}\psi(\mathbf{r},t) = \left[-\frac{\hbar^2}{2m}\nabla^2 + U(\mathbf{r}) + g|\psi(\mathbf{r},t)|^2 - i\Lambda g\left(|\psi(\mathbf{r},t)|^2 - n_0\right)\right]\psi(\mathbf{r},t). \quad (1.67)$$

Hybrid Boltzmann Gross-Pitaevskii model. This model is also formulated via the system of the two coupled equations for the dynamics of the density in reservoir [68]

$$\frac{\partial}{\partial t}n_R(\mathbf{r},t) = P_R(\mathbf{r},t) - \gamma_R n_R(\mathbf{r},t) - \int\left(\kappa - \beta\frac{\hbar k^2}{2m}\right)n_c(k,t)\rho_k^d dk, \quad (1.68)$$

and for the condensate wave function

$$i\hbar\frac{\partial}{\partial t}\psi(\mathbf{r},t) = \left[-(1-i\beta/2)\frac{\hbar^2}{2m}\nabla^2 + U(\mathbf{r}) + g\left(|\psi(\mathbf{r},t)|^2 + n_R + i\hbar\kappa/2\right)\right]\psi(\mathbf{r},t), \quad (1.69)$$

where $\kappa = n_R M_{XX}\,(n_R - f(T)) - \Gamma_{\rm pol}$, $\beta = \frac{\hbar n_R M_{XX} f(T)}{kT} - \frac{\Gamma_{\rm pol}}{\Omega_R}$, $f(T) = \frac{m_X kT}{2\pi\hbar^2}\exp(-E_x/kT)$. The excitonic reservoir and polaritons are coupled via exciton-exciton scattering, which implies the explicit presence of the corresponding matrix element in the formulas below. In this model, dissipation is proportional exclusively to the energy of the elementary excitations of the condensate (Bogolons), and not to the total energy (which includes non-linear interaction term). In the contrast with Diffusive Gross-Pitaevskii model, the BGP model can correctly describe the condensate in motion with the excitations dispersion satisfying the Landau superfluidity criterion described in the next chapter (see Fig. 5 from Ref. [68]). The mutual effects in the system reservoir-polariton "condensate" lead to the intriguing type of instabilities [69, 70, 71]. Briefly, the local spot of the high polariton density leads to creation of density dip in the reservoir, which leads to formation of potential well due to local lowering of $2g_r n_R$ term. This well attracts the polaritons and as a result a positive feedback loop is created.

The description of the models accounting for the case of non-resonant pumping was given here for general scope, as very important practical case, actual e.g. for formation of polariton Bose-Einstein condensates. In present work, the results were obtained in the conservative case or using the quasi-resonant pumping scheme. From the point of view of the studies of topological defects in polariton quantum fluids, the advantage of the off-resonant pumping scheme is that is avoids the effect of phase fixing by laser, but its issue is less direct optical control of the polariton quantum fluid wave function.

Bibliography

[1] J. Bardeen, "Semiconductor research leading to the point contact transistor," *Great Solid State Physicists Of The 20th Century*, pp. 234–260, 2003.

[2] Z. I. Alferov, "Nobel lecture: The double heterostructure concept and its applications in physics, electronics, and technology," *Rev. Mod. Phys.*, vol. 73, pp. 767–782, Oct 2001.

[3] N. W. Ashcroft and N. D. Mermin, "Solid state physics (saunders college, philadelphia, 1976)," *Appendix N*, 2010.

[4] M. O. Ali, *Elementary Solid State Physics: Principles and Applications*. Addison-Wesley Publishing Company, 1993.

[5] *Ioffe Institute Electronic archive. GaAs band structure and carrier concentration*, Accessed 19 Nov 2019. `http://www.ioffe.ru/SVA/NSM/Semicond/GaAs/bandstr.html`.

[6] A. Sharma, N. Ravindra, S. Auluck, and V. Srivastava, "Temperature-dependent effective masses in iii-v compound semiconductors," *physica status solidi (b)*, vol. 120, no. 2, pp. 715–721, 1983.

[7] I. Vurgaftman, J. á. Meyer, and L. á. Ram-Mohan, "Band parameters for iii–v compound semiconductors and their alloys," *Journal of applied physics*, vol. 89, no. 11, pp. 5815–5875, 2001.

[8] A. Nalitov, *Spin dynamics and topological effects in physics of indirect excitons and microcavity polaritons*. PhD thesis, Université Blaise Pascal-Clermont-Ferrand II, 2015.

[9] I. Shelykh, *Spin and polarization dynamics in strong coupling regime of light-matter coupling (in Russian)*. Dr. Sci. thesis, ITMO University, St. Peterburg, Russia, 2018.

[10] L. D. Landau and E. M. Lifshitz, *Quantum mechanics: non-relativistic theory*, vol. 3. Elsevier, 2013.

[11] P. Andreakou, S. Cronenberger, D. Scalbert, A. Nalitov, N. Gippius, A. Kavokin, M. Nawrocki, J. Leonard, L. Butov, K. Campman, *et al.*, "Nonlinear optical spectroscopy of indirect excitons in coupled quantum wells," *Physical Review B*, vol. 91, no. 12, p. 125437, 2015.

[12] A. Nalitov, M. Vladimirova, A. Kavokin, L. Butov, and N. Gippius, "Nonlinear optical probe of indirect excitons," *Physical Review B*, vol. 89, no. 15, p. 155309, 2014.

[13] J. Shinar, *Optical and electronic properties of fullerenes and fullerene-based materials*. CRC Press, 1999.

[14] E. Bernstein, S. Colson, R. Kopelman, and G. Robinson, "Electronic and vibrational exciton structure in crystalline benzene," *The Journal of Chemical Physics*, vol. 48, no. 12, pp. 5596–5610, 1968.

[15] J. Frenkel, "On the transformation of light into heat in solids. i," *Physical Review*, vol. 37, no. 1, p. 17, 1931.

[16] G. H. Wannier, "The structure of electronic excitation levels in insulating crystals," *Physical Review*, vol. 52, no. 3, p. 191, 1937.

[17] E. Courtade, M. Semina, M. Manca, M. Glazov, C. Robert, F. Cadiz, G. Wang, T. Taniguchi, K. Watanabe, M. Pierre, *et al.*, "Charged excitons in monolayer wse 2: experiment and theory," *Physical Review B*, vol. 96, no. 8, p. 085302, 2017.

[18] M. V. Durnev and M. M. Glazov, "Excitons and trions in two-dimensional semiconductors based on transition metal dichalcogenides," *Physics-Uspekhi*, vol. 61, no. 9, p. 825, 2018.

[19] E. Gross, "Optical spectrum of excitons in the crystal lattice," *Il Nuovo Cimento (1955-1965)*, vol. 3, pp. 672–701, 1956.

[20] J. Heckötter, M. Freitag, D. Fröhlich, M. Aßmann, M. Bayer, M. Semina, and M. Glazov, "Scaling laws of Rydberg excitons," *Physical Review B*, vol. 96, no. 12, p. 125142, 2017.

[21] T. Kazimierczuk, D. Fröhlich, S. Scheel, H. Stolz, and M. Bayer, "Giant Rydberg excitons in the copper oxide Cu_2o," *Nature*, vol. 514, no. 7522, p. 343, 2014.

[22] V. Srinivas, J. Hryniewicz, Y. J. Chen, and C. E. Wood, "Intrinsic linewidths and radiative lifetimes of free excitons in GaAs quantum wells," *Physical Review B*, vol. 46, no. 16, p. 10193, 1992.

[23] J. H. Chu, J.-C. Seo, E.-J. Shin, S.-K. Yu, D. Kim, Y.-N. Hwang, S.-H. Park, U. Kim, and P. S. Kop'ev, "Temperature and density dependence of exciton lifetimes in GaAs/AlGaAs multiple quantum wells," *Optical and quantum electronics*, vol. 27, no. 5, pp. 387–393, 1995.

[24] F. Tassone and Y. Yamamoto, "Exciton-exciton scattering dynamics in a semiconductor microcavity and stimulated scattering into polaritons," *Physical Review B*, vol. 59, no. 16, p. 10830, 1999.

[25] C. Ciuti, V. Savona, C. Piermarocchi, A. Quattropani, and P. Schwendimann, "Role of the exchange of carriers in elastic exciton-exciton scattering in quantum wells," *Physical Review B*, vol. 58, no. 12, p. 7926, 1998.

[26] K. D. Choquette and H. Q. Hou, "Vertical-cavity surface emitting lasers: moving from research to manufacturing," *Proceedings of the IEEE*, vol. 85, no. 11, pp. 1730–1739, 1997.

[27] C. Sheppard, "Approximate calculation of the reflection coefficient from a stratified medium," *Pure and Applied Optics: Journal of the European Optical Society Part A*, vol. 4, no. 5, p. 665, 1995.

[28] A. Kavokin and G. Malpuech, *Cavity polaritons*, vol. 32. Elsevier, 2003.

[29] S. Schön, M. Haiml, and U. Keller, "Ultrabroadband AlGaAs/CaF_2 semiconductor saturable absorber mirrors," *Applied Physics Letters*, vol. 77, no. 6, pp. 782–784, 2000.

[30] J. Boucart, C. Starck, F. Gaborit, A. Plais, N. Bouche, E. Derouin, L. Goldstein, C. Fortin, D. Carpentier, P. Salet, *et al.*, "1-mW CW-RT monolithic VCSEL at 1.55 μm," *IEEE Photonics Technology Letters*, vol. 11, no. 6, pp. 629–631, 1999.

[31] J. Hopfield, "Theory of the contribution of excitons to the complex dielectric constant of crystals," *Physical Review*, vol. 112, no. 5, p. 1555, 1958.

[32] L. D. Landau and E. M. Lifshitz, *Course of theoretical physics*. Elsevier, 2013.

[33] A. Kavokin, J. J. Baumberg, G. Malpuech, and F. P. Laussy, *Microcavities*. Oxford university press, 2017.

[34] J. Gérard, B. Sermage, B. Gayral, B. Legrand, E. Costard, and V. Thierry-Mieg, "Enhanced spontaneous emission by quantum boxes in a monolithic optical microcavity," *Physical review letters*, vol. 81, no. 5, p. 1110, 1998.

[35] C. M. Bender and S. Boettcher, "Real spectra in non-hermitian hamiltonians having p t symmetry," *Physical Review Letters*, vol. 80, no. 24, p. 5243, 1998.

[36] J. Wen, X. Jiang, L. Jiang, and M. Xiao, "Parity-time symmetry in optical microcavity systems," *Journal of Physics B: Atomic, Molecular and Optical Physics*, vol. 51, no. 22, p. 222001, 2018.

[37] Ş. Özdemir, S. Rotter, F. Nori, and L. Yang, "Parity–time symmetry and exceptional points in photonics," *Nature materials*, vol. 18, no. 8, pp. 783–798, 2019.

[38] R. Houdré, C. Weisbuch, R. Stanley, U. Oesterle, P. Pellandini, and M. Ilegems, "Measurement of cavity-polariton dispersion curve from angle-resolved photoluminescence experiments," *Physical Review Letters*, vol. 73, no. 15, p. 2043, 1994.

[39] R. Houdré, C. Weisbuch, R. Stanley, U. Oesterle, P. Pellandini, and M. Ilegems, "Measurement of cavity polariton dispersion curve," *Superlattices and microstructures*, vol. 15, no. 3, p. 263, 1994.

[40] E. Wertz, L. Ferrier, D. Solnyshkov, R. Johne, D. Sanvitto, A. Lemaître, I. Sagnes, R. Grousson, A. V. Kavokin, P. Senellart, *et al.*, "Spontaneous formation and optical manipulation of extended polariton condensates," *Nature physics*, vol. 6, no. 11, p. 860, 2010.

[41] A. Amo, J. Lefrère, S. Pigeon, C. Adrados, C. Ciuti, I. Carusotto, R. Houdré, E. Giacobino, and A. Bramati, "Superfluidity of polaritons in semiconductor microcavities," *Nature Physics*, vol. 5, no. 11, p. 805, 2009.

[42] A. Amo, S. Pigeon, C. Adrados, R. Houdré, E. Giacobino, C. Ciuti, and A. Bramati, "Light engineering of the polariton landscape in semiconductor microcavities," *Phys. Rev. B*, vol. 82, p. 081301, Aug 2010.

[43] A. Amo, S. Pigeon, D. Sanvitto, V. Sala, R. Hivet, I. Carusotto, F. Pisanello, G. Leménager, R. Houdré, E. Giacobino, *et al.*, "Polariton superfluids reveal quantum hydrodynamic solitons," *Science*, vol. 332, no. 6034, pp. 1167–1170, 2011.

[44] T. Boulier, H. Terças, D. Solnyshkov, Q. Glorieux, E. Giacobino, G. Malpuech, and A. Bramati, "Vortex chain in a resonantly pumped polariton superfluid," *Scientific reports*, vol. 5, p. 9230, 2015.

[45] R. Hivet, E. Cancellieri, T. Boulier, D. Ballarini, D. Sanvitto, F. M. Marchetti, M. H. Szymanska, C. Ciuti, E. Giacobino, and A. Bramati, "Interaction-shaped vortex-antivortex lattices in polariton fluids," *Phys. Rev. B*, vol. 89, p. 134501, Apr 2014.

[46] R. Houdré, C. Weisbuch, R. P. Stanley, U. Oesterle, and M. Ilegems, "Coherence effects in light scattering of two-dimensional photonic disordered systems: Elastic scattering of cavity polaritons," *Phys. Rev. B*, vol. 61, pp. R13333–R13336, May 2000.

[47] M. Gurioli, F. Bogani, L. Cavigli, H. Gibbs, G. Khitrova, and D. Wiersma, "Weak localization of light in a disordered microcavity," *Physical review letters*, vol. 94, no. 18, p. 183901, 2005.

[48] C. Pöllmann, U. Leierseder, E. Galopin, A. Lemaître, A. Amo, J. Bloch, R. Huber, and J.-M. Ménard, "Microcavity design for low threshold polariton condensation with ultrashort optical pulse excitation," *Journal of Applied Physics*, vol. 117, no. 20, p. 205702, 2015.

[49] R. Schmidt-Grund, B. Rheinländer, C. Czekalla, G. Benndorf, H. Hochmuth, M. Lorenz, and M. Grundmann, "Exciton–polariton formation at room temperature in a planar zno resonator structure," *Applied Physics B*, vol. 93, no. 2-3, pp. 331–337, 2008.

[50] R. Johne, D. Solnyshkov, and G. Malpuech, "Theory of exciton-polariton lasing at room temperature in zno microcavities," *Applied Physics Letters*, vol. 93, no. 21, p. 211105, 2008.

[51] J.-R. Chen, T.-C. Lu, Y.-C. Wu, S.-C. Lin, W.-R. Liu, W.-F. Hsieh, C.-C. Kuo, and C.-C. Lee, "Large vacuum rabi splitting in zno-based hybrid microcavities observed at room temperature," *Applied Physics Letters*, vol. 94, no. 6, p. 061103, 2009.

[52] F. Li, L. Orosz, O. Kamoun, S. Bouchoule, C. Brimont, P. Disseix, T. Guillet, X. Lafosse, M. Leroux, J. Leymarie, *et al.*, "From excitonic to photonic polariton condensate in a zno-based microcavity," *Physical review letters*, vol. 110, no. 19, p. 196406, 2013.

[53] A. Gianfrate, O. Bleu, L. Dominici, V. Ardizzone, M. De Giorgi, D. Ballarini, K. West, L. Pfeiffer, D. Solnyshkov, D. Sanvitto, *et al.*, "Direct measurement of the quantum geometric tensor in a two-dimensional continuous medium," *arXiv preprint arXiv:1901.03219*, 2019.

[54] E. Ivchenko, V. Kochereshko, P. Kop'ev, V. Kosobukin, I. Uraltsev, and D. Yakovlev, "Exciton longitudinal-transverse splitting in gaas/algaas superlattices and multiple quantum wells," *Solid state communications*, vol. 70, no. 5, pp. 529–534, 1989.

[55] M. Maialle, E. d. A. e Silva, and L. Sham, "Exciton spin dynamics in quantum wells," *Physical Review B*, vol. 47, no. 23, p. 15776, 1993.

[56] I. Rosenberg, Y. Mazuz-Harpaz, R. Rapaport, K. West, and L. Pfeiffer, "Electrically controlled mutual interactions of flying waveguide dipolaritons," *Physical Review B*, vol. 93, no. 19, p. 195151, 2016.

[57] I. Rosenberg, D. Liran, Y. Mazuz-Harpaz, K. West, L. Pfeiffer, and R. Rapaport, "Strongly interacting dipolar-polaritons," *Science advances*, vol. 4, no. 10, p. eaat8880, 2018.

[58] Y. N. Gartstein, X. Li, and C. Zhang, "Exciton polaritons in transition-metal dichalcogenides and their direct excitation via energy transfer," *Physical Review B*, vol. 92, no. 7, p. 075445, 2015.

[59] V. Ardizzone, L. De Marco, M. De Giorgi, L. Dominici, D. Ballarini, and D. Sanvitto, "Emerging 2d materials for room-temperature polaritonics," *Nanophotonics*, vol. 8, no. 9, pp. 1547–1558, 2019.

[60] N. Gippius, S. Tikhodeev, V. Kulakovskii, D. Krizhanovskii, and A. Tartakovskii, "Nonlinear dynamics of polariton scattering in semiconductor microcavity: Bistability vs. stimulated scattering," *EPL (Europhysics Letters)*, vol. 67, no. 6, p. 997, 2004.

[61] A. Baas, J. P. Karr, H. Eleuch, and E. Giacobino, "Optical bistability in semiconductor microcavities," *Phys. Rev. A*, vol. 69, p. 023809, Feb 2004.

[62] D. M. Whittaker, "Effects of polariton-energy renormalization in the microcavity optical parametric oscillator," *Phys. Rev. B*, vol. 71, p. 115301, Mar 2005.

[63] N. A. Gippius, I. A. Shelykh, D. D. Solnyshkov, S. S. Gavrilov, Y. G. Rubo, A. V. Kavokin, S. G. Tikhodeev, and G. Malpuech, "Polarization multistability of cavity polaritons," *Phys. Rev. Lett.*, vol. 98, p. 236401, Jun 2007.

[64] S. Rahimzadeh Kalaleh Rodriguez, A. Amo, I. Carusotto, I. Sagnes, L. Le Gratiet, E. Galopin, A. Lemaitre, and J. Bloch, "Nonlinear polariton localization in strongly coupled driven-dissipative microcavities," *ACS Photonics*, vol. 5, no. 1, pp. 95–99, 2017.

[65] O. Bozat, I. G. Savenko, and I. A. Shelykh, "Spin multistability in dissipative polariton channels," *Phys. Rev. B*, vol. 86, p. 035413, Jul 2012.

[66] A. Amo, D. Sanvitto, and L. Vina, "Collective dynamics of excitons and polaritons in semiconductor nanostructures," *Semiconductor Science and Technology*, vol. 25, no. 4, p. 043001, 2010.

[67] M. Wouters and I. Carusotto, "Excitations in a nonequilibrium bose-einstein condensate of exciton polaritons," *Physical review letters*, vol. 99, no. 14, p. 140402, 2007.

[68] D. Solnyshkov, H. Terças, K. Dini, and G. Malpuech, "Hybrid boltzmann–gross-pitaevskii theory of bose-einstein condensation and superfluidity in open driven-dissipative systems," *Physical Review A*, vol. 89, no. 3, p. 033626, 2014.

[69] E. Estrecho, T. Gao, N. Bobrovska, M. Fraser, M. Steger, L. Pfeiffer, K. West, T. Liew, M. Matuszewski, D. Snoke, *et al.*, "Spontaneous condensation of exciton polaritons in the single-shot regime," *arXiv preprint arXiv:1705.00469*, 2017.

[70] F. Baboux, D. De Bernardis, V. Goblot, V. Gladilin, C. Gomez, E. Galopin, L. Le Gratiet, A. Lemaître, I. Sagnes, I. Carusotto, *et al.*, "Unstable and stable regimes of polariton condensation," *Optica*, vol. 5, no. 10, pp. 1163–1170, 2018.

[71] N. Bobrovska, M. Matuszewski, K. S. Daskalakis, S. A. Maier, and S. Kéna-Cohen, "Dynamical instability of a nonequilibrium exciton-polariton condensate," *ACS Photonics*, vol. 5, no. 1, pp. 111–118, 2018.

Chapter 2

Introduction to quantum fluids of light

Contents

The chapter is organized as follows. In the first section we will describe the phenomenon of Bose-Einstein condensation paying a special attention to the case of polaritons. Sections 2, 3, and 4 are devoted to the description of typical solutions of the Gross-Pitaevskii equation: bogolons, solitons, and quantum vortices, respectively. In section 5, we will describe the fundamental experiments showing the superfluid nature of polaritons at high densities, and in section 6 – the techniques of potential shaping for polaritons.

2.1 Bose-Einstein condensation of exciton-polaritons

As we have already pointed out, a polariton is a composite particle having a photon and an exciton components. In terms of statistic properties, polaritons are bosons. More precisely, they exhibit bosonic properties when their concentration is sufficiently small and the average distance between the excitons is much larger than the exciton radius, which allows avoiding the overlap of real fermionic components of the excitons: the electron and the hole [1]. This condition reads

$$na_B^d \ll 1, \tag{2.1}$$

where d is the dimension of the system (the excitons in quantum wells are two-dimensional and $d = 2$). Thus, in microcavities it is possible to observe the phenomena associated with the transition of the system to a state of polariton Bose-Einstein condensate. Polariton condensation is of the highest interest from the point of view of fundamental physics.

Other examples of solid state systems with observed condensation are the magnons [2, 3] and excitons [4, 5]. However, the most developed, both theoretically and experimentally, is the system of atomic Bose-Einstein condensates and thus the comparison, when it will be given, will be carried between the polariton and the atomic condensates. E.g. due to the extremely small effective mass of polaritons, the observed critical temperature is several tens of Kelvin, which is many orders of magnitude higher than the characteristic critical condensation temperatures of cold atoms.

Theoretical description of Bose-Einstein condensation [6] starts from the Bose distribution [7] of the occupation numbers

$$n_i\left(T,\mu\right) = \frac{1}{L^d}\frac{1}{\exp\left(\frac{E_i-\mu}{T}\right)-1}, \tag{2.2}$$

where μ is the chemical potential of these particles, E_i is the energy in the quantum state i, and T is the temperature. The total density of particles in the system is found by the summation of densities given by Eq. (2.2) over all states i in the system:

$$n(T,\mu) = \sum_{i=0}^{N} n_i(T,\mu). \tag{2.3}$$

The chemical potential should be below the ground state E_0, otherwise the nonphysical negative density occurs. One sees that n_i grows with the increase of the chemical potential and the temperature. Due to this behavior, at fixed temperature T, it exists some maximal

density of particles which occupy all the states above the ground state:

$$n_{max}(T) = \sum_{i=1}^{N} n_i(T, \mu = 0). \tag{2.4}$$

For the bosons with isotropic parabolic dispersion in a sufficiently big "box" providing the sufficient density of levels of quantized kinetic energy Eq. (2.4) can be rewritten as

$$n_{max}\left(T\right) = \frac{1}{\left(2\pi\right)^d} \int_0^{+\infty} f\left(k, T, \mu = 0\right) k^{d-1} dk, \tag{2.5}$$

where

$$f\left(k, T, \mu\right) = \frac{1}{\exp\left(\frac{1}{T}\left(\frac{\hbar^2 k^2}{2m} - \mu\right)\right) - 1}. \tag{2.6}$$

In case $d = 3$ this integral can be evaluated analytically:

$$n_{max}\left(T\right) = \zeta(3/2) \cdot \left(\frac{mT}{2\pi\hbar^2}\right)^{\frac{3}{2}}, \tag{2.7}$$

where ζ is the Riemann Zeta function. One sees that the expression in the brackets in the second multiplier in Eq. (2.7) is in fact a thermal de Broigle wave vector obtained from the estimation $T = \frac{\hbar^2 k_{TdB}^2}{2m}$.

Also one can find a critical temperature as a function of particle density n as:

$$T_c = \frac{2\pi\hbar^2}{m} \cdot \left(\frac{n}{\zeta(3/2)}\right)^{2/3}. \tag{2.8}$$

Obviously, with lowering the temperature, $n_{max}(T)$ also becomes smaller. Let us now fix the number of bosons in the system, which is quite natural for the case of atoms, and begin to decrease the temperature. While the temperatures are larger than T_c, the states above the ground states can store all the bosons present in the system. However, once T_c is reached, the states above the ground state are not enough despite they are completely filled according to the distribution function. The "excess" of the bosons will go to the ground state because its occupation number has not such restriction when the chemical potential approaches the energy of ground state. Such process is called a Bose-Einstein condensation. The Bose-Einstein condensation requires the bosonic system to be cold enough, so that the thermal de Broglie wavelength becomes larger than the mean distance between particles $n^{-1/3}$, which is similar to the condition of degeneracy for the gas of fermions.

One can outline the following fingerprints of the Bose-Einstein condensation:

- Domination of the occupation of the ground state of a system
- Bose distribution of occupation of other states with chemical potential close to zero

The description of condensation was started from 3D systems from the historical point of view and for consistency. I.e. for the systems of lower dimensions ($d < 3$), the integral in Eq. (2.5) diverges. However this fact does not result in the impossibility to observe the

the Bose-Einstein condensation in such systems. Due to the finite size of a system, the number of energy levels in the system is finite and thus quasi-Bose-Einstein condensation can still exist in the systems of low dimensions.

Firstly, the Bose-Einstein condensation was observed for cold atomic vapor [8]. The experiment required the temperatures as low as 170 nK obtained by the sequential laser and evaporative cooling. Such low temperatures are required because the critical temperature is proportional to the inverse particle mass (see Eq. (2.8)). The polariton Bose-Einstein condensation was firstly observed in the famous work in 2006 [9]. The CdTe/CdMgTe microcavity with 26 meV Rabi splitting was used in the experiment. Further the effect of condensation was observed in GaAs microcavities [10, 11, 12]. The polariton mass is much lower than the mass of atoms and thus for the polaritons the condensation can be observed at much higher temperatures.

However, there exists a fundamental difference between the atomic and the polaritonic systems in the context of condensate formation. Atoms are long-living particles (seconds, [8]) while the polaritons undergo a strong radiative decay (dozens of picoseconds typically, hundreds in the best samples, see previous chapter for the details). Either their density rapidly drops (with the time scales of hundreds of picoseconds in the best cavities) or it is necessary to maintain the density by injection (optical quasi-resonant or non-resonant pumping or electrical injection[13]). Thus, the polariton condensates are often out of equilibrium. This is determined by the balance between the decay time and the thermalization time. However, it is also possible to have the thermalization time much shorter than the decay time, and thus to have a well-thermalized polariton condensation occurring as an equilibrium phase transition [14, 15].

To overcome the polariton decay, in Ref. [9] the experiment was held with a sufficiently intensive non-resonant pumping, see Fig. 2.1. Such pumping creates a plasma of free carriers (electrons and holes) in the quantum wells significantly above the energies of polaritons, which then form excitons and polaritons and after multiple scattering events (involving also the phonons) relax to the ground state. Such process can be described on the basis of the system of Boltzmann kinetic equations. The main fingerprint of a Bose-Einstein condensation, namely the appearance of the domination of the occupation of the ground state, is well visible in Fig. 2.2.

Although the polariton condensate is a non-equilibrium system in which the radiative decay of polaritons is constantly compensated by optical pumping, it nevertheless demonstrates a number of properties characteristic of Bose-Einstein condensates in a state of thermodynamic equilibrium. In addition to the dominating occupation number of a ground state, it was experimentally observed the stationary distribution function of polaritons in excited states described with a high degree of accuracy by the Bose distribution. The latter can be seen from the linear decay of excited states occupation number versus their energy in the logarithmic plot on the panel b) of Fig. 2.3.

It should be noted that although the Boltzmann system of equations satisfactorily describes the appearance of a macroscopically populated state at zero wave vector and moreover allows one to calculate the pump threshold for a given microcavity geometry with a good accuracy, it cannot be used to describe the dynamic properties of a polariton condensate. In fact, Bose condensation is accompanied not only by the appearance of a macroscopic population, but also by the spontaneous appearance of coherence in the system. In this case, the condensate should be described using an order parameter, which

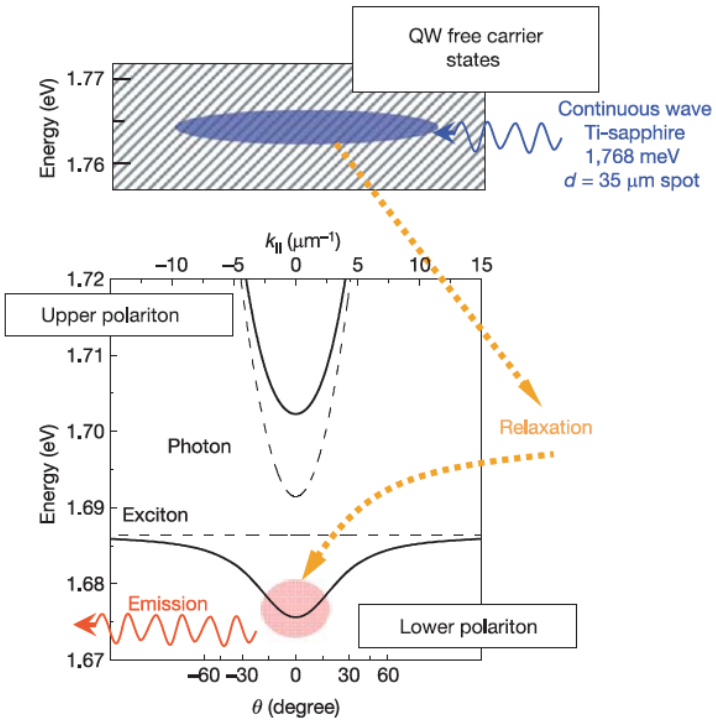

Figure 2.1: Scheme of the experiment to observe the polariton Bose-Einstein condensation using the non-resonant pumping. Adapted from Ref. [9].

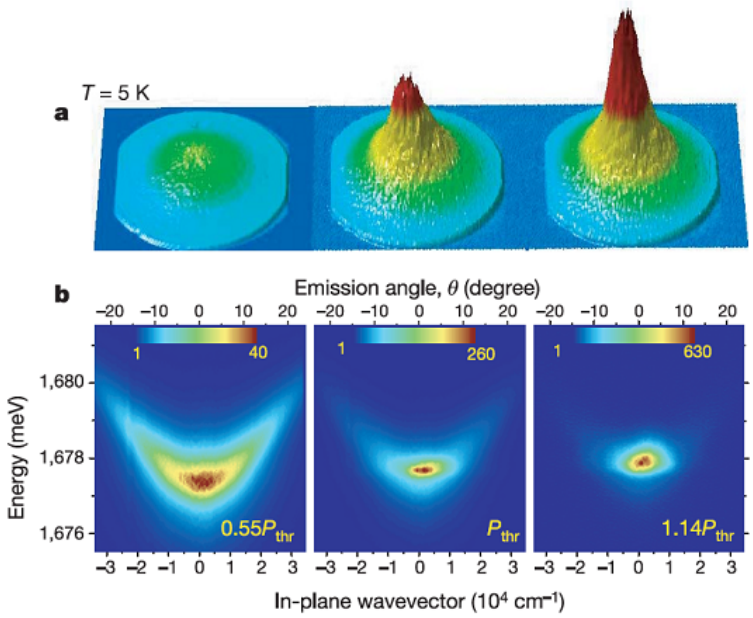

Figure 2.2: Experimentally observed polariton Bose-Einstein condensation. Maybe, the most famous image from the domain of the physics of polaritons. Adopted from Ref. [9].

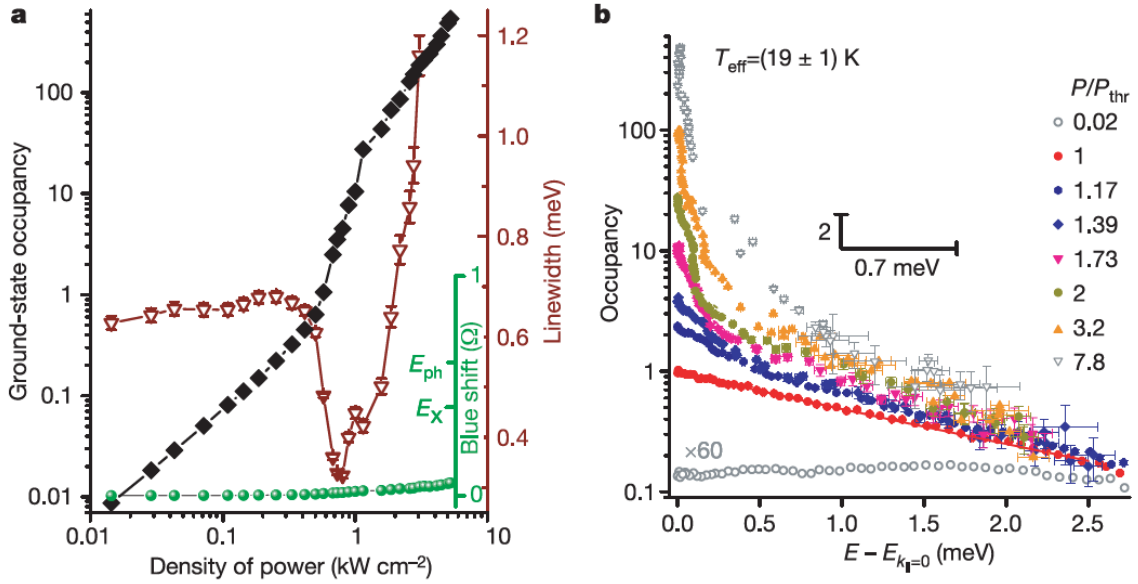

Figure 2.3: Statistical justification of polariton Bose-Einstein condensation. Panel a). Occupation number of a ground state (zero wave vector state) versus the pumping laser power is plotted with black diamonds. Panel b). Occupation number of the states above the ground state versus their energy. Adopted from Ref. [9].

has not only a macroscopic amplitude, but also a well-defined phase, and the presence of the latter is not reflected in any way in the Boltzmann equations. Such an order parameter required to describe the condensate dynamics is the shared wave function of a polaritons in the condensate. The bosons in the condensate indeed occupy the same state which results in the same phase of all particles and share the same single-particle wave function, which also results in the coherence at large length scales. The Onsager-Penrose criterion [16, 17] of the condensation involves the eigenvalue spectrum of the single-particle density matrix $\rho(\mathbf{r}, \mathbf{r}')$. Let

$$\int \rho(\mathbf{r}, \mathbf{r}')\phi_k(\mathbf{r}')d\mathbf{r}' = n_k\mathbf{r}', \tag{2.9}$$

be and eigenvalue problem with the corresponding eigenvalues and eigenfunctions whose the largest eigenvalue gives the number of condensed particles N_0. The criterion itself requires that the fraction of condensed particles remains greater than zero in the limit of macroscopic system:

$$\lim_{N\to\infty} \frac{N_0}{N} > 0. \tag{2.10}$$

This criterion is satisfied only in the case of long-range density-correlation order in the system expanding to the scales comparable with the size of the system.

Experimentally, for polaritons or excitons it means that the spatial coherence of emitted light observable at large distances visible e.g. in the homodyne interference experiments. The Boltzmann kinetic equations can not describe the behavior and dynamics of such wave function.

The appearance of such macroscopic wave function allows referring to polariton condensates as to quantum fluid. Even in the case of resonant pumping when the system is even more strongly constrained by the field of a laser, such properties as spatial and temporal coherence remain as well as the shared polariton wave function.

Such wave function of the condensate of interacting bosons obeys the Gross-Pitaevskii equation (introduced in Chapter 1 for the interacting polaritons) and thus the GPE becomes a powerful tool to investigate the dynamics of the condensate. Unlike the kinetic equations, GPE can not describe the formation of the condensate and can just describe its dynamics, after the condensation occurred. Thus GPE and kinetic equations describe different particularities of the same phenomena, but a unified approach is highly desired and numerous attempts are made in this direction [18, 19, 20, 21, 22].

To provide some grounds to introducing the Gross-Pitaevskii equation, one can start with the many-body wave fucntion of N bosons [23]:

$$|\Psi\rangle = \psi_1 \otimes \psi_2 \otimes ... \otimes \psi_N \equiv \psi \otimes \psi \otimes ... \otimes \psi, \tag{2.11}$$

with the equivalence stemming from the same wave function shared by all bosons. The stationary ground state of such system can be found via minimization of the free energy $F = E - \mu N$ with the energy $E = \langle\Psi|\hat{H}|\Psi\rangle/\langle\Psi|\Psi\rangle$ obtained based on the Hamiltonian

$$\hat{H} = -\frac{\hbar^2}{2m}\sum_i \nabla_i^2 + \sum_i U(\mathbf{r}_i) + \sum_{i,j>i} V(|\mathbf{r}_i - \mathbf{r}_j|). \tag{2.12}$$

In the next subsections we will describe the pool of typical solutions of Gross-Pitaevskii equation. The infinitesimal variation of the wave function $\psi \to \psi + \delta\psi$ (the same for its complex conjugate) causes the variation (necessarily equal to zero) of free energy:

$$N\int d\mathbf{r}\delta\psi^*(\mathbf{r})\left[-\frac{\hbar^2\Delta}{2m} + U(\mathbf{r}) - \mu + \frac{N-1}{2}\int d\mathbf{r}'|\psi(\mathbf{r}')|^2 V(|\mathbf{r}-\mathbf{r}'|)\right]\psi(\mathbf{r}), \tag{2.13}$$

where square braces multiplied by $\psi(\mathbf{r})$ in fact is an expression, which after taking a δ-function potential, becomes a Gross-Pitaevskii equation.

The time-dependent Gross-Pitaevskii equation (without μ-term) can be obtained using the least action principle and very similar variation of the action, see Ref. [24].

2.2 Bogoliubov excitations

2.2.1 Bogoliubov excitation dispersion

In fact, the typical solutions of the Gross-Pitaevskii equation have their analogs in the domain of classical hydrodynamics. They are the acoustic wave-like excitations, solitons, vortices, including also the phenomenon of turbulence. This brings a fascinating parallel between the classical and the quantum fluids. This section (as well as the two following sections) describes the typical classes of excitations of Bose-Einstein condensates.

However, we will start this section not from the Gross-Pitaevskii equation. Let us write the second quantization Hamiltonian for the system of weakly interacting bosons in

its general form:

$$\hat{H} = \sum_k \frac{\hbar^2 k^2}{2m} \hat{a}_k^\dagger \hat{a}_k + \frac{g}{2L^3} \sum_{k_1,k_2,q} \hat{a}_{k_1+q}^\dagger \hat{a}_{k_2-q}^\dagger \hat{a}_{k_1} \hat{a}_{k_2}, \tag{2.14}$$

where $\hat{a}_k, \hat{a}_k^\dagger$ are annihilation and creation operators for a boson with k wave-vector, respectively, g is an interaction constant and L is a size of a system. Now it is important to consider the case of condensate. Mathematically it means following the "Bogoliubov prescription"[25, 26] consisting in the replacement

$$\hat{a}_0 = \hat{a}_0^\dagger = \sqrt{N_0}, \tag{2.15}$$

where N_0 is number of particles in condensate. At zero temperature N_0 equals the total number of particles in the system N and the ground state energy reads

$$E_0 = \frac{N^2 g}{2L^3}. \tag{2.16}$$

From the energy of the system one can find the pressure:

$$P = -\frac{\partial E_0}{\partial V} = \frac{gn^2}{2}, \tag{2.17}$$

where $n = N/V$. Next, from the hydrodynamic relation $(mc^2)^{-1} = \frac{\partial n}{\partial P}$ one can find the sound velocity:

$$c = \sqrt{\frac{gn}{m}}. \tag{2.18}$$

This is a fundamental quantity for the quantum fluids and it will appear a lot in the formulas below. Also here one can introduce the chemical potential in the system:

$$\mu = gn. \tag{2.19}$$

Taking into account the high occupation number of a ground state and low occupation numbers of the states with $\mathbf{p} \neq 0$, one can pick up from the Hamiltonian in Eq. (2.14) only the terms containing a pair of operators with $\mathbf{p} \neq 0$ and the term giving the energy of a ground state:

$$\hat{H} = \frac{g}{2L^3} \hat{a}_0^\dagger \hat{a}_0^\dagger \hat{a}_0 \hat{a}_0 + \sum_{\mathbf{k}} \frac{\hbar^2 \mathbf{k}^2}{2m} \hat{a}_{\mathbf{k}}^\dagger \hat{a}_{\mathbf{k}} + \frac{g}{2L^3} \sum_{\mathbf{k}\neq 0} \Big(4\hat{a}_0^\dagger \hat{a}_{\mathbf{k}}^\dagger \hat{a}_0 \hat{a}_{\mathbf{k}} + \hat{a}_{\mathbf{k}}^\dagger \hat{a}_{-\mathbf{k}}^\dagger \hat{a}_0 \hat{a}_0 + \hat{a}_0^\dagger \hat{a}_0^\dagger \hat{a}_{\mathbf{k}} \hat{a}_{-\mathbf{k}} \Big). \tag{2.20}$$

The total particle number writes:

$$N = \hat{a}_0^\dagger \hat{a}_0 + \sum_{\mathbf{k}\neq 0} \hat{a}_{\mathbf{k}}^\dagger \hat{a}_{\mathbf{k}}, \tag{2.21}$$

and thus the sequence of 4 operators in the first term in Eq. (2.20) representing the square of the number of particles in the condensate can be written as

$$a_0^\dagger \hat{a}_0^\dagger \hat{a}_0 \hat{a}_0 \approx N^2 - 2N \sum_{\mathbf{k}\neq 0} \hat{a}_{\mathbf{k}}^\dagger \hat{a}_{\mathbf{k}}. \tag{2.22}$$

Using Eqs. (2.21) and (2.22) one obtains from the Hamiltonian (2.20) the following quadratic Hamiltonian

$$\hat{H} = \frac{1}{2} gnN + \sum_{\mathbf{k}} \frac{\hbar^2 k^2}{2m} \hat{a}_{\mathbf{k}}^\dagger \hat{a}_{\mathbf{k}} + \frac{1}{2} gn \sum_{\mathbf{k}\neq 0} \Big(2\hat{a}_{\mathbf{k}}^\dagger \hat{a}_{\mathbf{k}} + \hat{a}_{\mathbf{k}}^\dagger \hat{a}_{-\mathbf{k}}^\dagger + \hat{a}_{\mathbf{k}} \hat{a}_{-\mathbf{k}} \Big). \tag{2.23}$$

which can be diagonalized using the standard procedure of Bogoliubov linear transformations:

$$\begin{aligned} \hat{a}_{\mathbf{k}} &= u_{\mathbf{k}} \hat{b}_{\mathbf{k}} + v_{-\mathbf{k}} \hat{b}_{-\mathbf{k}}^\dagger, \\ \hat{a}_{\mathbf{k}}^\dagger &= u_{\mathbf{k}} \hat{b}_{\mathbf{k}}^\dagger + v_{-\mathbf{k}} \hat{b}_{-\mathbf{k}}. \end{aligned} \tag{2.24}$$

To obey the Bose particles commutation relation $\hat{b}_{\mathbf{k}} \hat{b}_{\mathbf{k}'}^\dagger - \hat{b}_{\mathbf{k}'}^\dagger \hat{b}_{\mathbf{k}} = \delta_{\mathbf{k}\mathbf{k}'}$, the new operators should obey the normalization

$$|u_{\mathbf{k}}|^2 - |v_{-\mathbf{k}}|^2 = 1. \tag{2.25}$$

The parameters $u_{\mathbf{k}}, v_{-\mathbf{k}}$ can be explicitly written as:

$$u_{\mathbf{k}}, v_{-\mathbf{k}} = \pm \left(\frac{\hbar^2 k^2 / 2m + \alpha n}{2\varepsilon(k)} \pm \frac{1}{2} \right)^{1/2}, \tag{2.26}$$

and this form leads to vanishing of the off-diagonal term of a new Hamiltonian. The energy dispersion relation of new excitation described by the operators $b_{\mathbf{k}}$ and $b_{\mathbf{k}}^\dagger$ reads:

$$\varepsilon(k) = \pm \left[\frac{gn}{m} \hbar^2 k^2 + \left(\frac{\hbar^2 k^2}{2m} \right)^2 \right]^{1/2}. \tag{2.27}$$

As one can see, there are two dispersion branches - with positive and negative values of energy.

In the new basis the Hamiltonian (2.20) takes a form

$$\hat{H} = E_0 + \sum_{k\neq 0} \varepsilon(k) \hat{b}_k^\dagger \hat{b}_k. \tag{2.28}$$

It is a Hamiltonian of a new non-interacting quasiparticle obeying the Bose statistics. These quasiparticles are called *bogolons*. By their nature, bogolons are the small perturbations of the density of homogeneous condensate and resemble the waves on the deep water. Their lowest energy is the energy of an unperturbed condensate given by Eq. (2.16). The dispersion was observed both in atomic systems [27] and in exciton-polariton quantum fluids [28, 29]. Some theoretical models predict that because of the out of equilibrium properties of polariton condensates, the dispersion is actually flat at low wave vectors [18]. This actually appears to be a model-dependent results [22].

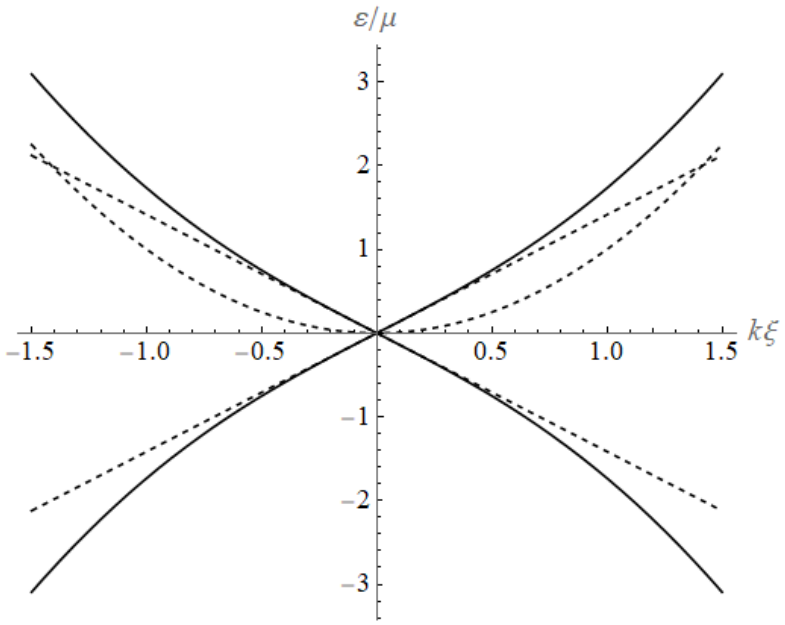

Figure 2.4: The dispersion of Bogoliubov excitations is plotted in black. Dashed curves are for parabolic dispersion of the bare bosons and for acoustic wave-like dispersion given by Eq. (2.29).

In the long wavelength limit, the dispersion becomes linear with the group velocity coinciding with the sound velocity introduced above:

$$E(k) = \hbar c k. \tag{2.29}$$

On the contrary, at large wave vectors, the dispersion in Eq. (2.31) becomes parabolic and coincides with the bare dispersion $E(k) = \frac{\hbar^2 k^2}{2m}$ (up to a constant).

The energy of bare particles $E(k)$ grows with the wave vector and at some wave vector k_{hl} reaches the value of the chemical potential in the system: $\frac{\hbar^2 k_{hl}^2}{2m} = 2gn$. This wave vector corresponds to some characteristic length

$$\xi = \frac{\hbar}{\sqrt{2mgn}} = \frac{\hbar}{\sqrt{2}mc}, \tag{2.30}$$

called healing length, a typical scale of density variations in a condensate. Its meaning will be illustrated best of all for the special (soliton and vortex) solutions of the GPE, which is a particularly efficient tool to describe the Bose-Einstein condensates and quantum fluids. Briefly, if a phase and an amplitude of a condensate wave function change at the length scale of ξ, strong fluxes appear in the system that correspond to the kinetic energy comparable with the interaction energy gn. Returning to Eq. (2.31), the wave vector ξ^{-1} separates the infrared and ultraviolet limits. Using the dimensionless wave vector $k_0 = k\xi$, the dispersion reads:

$$\varepsilon(k) = \pm\mu \left[2k_0^2 + k_0^4\right]^{\frac{1}{2}}. \tag{2.31}$$

This dispersion is plotted in Fig. 2.4.

2.2.2 Bogolons as a linearized solutions of GPE

The result from the previous section can be obtained within the seemingly differing formalism, namely by the linearization of the Gross-Pitaevskii equation. First of all it is instructive to set the reference energy to the chemical potential in the system:

$$i\hbar\frac{\partial}{\partial t}\psi(\mathbf{r},t) = \left[-\frac{\hbar}{2m}\nabla^2 + g|\psi(\mathbf{r},t)|^2 - \mu\right]\psi(\mathbf{r},t), \tag{2.32}$$

The stationary in time and homogeneous in space solution $\psi_0(\mathbf{r},t) = \sqrt{n}$ obeys this equation. Let us now try to find the solutions in the slightly perturbed form:

$$\psi = \psi_0 + \delta\psi. \tag{2.33}$$

As far as $\delta\psi$ is a complex-valued function, the following equations in the first order on $\delta\psi$ and $\delta\psi^*$ can be written to find both its real and imaginary parts:

$$\begin{aligned} i\hbar\frac{\partial}{\partial t}\delta\psi &= \left[-\frac{\hbar}{2m}\nabla^2 + 2g|\psi_0|^2 - \mu\right]\delta\psi + g\psi_0^2\delta\psi^*, \\ -i\hbar\frac{\partial}{\partial t}\delta\psi^* &= \left[-\frac{\hbar}{2m}\nabla^2 + 2g|\psi_0|^2 - \mu\right]\delta\psi^* + g\psi_0^{*2}\delta\psi. \end{aligned} \tag{2.34}$$

Let us try find $\delta\psi$ in the form

$$\delta\psi(\mathbf{r},t) = A\cdot\exp(i\mathbf{kx} - i\omega t) - B^*\cdot\exp(-i\mathbf{kx} + i\omega t), \tag{2.35}$$

with $A, B \ll \sqrt{n}$. After making this ansatz one collects the terms containing $\exp(-i\omega t)$ and $\exp(i\omega t)$. These terms are linear in A and B, and the whole procedure is a linearization of GPE. Thus we find the first order correction to the background homogeneous wave function. This procedure corresponds to keeping only terms with pair of creation/annihilation operators $(a_{\mathbf{k}}^\dagger/a_{\mathbf{k}})$ in previous section for $\mathbf{k}\neq 0$. The pair of operators $a_0^\dagger/a_0$ gives the density corresponding to the mentioned above background homogeneous wave function ψ_0. As a result, one obtains from Eqs. (2.34) the following system:

$$\begin{bmatrix} \frac{\hbar^2k^2}{2m} + gn & gn \\ -gn & -\frac{\hbar^2k^2}{2m} - gn \end{bmatrix}\begin{bmatrix} A \\ B \end{bmatrix} = \hbar\omega\begin{bmatrix} A \\ B \end{bmatrix} \tag{2.36}$$

The solutions of this system $\hbar\omega(k)$ coincide with the excitiation dispersion in Eq. (2.31). This matching of dispersion as well as the same assumptions, namely presence of a homogeneous background of particle density and the small perturbations of the latter, ascertain that in fact the same phenomenon was described within these approaches, which look different but present in fact two formulations of the same approximation.

2.2.3 Landau criterion of superfluidity

The Landau criterion of superfluidity is obtained starting from the Galilean transformations:

$$E' = E - \mathbf{P}\cdot\mathbf{V} + \frac{1}{2}MV^2,\ \mathbf{P}' = \mathbf{P} - M\mathbf{V} \tag{2.37}$$

where $\mathbf{P}$ and E are the momentum of a fluid in some reference frame and $\mathbf{V}$ is the velocity of a second reference frame with respect to a first one. The quantities in the second reference frame are denoted with the primes.

This construction can be applied to the case of a fluid flowing through a capillary with the velocity $\mathbf{v}$. The question of superfluidity in this context is a question of the kinetic energy dissipation to a heat. And the heat is carried by the fluid elementary excitations. Let E_0 be the energy of the fluid's ground state in its own reference frame. The energy of such fluid with a single excitation of wave vector $\mathbf{p}$ will write $E_0 + \varepsilon(\mathbf{p})$, where the second term gives the excitations dispersion. In the lab reference frame, where the capillary does not move (it has velocity $-\mathbf{v}$ with respect to the fluid), the energy and momentum of fluid in such state are

$$E' = E_0 + \varepsilon(\mathbf{p}) + \mathbf{p} \cdot \mathbf{v} + \frac{1}{2} M v^2, \ \mathbf{P}' = \mathbf{p} + M\mathbf{v}. \tag{2.38}$$

Thus in the laboratory coordinate frame the excitation energy is

$$\varepsilon_{lab}(\mathbf{p}) = \varepsilon(\mathbf{p}) + \mathbf{p} \cdot \mathbf{v}. \tag{2.39}$$

The excitation is favorable to be created only while having a negative energy, that is, when $\varepsilon_{lab}(\mathbf{p}) < 0$. It is possible to obey such criterion only if $v > v_{crit}$, where

$$v_{crit} = \min \left(\frac{\varepsilon(\mathbf{p})}{|\mathbf{p}|} \right), \tag{2.40}$$

thus finding a point where

$$\frac{d\varepsilon}{dp} = \frac{\varepsilon}{p}. \tag{2.41}$$

For the case of Bose-Einstein condensates with the bogolons being such excitations, $v_{crit} \equiv v_s$. To better explain this phenomenon the case of liquid He^4 is more illustrative [30, 31]. The dispersion of the excitations of liquid He^4 is linear at small wave vectors (phonon part) and has a minimum at p_0 (roton part). The rotons are the quasiparticles corresponding to the presence of curls in the superfluids. Roton part of the spectrum leads to lowering the critical velocity to 80 m/s while the sound velocity is approx. 240 m/s.

Importantly, in the employed logical construction the excitations were created for the case when the walls of the capillary were moving with respect to the condensate. However, it remains valid when some obstacle is moving inside the condensate or if the condensate is flowing around the obstacle. The consequences of realization of superfluid regime for polariton quantum fluids will be discussed in the "Quantum fluids of light" section of this chapter. Finally, we note that the Landau criterion allows to prove the superfluidity of the quantum fluids only because of the absence of the single-particle excitations.

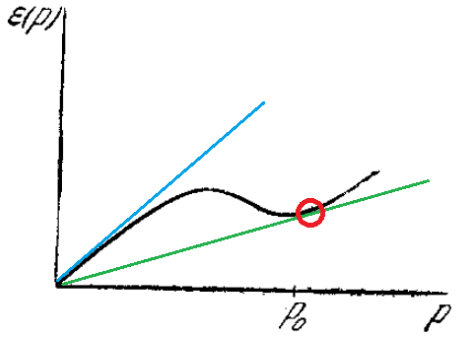

Figure 2.5: Excitation spectrum in liquid He^4 proposed by Lev Landau. Blue tangent line slope is a sound velocity and green tangent line is for the critical velocity v_{cri} affected by the presence of roton peak. Adopted from [31].

Figure 2.6: The interacting solitons in shallow water. Photo from free sources [33].

2.3 Solitons

2.3.1 Solitons in 1D

The solitons were firstly observed as solitary waves in the channel with water travelling without significant changing of the shape for a very long distance [32]. The example of soliton in water is given in Fig. 2.6. Such behavior is possible only in non-linear systems, because a wave packet in a linear system, being composed of the harmonics with different wave vectors, normally rapidly delocalizes due to velocity dispersion.

To obtain the solitonic solution, the minimal equation is a one-dimensional time-dependent Gross-Pitaevskii equation without external potential [34]:

$$i\frac{\partial}{\partial t}\psi(x,t) = -\frac{\hbar^2}{2m}\frac{\partial^2}{\partial^2 x}\psi(x,t) + g|\psi(x,t)|^2\psi(x,t). \tag{2.42}$$

It is reasonable to look for the wave function in a form

$$\psi(x,t) = \sqrt{n} f(x,t) \exp(-i\mu t/\hbar), \tag{2.43}$$

where n is the density of unperturbed condensate. Introducing the new variable

$$\zeta = \frac{x - v_s t}{\xi}, \tag{2.44}$$

and a single parameter of a problem, a dimensionless velocity

$$U = \frac{mv\xi}{\hbar} = \frac{v_s}{\sqrt{2}c}, \tag{2.45}$$

one obtains from Eq. (2.42) the following dimensionless equation:

$$2iU\frac{df}{d\zeta} = \frac{d^2 f}{d\zeta^2} + f(1 - |f|^2). \tag{2.46}$$

By making the ansatz $f = f_1 + iv/c$ and considering the imaginary part of Eq. (2.46), one obtains

$$\sqrt{2}\frac{df_1}{d\zeta} = \left(1 - \frac{v_s^2}{c^2} - f_1^2\right). \tag{2.47}$$

As a main result, after all algebra one obtains the following solution:

$$\psi_S(x - v_s t) = \sqrt{n}\left[\sqrt{1 - \frac{v_s^2}{c^2}} \tanh\left(\frac{x - v_s t}{\xi\sqrt{2}}\sqrt{1 - \frac{v_s^2}{c^2}}\right) + i\frac{v_s}{c}\right]. \tag{2.48}$$

This solution corresponds to a dip in the density of the condensate corresponding to a zero argument of the tanh function and thus having a coordinate $x = v_s t$. Thus the soliton is propagating with velocity v_s. The minimal value of the density in the dip is $n_{min} = n(v_s/c)^2$. The argument of tanh changes at the scale of $\xi/\sqrt{1 - v_s^2/c^2}$, or simply at ξ if the soliton velocity c_s is much lower than sound velocity c. If $v_s = 0$, the soliton is completely dark. When its velocity becomes comparable with the sound velocity, the soliton becomes gray and blurred due to the "relativistic" factor. The phase jump of the wave function between $x = +\infty$ and $x = -\infty$ is

$$\Delta\phi = 2\arccos(v_s/c). \tag{2.49}$$

Fig. 2.7 shows the density and phase profile of the soliton in 1D for various value of its velocity.

The distances $x \leq \xi$ correspond to the density dip in the soliton center. In this region the interaction energy dominating at large distances is converted to the kinetic energy. And again, if the condensate experiences the fluctuations in amplitude and in phase at the scale of ξ, the kinetic energy of the corresponding fluxes becomes comparable with μ. In some cases the soliton behaves as a massive particle. The energy (per unit of the length) of the soliton is

$$\varepsilon = \frac{4}{3}\hbar c n \left(1 - \frac{v_s^2}{c^2}\right)^{\frac{3}{2}}. \tag{2.50}$$

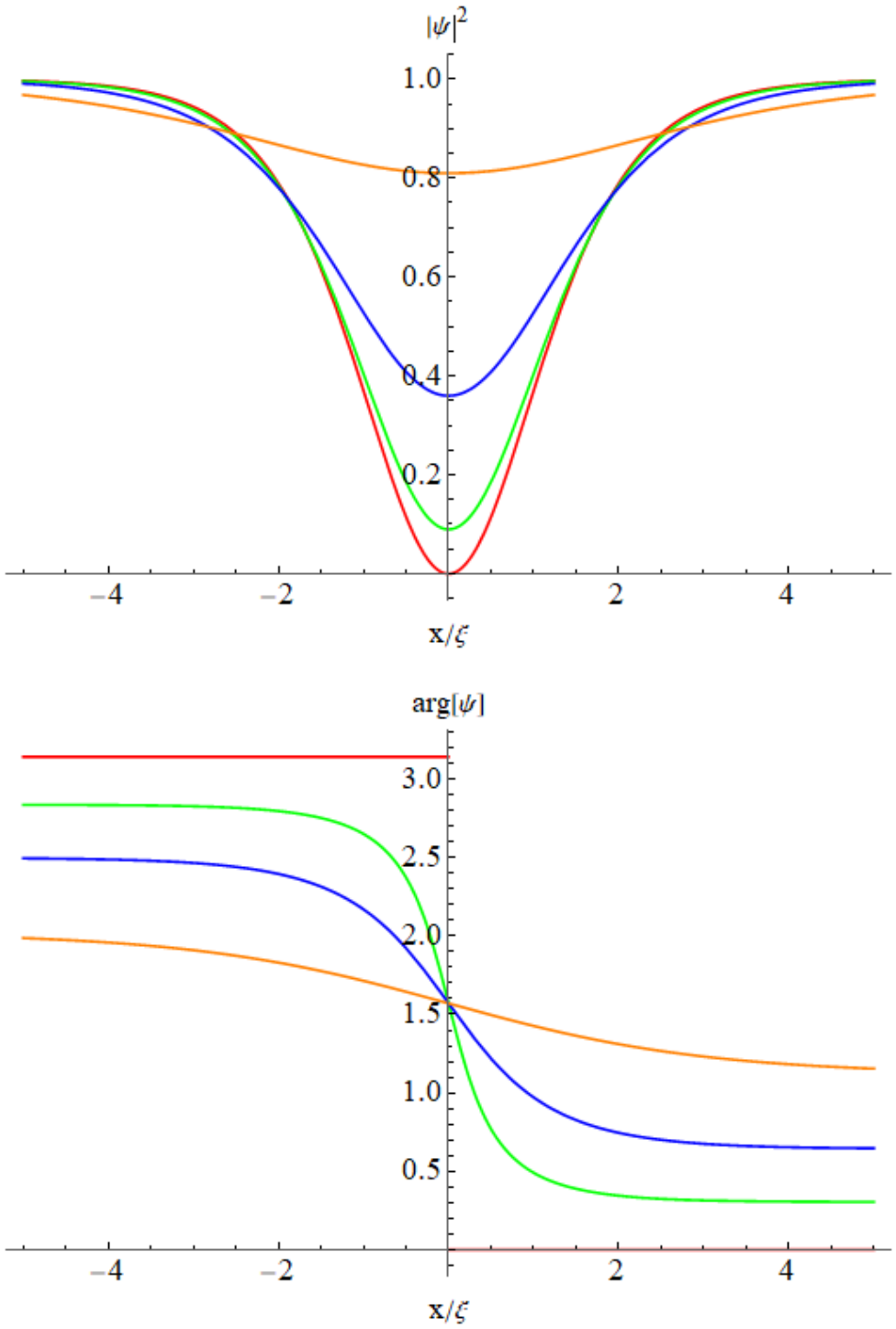

Figure 2.7: Condensate density (upper panel) and wave function argument (lower panel) corresponding to the solitonic solutions of 1D time-dependent GPE in the soliton mass center reference frame. Red, green, blue and orange curves correspond to $v_s/c = 0$, $v_s/c = 0.3$, $v_s/c = 0.6$, and $v_s/c = 0.9$, respectively.

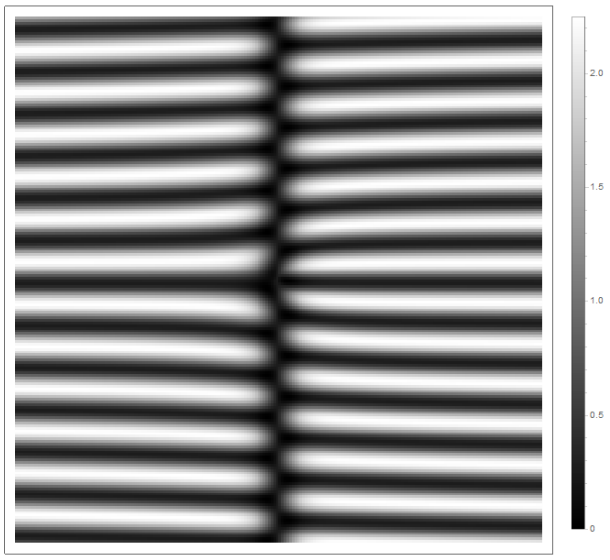

Figure 2.8: The space 2D pattern of an interference pattern $I_{CCD}(\mathbf{r})$ for the soliton wave function $\psi(\mathbf{r})$ and a reference beam having the amplitude 0.5 of the amplitude of wave function. The soliton is visible as a shift of the fringes.

One can also attribute to soliton a negative mass (also per unit of the length)

$$m_{sol} = -4\hbar n/c, \tag{2.51}$$

which is in fact a mass of condensate absent in the density dip. The well defined phase jump also provides to the soliton additional stability. All this allows to refer to the solitons as to topological defects in the condensate wave function.

2.3.2 Snake instability of solitons in 2D

The phase patterns of polariton wave function in real experiments (dimension of space is 2) including the case of the wave function of soliton can be efficiently visualized using the homodyne interference configuration, when the real 2D pattern of the electromagnetic wave emitted from the cavity proportional to $\psi(\mathbf{r})$ is mixed with a reference beam having a specific wave vector: $A_0 e^{-i\mathbf{k_0 r}}$. Mathematically, it means the following equation for the intensity going to the camera:

$$I_{CCD}(\mathbf{r}) = |\psi(\mathbf{r}) + A_0 e^{-i\mathbf{k}_0\mathbf{r}}|^2. \tag{2.52}$$

Figure 2.8 shows such interference pattern for the soliton wave function $\psi(\mathbf{r}) \equiv \psi(x, y) \equiv \psi(x)$, where $\psi(x)$ is taken from Eq. (2.48) at $t = 0$.

However, unlike the case of 1D, the solitons in 2D exhibit sufficiently differing properties. While in 1D the soliton is stable, in 2D space the solitons experience the so-called transverse (or snake, or modulational) instability, which leads to their bending and finally to their decomposition into vortex-antivortex pairs.

Returning to the case of bogolons obtained as a linearized solution of GPE (see Eq. (2.35)), it is worth mentioning that the eigenvalues of a problem Eq. (2.36) were

real. It means that these excitations are really the stationary eigenmodes of the system, and they neither grow nor decay in time. In the case of negative imaginary contribution to the frequency, such excitation would decay and, on the contrary, in the case of positive imaginary part it would grow in time, until the amplitude becomes comparable with $\sqrt{n}$, which means that the approach with linearization becomes inapplicable.

For bogolons, the unperturbed function ψ_0 was chosen as initial one. However, nothing restricts us to this. One can take e.g. the solitonic wave function from Eq. (2.48) for ψ_0. In this case, the linearized Gross-Pitaevskii equation transforms to a system of the so called Bogoliubov-de Gennes equations:

$$\begin{aligned} L(\mathbf{r})u(\mathbf{r}) + g\psi_0(\mathbf{r})^2 v(\mathbf{r}) &= \hbar\omega u(\mathbf{r}), \\ L(\mathbf{r})v(\mathbf{r}) + g(\psi_0^*(\mathbf{r}))^2 u(\mathbf{r}) &= -\hbar\omega v(\mathbf{r}), \end{aligned} \tag{2.53}$$

where

$$L(\mathbf{r}) = -\hbar^2\nabla^2/2m + 2g|\psi_0(\mathbf{r})|^2 - \mu, \tag{2.54}$$

and

$$\psi(\mathbf{r}) = \psi_0(\mathbf{r}) + u(\mathbf{r})\exp(-i\omega t) - v^*(\mathbf{r})\exp(i\omega t) \tag{2.55}$$

Not surprisingly, in case of $\psi_0(\mathbf{r}) = \sqrt{n}$, these equations lead to the eigenproblem from Eq. (2.36).

Such equations can be solved numerically in 2D. In the case of N x N mesh for $\psi_0(\mathbf{r})$, the resulting eigenproblem has $2N^2$ x $2N^2$ dimensions. It makes this problem challenging even for powerful office workstations in 2020. Fig. 2.9 shows the spatial structure of $u(\mathbf{r})$ imaginary part for a "bogolon" with the analytically defined bare wavefunction $\psi_0(\mathbf{r})$ based on the solution of a dark soliton (Eq. (2.48) with $v_s = 0$). Fig. 2.10 shows the imaginary parts of eigenvalues for several eigenvectors. Both positive and negative values are present due to the structure of the matrix. The solutions with positive values of imaginary part gives rise to the snake instability.

As far as the "bogolon" is symmetric and the soliton has an antisymmetric wave function, their superposition leads to the "curling" of the soliton. Such curling is clearly visible in Fig. 2.11. The latter shows the first experimental image of dark soliton instability obtained with the condensate of sodium atoms.

In fact, the problem of snake instability for the solitons is a 1D problem and can be solved analytically [36]. The main result is the instability growth rate as a function of excitation wave vector along the soliton. This result is presented in Fig. 2.12 and matches with the numerical one in Fig. 2.11. The reciprocal wave vector corresponding to the maximum of the dispersion estimates the size scale of the soliton curling, which is of the order of ξ in any case.

Noteworthy, the Bogoliubov-ge Gennes approach allows demonstrating that the parts of bistability curves with negative slope are unstable, see Fig. 2.13.

2.4 Quantum vortices

Another type of topological defects specific to 2D condensates are the quantum vortices. Due to their rotational nature they strictly require the demension of the system larger

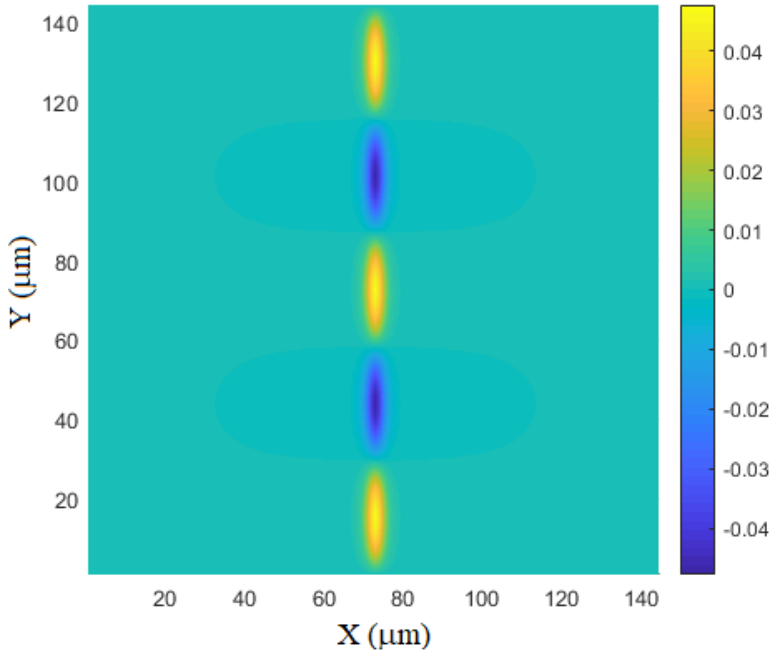

Figure 2.9: The example of profile of the imaginary part of $u(\mathbf{r})$ function obtained using the Bogoliubov-de Gennes approach for the bare wave function ψ_0 corresponding to the dark soliton. One sees that such excitation has a well defined wave vector directed along Y axis and confined along X axis.

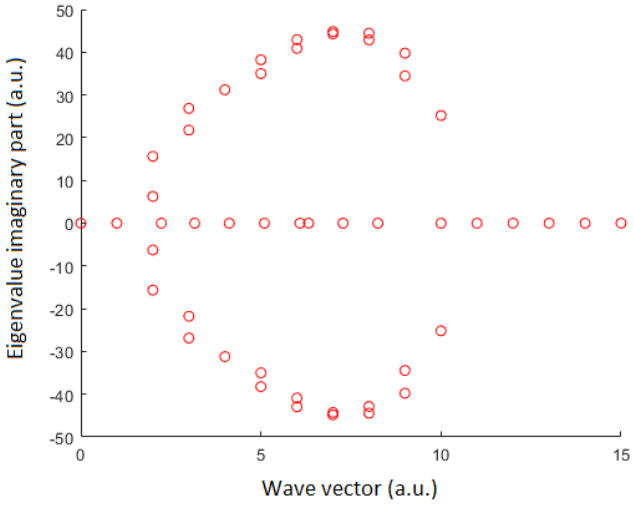

Figure 2.10: The numerically obtained imaginary parts of several eigenvalues of the Bogoliubov-de Gennes system versus the wave vector of corresponding solutions. Discreteness of wave vectors is due to periodic boundary conditions.

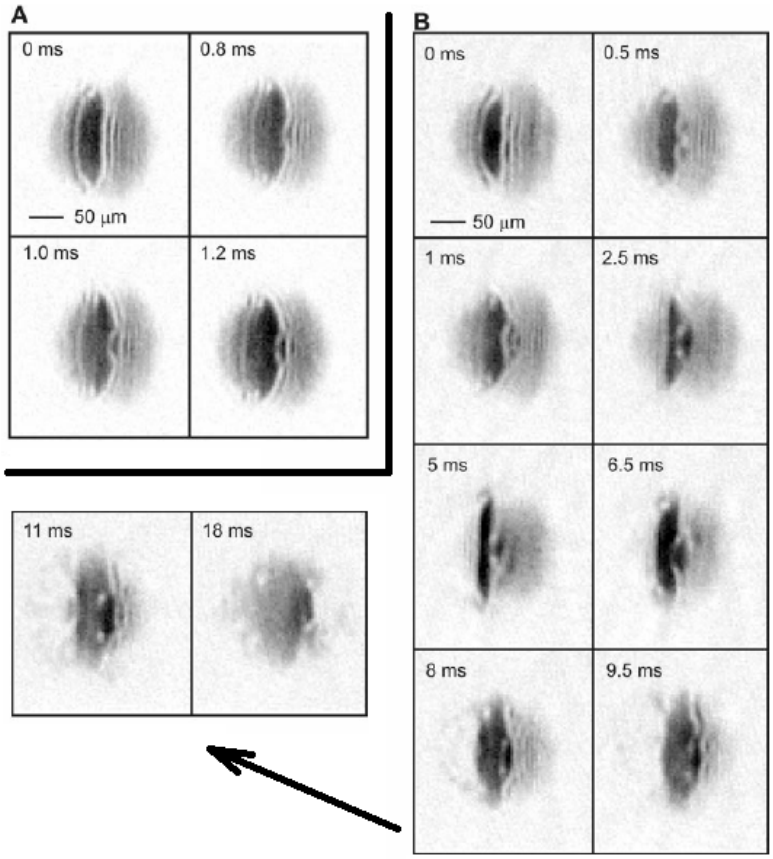

Figure 2.11: Experimental observation of snake instability in atomic Bose-Einstein condensate. Panel A: First moments of instability development visible as curling the soliton. Panel B: Longer time dynamics of the instability development. The appearance of quantum vortices is visible. Adopted from [35].

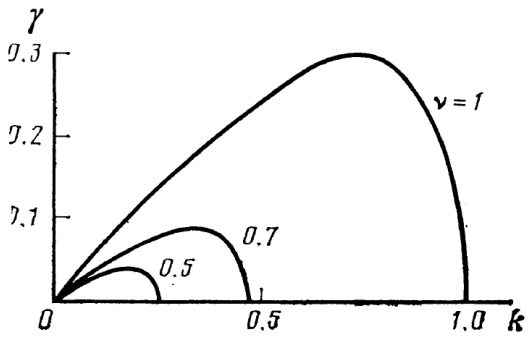

Figure 2.12: Imaginary part of spectrum versus wave vector (in the units of healing length). The parameter ν is the normalized soliton velocity v_s/c. Adopted from [36].

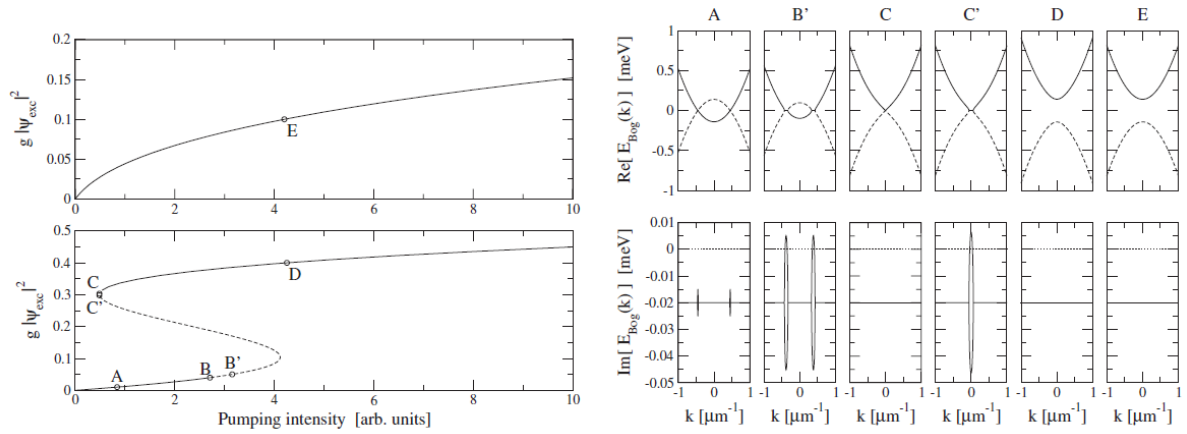

Figure 2.13: Bogoluibov-de Gennes analyis (right panel) of several points on a bistability curve (left panel). Presence of positive imaginary values of Bogoliubov eigenfrequencies indicates the growth of such excitation and thus the instability of such value of condensate density. Adopted from [37].

than 1D. Due to specific phase pattern of the vortex it is useful to present its wave function in the polar form used also for the Madelung formulation of Schrödinger equation [38, 39]. This form reads

$$\psi(\mathbf{r}) = \sqrt{n(\mathbf{r})}\exp(iS(\mathbf{r})/\hbar), \tag{2.56}$$

which leads to the fact that the velocity obtained with the relation

$$\mathbf{v} = -\frac{i\hbar}{2m}\cdot(\psi^*\nabla\psi - \psi\nabla\psi^*)\frac{1}{|\psi|^2}, \tag{2.57}$$

has a form

$$\mathbf{v} = \frac{1}{m}\nabla S(\mathbf{r}). \tag{2.58}$$

The vorticity is defined as

$$\omega = \nabla \times \mathbf{v}. \tag{2.59}$$

If S is defined on a simply connected space (in topology, a space where each 2 paths between two arbitrary chosen points can be continuously mutually transformed within this space), the vorticity Ω equals zero everywhere.

To preserve the property of having unambiguous value and thus a physical meaning for the wave function, the velocity and vorticity should obey the following relations:

$$\oint d\mathbf{r}(\nabla S(\mathbf{r})) = m\oint d\mathbf{r}\mathbf{v} = m\int dS\omega = 2\pi N\hbar, \tag{2.60}$$

where N is an integer.

Consider from now (and everywhere below in this section) the wave function with cylindrical symmetry

$$\psi(\mathbf{r}) = \sqrt{n(r)}\exp(iN\theta) = f(r)\exp(iN\theta). \tag{2.61}$$

Such wave function has a phase singularity in the point $r = 0$. Plotting the phase of such function one will also observe the phase dislocation: a 2D curve corresponding to the phase jump from 0 to 2π in case of $N = 1$ (or several dislocations in case $|N| \geq 2$). In this case one obtains

$$\mathbf{v} = \mathbf{e}_\theta \frac{\hbar N}{mr}, \tag{2.62}$$

where $\mathbf{e}_\theta$ is polar coordinate frame wave vector orthogonal to $\mathbf{e}_r$. The quantity N can be also referred as a vortex charge. The sign of N regulates the direction of condensate rotation around the vortex core.

To preserve the quantum mechanical probability current from having a divergence, the density at such point should have a zero value with the asymptotic behavior r^p, where $p \geq 1$. Thus the phase singularity is necessarily associated with a dip (with a zero value in the center) in the amplitude of wave function. Such phase singularity is in fact a topological defect, protected by the topological invariant called the "winding number".

The form of $n(r)$ is shaped by a peculiar form of an equation for the wave function. It will be affected both by the potential energy radial dependence (if it is present in the equation) and by type of non-linear interactions. For the exciton polaritons the introduced above Gross-Pitaevskii equation is of interest. The process of solution and further analysis are described in details in Ref. [40]. The solution can be found in the form

$$\psi = \sqrt{n_0}\chi(\zeta)\exp(i\theta), \tag{2.63}$$

where $\zeta = r/\xi$. The boundary conditions are

$$\chi(\zeta) = \begin{cases} 0, \zeta = 0 \\ 1, \zeta = \infty \end{cases}$$

The dimensionless GPE for the radial dependence reads

$$\left(-\frac{1}{\zeta}\frac{\partial}{\partial\zeta}\zeta\frac{\partial}{\partial\zeta} + \frac{1}{\zeta^2}\right)\chi = 2\chi(1-\chi^2), \tag{2.64}$$

whose solution can be found numerically. However it is useful write its simple analytical approximate form

$$\chi(\zeta) = \frac{\zeta}{\sqrt{\zeta^2 + \Lambda^{-2}}}, \tag{2.65}$$

where $\Lambda \approx 0.8249$. Equations (2.63) and (2.65) are essential to calculate the energy of an arbitrary given vortex spatial configuration based on their coordinates and signs. This approach will be actively used in the Chapter 3 devoted to the quantum turbulence, the phenomenon strictly based on the spatial correlations of quantum vortex positions. Fig. 2.14 shows the profiles of exact numerically obtained χ and the introduced ansatz. At short distances $r \ll \xi$ one sees that $\chi \propto r$, which shapes the vortex core with the density dip, and at large distances ($r \gg \xi$) the density becomes a constant. The transition between these two regimes takes place at distances $r \approx \xi$ and thus the healing length is in fact a size of vortex core size. Fig. 2.15 shows the vortex phase pattern and a interference fringes pattern for the homodyne experiment.

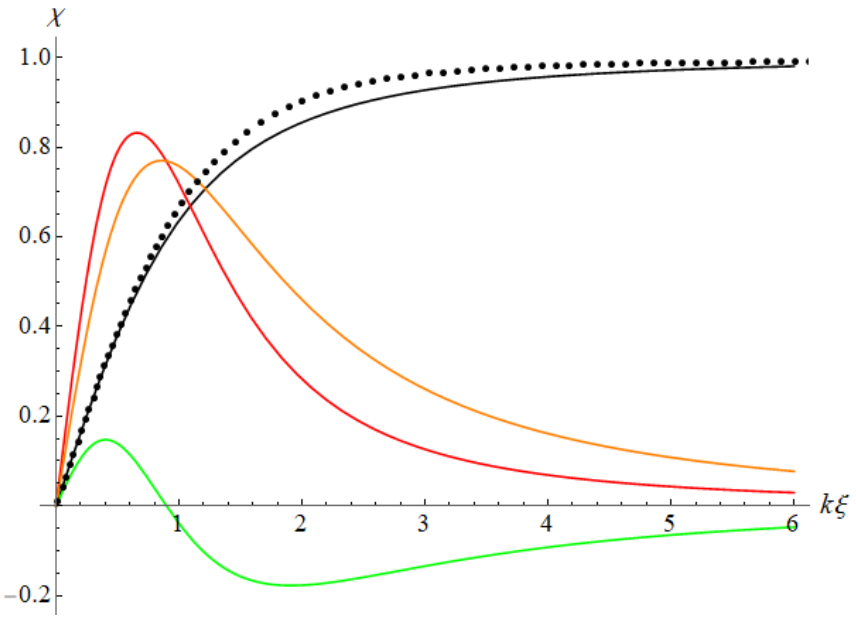

Figure 2.14: Radial part χ of the quantum vortex wave function. Black dots are for numerical solution and black curve is for the ansatz from Eq. (2.65). Red and orange curves are for l.h.p. and r.h.p. of Eq. (2.64) when the ansatz is used, respectively, and green curve is for their difference. Adopted from [40].

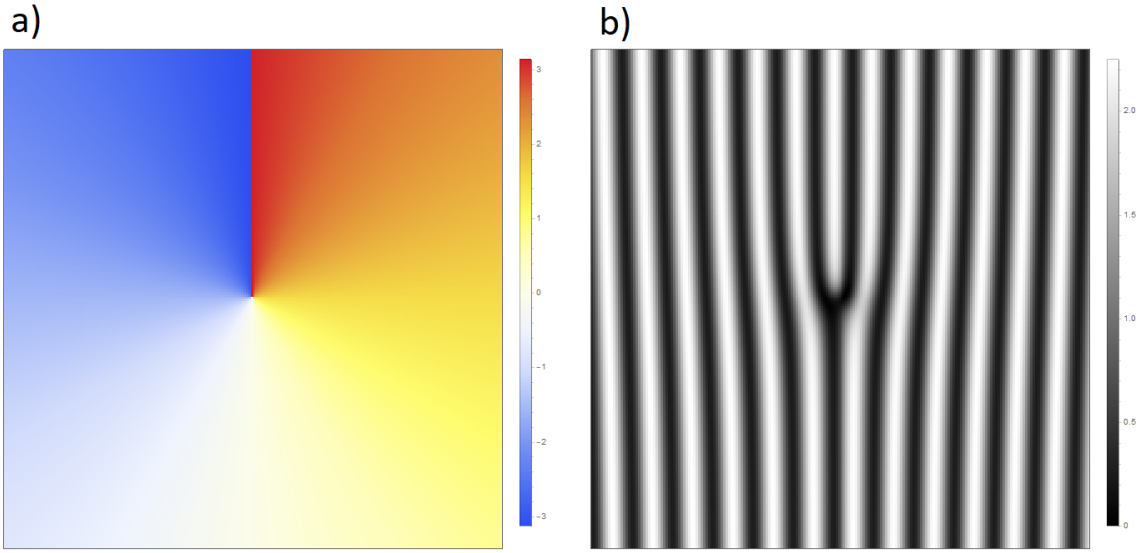

Figure 2.15: Panel a). Phase pattern of a quantum vortex. Panel b). The space 2D pattern of $I_{CCD}(\mathbf{r})$ for the vortex wave function obtained in the homodyne interference experiment. The votrex is visible as a dislocation of the fringes.

The important value is the energy of the vortex, which is in fact a difference between the energy of a homogeneous condensate and that of a condensate with a single vortex.

$$E_v = \int \left(\frac{\hbar^2}{2m} |\nabla \psi|^2 + \frac{g}{2} \left(|\psi|^2 - n \right)^2 \right) r dr d\theta \tag{2.66}$$

The main contribution comes from the condensate kinetic energy at the distances $r \gg \xi$. The estimation of the vortex energy is quite simple. According to Eq. (2.62) the velocity behaves like $1/r$ and the rotational kinetic energy $\propto \int r dr (1/r)^2$, which is $\ln(R/\xi)$. ξ is logically the lower cutoff corresponding to the vortex core size. Upper cutoff is a distance at which the phase dislocation propagates away from the vortex core. In case of a condensate with single vortex inside, R estimates the physical size of the condensate. The exact equation for the energy reads

$$E(N) = \pi n N^2 \hbar^2 \ln(CR/\xi), \tag{2.67}$$

where C is a constant of the order of 1.

The important consequence of this dependence of the vortex energy on the vortex charge is that N vortices with charges $+1$ are energetically more favorable with respect to single vortex of a charge $+N$. As a result, the latter is unstable and quickly becomes torn to single-charged vortices. This can be referred as "splitting instability" and can be also analyzed using the Bogoliubov de-Gennes approach [41, 42].

In fact, all three described types of excitations of the condensate are very closely related with each other with a possibility of mutual transformation. The very deep "bogolon" generates so high condensate fluxes that the corresponding phase jump becomes comparable with solitonic one. Also, a density dip in the presence of background inhomogeneous condensate fluxes can be torn into a vortex-antivortex pair. On the contrary, the vortex and the antivortex can form a pair and continue their approaching, and can finally annihilate, with the creation of a deep bogolon. As shown above, solitons in 2D are unstable by their nature and are destroyed by the snake instability with the formation of vortex-antivortex pairs.

2.5 Quantum fluids of light

Due to the essential part of the photon properties possessed by polaritons, one often refers to polaritons at high densities as to "Quantum fluids of light". In this section, we will describe the recent experiments proving the real quantum fluid nature of polaritons in microcavities. Such phenomena are the presence of the superfluidity and the observed typical solutions of GPE as solitons and quantum vortices.

The superfluid regime corresponds to the case when all flows in the quantum fluid are subsonic. However, if a supersonic flow passes in the vicinity of an obstacle, this obstacle begins producing the excitaions visible as a shock waves. Fig. 2.16 shows the various experimentally measured regimes of polariton quantum fluid passing around a defect in a cavity, playing the role of such obstacle. The superfluid regime corresponds to presence of the shock waves, which are in fact the excitations with lead to the energy dissipation. In the case of subsonic flows, the shock waves disappear.

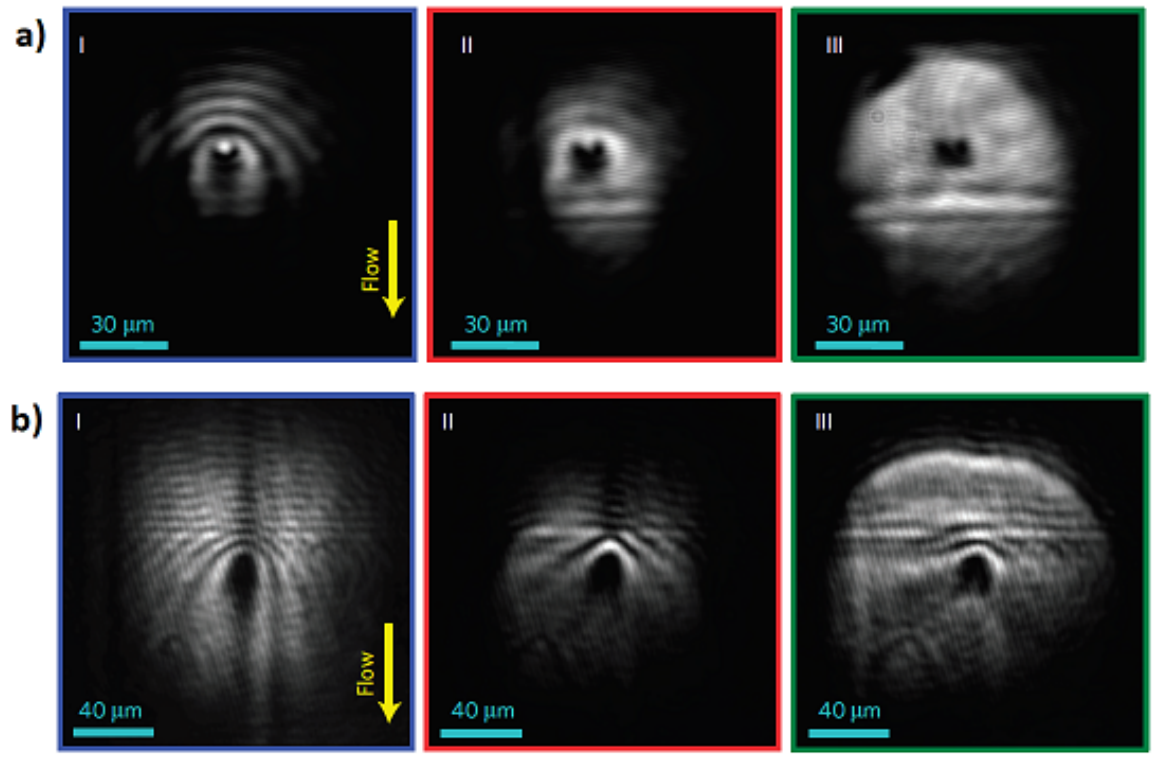

Figure 2.16: The polariton quantum fluid under scattering by a cavity defect in various regimes. Row a) corresponds to low in-plane wave vector of the exciting laser (and thus the subsonic flow). Polariton density increases from the frames I to III. In the row b) the in-plane wave vector is larger, providing a supersonic flow evidenced by the presence of the shock waves. Adopted from [43].

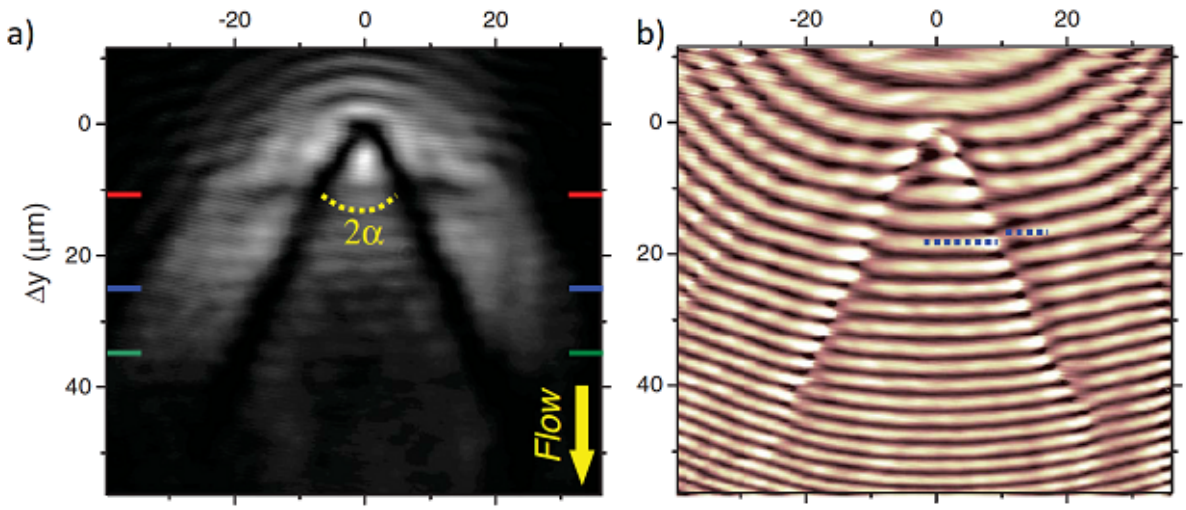

Figure 2.17: Dark oblique solitons created in the the system of resonantly pumped cavity. The in-plane wave vector creates the supersonic flow. Panel a) shows the emission intensity spatial map and panel b) shows the interference map. Adopted from [45].

Fig. 2.17 also shows the solitons detected in the system in exciton-polariton quantum fluids. From the point of view of the structure of GPE, this case is much more complicated than the case of 1D dark or gray solitons. This is a 2D system, with resonant pumping by a laser with the in-plane wave vector, also with the finite lifetime, and the presence of a potential barrier. All this leads to formation of a pair of solitons having an angle 2α and originating from the density dip created by the defect. The solitons are well visible as dislocations in the interference fringes like in the theoretical Fig. 2.8. The connection with the refined theoretical situation described above is more evident if one realizes that the vertical dimension in the 2D image is in fact an effective time (because the regime is supersonic) and thus the distance between the solitons increases with time. The solitons do not experience the snake instability because due to the supersonic regime they are effectively 1D. The truly 1D solitons were studied in the wire microcavity in Ref. [44]. To be really 1D in this context, the width of the cavity should not exceed the healing length. The fingerprints of the solitons were visible as the typical spatial and phase solitonic profiles along the cavity.

Finally, quantum fluids of light reveals such solutions of GPE as quantum vortices. Fig. 2.19 shows such results. Normally, the vortices can move freely in the condensate dragged by the existing flows. However, in real cavities it is more energetically favorable for the vortices to be pinned to the defects in the shape of point-like potential barriers. This allows their detection in the cw experiments.

Some other experiments when the polatrions behave as quantum fluids involve necessarily engineering the potential profile or a shape of the laser beam. They will be described in the next subsection.

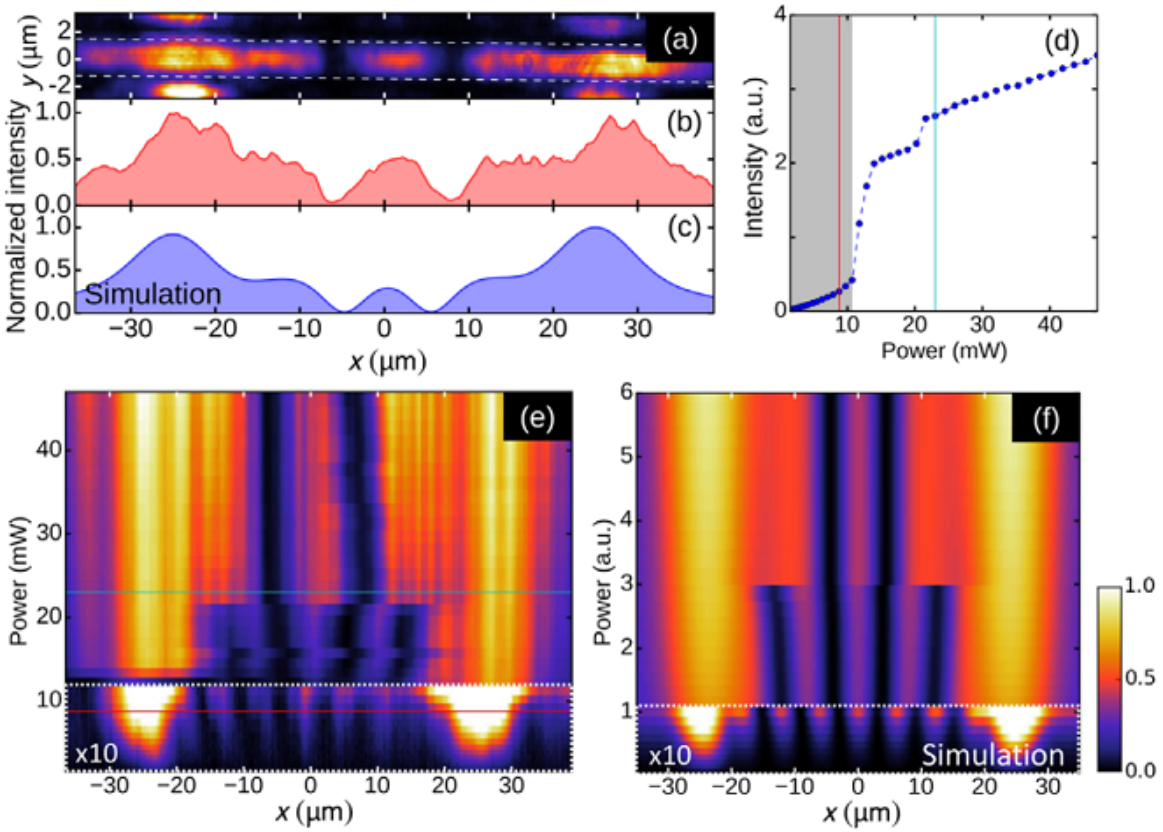

Figure 2.18: Observation of 1D solitons in wire cavity. Panel a) shows the 2D emission profile transferred then to 1D geometry (panel b). Panel c) shows the results of the simulations. Panel d) is for total emission intensity vs the laser power showing the jump to the upper bistability branch. Panels e) and f) show the experimental and numerical evolution of emission profile when raising the laser power. Adopted from [44].

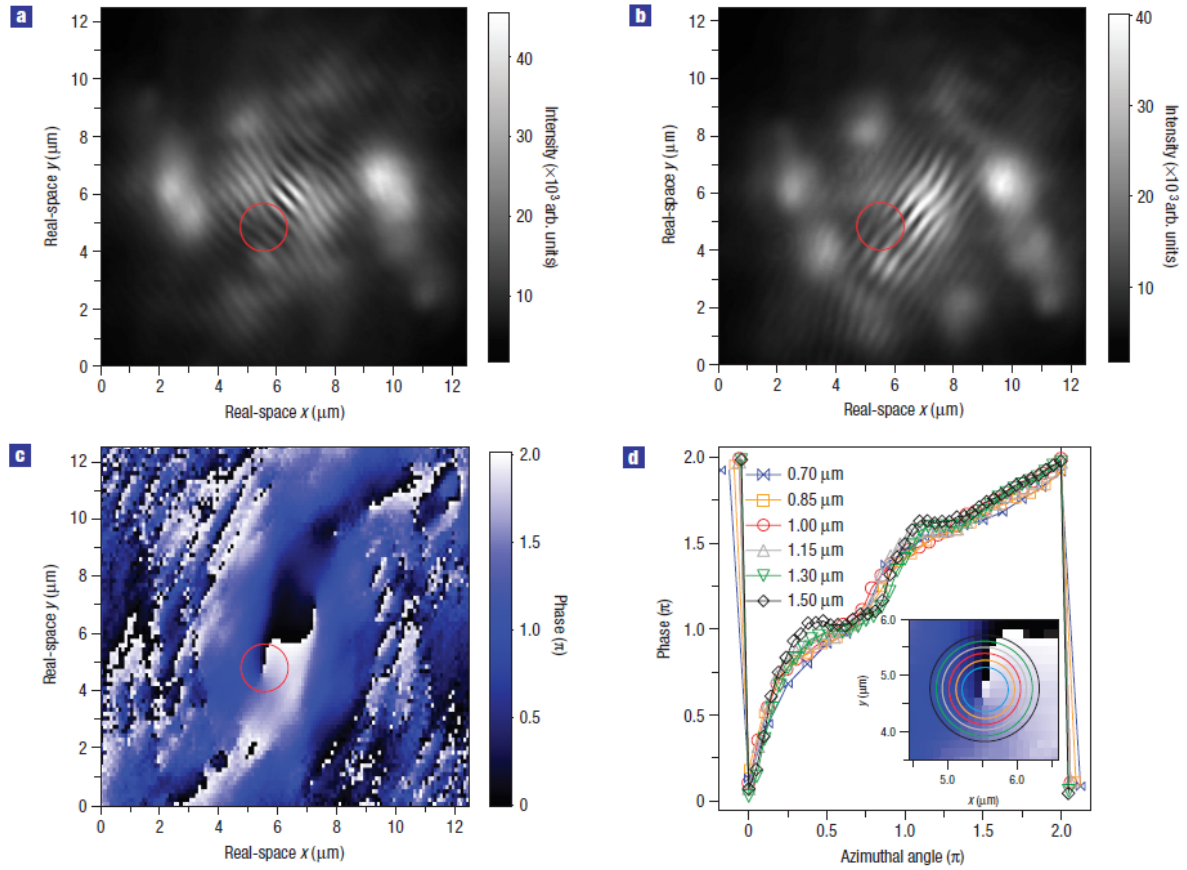

Figure 2.19: Observation of vortices in the system of cavity exciton polatitons. Panels a) and b) show the interferograms with the reference beams coming from two different remote regions of polariton condensate. Vortices are seen as a fringes dislocations. Panel c) shows the reconstructed phase and panel d) plots the phase around one of the vortices. Adopted from [46].

2.6 Shaping polariton wave function and potential

For electrons, excitons, and of course for polaritons in semiconductors the potential and wave function shaping is of high importance and can generate multiple effects like non-linear transport phenomena, open possibilities to study the **analog physics**, creating polariton molecules and crystals with the specific band structure resembling the band structure of real 2D crystalline materials [47]. First, the quantum wires can be also considered as a type of a patterning of the in-plane potential for quantum 2D well structures. In this context, one should also mention the distributed feedback lasers with the grating creating the photon stopband obtained as a periodic modulation of a 2D potential. Due to the photonic component of the polaritons, one can also obtain a possibility to fully control the wave function, namely tune its amplitude and shape, by controlling the phase and amplitude of electromagnetic field of a pumping laser in the quasi resonant regime. Such wave function engineering can be used in multiple ways, e.g. for setting the GPE initial conditions in pulsed experiment or allowing to sustain the polariton density in a cw experiment, overcoming the effect of polariton decay.

2.6.1 Various techniques

The potential for polaritons (as well as for other quasiparticles in semiconductors) can be organized via the metallic masks deposition. The purposes of such patterning can be various. E.g. the metallic stripes on the heterostructure surface can change the symmetry of the system and, as a result, generate a class of non-linear phenomena: photogalvanic and ratchet effects [48]. Using the metallic film with the round apertures in the square lattice allowed the observation of the formation of a polaritonic band structure induced by such superlattice [49]. The potential in the shape of a square lattice was also obtained using the two crossing standing acoustic waves [50]. Such technique of crossing the beams is very common in the optics of atoms [51], but with the crossing of laser beams. Due to exciton-exciton interaction, the polaritons can create the potential for themselves. In fact, it means that the points in the sample intensively irradiated by the laser start acting as a potential barrier. It was demonstrated e.g. in Ref. [52].

2.6.2 Progress in etching

Wire microcavities are one of the first (middle of 90s) examples of polariton potential shaping by the means of lithography and etching [53]. Nowadays, much more complicated structures are under investigation. Along with sophistication of the pattern itself, the progress was achieved in the increasing of polariton lifetime. The cavities in the shape of wire were also used in the studies of confinement of polariton quantum fluids by the optically-induced potentials [54, 55, 44]. Such shape of the cavity changes the dimension of the system from 2D to 1D, which is important e.g. in the context of the soliton stability in the quantum fluids. Other direction, which also involves the state-of-the-art techniques in lithography and etching, is creating the polaritonic systems exhibiting the states resembling the molecule-like and crystal-like electronic structures. The molecule-like behavior, such as the manifestation of bonding and anti-bonding orbitals originating from "atomic" states with various angular momenta were observed in Ref. [56, 57].

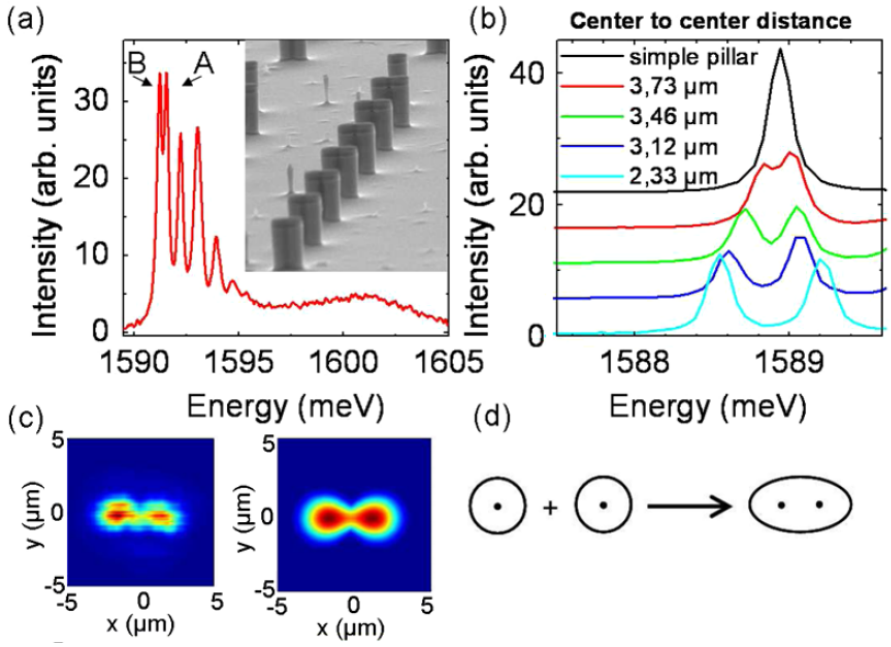

Figure 2.20: Polariton molecules. a) Emission spectrum of a single molecule (inset with SEM image of a structure). Bonding (B) and antibonding (A) orbitals fingerprints are observable. b) Process of hybridization. Emission spectra for various interpillar distances. c) Experimentally measured and theoretical luminecsence intensity profiles d) sketch of molecule formation. Adopted from [57].

Manufacturing a polariton honeycomb crystal and observation of a graphene-like polariton band structure including the famous Dirac cones was reported in [58]. The progress in the sample manufacturing allowed touching much more fine effects, such as the deformation of the Dirac cones with an anisotropic modification of the hopping between the pillars [59] or even observation of the Landau levels [60]. The topological edge states in a polariton honeycomb lattice, predicted in [61], were recently observed in real experiments [62]. Based on the polariton Mach–Zehnder interferometer obtained by the means of cavity etching [63], the possibility of all-optical polariton phase control was demonstrated, see Fig. 2.23.

2.6.3 Spatial light modulator

The spatial light modulator (SLM) is an electro-optical device, which allows regulating amplitude and phase of an electromagnetic wave. There are various types of device which are used either as phase or amplitude modulators. SLMs are actively used for the shaping of laser beams in the physics of quantum fluids based both on atomic gases [64] and cavity polaritons [65].

SLM is composed of an array of discrete pixels each acting as a variable waveplate. Typically, SLM devices are based on the liquid crystal technology and operate either in the reflection or in the transmission geometry. Due to rather moderate refresh rate of the liquid crystals, the frequency of SLMs is typically lower than kHz, which is many orders of magnitude longer than typical characteristic times of the physics of polaritons.

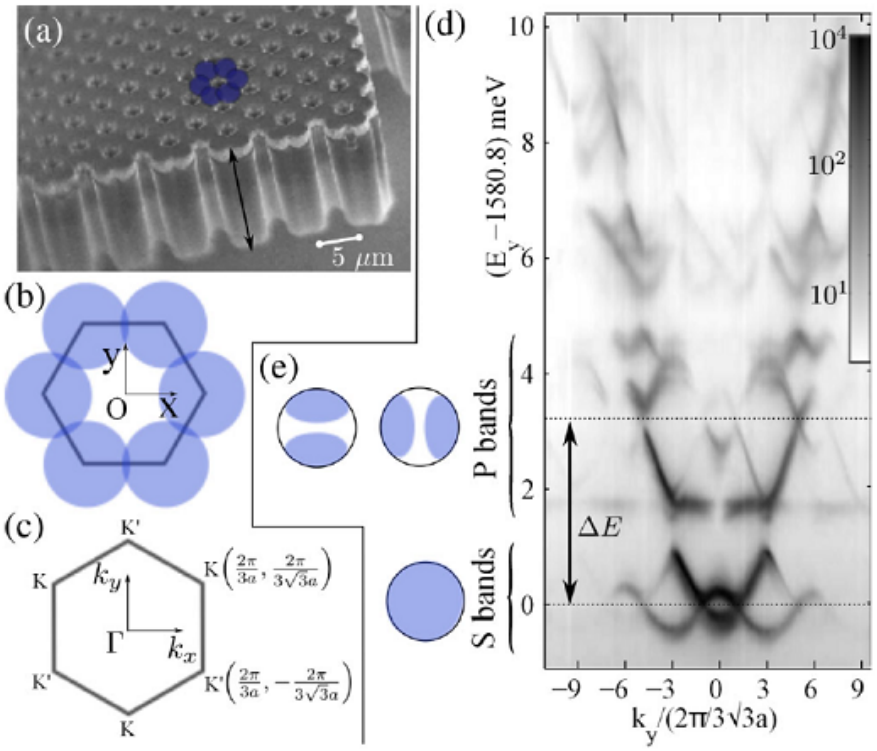

Figure 2.21: Polariton honeycomb crystal. The SEM image of the grown and etched structure with the hexagonal element of honeycomb lattice highlighted. Adopted from Ref. [58]

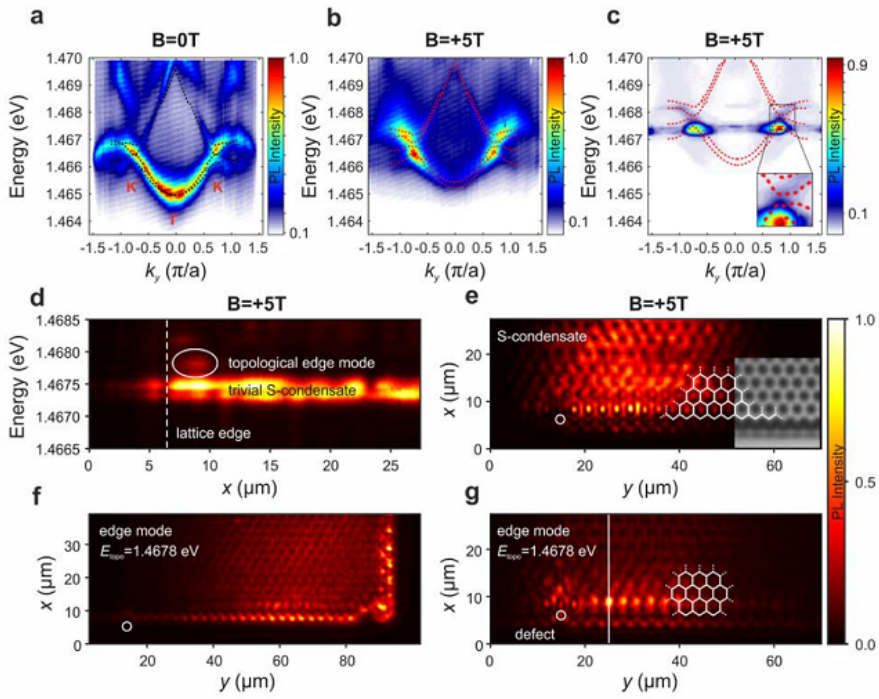

Figure 2.22: Detection of a polariton condensate in a topological edge mode. a) Adopted from [62]

.

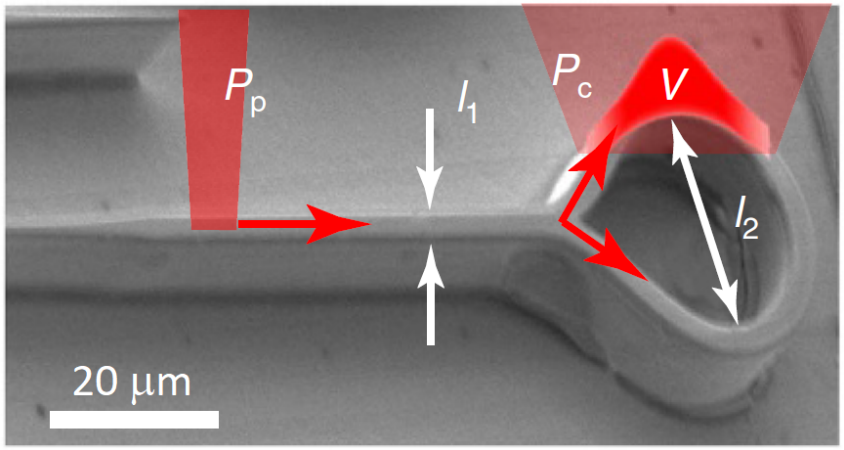

Figure 2.23: The polariton Mach–Zehnder interferometer based on the etched microcavity. Adopted from [63]

.

E.g. for the excitation wave vectors of the order of 1 μm^{-1} the typical group velocities estimate several μm/ps. In case of quantum fluids, the specific sound velocity (Bogoluibov excitation or polariton density wave propagation speed) is of the same order. Thus, for the sample sizes of the dozens of microns one obtains characteristic times of dozens of picoseconds. The same magnitude is for the polariton lifetime (mainly due to relatively short cavity photon lifetime) for many semiconductor cavities [66] and only the state-of-the-art cavities can reach hundreds of picoseconds [67]. According to all this, the SLM can not be an active real-time player in the processes with polariton wave function evolution. But it can effectively replace the processes of the sample microfabrication (making the masks or cavity etching). Thus the straight possibilities are opened to implement a lot of configurations with the same sample and even in the same setup run. Such opportunity would be appreciated e.g. for the experimental realization of the polaritonic neuron concept [68], requiring creating the corridors of a complex shape. Spatial resolution of SLMs estimates to 512x512 pixels (with a physical size of an active area of a device of the order of 1 cm), which allows creating very complex patterns. This image can be then projected using the lenses to the area of the order of micromenters in size, which is typical scale for the physics of polaritons.

An example of the SLM usage is Ref. [69] where the SLM was used to imprint the beam with a high angular momentum (Lauss-Laguerre) leading to the formation of a stationary and thus observable in cw experiment quantum vortices in the polariton quantum fluid. Developed configuration allowed the observation of the transition from the linear regime (wave function follows the pumping laser profile) to the non-linear regime (thanks to the interactions the wave function is not completely constrained by the laser, but the topologically-protected solutions are stable, in this case the so-called quantum vortices).

Optical potential created using SLM allows trapping the condensates to the various confined areas, e.g. having the ring geometry [65], and to observe the states with high angular momentum. Besides the direct spatial imprinting of the optical potential or of the polariton wave function, the SLM can act as an analogue optical component, e.g. controlling the beam angles for dispersion measurements [70].

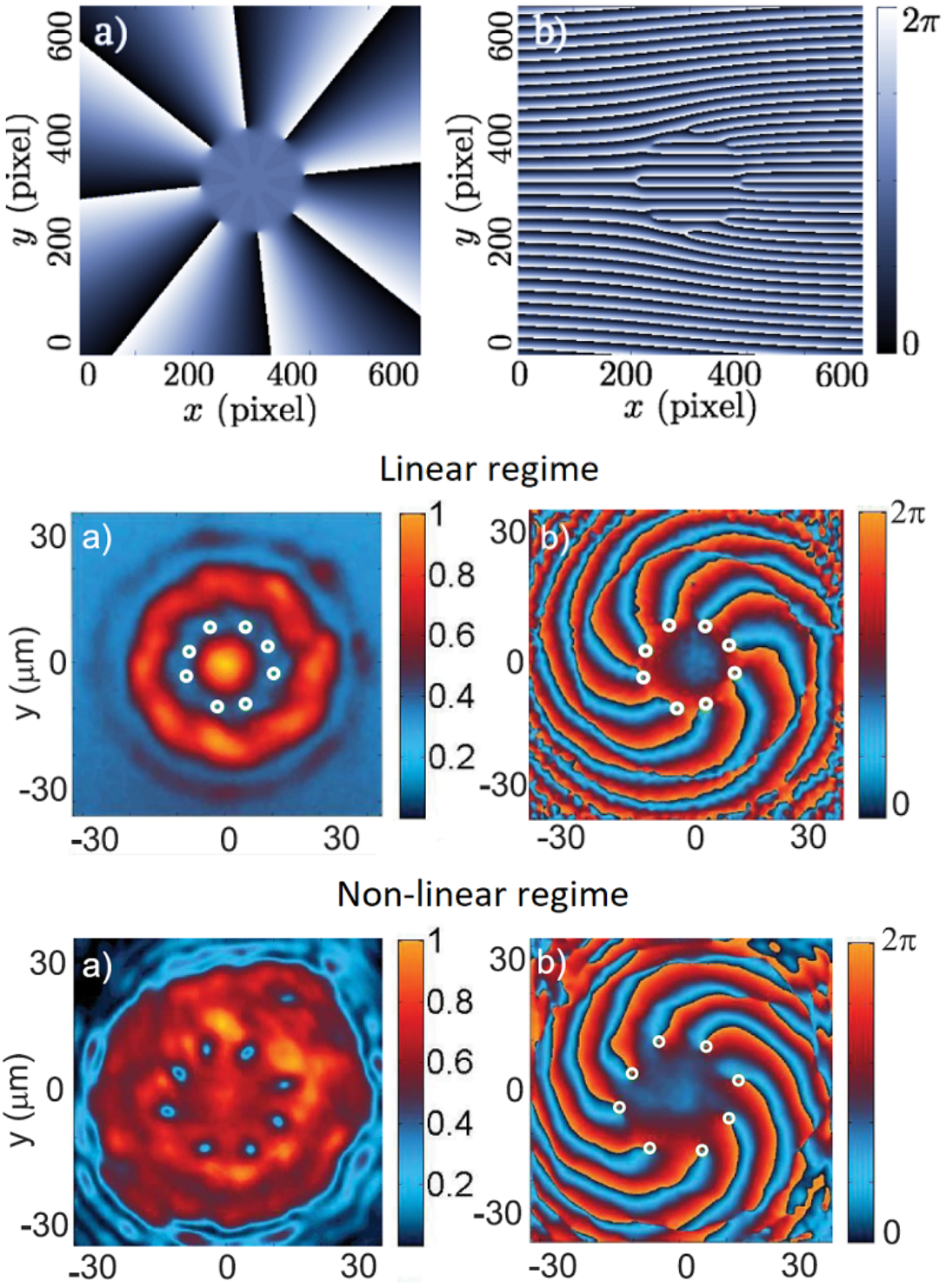

Figure 2.24: Imprinting the vortices using the Gauss-Laguerre-like SLM-generated laser profile. Upper row: the sent SLM "hologram" (phase only (a) and phase + grating (b) profiles), middle row: linear regime (density (a) and phase(b) of the polaritons), bottom row: non-linear regime (density (a) and phase(b) of the polaritons). The quantum vortices are clearly visible as the density defects of low density [69]

.

Bibliography

[1] M. M. Glazov, H. Ouerdane, L. Pilozzi, G. Malpuech, A. V. Kavokin, and A. D'Andrea, "Polariton-polariton scattering in microcavities: A microscopic theory," *Phys. Rev. B*, vol. 80, p. 155306, Oct 2009.

[2] S. O. Demokritov, V. E. Demidov, O. Dzyapko, G. A. Melkov, A. A. Serga, B. Hillebrands, and A. N. Slavin, "Bose–einstein condensation of quasi-equilibrium magnons at room temperature under pumping," *Nature*, vol. 443, no. 7110, pp. 430–433, 2006.

[3] A. A. Serga, V. S. Tiberkevich, C. W. Sandweg, V. I. Vasyuchka, D. A. Bozhko, A. V. Chumak, T. Neumann, B. Obry, G. A. Melkov, A. N. Slavin, *et al.*, "Bose–einstein condensation in an ultra-hot gas of pumped magnons," *Nature communications*, vol. 5, no. 1, pp. 1–8, 2014.

[4] L. Butov, A. Ivanov, A. Imamoglu, P. Littlewood, A. Shashkin, V. Dolgopolov, K. Campman, and A. Gossard, "Stimulated scattering of indirect excitons in coupled quantum wells: Signature of a degenerate bose-gas of excitons," *Physical Review Letters*, vol. 86, no. 24, p. 5608, 2001.

[5] A. Brichkin, S. Novikov, A. Larionov, V. Kulakovskii, M. Glazov, C. Schneider, S. Höfling, M. Kamp, and A. Forchel, "Effect of coulomb interaction on exciton-polariton condensates in gaas pillar microcavities," *Physical Review B*, vol. 84, no. 19, p. 195301, 2011.

[6] A. Einstein, "Quantentheorie des einatomigen idealen gases," *SB Preuss. Akad. Wiss. phys.-math. Klasse*, 1924.

[7] S. N. Bose, "Plancks gesetz und lichtquantenhypothese," *Zeitschrift für Physik*, vol. 26, p. 178, 1924.

[8] M. H. Anderson, J. R. Ensher, M. R. Matthews, C. E. Wieman, and E. A. Cornell, "Observation of bose-einstein condensation in a dilute atomic vapor," *science*, pp. 198–201, 1995.

[9] J. Kasprzak, M. Richard, S. Kundermann, A. Baas, P. Jeambrun, J. Keeling, F. Marchetti, M. Szymańska, R. André, J. Staehli, *et al.*, "Bose–Einstein condensation of exciton polaritons," *Nature*, vol. 443, no. 7110, p. 409, 2006.

[10] H. Deng, G. Weihs, C. Santori, J. Bloch, and Y. Yamamoto, "Condensation of semiconductor microcavity exciton polaritons," *Science*, vol. 298, no. 5591, pp. 199–202, 2002.

[11] R. Balili, V. Hartwell, D. Snoke, L. Pfeiffer, and K. West, "Bose-einstein condensation of microcavity polaritons in a trap," *Science*, vol. 316, no. 5827, pp. 1007–1010, 2007.

[12] C. Lai, N. Kim, S. Utsunomiya, G. Roumpos, H. Deng, M. Fraser, T. Byrnes, P. Recher, N. Kumada, T. Fujisawa, *et al.*, "Coherent zero-state and π-state in an exciton–polariton condensate array," *Nature*, vol. 450, no. 7169, pp. 529–532, 2007.

[13] M. Amthor, T. C. H. Liew, C. Metzger, S. Brodbeck, L. Worschech, M. Kamp, I. A. Shelykh, A. V. Kavokin, C. Schneider, and S. Höfling, "Optical bistability in electrically driven polariton condensates," *Physical Review B*, vol. 91, no. 8, p. 081404, 2015.

[14] J. Kasprzak, D. D. Solnyshkov, R. André, L. S. Dang, and G. Malpuech, "Formation of an exciton polariton condensate: Thermodynamic versus kinetic regimes," *Phys. Rev. Lett.*, vol. 101, p. 146404, Oct 2008.

[15] Y. Sun, P. Wen, Y. Yoon, G. Liu, M. Steger, L. N. Pfeiffer, K. West, D. W. Snoke, and K. A. Nelson, "Bose-einstein condensation of long-lifetime polaritons in thermal equilibrium," *Physical review letters*, vol. 118, no. 1, p. 016602, 2017.

[16] O. Penrose and L. Onsager, "Bose-einstein condensation and liquid helium," *Physical Review*, vol. 104, no. 3, p. 576, 1956.

[17] V. Yukalov, "Basics of bose-einstein condensation," *Physics of Particles and Nuclei*, vol. 42, no. 3, pp. 460–513, 2011.

[18] M. Wouters and I. Carusotto, "Excitations in a nonequilibrium bose-einstein condensate of exciton polaritons," *Physical review letters*, vol. 99, no. 14, p. 140402, 2007.

[19] M. Wouters and V. Savona, "Stochastic classical field model for polariton condensates," *Physical Review B*, vol. 79, no. 16, p. 165302, 2009.

[20] I. Shelykh, R. Johne, D. Solnyshkov, A. Kavokin, N. Gippius, and G. Malpuech, "Quantum kinetic equations for interacting bosons and their application for polariton parametric oscillators," *Physical Review B*, vol. 76, no. 15, p. 155308, 2007.

[21] D. Sarchi, P. Schwendimann, and A. Quattropani, "Effects of noise in different approaches for the statistics of polariton condensates," *Physical Review B*, vol. 78, no. 7, p. 073404, 2008.

[22] D. Solnyshkov, H. Terças, K. Dini, and G. Malpuech, "Hybrid boltzmann–gross-pitaevskii theory of bose-einstein condensation and superfluidity in open driven-dissipative systems," *Physical Review A*, vol. 89, no. 3, p. 033626, 2014.

[23] J. Rogel-Salazar, "The gross–pitaevskii equation and bose–einstein condensates," *European Journal of Physics*, vol. 34, no. 2, p. 247, 2013.

[24] D. H. Kobe, "Lagrangian densities and principle of least action in nonrelativistic quantum mechanics," *arXiv preprint arXiv:0712.1608*, 2007.

[25] N. Bogoliubov, "On the theory of superfluidity," *J. Phys*, vol. 11, no. 1, p. 23, 1947.

[26] L. Pitaevskii and S. Stringari, *Bose-Einstein condensation and superfluidity*, vol. 164. Oxford University Press, 2016.

[27] D. Stamper-Kurn, A. Chikkatur, A. Görlitz, S. Inouye, S. Gupta, D. Pritchard, and W. Ketterle, "Excitation of phonons in a Bose-Einstein condensate by light scattering," *Physical review letters*, vol. 83, no. 15, p. 2876, 1999.

[28] S. Utsunomiya, L. Tian, G. Roumpos, C. Lai, N. Kumada, T. Fujisawa, M. Kuwata-Gonokami, A. Löffler, S. Höfling, A. Forchel, *et al.*, "Observation of Bogoliubov excitations in exciton-polariton condensates," *Nature Physics*, vol. 4, no. 9, p. 700, 2008.

[29] T. Byrnes, T. Horikiri, N. Ishida, M. Fraser, and Y. Yamamoto, "Negative Bogoliubov dispersion in exciton-polariton condensates," *Physical Review B*, vol. 85, no. 7, p. 075130, 2012.

[30] R. P. Feynman, "Superfluidity and superconductivity," *Reviews of modern physics*, vol. 29, no. 2, p. 205, 1957.

[31] A. A. Abrikosov, L. P. Gorkov, and I. E. Dzyaloshinski, *Methods of quantum field theory in statistical physics*. Courier Corporation, 2012.

[32] J. S. Russell, "Report on waves," in *14th meeting of the British Association for the Advancement of Science*, vol. 311, p. 1844, 1844.

[33] M. J. Ablowitz, *Photographs of line soliton interactions*, Accessed 19 Nov 2019. `https://sites.google.com/site/ablowitz/line-solitons/x-type-interactions`.

[34] T. Tsuzuki, "Nonlinear waves in the Pitaevskii-Gross equation," *Journal of Low Temperature Physics*, vol. 4, no. 4, pp. 441–457, 1971.

[35] Z. Dutton, M. Budde, C. Slowe, and L. V. Hau, "Observation of quantum shock waves created with ultra-compressed slow light pulses in a Bose-Einstein condensate," *Science*, vol. 293, no. 5530, pp. 663–668, 2001.

[36] E. Kuznetsov and S. Turitsyn, "Instability and collapse of solitons in media with a defocusing nonlinearity," *Zh. Eksp. Teor. Fiz*, vol. 94, p. 129, 1988.

[37] I. Carusotto and C. Ciuti, "Quantum fluids of light," *Reviews of Modern Physics*, vol. 85, no. 1, p. 299, 2013.

[38] E. Madelung, "Eine anschauliche deutung der gleichung von schrödinger," *Naturwissenschaften*, vol. 14, no. 45, pp. 1004–1004, 1926.

[39] E. Madelung, "Quantentheorie in hydrodynamischer form," *Zeitschrift für Physik A Hadrons and Nuclei*, vol. 40, no. 3, pp. 322–326, 1927.

[40] A. S. Bradley and B. P. Anderson, "Energy spectra of vortex distributions in two-dimensional quantum turbulence," *Physical Review X*, vol. 2, no. 4, p. 041001, 2012.

[41] H. Saito and M. Ueda, "Split instability of a vortex in an attractive Bose-Einstein condensate," *Physical review letters*, vol. 89, no. 19, p. 190402, 2002.

[42] Y. Kawaguchi and T. Ohmi, "Splitting instability of a multiply charged vortex in a bose-einstein condensate," *Physical Review A*, vol. 70, no. 4, p. 043610, 2004.

[43] A. Amo, J. Lefrère, S. Pigeon, C. Adrados, C. Ciuti, I. Carusotto, R. Houdré, E. Giacobino, and A. Bramati, "Superfluidity of polaritons in semiconductor microcavities," *Nature Physics*, vol. 5, no. 11, p. 805, 2009.

[44] V. Goblot, H. S. Nguyen, I. Carusotto, E. Galopin, A. Lemaître, I. Sagnes, A. Amo, and J. Bloch, "Phase-controlled bistability of a dark soliton train in a polariton fluid," *Phys. Rev. Lett.*, vol. 117, p. 217401, Nov 2016.

[45] A. Amo, S. Pigeon, D. Sanvitto, V. Sala, R. Hivet, I. Carusotto, F. Pisanello, G. Leménager, R. Houdré, E. Giacobino, *et al.*, "Polariton superfluids reveal quantum hydrodynamic solitons," *Science*, vol. 332, no. 6034, pp. 1167–1170, 2011.

[46] K. G. Lagoudakis, M. Wouters, M. Richard, A. Baas, I. Carusotto, R. André, L. S. Dang, and B. Deveaud-Plédran, "Quantized vortices in an exciton–polariton condensate," *Nature Physics*, vol. 4, no. 9, p. 706, 2008.

[47] T. Ozawa, H. M. Price, A. Amo, N. Goldman, M. Hafezi, L. Lu, M. C. Rechtsman, D. Schuster, J. Simon, O. Zilberberg, and I. Carusotto, "Topological photonics," *Rev. Mod. Phys.*, vol. 91, p. 015006, Mar 2019.

[48] P. Olbrich, J. Karch, E. L. Ivchenko, J. Kamann, B. März, M. Fehrenbacher, D. Weiss, and S. D. Ganichev, "Classical ratchet effects in heterostructures with a lateral periodic potential," *Phys. Rev. B*, vol. 83, p. 165320, Apr 2011.

[49] N. Y. Kim, K. Kusudo, C. Wu, N. Masumoto, A. Löffler, S. Höfling, N. Kumada, L. Worschech, A. Forchel, and Y. Yamamoto, "Dynamical d-wave condensation of exciton–polaritons in a two-dimensional square-lattice potential," *Nature Physics*, vol. 7, no. 9, p. 681, 2011.

[50] E. A. Cerda-Méndez, D. Sarkar, D. N. Krizhanovskii, S. S. Gavrilov, K. Biermann, M. S. Skolnick, and P. V. Santos, "Exciton-polariton gap solitons in two-dimensional lattices," *Phys. Rev. Lett.*, vol. 111, p. 146401, Oct 2013.

[51] Z. Zhang, F. Li, G. Malpuech, Y. Zhang, O. Bleu, S. Koniakhin, C. Li, Y. Zhang, M. Xiao, and D. Solnyshkov, "Particlelike behavior of topological defects in linear wave packets in photonic graphene," *Physical Review Letters*, vol. 122, no. 23, p. 233905, 2019.

[52] A. Amo, S. Pigeon, C. Adrados, R. Houdré, E. Giacobino, C. Ciuti, and A. Bramati, "Light engineering of the polariton landscape in semiconductor microcavities," *Phys. Rev. B*, vol. 82, p. 081301, Aug 2010.

[53] A. I. Tartakovskii, V. D. Kulakovskii, A. Forchel, and J. P. Reithmaier, "Exciton-photon coupling in photonic wires," *Phys. Rev. B*, vol. 57, pp. R6807–R6810, Mar 1998.

[54] L. Ferrier, E. Wertz, R. Johne, D. D. Solnyshkov, P. Senellart, I. Sagnes, A. Lemaître, G. Malpuech, and J. Bloch, "Interactions in confined polariton condensates," *Physical Review Letters*, vol. 106, no. 12, p. 126401, 2011.

[55] E. Wertz, A. Amo, D. D. Solnyshkov, L. Ferrier, T. C. H. Liew, D. Sanvitto, P. Senellart, I. Sagnes, A. Lemaître, A. V. Kavokin, G. Malpuech, and J. Bloch, "Propagation and amplification dynamics of 1d polariton condensates," *Phys. Rev. Lett.*, vol. 109, p. 216404, Nov 2012.

[56] D. Bajoni, P. Senellart, E. Wertz, I. Sagnes, A. Miard, A. Lemaître, and J. Bloch, "Polariton laser using single micropillar GaAs−GaAlAs semiconductor cavities," *Phys. Rev. Lett.*, vol. 100, p. 047401, Jan 2008.

[57] M. Galbiati, L. Ferrier, D. D. Solnyshkov, D. Tanese, E. Wertz, A. Amo, M. Abbarchi, P. Senellart, I. Sagnes, A. Lemaître, E. Galopin, G. Malpuech, and J. Bloch, "Polariton condensation in photonic molecules," *Phys. Rev. Lett.*, vol. 108, p. 126403, Mar 2012.

[58] T. Jacqmin, I. Carusotto, I. Sagnes, M. Abbarchi, D. D. Solnyshkov, G. Malpuech, E. Galopin, A. Lemaître, J. Bloch, and A. Amo, "Direct observation of dirac cones and a flatband in a honeycomb lattice for polaritons," *Phys. Rev. Lett.*, vol. 112, p. 116402, Mar 2014.

[59] M. Milićević, G. Montambaux, T. Ozawa, O. Jamadi, B. Real, I. Sagnes, A. Lemaître, L. Le Gratiet, A. Harouri, J. Bloch, and A. Amo, "Type-iii and tilted dirac cones emerging from flat bands in photonic orbital graphene," *Phys. Rev. X*, vol. 9, p. 031010, Jul 2019.

[60] O. Jamadi, E. Rozas, M. Milićević, G. Salerno, T. Ozawa, I. Carusotto, L. Le Gratiet, I. Sagnes, A. Lemaître, A. Harouri, *et al.*, "Observation of photonic landau levels in strained honeycomb lattices," in *European Quantum Electronics Conference*, p. ec_3_2, Optical Society of America, 2019.

[61] A. V. Nalitov, D. D. Solnyshkov, and G. Malpuech, "Polariton $\mathbb{Z}$ topological insulator," *Phys. Rev. Lett.*, vol. 114, p. 116401, Mar 2015.

[62] S. Klembt, T. Harder, O. Egorov, K. Winkler, R. Ge, M. Bandres, M. Emmerling, L. Worschech, T. Liew, M. Segev, *et al.*, "Exciton-polariton topological insulator," *Nature*, vol. 562, no. 7728, p. 552, 2018.

[63] C. Sturm, D. Tanese, H. Nguyen, H. Flayac, E. Galopin, A. Lemaître, I. Sagnes, D. Solnyshkov, A. Amo, G. Malpuech, *et al.*, "All-optical phase modulation in a cavity-polariton Mach–Zehnder interferometer," *Nature communications*, vol. 5, p. 3278, 2014.

[64] D. McGloin, G. C. Spalding, H. Melville, W. Sibbett, and K. Dholakia, "Applications of spatial light modulators in atom optics," *Optics Express*, vol. 11, no. 2, pp. 158–166, 2003.

[65] A. Dreismann, P. Cristofolini, R. Balili, G. Christmann, F. Pinsker, N. G. Berloff, Z. Hatzopoulos, P. G. Savvidis, and J. J. Baumberg, "Coupled counterrotating polariton condensates in optically defined annular potentials," *Proceedings of the National Academy of Sciences*, vol. 111, no. 24, pp. 8770–8775, 2014.

[66] R. Houdré, C. Weisbuch, R. P. Stanley, U. Oesterle, and M. Ilegems, "Coherence effects in light scattering of two-dimensional photonic disordered systems: Elastic scattering of cavity polaritons," *Phys. Rev. B*, vol. 61, pp. R13333–R13336, May 2000.

[67] A. Gianfrate, O. Bleu, L. Dominici, V. Ardizzone, M. De Giorgi, D. Ballarini, K. West, L. Pfeiffer, D. Solnyshkov, D. Sanvitto, *et al.*, "Direct measurement of the quantum geometric tensor in a two-dimensional continuous medium," *arXiv preprint arXiv:1901.03219*, 2019.

[68] T. C. H. Liew, A. V. Kavokin, and I. A. Shelykh, "Optical circuits based on polariton neurons in semiconductor microcavities," *Phys. Rev. Lett.*, vol. 101, p. 016402, Jul 2008.

[69] T. Boulier, H. Terças, D. Solnyshkov, Q. Glorieux, E. Giacobino, G. Malpuech, and A. Bramati, "Vortex chain in a resonantly pumped polariton superfluid," *Scientific reports*, vol. 5, p. 9230, 2015.

[70] P. Mai, B. Pressl, M. Sassermann, Z. Vörös, G. Weihs, C. Schneider, A. Löffler, S. Höfling, and A. Forchel, "Multi-dimensional laser spectroscopy of exciton polaritons with spatial light modulators," *Applied Physics Letters*, vol. 100, no. 7, p. 072109, 2012.

Chapter 3

Quantum turbulence in the system of cavity exciton-polaritons quantum fluids

Contents

3.1 Introduction

3.1.1 Cascades in classical 3D and 2D turbulence

The classical turbulence is a complex behavior (also with a significant role of stochasticity) of liquids at high Reynolds numbers, when in the Navier-Stokes equations (one can consider the incompressible case for simplicity) the second (convective) term overcomes the third one, governed by the diffusion (viscous) term. This hierarchy of terms makes the Navier-Stokes equations non-linear ones, which leads to the complex chaotic behavior mentioned above. The equation for the velocity $\mathbf{u}$ within this framework writes:

$$\frac{\partial \mathbf{u}}{\partial t} + (\mathbf{u} \cdot \nabla)\mathbf{u} - \nu \nabla^2 \mathbf{u} = \mathbf{g}, \tag{3.1}$$

where ν is kinematic viscosity and $\mathbf{g}$ is the external force (like gravity). The additional continuity equation is $\nabla \mathbf{u} = \mathbf{0}$.

At low fluid velocity, the second term is smaller than the third and thus no turbulence occurs. In the case of static solution, no external forces, and no curls in the flow (the so called *potential flow*), one can write

$$\mathbf{u} = \nabla \varphi, \tag{3.2}$$

while the problem to be solved becomes

$$\Delta \varphi = 0. \tag{3.3}$$

This is the simplest case of a *linear* hydrodynamics problem.

In general, the phenomenon of turbulence can be described as follows. We suppose that the injection of energy takes place at a certain size scale. The injected energy becomes the kinetic energy of the liquid, providing its motion (or "pulsations" as said in Ref. [1]) at the size scale λ_{inj}. Such pulsations typically have a shape of eddies/vortices. At this scale, the convection non-linear (second) term in Eq. (3.1) is higher than the dissipative one (third term).

Then, the kinetic energy is transferred to the pulsations of the lower scales $\lambda_1 < \lambda_{\text{inj}}$, which form the eddies at the corresponding scale. And this process repeats by the transfer of energy and creating the vortices of corresponding size for $\lambda_{\text{inj}} > \lambda_1 > \lambda_2 > ... > \lambda_n > ... > \lambda_{\text{Kolm}}$. The last scale in this chain is the so called Kolmogorov scale [2, 3, 4, 5, 6] at which the viscous term becomes comparable with convection term. In fact, it means that kinetic energy starts effective dissipation into the heat and the process of its transfer stops. Such structure of nested eddies was proposed by Lewis F. Richardson in 1922 [7].

The classical derivation of the Richardson cascade by Kolmogorov involves significantly the reasoning by the method of dimensions. Let the value ε be an energy quantity that is dissipated in one second per gramm of the liquid. The dimension of ε is $\text{erg}/(\text{cm} \cdot \text{s}) = \text{cm}^2/\text{s}^3$. This energy comes to the system from the macroscopic motion at the scale λ_{inj} with the velocity of liquid displacement v_{inj}. The macroscopic motion does not depend on the value of the viscosity (since the corresponding term in the Navier-Stokes equations is small). It means that ε should be expressed only via λ_{inj} and v_{inj}. The only possible combination giving the correct dimension is

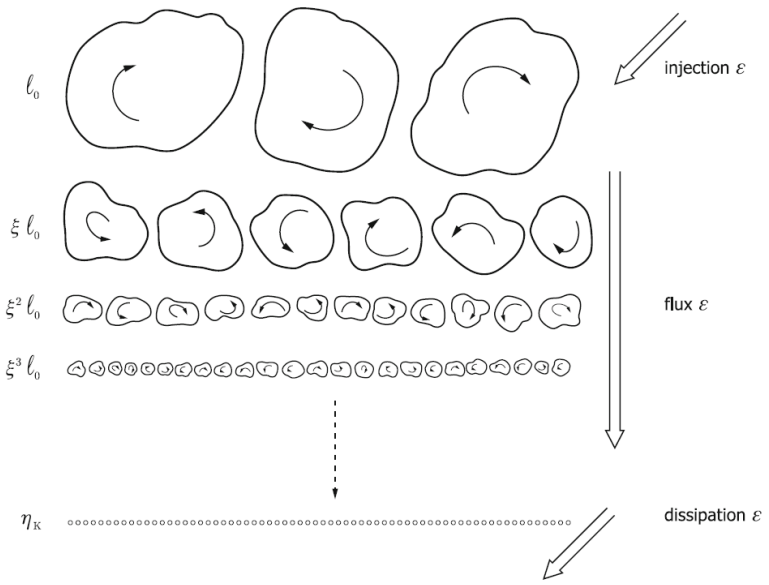

Figure 3.1: Scheme of energy transfer in the case of 3D classical turbulence resulting in the Richardson cascade. Adopted from Ref. [8].

$$\varepsilon = \frac{v_{\text{inj}}^3}{\lambda_{\text{inj}}}. \tag{3.4}$$

For the liquid velocity at the size scale λ, using the same reasoning of the dimensions, one can write

$$v_\lambda = (\varepsilon\lambda)^{1/3}. \tag{3.5}$$

A parameter which is crucial for the turbulence is the so-called spectral energy density $E(k)$, defined as a kinetic energy density (or a kinetic energy per gram of a liquid) stored in the wave vector interval dk. This definition implies that

$$E_{\text{kinetic}} = \int_0^\infty E(k)dk. \tag{3.6}$$

The dimension of $E(k)$ is cm^3/s^2. As a result, to correctly "construct" $E(k)$ from ε and k, only the following combination is valid:

$$E(k) = \text{const} \cdot \varepsilon^{2/3} k^{-5/3}. \tag{3.7}$$

This is the so-called Kolmogorov law for the Richardson cascade.

If one integrates $E(k)$ from some k' to infinity, one obtains the energy stored in the pulsations of the scales smaller than $\lambda' = 1/k'$:

$$\int_{k'}^\infty E(k)dk \propto \frac{\varepsilon^{2/3}}{k^{2/3}} \propto (\varepsilon\lambda')^{2/3} \propto v_{\lambda'}^2. \tag{3.8}$$

However, for the 2D turbulence this scheme is not relevant, as it was shown by Kraichnan[9]. He considered the transfer of energy between the bins of various wave

vectors: $... < k_{i-1} < k_i < k_{i+1} < ....$ The basic event for the energy transfer is the elementary excitation (wave) scattering. For the 3D case, the pair interaction can satisfy both energy and vorticity conservation laws. For the 2D case, the "three-particle collisoins" are obligatory. As a result, in 2D two different cascades take place. Let λ_{inj} be the size scale at which the energy is injected into the 2D fluid. The energy cascade in the 2D case is inverse and has a power law $-5/3$. Such a direction of energy transfer leads to the fact that liquid becomes excited at larger and larger scales, finally at all scales up to the size of the vessel. The flow of vorticity in this inverse energy cascade is zero. The vorticity is involved in another cascade, which is direct. In this cascade, the energy flow is zero with a steady state of $E(k) \propto \eta^{2/3} k^{-3}$, where η is the vorticity transfer rate.

Kraichnan states that the considered 2D case is relevant for the atmospheric flows and also gives a parallel with quantum fluids based on Bose-Einstein condensates:

There is a fairly close dynamical analogy in which the number density and kinetic-energy density of the bosons play the respective roles of kinetic-energy density and squared vorticity. (The flow of vorticity into small scales in two dimensional turbulence is then analogous to the flow of kinetic energy into high wave numbers during the formation of the boson condensate.)

So, the direct energy flow (larger to smaller scales) according to Kraichnan takes place during the formation of a condensate. However, the process of condensate formation is not a process of the excitation of the already existing condensate by applying the potential obstacle "in motion". Still, the direction of energy cascade in 2D quantum turbulence is under debates, the results that support both direct and inverse energy cascades were obtained, as we will see below.

3.1.2 Current discussions on existence of cascades in 2D quantum turbulence

The existence of a similar inverse cascade, suggested for quantum 2D turbulence [10], is actually still a matter of a strong debate [11]. Contrary to the 3D quantum turbulence, observed in liquid helium [12, 13, 14] and atomic condensates [15, 16, 17, 18, 19, 20], the inverse cascade of 2D quantum turbulence remains elusive even in numerical simulations, let alone real experiments [11, 20]. Indeed, while several works[10, 21] report the numerical observation of an inverse cascade with a scaling of $-5/3$, others argue against it [22]. The enstrophy in quantum fluids is proportional to the total number of quantum vortices, which can appear and (most importantly) disappear only in pairs. While there are arguments in favor of the formation of the enstrophy cascade [23], it is also argued by other authors [22] that the dissipation of enstrophy in quantum fluids could be expected to occur differently from the classical ones: instead of requiring a transfer to smallest scales, it could on the contrary be dissipated at any scale above the vortex size (healing length). For example, two very large clusters rotating in opposite directions and forming a dipole could dissipate vorticity along their mutual boundary, without requiring any transfer to smaller scales associated with the redistribution of vortices and formation of smaller clusters and isolated vortex pairs. So, the enstrophy cannot be *a priori* considered as a conserved quantity which is transferred over scales in order to be dissipated

at the smallest ones, and thus the incompatibility of the scaling of cascades cannot be used to prove the existence of the inverse energy cascade. Still, the self-organization of individual vortices into clusters discussed theoretically [24, 25, 26, 27] and observed in recent experiments [28, 29] strongly suggests that the inverse cascade should exist.

Not only the conclusions of the scaling arguments are controversial, but the mathematical limits, imposed on numerical simulations by the properties of the real systems are so stringent, that they prevent one from drawing definite conclusions from the numerically observed energy cascades published in the most recent works. Indeed, one never observes a cascade over more than 1 decade of wave vectors in such simulations (and even in recent experiments with 3D condensates[19]), and the suggested scaling is usually not a *fit* of the spectral density, but only a guide for the eyes. Actually, since the spectral energy density often presents a transition between large and small scales (either at the injection scale or at the vortex size), any scaling exponent can be suggested as a tangent to such bell-like curve, and the interpretation is therefore highly arbitrary.

The chapter is organized as follows. Next section is devoted to introducing the methods of analysis used in the chapter: numerical solution of the GPE, calculation of the incompressible kinetic energy (IKE) spectrum based on the Fourier transformation and its semi-analytical calculation via the positions of vortices. Also the procedure of vortex cluster separation is described. In the 3$^{\text{rd}}$ section, the main results are given: the obtained IKE spectra for various quantum fluid stirring (excitation) methods, separating of the contribution from clustered vortices, analysis of the obtained power laws, analysis of the fractal dimensions of the structures of clustered vortices, analysis of energy transfer between various size scales while exciting the quantum fluid. Finally, the conclusions will be given.

3.2 Developing the tools to study quantum turbulence

3.2.1 Gross Pitaevskii equation numerical solution

As it was discussed in the previous chapters, the basic tool for numerical simulations of an interacting bosonic quantum fluid is the Gross-Pitaevski equation [30, 31]. It has been used for the simulation of quantum turbulence in numerous papers [11, 24, 32], including ones devoted to studying the energy cascade[33, 34, 21] and behavior of single vortices[35, 36]. This equation can also be extended, to account for the thermal (uncondensed) part of the fluid [37, 38], and for other effects, such as the energy relaxation [39], finite lifetime and pumping [40]. However, the description of large-scale systems is difficult to be carried out at the level of full GPE numerical simulation of the quantum fluid, and in this case other models are used, such as the point particle gas approximation with the specific vortex-vortex potentials [25, 41, 42, 23].

The polaritonic quantum fluid is particularly well known for its non-equilibrium driven-dissipative features, due to the finite lifetime of polaritons usually determined by the quality factor of a cavity. In present chapter, I deliberately neglect these features, trying to make an additional step towards the solution of the problem of inverse or direct nature of the quantum turbulence in the general case of conservative quantum fluids. Such

description of the polariton fluid corresponds to the limiting case of long lifetime and fast relaxation processes [43]. It is valid for pulsed excitation case with long lifetime, where the finite lifetime does not modify the dispersion; its only effect is the slow decay of density with the corresponding change of the healing length. For this reason, liquid helium and atomic condensates are usually considered as conservative, despite their decay via evaporation, which is clearly non-zero. It was also shown previously that polariton condensates can in many cases be well described as being at thermodynamic equilibrium [43, 44, 45, 46, 47]. On the contrary, these predictions should not be extended to the case of quasi-resonant pumping, where the laser is driving the system with a fixed frequency, and where the effects such as bistability are known to occur [48]. The study of such configurations is left for future works. One also can not make any conclusions on non-resonantly pumped polariton condensates in the non-equilibrium (kinetic) limit, where the relaxation is not sufficiently fast. These two configurations are described by various versions of the Gross-Pitaevskii equation with model-dependent additional terms, known to lead to different types of behavior [49, 50, 51, 52, 53, 54, 47, 55, 56]. In this sense, present results are meant to be used as a reference for comparison.

The Gross-Pitaevskii equation in dimensionless units reads:

$$i\frac{\partial\psi}{\partial t} = -\Delta\psi + V\psi + \left(|\psi|^2 - 1\right)\psi, \tag{3.9}$$

where $(x, y) = (x_0, y_0)/\xi$ (with healing length $\xi = \hbar/\sqrt{2gnm}$), $t = t_0 gn/\hbar$, $V = V_0/gn$, $\psi = \psi_0/\sqrt{n}$ (the index 0 marks dimensional variables, $n = |\psi_0|^2$ is the density of the fluid). Having in mind a particular implementation of a quantum fluid based on the exciton-polariton system, $m = 5 \times 10^{-5} m_0$ for the polariton mass (twice the cavity photon mass at zero detuning) is used. g is the strength of the polariton-polariton interaction governed by the exciton-exciton interaction. It can be written as

$$g = 6E_b X_c^2 a_B^2, \tag{3.10}$$

where E_b is an exciton binding energy, a_B is the exciton Bohr radius and X_c is the excitonic fraction. The parameter g equal to 5 μeVμm^2, which coincides with the values given in Ref. [57] for GaAs 2D microcavities [58] is taken. Operating with densities $n \approx 200$ μm^{-2} yields healing length ξ close to 1μm. A typical time scale for polaritons $t_0 = 1$ ps corresponds to dimensionless $t = 0.9$. Thus, one concludes that micrometers and picoseconds are quite natural units for consideration of the problem of turbulence in polariton quantum fluids.

In general, the parameters are taken to be corresponding to the state-of-the-art GaAs microcavities, which offer the best performance for the possible observation of the studied effects. As said above, one neglects the finite lifetime, except in the subsection 3.3.5 shown for comparison. The polarization effects, and the non-parabolicity of the polariton dispersion (which could change the k^{-3} spectrum of the vortex core) are also neglected. One also entirely neglects structural disorder effects which in real systems might play an important role in vortex dynamics. Indeed, the chemical potential is one order of magnitude higher than the typical disorder amplitude in high-quality cavities. This is why it is reasonable to neglect such disorder as a first approximation. All these effects are left for future studies, for which the present results and methodologies will serve as

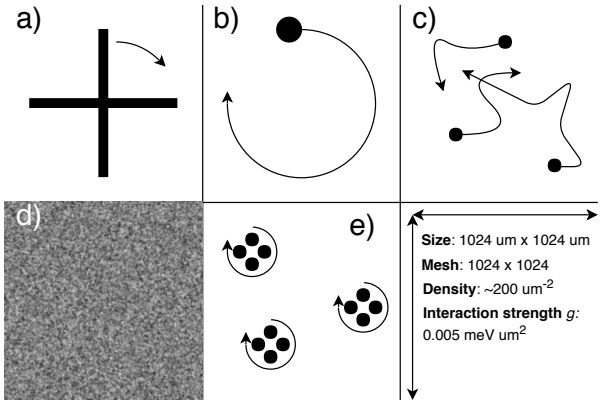

Figure 3.2: Schematic representation of the employed stirring strategies. a) Large cross, b) Classical spoon, c) Brownian spots d) White noise e) Gauss-Laguerre potential

a reference. The choice of the polariton system is important because of the possibility of performing single-shot interference measurements, allowing the detection of the spatial position of vortices, as will be discussed below. The choice of the polariton system is also motivated by its extended coherence [59], providing a large ratio between the maximal system size and the healing length.

In present numerical simulations, the time step was 0.01 ps and an $N \times N = 1024 \times 1024$ mesh was used. The Laplace operator was calculated using the Fourier transform with massive parallelization provided by the GPU ensuring a 14-fold speed increase. The third order Adams–Bashforth scheme was used for the integration over time. The MATLAB and MATHEMATICA packages are used for numerical solution of DDGPE and further analysis. The size of the square-shaped space region where the simulation was performed was L =1024 μm, which corresponds to the maximal wave vector $k_{max} = \sqrt{2}\pi N/L \approx 4\mu\text{m}^{-1}$. Higher wave vectors are required only for a better description of the vortex core.

3.2.2 Strategies of stirring the quantum fluid

The main feature of the turbulence is the energy flow from the injection scale towards other scales. It is this flow that leads to the formation of self-similar spatial structures. A cascade should manifest itself in the so-called incompressible energy part, associated with rotation (see below). Thus, the observation of cascades, either direct or inverse, absolutely requires the formation of quantum vortices, and not just of density waves. In classical 2D turbulence, a simplest random-potential scheme has been shown to be sufficiently efficient for the observation of a large-scale inverse energy cascade [60]. In quantum 2D turbulence, such method does not allow to create vortices efficiently, because, contrary to the classical case, creating a pair of well-defined vortices with a vanishing order parameter in their centres requires a finite amount of energy [61] $E_{pair} \approx 6\hbar^2 n/m$ precisely because these vortices are quantum. A single quantum vortex requires even a larger minimal energy $E_{\text{v}} = \pi n\hbar^2 \ln\left(1.46 R_0/\xi\right)/m$ (R_0 is the system size) for its creation [62].

As mentioned above, the first strategy used was the stirring by a propagating potential defect [32] or flow around stationary defects [34, 21]. Random imprinting of vortices followed by healing by simulation with imaginary time has also been used[63, 24]. In

polariton condensates, persistent vortices have already been shown to appear because of the flow of the condensate against a random potential [64].

In the present manuscript, several different quantum fluid stirring strategies were compared (see Fig. 3.2):

- Large cross-like potential
- Classical rotating spoon
- Several spots in brownian motion
- White noise with spatial correlations (for comparison with a classical fluid [60])
- Several small potential wells defined by the intensity of the interference of 2 Gauss-Laguerre (GL) beams

As it will be discussed below, these procedures inject energy at different scales. To obtain a quasistationary configuration, very long times for the stirring of the quantum fluid (5 ns), for its relaxation (20 ns), and for the averaging during the extraction of the cascade (5 ns) were used. However, the analysis of the dynamics presented in the final part of the work demonstrates that the characteristic formation time of the cascade is of the order of 200 ps, which is much closer to the lifetimes of the state-of-the-art cavities.

1. *Large cross-like potential*
The length of the cross was 860 μm and the width 100 μm (with additional 64 μm Gaussian filter-based smoothing of borders). The full 360° rotation took 1280 ps. The potential depth $V = 10$ meV. Duration of stirring was 1.5 ns and total simulation time was 25 ns.

2. *Gauss-Laguerres*
The stirring was performed by 32 randomly placed rotating potentials during first 0.5 ns (total simulation time was 25 ns). The potential depth $V = 10$ meV. Profile of each stirrer was given by a superposition of the two 2$^{\text{nd}}$ order Gauss-Laguerre beams. One of them was stationary and the second one was rotating. To obtain the potential profile, the electric field magnitude square was taken. The resulting profile resembled the 4 smoothed spots with the distance between the opposite ones 20 μm, see also the sketch in Fig. 3.2. The full 360° rotation of resulting potential (not the electric field) took 45 ps, which yields approximately the same linear velocity as for large cross strategy.

3. *Classical rotating spoon*
The orbit diameter of the spoon was 632 μm. The shape of the spoon was given by $\tilde{V}(r) = (\exp((r - 32\mu\text{m})/(2.5\mu\text{m})) + 1)^{-1}$. The full 360° rotation took 1280 ps, as for the cross. The potential depth $V = 10$ meV. Duration of stirring was 3.0 ns and total simulation time was 25 ns.

4. *Several spots in Brownian motion*
The trajectory was obtained as a Beta Spline curve defined by the points obtained by random walks. Distance of each step was fixed to 50 μm and the direction was random (30 ps between two steps). Hence, the speed of the spots was approx 2 μm/ps. Number

of spots was 10, total simulation time 50 ns, stirring time 1.5 ns. The spots were in the shape of Gaussian profiles with the radii of 7 μm and the potential depth $V = 10$ meV. The routine BSplineFunction in the Mathematica package was used to obtain the curve.

5. *White noise*

White noise was obtained from 1024x1024 matrix of uniform random values from 0 to 1 multiplied by the amplitude 80 meV. Then for smoothing and thus bringing some finite spatial correlations the Fourier image was filtered with the Gaussian function in reciprocal space. The width was of Gaussian was $\frac{2\pi}{r_{\text{correl}}}$, where the correlation length $r_{\text{correl}} = 75$ μm. Instantaneous switching the potential to the new random realization was performed each 0.4 ps. Total simulation time was 50 ns and the white noise potential was applied during the first 5 ns.

3.2.3 Definition of IKE spectrum

Once the numerical solution of GPE is performed, one obtains the possibility to extract the polariton wave function (as a function of spatial coordinates and time) and to provide the analysis essential for the studies of the turbulence. This analysis is based on the spatial distribution of polarion velocity and density.

The kinetic energy associated with turbulent motion of quantum fluid is defined by the incompressbile part of the velocity. Meanwhile, the compressible part is associated with the Bogolons, introduced in previous chapter. The nature of Bogolons implies the variation of fluid density, which corresponds to the characteristic feature of compressibility.

The quantum fluid velocity is closely related with the current operator and writes

$$\mathbf{v}(\mathbf{r}) = \frac{1}{|\psi(\mathbf{r})|^2} \cdot \frac{\hbar}{2mi} \cdot \left(\psi^*(\mathbf{r})\nabla\psi(\mathbf{r}) - \psi(\mathbf{r})\nabla\psi^*(\mathbf{r})\right), \tag{3.11}$$

where m is the polariton mass.

According to Ref. [34], the kinetic energy can be calculated for the wave function via the density weighted velocity field in space domain:

$$E^{(i,c)} = \frac{m}{2}\int d\mathbf{r} n(\mathbf{r}) \left(|v_x^{(i,c)}(\mathbf{r})|^2 + |v_y^{(i,c)}(\mathbf{r})|^2\right), \tag{3.12}$$

where i and c indexes correspond to incompressible and compressible velocity parts and $n = |\psi|^2$ is the density. This requires obtaining an instantaneous information on both density and phase of the quantum fluid, which can be obtained using interferometry [65]. The equation above can be rewritten as

$$E^{(i,c)} = \frac{m}{2}\int d\mathbf{r} \left(|u_x^{(i,c)}(\mathbf{r})|^2 + |u_y^{(i,c)}(\mathbf{r})|^2\right), \tag{3.13}$$

where the density-weighted velocity $\mathbf{u}^{(i,c)}$ is defined as follows: $\mathbf{u}^{(i,c)} = \sqrt{n}\mathbf{v}^{(i,c)}$. The incompressible and compressible density-weighted velocity parts should obey the following relations:

$$\nabla \cdot \mathbf{u}^{(i)} = 0$$
$$\nabla \times \mathbf{u}^{(c)} = 0$$

These definitions straightly match with the Helmholtz decomposition of a vector field to the incompressible and compressible parts.

Eq. (3.13) can be rewritten in the momentum domain

$$E^{(i,c)} = \frac{m}{2} \int d\mathbf{k} \left(|u_x^{(i,c)}(\mathbf{k})|^2 + |u_y^{(i,c)}(\mathbf{k})|^2 \right), \tag{3.14}$$

where $\mathbf{u}^{(i,c)}(\mathbf{k})$ are the Fourier images of $\mathbf{u}^{(i,c)}(\mathbf{r})$. The Fourier components $\mathbf{u}^{(i,c)}(\mathbf{k})$ of the incompressible and compressible density-weighted velocity parts obey the following relation in the momentum domain:

$$\mathbf{k} \cdot \mathbf{u}^{(i)}(\mathbf{k}) = 0,$$
$$\mathbf{k} \times \mathbf{u}^{(c)}(\mathbf{k}) = 0.$$

If the angular dependence is integrated out, the spectral energy density can be written as:

$$E^{(i,c)}(k) = \frac{mk}{2} \int d\theta \left(|u_x^{(i,c)}(\mathbf{k})|^2 + |u_y^{(i,c)}(\mathbf{k})|^2 \right), \tag{3.15}$$

where the absolute value k and the polar angle θ define the wave vector $\mathbf{k}$.

This is the same spectral energy density, which figures in Eqs. (3.6) and (3.7).

It is this spectral energy density which is expected to scale as $E^{(i)}(k) \propto k^{-5/3}$ in both the direct and the inverse energy cascades.

3.2.4 Decomposition of velocity field to incompressible and compressible components

In order to ensure that the obtained results are not method-dependent, the several techniques of numerical decomposition of the *velocity field* into compressible and incompressible parts were used. I present them in this section.

(i) **The composition in the Fourier (momentum) domain**

Incompressible components can be obtained from a given density-weighted velocity field in the momentum domain $\mathbf{u}(\mathbf{k})$ as follows:

$$u_\alpha^{(i)}(\mathbf{k}) = \sum_{\beta=x,y} \left(\delta_{\alpha,\beta} - \frac{k_\alpha k_\beta}{k^2} \right) u_\beta(\mathbf{k}), \tag{3.16}$$

$$u_\alpha^{(c)}(\mathbf{k}) = \sum_{\beta=1,2} \frac{k_\alpha k_\beta}{k^2} u_\beta(\mathbf{k}), \tag{3.17}$$

where α and β indices are the Cartesian coordinate directions.

(ii) **Decomposition in the spatial domain**

Here, one operates fully in the spatial domain and the incompressible and compressible velocity parts are defined via the vector potential Φ and scalar potential ϕ as follows[66]:

$$\mathbf{u}^{(i)}(\mathbf{r}) = \nabla \times \Phi(\mathbf{r}),$$
$$\mathbf{u}^{(c)}(\mathbf{r}) = \nabla \cdot \phi(\mathbf{r}).$$

The vector potential can be derived via

$$\Phi(\mathbf{r}') = \int d\mathbf{r}(\nabla \times \mathbf{u})(\mathbf{r}) \cdot G(\mathbf{r} - \mathbf{r}') - \oint d\mathbf{s}(\mathbf{n} \times \mathbf{u})(\mathbf{r}) \cdot G(\mathbf{r} - \mathbf{r}'), \tag{3.18}$$

where G is the Green's function of Poisson equation in the space of a given dimensions. For the considered here 2D problem it is $G(\mathbf{r} - \mathbf{r}') = \frac{1}{2\pi} \ln(|\mathbf{r} - \mathbf{r}'|)$. In 3D one should use $G(\mathbf{r} - \mathbf{r}') = \frac{1}{4\pi|\mathbf{r}-\mathbf{r}'|}$.

For the scalar potential ϕ one can write in the same manner

$$\phi(\mathbf{r}') = \int d\mathbf{r}(\nabla \cdot \mathbf{u})(\mathbf{r}) \cdot G(\mathbf{r} - \mathbf{r}') - \oint d\mathbf{s}(\mathbf{n} \cdot \mathbf{u})(\mathbf{r}) \cdot G(\mathbf{r} - \mathbf{r}'). \tag{3.19}$$

In the numerical implementation, the integrals (3.18) and (3.19) can be taken as a convolution of a matrix representing the curl of the velocity field $\nabla \times \mathbf{u}$ and a matrix for a Green's function $G(\mathbf{r})$. The latter has a size of $2N \times 2N$ with the $\mathbf{r} = 0$ corresponding to the center of the matrix: (N, N) cell (here N is the mesh size).

After the incompressible $\mathbf{u}^{(i)}(\mathbf{r})$ and compressible $\mathbf{u}^{(c)}(\mathbf{r})$ parts of the density-weighted velocity are derived, one makes the Fourier transform and uses the formula (3.15). The second terms in Eqs. (3.18) and (3.19) can be omitted due to periodic boundary conditions. The same is for widely used "cup" simulations due to zero density n at the boundaries.

(iii) **Mixed decomposition**

Eqs. (3.18) and (3.19) are *de facto* the solution of the following spatial domain Poisson equations for the vector and scalar potentials:

$$\Delta\Phi = \nabla \times \mathbf{u},$$
$$\Delta\phi = \nabla \cdot \mathbf{u},$$

with the source terms being the curl and the divergence of the given velocity field $\mathbf{u}$. These Poisson equations can be solved using the Fourier transform scheme:

$$k^2\Phi = (\nabla \times \mathbf{u})(\mathbf{k}),$$
$$k^2\phi = (\nabla \cdot \mathbf{u})(\mathbf{k}),$$

In 3D space, the systems written above contain 4 equations. For the present 2D case, the curl of the field $\mathbf{u}$ aligned in (x, y) plane has only the z component and thus one has only two equations.

3.2.5 Analytical derivation of the IKE spectra via the position of vortices

The Kolmogorov energy cascade is expected to form in the IKE spectral density, and its observation requires the separation of the density-weighted velocity field into the compressible and incompressible part [34, 66], with the selection of the latter. Importantly, the spectral energy density of the incompressible part of the velocity field can also be calculated analytically from the positions and the signs of the quantum vortices [34, 33]. This is possible because the quantum fluid is irrotational and all the vorticity is concentrated only in vortices. One also needs such parameters of the quantum fluid as its density n, interaction constant g, and polariton mass m. One writes the IKE spectral density (IKE spectrum) as

$$E^{(i)}(k) = N_{\mathrm{vort}} \Omega \xi^3 F(k\xi) G(k), \tag{3.20}$$

where $F = \Lambda^{-1} f(k\xi\Lambda^{-1})$ is the single vortex spectrum, N_{vort} is the total amount of vortices, $\Omega = 2\pi\hbar^2 n/(m\xi^2)$ is the ensthropy quantum, the parameter $\Lambda = 0.8249...$ and the function $f(z)$ writes

$$f(z) = \frac{z}{4}\left(I_1\left(\frac{z}{2}\right) K_0\left(\frac{z}{2}\right) - I_0\left(\frac{z}{2}\right) K_1\left(\frac{z}{2}\right)\right). \tag{3.21}$$

The function $G(k)$ is shaped by the coordinates $\mathbf{r}_{i,j}$ and the signs $\kappa_{i,j}$ of the vortices:

$$G(k) = 1 + \frac{2}{N_{\mathrm{vort}}} \sum_{i=1}^{N_{\mathrm{vort}}-1} \sum_{j=i+1}^{N_{\mathrm{vort}}} \kappa_i \kappa_j J_0\left(k|\mathbf{r}_i - \mathbf{r}_j|\right), \tag{3.22}$$

where the indices i and j enumerate all vortices.

This approach allows not only to find the total incompressible energy spectrum, but also to consider the contributions of single vortices and clusters separately [42, 33], which turns out to be important in order to observe the Kolmogorov cascade at a large scale. The cluster selection algorithm was adopted from Refs. [32, 42] with an additional optimization available in MATHEMATICA. The positions of vortices were determined from the phase of the wave function.

The result of the comparison of 3 numerical schemes of IKE derivation introduced in previous section (Fourier, spatial and mixed) and analytical approach is given in Fig. 3.3. Unlike other figures below, the lower quantum fluid density (9 $\mu\mathrm{m}^{-2}$) was used to give the possibility to look closer into the vortex core. The total kinetic energy is slightly higher than its incompressible part, which means that the amplitude and the concentration of Bogolons are relatively weak.

3.2.6 Clustering procedure

The formation of an energy cascade is necessarily accompanied with the formation of spatial structures at different scales. For the incompressible part of the quantum fluid, it means the formation of clusters of quantum vortices of different sizes. To confirm the formation of such clusters and to separate their contribution from that of an uncorrelated

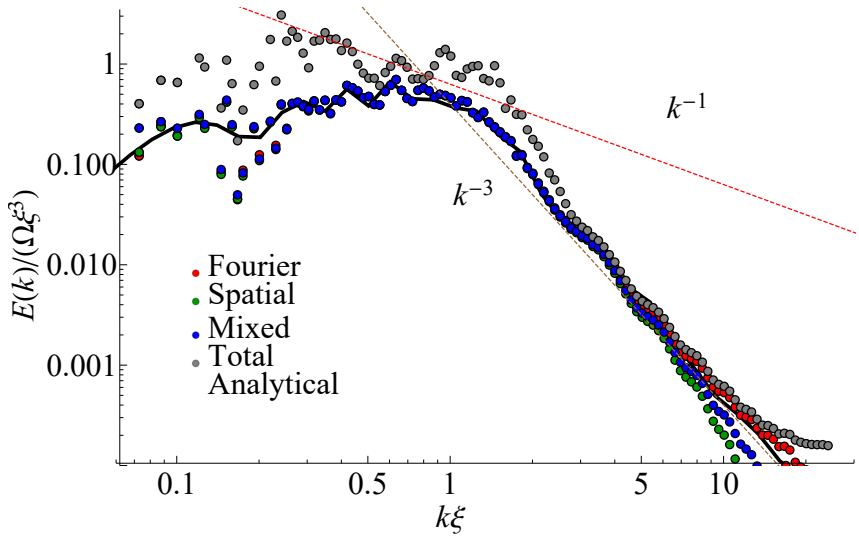

Figure 3.3: Verification of IKE spectra calculation. 3 numerical schemes: Fourier, Spatial, Mixed (points), and analytical (curve). Gray points show the total kinetic energy (mostly rotational and affected by bogolons only at low wave vectors). The mesh and the region size parameters were the same as in other simulations, but the quantum fluid density was approx. 9 μm^{-2} (healing length $\xi \approx 5.5\mu$m). Stirring was performed using four spoons. 8 vortices were generated.

vortex gas, the cluster detection technique was used. This technique will be described in the present section.

One generally follows the cluster selection procedure described in section VI of Ref. [42]. One begin with the creating the list of vectors $\mathbf{l}_i = (l(i,1), l(i,2), ..., l(i,\text{NOS}_i))$, consisting of the indices of the neighbors of i-th vortex sorted by increasing the distance ($i = 1..N_{\text{vort}}$, where N_{vort} it the total amount of vortices). The latter (or the only) member of $\mathbf{l}_i$ is the index of the nearest vortex of the opposite sign, thus $\text{NOS}_i - 1$ is the number of the same-signed neighbors of i-th vortex lying closer than the Nearest Opposite Sign neighbor. After that, one creates the $\mathbf{l}'_i$ vectors by dropping the last element and thus $\mathbf{l}'_i$ vectors list only the neighbors of the same sign of i-th vortex. In some cases (e.g. for vortex belonging to the dipole) $\mathbf{l}'_i$ can be empty.

At the first step, one finds the vortex pairs by finding the pairs of i and j indices so that $\text{NOS}_i = 1$ and $\text{NOS}_{l(i,1)} = 1$ is also equal to one. After that the pair $(i, l(i,1))$ is put to the list of connected vortices $\mathbf{L}$.

At the second step, for all i and for all $j \leq \text{NOS}_i - 1$ one adds the pair $(i, l'(i,j))$ to the list of connected vortices $\mathbf{L}$ if $\mathbf{l}'_{l(i,j)}$ contains index i. This procedure is in fact the finding of mutual vortex pairings.

Then one considers the list of connected vortices $\mathbf{L}$ (containing both vortex pairs and the clusters of the same-sign vortices) as a graph and separate its connectivity components using the `ConnectedGraphComponents` routine of the MAHTEMATICA package. Each connectivity component is thus a cluster. If the connectivity component consist of exactly two vortices with opposite circulation, it is marked as a pair, otherwise it is counted as a cluster.

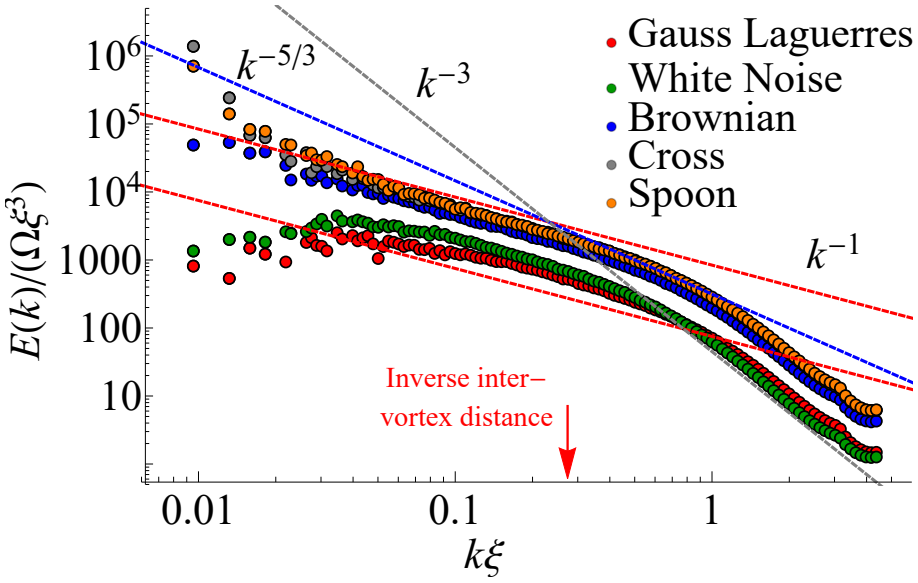

Figure 3.4: The IKE spectra obtained numerically by decomposition in the reciprocal space for different stirring strategies. The red arrow is for the inverse intervortex distance k_l.

3.3 Results

In this section, the total incompressible energy spectra for different stirring strategies are first studied. It will be shown that, independently of the stirring strategy, such spectra are strongly dominated by the contribution of individual vortices, which prevents the observation of the cascade over large energy scales. In the second subsection, the contribution of individual vortices will be removed while keeping only the one belonging to clusters. This procedure reveals the cascade over a significantly large range, which confirms the arrangement of clustered vortices in large scale self-similar structures. In the last subsection, the inverse nature of the cascade will be demonstrated by analyzing the time evolution of the energy distribution during the stirring procedure.

3.3.1 Total incompressible kinetic energy spectra

Figure 3.4 shows the IKE spectra obtained for various stirring strategies. The incompressible energy part was separated by decomposition in the reciprocal space (see Methods). One can expect to observe the $-5/3$ power law cascade in the IKE spectrum only between the wave vectors $k_L = 2\pi/L$ (L is the system size) and $k_l = 2\pi/l$, where l is the mean inter-vortex distance (l was approximately 20 μm in most of conducted simulations and thus $k_l\xi \approx 0.3$). In Fig. 3.4, such power law is visible only for the cross and spoon stirring, and only in a narrow wave vector range (in the vicinity of $k\xi = 0.02$). In this figure, k_l is marked by a red arrow. The difficulty to observe the $-5/3$ power law characteristic for the formation of multiscale structures is explained by the large contribution of single vortices, as will be shown in the next section.

It is natural [34] to measure the IKE spectral density in the units of ensthropy $\Omega\xi^3$. According to the definition, the function $F(k\xi)$ is of the order of 1 at $k\xi = 1$ and the

function $G(k) \approx 1$ at $k \gg k_l$. Thus, in the vicinity of the point $k\xi = 1$ the magnitude of IKE spectrum estimates the total amount of vortices in the system $N_{\rm vort}$.

For $k\xi$ between $k_l\xi$ and 1, one should observe the energy spectrum of a single vortex: k^{-1}, because at this scale a vortex does not have any neighbors to form any structures. For wave vectors larger than $1/\xi$ (short length scale), one obligatory observes a k^{-3} law which is a fingerprint of the vortex core wave function (this might be different for exciton-polaritons in some regimes because of their non-parabolic dispersion that is neglected here). In Fig. 3.4, all stirring strategies exhibit similar behavior at wave vectors higher than k_l : there is a k^{-1} power law below $1/\xi$ and k^{-3} above $1/\xi$.

It is interesting to note that in Ref. [33] the $-5/3$ cascade signatures have been observed between k_l and $1/\xi$. In Refs. [34, 32] there was also no transitional k^{-1} regime between $1/\xi$ and k_l, and the $-5/3$ cascade started immediately after $1/\xi$. The absence of an intermediate region with k^{-1} power law in these works might be explained by the short inter-vortex distance which is close to the healing length, or by a large variation in the intervortex distance.

Finally, the differences between stirring strategies can be observed in Fig. 3.4 at $k\xi$ smaller than 0.02-0.03. Indeed, the stirring based on the classical spoon and large cross generates large-scale vortex clusters. The energy injection for these strategies is still efficient at the scales of $k\xi = 0.01$. The three other stirring procedures do not inject energy at large scales and the IKE spectra drop below $k\xi = 0.03$. However, in all cases most of the energy spectrum is dominated by the signal arising from single vortices, which strongly hinders the observation of the Kolmogorov energy cascade because of the wide spreading of single vortex energy in k-space. So in the next subsection, the treatment procedure will be changed to the procedure using the real space selection allowing to eliminate single vortices in order to keep only the part of the IKE stored in clusters.

3.3.2 Incompressible kinetic energy spectra of clustered vortices

Here the IKE spectra will be computed using the analytical procedure described in the "Tools" section. This procedure is based on the detection of vortices in real space. Indeed, the knowledge of the wave function at any time allows to determine the position of all vortices. The velocity field induced by these vortices is the whole incompressible velocity field. Once the vortex position is known, the incompressible velocity field can be computed analytically (see Methods). Figure 3.5 shows the result of this procedure (for all stirring procedures). These results are compared with those obtained in the previous section based on a decomposition in reciprocal space. One can indeed check that the results obtained using both methods coincide for all stirring procedures, confirming the possibility to use the analytical treatment.

It is then possible to make one step further by determining if a given vortex is single, in a dipole, or in a cluster (details on the procedure are given in the Appendix). This is illustrated by Fig. 3.6 showing a snapshot of the phase of the quantum fluid stirred by Brownian potentials. The winding of each vortex is shown by colour (+1 - red, −1 - blue). Single and dipole vortices are marked by small circles. Vortices belonging to clusters are marked by large circles. One clearly sees that a large fraction of vortices (about 50%) belong to clusters. At the same time, it is natural that the signal from the other 50% that are not in clusters is quite important in the total IKE spectrum.

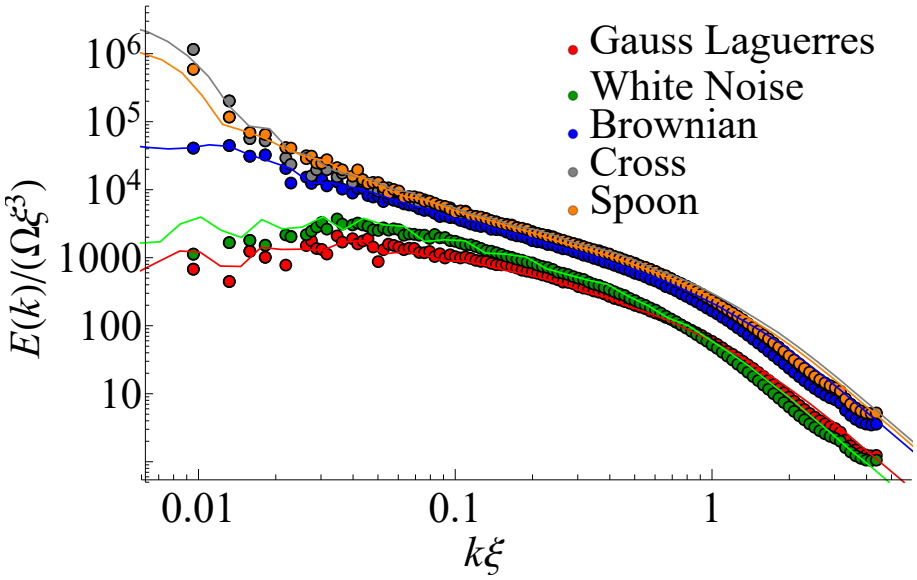

Figure 3.5: IKE spectra obtained numerically (points) and analytically for all vortices (solid lines). In the range from 0.02 to 1 $k\xi$ both methods give the same result.

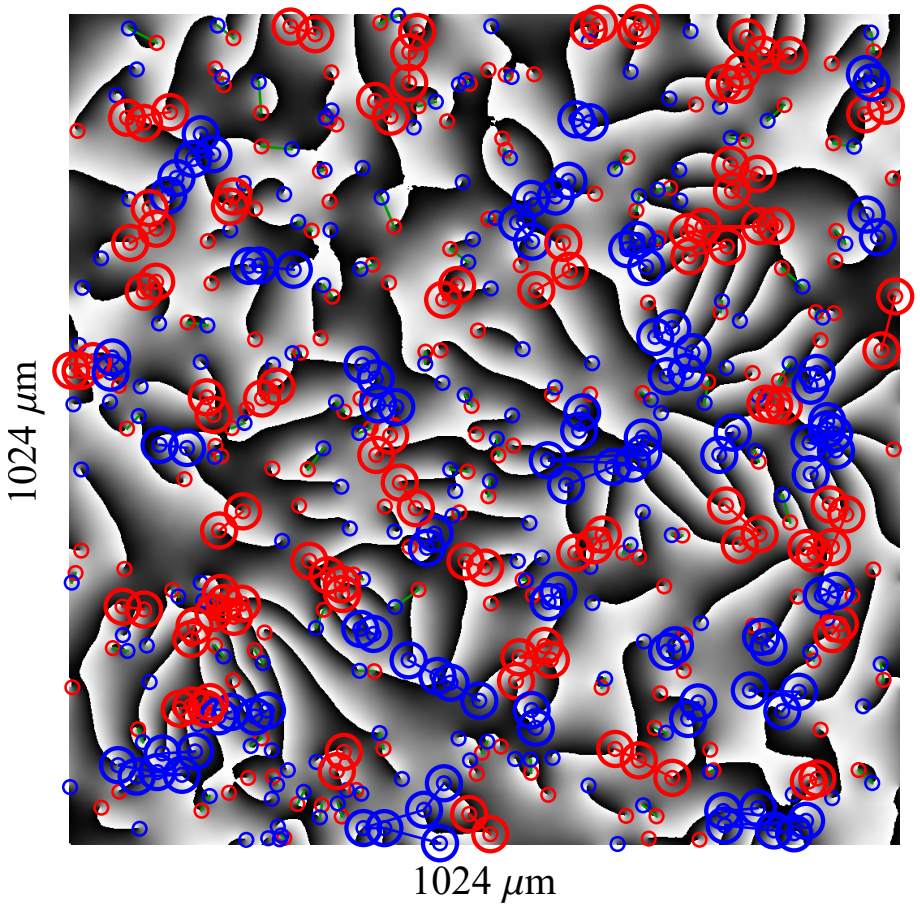

Figure 3.6: Phase of the wave function for Brownian stirrers combined with the results of clustering procedure. The vortices belonging to the clusters are highlighted with the large circles. Relatively rare vortex dipoles are connected by green lines.

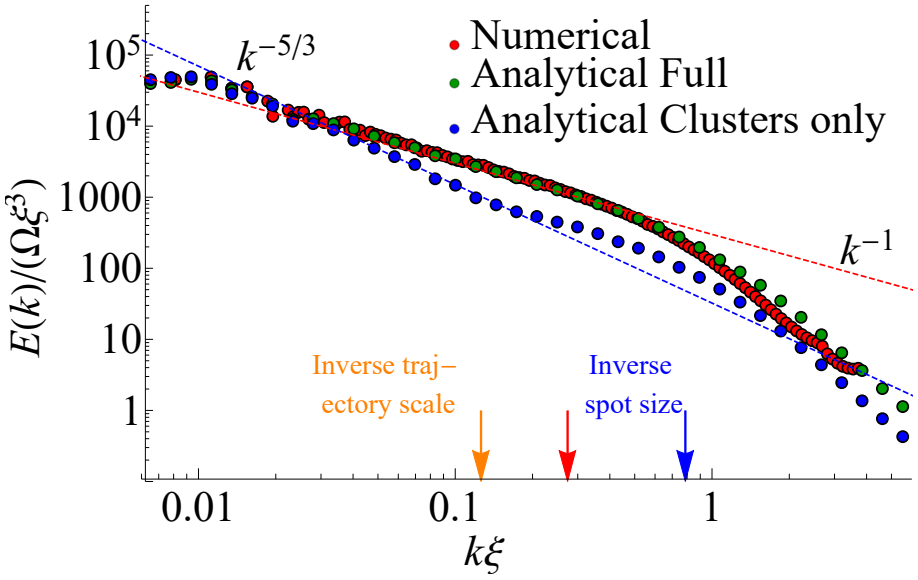

Figure 3.7: IKE spectra for Brownian stirrers. Red dots are for numerical procedure, green dots are for analytical procedure for all vortices, blue dots are for clustered vortices only. The dashed lines are the guides for the eye with $-5/3$ (blue dashed) and -1 (red dashed) power functions. The blue arrow shows the inverse potential spot size ($\sim 7\xi$) and the orange one shows the inverse characteristic scale of Brownian motion ($\sim 50\xi$). The red arrow is for k_l.

Figure 3.7 compares the IKE spectra with and without selection of clustered vortices. Arrows mark the characteristic scales from which the inverse cascade might be expected to start: the inverse Brownian trajectory scale (orange), the inverse intervortex distance k_l (red), and the inverse spot size (blue). A $-5/3$ power law is visible for all vortices and for clusters between $k\xi = 0.01$ and $k\xi = 0.05$, much lower than k_l. The spectra differ above $k\xi > 0.05$. The removal of the single vortex and dipole contributions reveals a very clear $-5/3$ slope over more than one order of magnitude, which was hidden in the total IKE spectra. It becomes clear therefore, that the removal of single vortices is crucial for the analysis of the turbulence phenomena via the incompressible energy spectrum. The excess of single vortices in the system is explained by the relatively low density of the vortex gas, preventing many vortices from participating in the interactions that allow building the inverse cascade starting from the inverse trajectory scale (orange arrow).

Fig. 3.8 compares the IKE spectra analytically for all vortices and for clustered vortices only for all employed strategies of fluid excitation. One sees that at low wave vectors the curves coincide with high accuracy. It means that the macroscopic motion of the quantum fluid is defined by the vortex clusters only. On the contrary, at the wave vectors larger than wave vector k_l the macroscopic motion can not be seen and IKE spectrum magnitude is proportional to the number of vortices only. For such stirring schemes like spoon or large cross number of clustered vortices is very large and thus IKE spectra for all vortices and for clustered vortices nearly coincide. On the contrary for GL, white noise, and Brownian spots schemes the difference is significant: the number of clustered vortices is lower.

The power spectra computed with the same spatial selection procedure for all five

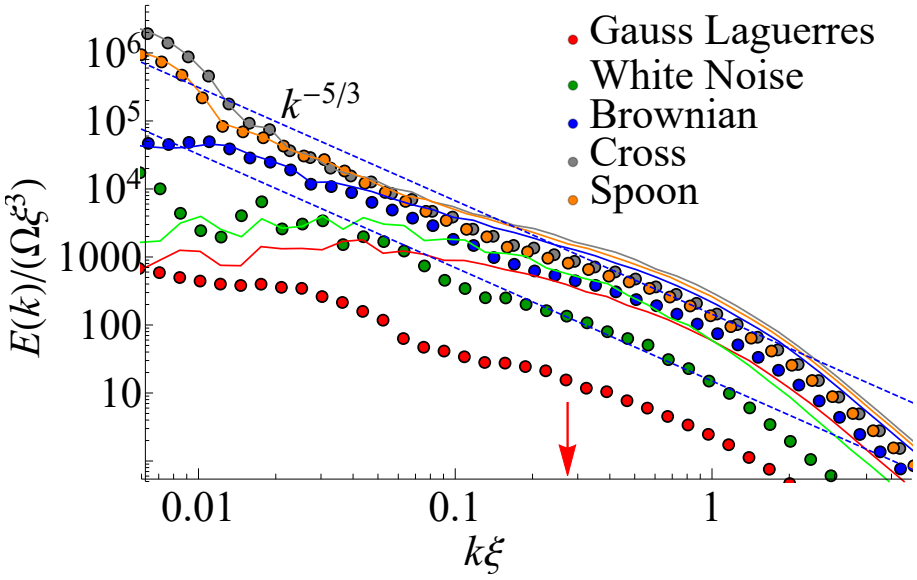

Figure 3.8: IKE spectra obtained analytically for clustered vortices only (points) and for all vortices (curves). One sees the high similarity at low wave vectors while for high wave vectors energy for clusters goes down due to "truncating" single vortices and dipoles. Red arrow denotes the inverse characteristic intervortex distance.

stirring procedures are shown in Fig. 3.9. A $-5/3$ power law is now visible in all cases, and also extends over more than one order of magnitude over k. This is demonstrating the presence of self-similar structures of vortices with their size varying from about 30 μm to 600 μm.

In order to check that the observed power law indeed corresponds to the expected scaling of $-5/3$, one should fit the IKE resulting from the analytical procedure with an allometric (power) function $f = ax^\gamma$ with fitting parameters a and γ (Fig. 3.10, dots and solid line). The non-linear least squares procedure used with the Levenberg-Marquardt error minimization algorithm, with the confidence interval for parameter values obtained from the variance-covariance matrix using the asymptotic symmetry method. The fit shows that the expected value $-1.(6)$ is within the bounds of the confidence interval: $\gamma = -1.5 \pm 0.2$, confirming the presence of the Kolmogorov scaling over more than one order of magnitude of wave vectors and energies. It should be stressed that although the precision is relatively low, this is a true fit of the numerical experiment, and not just a guide for the eyes. The importance of performing a fit is underlined by the fact that even for a completely random arrangement of vortices (vortex gas) obtained without solving the Gross-Pitaevskii equation and so without any possible self-organization effects linked with quantum turbulence, the IKE spectrum naturally demonstrates a bell-like curve, which can have a tangent slope of $-5/3$ in a certain region. Thus, a thorough analysis confirming the existence of a large scale cascade is really required to draw any conclusions on the quantum turbulence.

Analyzing power law dependencies can be particularly difficult, because one needs to confirm that the observed approximately linear distribution on the loglog plot is best explained by a power law [67], and not by some other distribution function (for example, exponential or log-normal). When there are no other means, one has to check if the

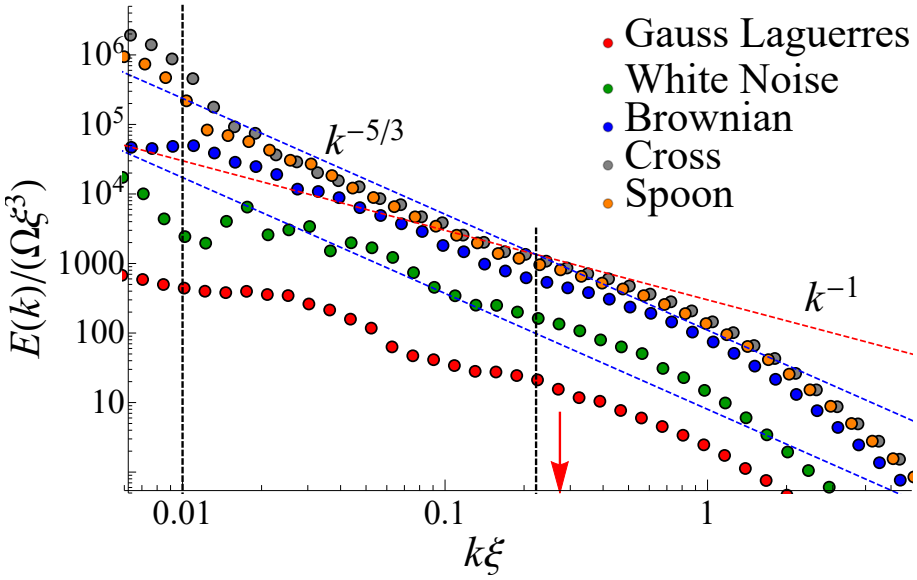

Figure 3.9: The analytically obtained IKE spectra for all 5 stirring strategies for the clustered vortices only. The red arrow is for inverse intervortex distance k_l. The vertical lines cut the range where -5/3 power law is observed.

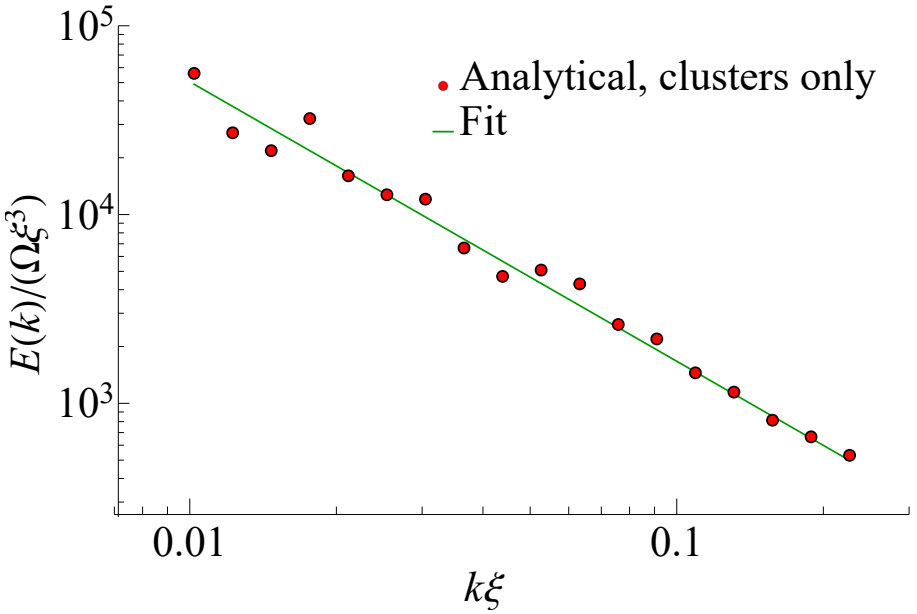

Figure 3.10: IKE spectrum for Brownian stirrers (clusters only) with a power-law fit giving $\gamma = -1.5 \pm 0.2$ (expected -1.66).

distance of the measured distribution from the ideal one is not higher than for simulated power-law distributions. In a particular physical system, however, the power law energy distribution arises from the formation of the self-similar spatial structures, that is, fractal clusters. In the next section, I will analyze the spatial distribution of vortices in order to confirm that the observed power-law distribution is not accidental.

3.3.3 Fractal dimension of vortex clusters

The Kolmogorov's arguments for the existence of cascade in classical turbulence are based on the self-similarity of observed spatial patterns at different scales. This self-similarity in mathematics is what characterizes fractal structures. An inherent property of fractals is their non-integer dimensionality: a fractal formed of an infinite number of points on a plane is neither a 2D object like a polygone, nor a 0D object like a point, but something between the two. Thus, checking if the clusters of vortices exhibit a non-integer (fractal) dimension, allows us to prove that their spatial patterns are indeed self-similar, as required for the formation of an energy cascade. Such methods could be applied to the recent observation of vortex clusters in atomic condensates [28, 29].

One way to obtain the fractal dimension is the box-counting approach, and the corresponding dimension is called box-counting or Minkowski-Bouligand dimension. This approach consists in covering the studied object by a mesh with the cells (boxes) of size ε and counting the number of boxes required to fully cover the object $N_{box}(\varepsilon)$ for various the mesh sizes ε. For present case, the curve of box count N_{box} to cover all vortices vs. box size ε is plotted. The slope of tangent line for this curve finally gives the box-counting fractal dimension of the pattern formed by the clusters of vortices. The asymptotics of the curve are always integer (non-fractal): at small scales, each vortex is just a 0D point, whereas at large scales the whole system is just a 2D object. It is the existence of a large transition region between the two limits which determines the fractal dimension.

It is reasonably to consider only the best configuration - the case of Brownian stirrer. Vortices were treated as points with coordinates $\mathbf{r_i}$ obtained from the wave function in the same manner as for analytical calculation of IKE spectra. The system size was 2048 μm. For this "fractal" analysis, only the vortices of the same sign were used.

The results of the analysis are shown in Fig. 3.11 together with the IKE spectrum shown for reference. The box size ε is given in terms of the corresponding wave vectors $2\pi/\varepsilon$, to have a common horizontal axis with the energy distribution plots. I calculate the fractal dimension for clustered vortices and compare it with that of all vortices (which serve as a non-fractal reference). For clustered vortices (red curve), a clear transitional regime is present between the 2D and 0D limits, with the fractional dimension of ≈ 0.6. The scale range at which this regime is present straightly matches with the region of $-5/3$ power law in IKE spectra, confirming that the energy cascade originates from the self-similarity. For comparison, the case of all vortices (black line) shows an immediate transition between the 0D and 2D asymptotics, confirming the absence of a fractal structure in this case. Therefore one can conclude that the clustered vortices exhibit a well-defined fractal dimension confirming the self-similarity of their structure at the same range of scales where the energy cascade is observed.

To check the applicability and robustness of the realization of the *box counting approach*, the comparison with a random distribution of points and with an artificially

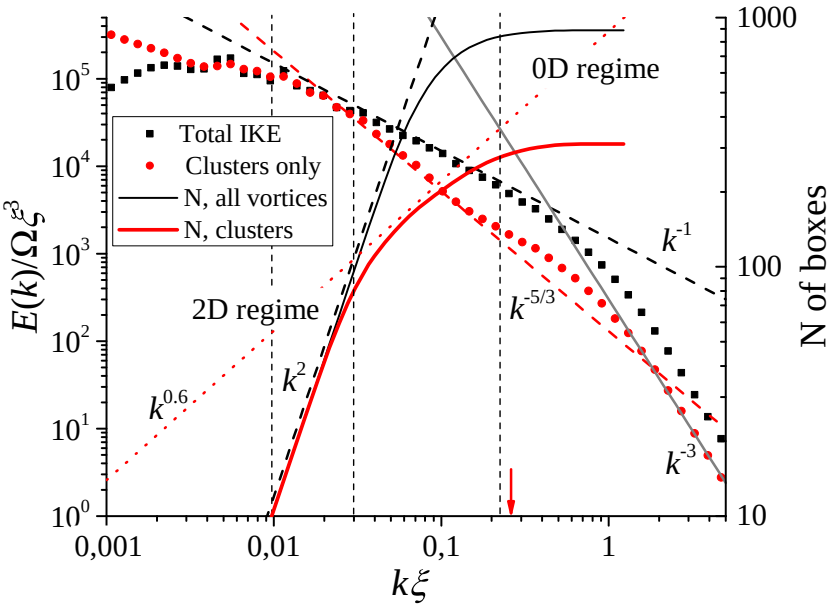

Figure 3.11: Fractal (box-counting) dimension of vortex clusters. Solid curves show the dependence of box counts to cover all vortices on the size of the boxes. Dots are for analytical IKE spectra. Red color is used for clustered vortices and black color is used for all vortices. Dashed lines give the eye guides for some important powers. Red arrow shows the characteristic intervortex distance (limit of the 0D regime).

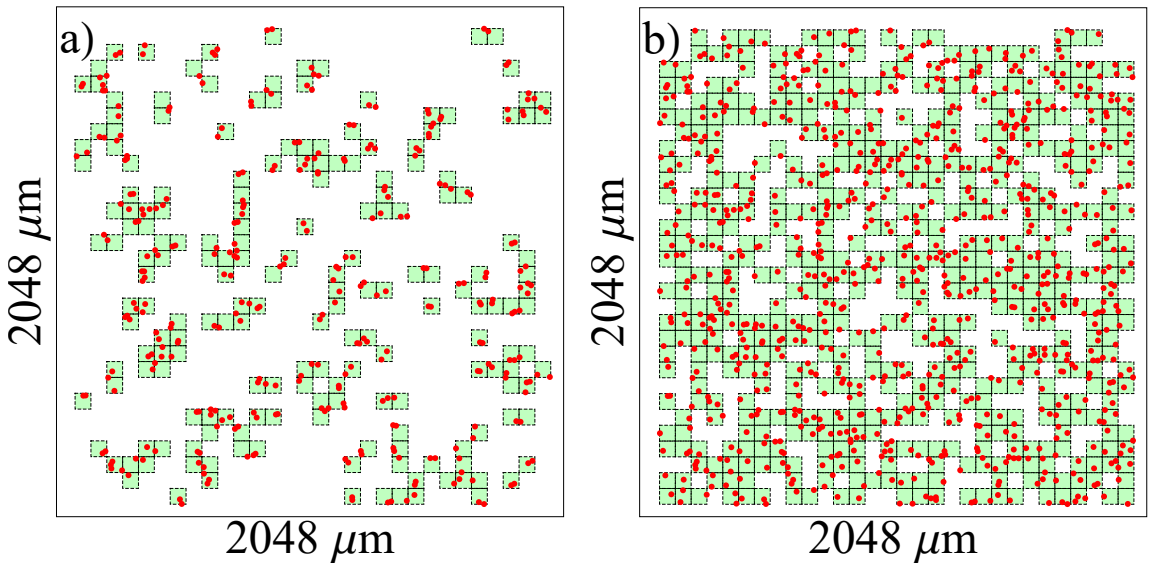

Figure 3.12: Illustration of the box counting algorithm applied to determine the fractal dimension of the patterns formed by votrtices. Box size corresponds to $k\xi = 0.9$. Each vortex is denoted with a red point. Only the same-sign vortices were taken into account. Panel a) is for clustered vortices only and panel b) is for all vortices.

created pattern in the shape of the Sierpinskii triangle have been carried out.

Figure 3.12 illustrates the box-counting algorithm that was used for the determination of the fractal dimension of the structures formed by vortices. As it was mentioned above, for this purpose, the clusters of vortices of the same sign were considered. For the opposite sign the picture is the same. The box size shown in the figure is chosen as an example of the transitional regime $2\pi\xi/\varepsilon = 0.9$. For smaller box sizes, each vortex is covered with a single box and the system is effectively 0D. On the contrary, for larger ε, all system is covered by boxes (without voids) and thus it is 2D. The spatial distribution of all vortices without cluster selection exhibits the 2D nature already at this size scale and does not exhibit an evident transitional regime.

To prove that the transitional region observed for clustered vortices indeed corresponds to what one would expect for a fractal structure, I have compared it with a set of randomly-distributed points and with a well-known fractal structure (Sierpinski triangle). The latter was generated by the so called chaos game method. Starting from a randomly chosen point $\mathbf{v}_1$ in the triangle with the vertices $\mathbf{p}_1$, $\mathbf{p}_2$, and $\mathbf{p}_3$, one consequentially makes the steps directed to randomly chosen triangle vertex but passing only half of required distance. The corresponding recurrent formula reads $\mathbf{v}_{i+1} = (\mathbf{v}_i + \mathbf{p}_{r_i})/2$, where r_i a random integer from 1 to 3. Such Sierpinski triangle-like patterns were generated for 320 points and then rescaled to give the same mean distance between the points as the one observed in the vortex distributions (approx. 25ξ). Finally, all space was tiled with a 2D lattice of such patterns to obey the transition to 2D regime at large scales.

Figure 3.13 allows to compare the size of the transitional region for randomly distributed points (blue), vortex structures arising from the turbulence (green), and a perfect fractal structure of the Sierpinski triangle (orange). For random points, this region is the smallest and no fractal dimension can be determined. For the vortex clusters and

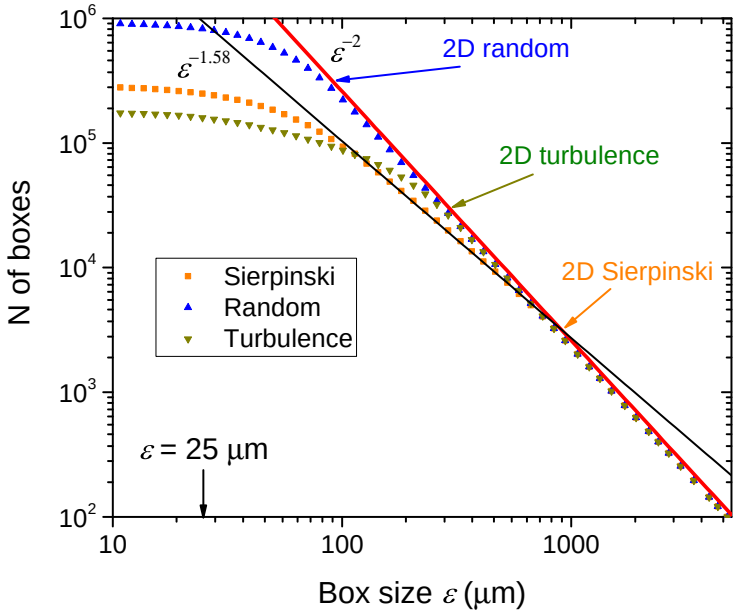

Figure 3.13: Comparison of vortex clustering algorithm for clusters of vortices and artificially generated patterns in the shape of Sierpinski triangle and random spatial distribution. The power function of $\log_2 3 \approx 1.58$ corresponds to the exact value of Sierpinski triangle fractal dimension.

the Sierpinski triangle, the transitional region is much larger, and a fractal dimension of $\log_2 3$ can be determined correctly for the Sierpinski triangle. One can thus conclude therefore that vortex clusters indeed form a fractal structure. The fact that the size of the transitional region for the vortex clusters is slightly smaller than for the triangle could be partially explained by the fact that the fractal dimensions are different, and the transition to the 2D exponent is therefore smoother in the case of the Sierpinski fractal.

At the same time, Fig. 3.13 shows clearly that in a finite-size system the fractal dimension region does not have an infinite extension even for a perfect self-similar distribution of points. In order to robustly observe the intermediate regime with fractional Minkowski-Bouligand dimension one requires the system size to be at least two orders higher than the average distance between the points. Practically, for polaritons such system sizes of several hundreds of microns are already achievable, and increasing them to the scale of 1 mm should allow to significantly increase the reliability of the determination of the fractal dimension.

In the next subsection, the time evolution of the energy spectra will be studied in order to establish the nature (direct or inverse) of the observed energy cascade.

3.3.4 Dynamics of the energy redistribution and cascade formation

In order to understand the formation of a $-5/3$ power law region in the IKE spectra, one should analyze the time dynamics during the first stages of stirring by Brownian potentials. In this section, the cluster selection procedure was not performed in order to keep track of the total IKE spectrum. Similar analysis of the time evolution of the energy distribution has been carried out in previous works [34, 21].

Fig. 3.14(a) shows the IKE spectra at four different times after the start of the stirring. The corresponding wave vectors are marked with dashed lines in panel (a). One sees that at the earlier time (225 ps, red dots) the kinetic energy is mostly concentrated at large wave vectors (small size scales), which corresponds to the injection scale (spot size, peak at approx. $k\xi = 0.3$). Then the kinetic energy is transferred from high wave vectors to lower wave vectors versus time. This is directly visible on the IKE spectra. It is also quantitatively confirmed in panel (b), showing the ratio of the spectral energy density measured at low and high wave vectors. This ratio grows from 0 at early times, when there is no energy at all at small wave vectors, to about 15. One can see that this process takes about 200 ps. This energy redistribution from small scales to large scales due to the intervortex interactions clearly confirms the formation of the inverse Kolmogorov cascade. The relative rapidity of this process provides an *a posteriori* justification for neglecting the polariton lifetime (which can be of the order of hundreds of ps) in the simulations. Interestingly, the energy spectrum at 500 ps shows a quite extended $-5/3$ slope without eliminating isolated vortices. This situation corresponds to an optimal moment of time, when the Kolmogorov cascade has built up, while the fraction of individual vortices remains low. The dashed curve with hollow circles shown for comparison in the same figure for the situation at 1 ns demonstrates a growth of the maximum at high wave vectors due to the single vortices, which leads to the narrowing of the $-5/3$ region. At even later moments of time, when the stirring stops, strong currents break up some of the clusters increasing the relative fraction of individual vortices even more (by up to 20%). The final conclusion is that at any moment of time removing the contribution of individual vortices allows to increase the scale of the observation of the $-5/3$ cascade.

The difference in the IKE spectra for different stirring strategies stems from the limited efficiency of the energy redistribution at large scales. If the energy is injected at a scale which is too low, then the structures of the largest scales just cannot form, because of the decay of the vorticity at all scales. Importantly, the observed signature of the inverse cascade does not rule out the presence of a direct one: the energy can be transferred from the injection point in both directions. For us, the most important was to demonstrate the possibility of the inverse cascade, debated for a long time.

3.3.5 Finite lifetime effects

Here, one can see the results of a single simulation with a finite lifetime, which confirm that present conclusions hold qualitatively for realistic polariton systems, provided that pulsed pumping is used. An additional decay term in GPE describing the finite lifetime was used:

$$i\frac{\partial\psi}{\partial t} = -\Delta\psi + (V - i\Gamma)\,\psi + \left(|\psi|^2 - 1\right)\psi, \tag{3.23}$$

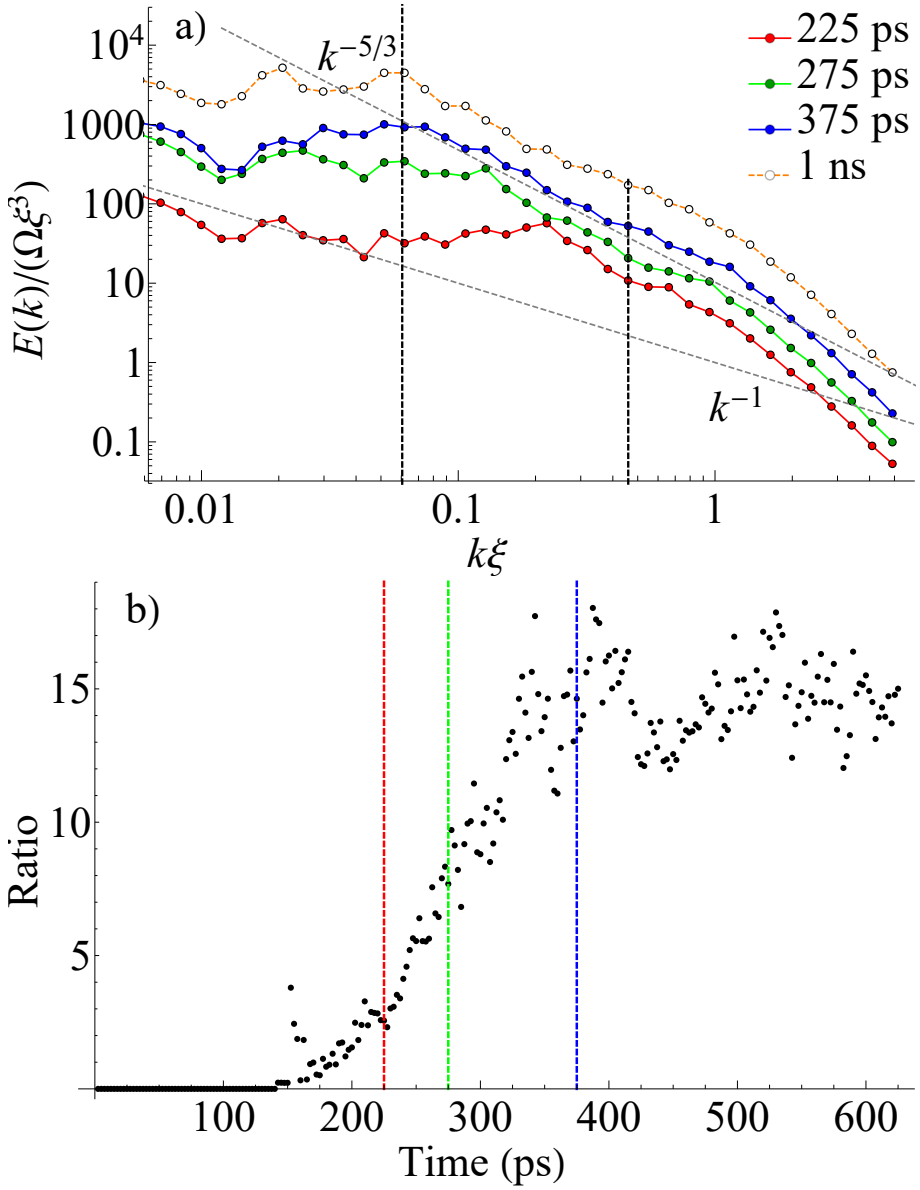

Figure 3.14: a). Net IKE spectra obtained analytically for Brownian stirrers at several time moments during stirring. b) Ratio of the spectral energy density at two wave vectors shown by dashed lines in (a), as a function of time. Vertical lines in (b) correspond to the moments of time in (a).

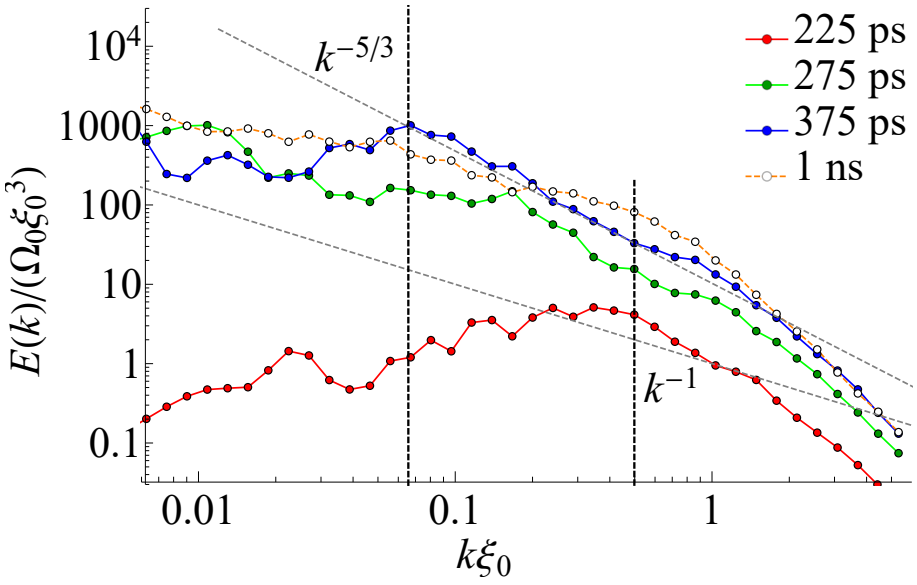

Figure 3.15: Net IKE spectra obtained analytically for Brownian stirrers at several time moments during stirring for a simulation with a finite lifetime $\tau = 300$ ps.

where $\Gamma = \hbar/2\tau g n_0$ is the dimensionless decay rate (n_0 is the initial density). As discussed in the main text, the only effect of this term is the decay of particle density and the associated increase of the healing length. This decay alone does not lead to any particular driven-dissipative instabilities. On the contrary, the finite lifetime reduces the instabilities existing in the conservative case, such as the modulational instability (see Ref. [68] and the next chapter) and, by reducing the growth rate of the perturbations (determined by the imaginary part of their energy). If the maximal growth rate drops to zero, the instability disappears, and therefore the system becomes more stable than in the conservative case. This may indeed affect the generation of vortex-antivortex pairs by the stirrers in the quantum turbulence under the study: if the decay is sufficiently fast, no vortices will be generated at all. However, in the limit of long lifetime $\Gamma \ll gn$ (almost conservative case), this reduction of the vortex generation is negligibly small, because the typical instability growth rate is of the order of the interaction energy gn.

Figure 3.15 shows the time evolution of the energy cascade during the stirring, similar to Fig. 3.14 of the main text, but with a finite lifetime of $\tau = 300$ ps. The same energy transfer from higher to lower wave vectors can be seen, and the formation of a large-scale $k^{-5/3}$ cascade at $t = 375$ ps are clearly visible, exactly like in the fully conservative simulation. Of course, at longer times ($t = 1000$ ps) the energy distribution starts to change, but there is a possibility to carry out the measurements before it happens.

In this simulation the density decreases in time. As a result, the value to which the energy is normalized (in fact the energy of a single vortex) is not constant in time. Healing length ξ also increases with time. Thus, the best option was to fix the energy normalization in Figure 3.15 to the value $\Omega_0\xi_0^3$ and the wave vector normalization to be $k\xi_0$, where the quantities with subscript 0 are obtained at 375 ps. In order to have a time-average density similar to that of Fig. 3.14, one starts here with a higher initial population.

3.4 Discussion and conclusion

The existence of the $-5/3$ cascade in 2D quantum turbulence is currently a matter of scientific debate, and its direct observation is quite difficult, even in numerical experiments. Even with the maximal efficiency of existing computing hardware, using the massive parallelization provided by the GPU but without recurring to supercomputers, it was possible to clearly observe and fit the cascade only over 1-2 orders of magnitude. In experiments, obtaining even 1 order of magnitude might be quite challenging. While the scales of the experimental observation in the best quality microcavity samples could cover several orders of magnitude in space or wave vector thanks to the extended coherence length of polariton quantum fluids, additional complications arise from the fact that the high-wave vector limit for the cascade is not the healing length ξ (of the order of 1 μm), but the mean intervortex distance determining $k_l = \frac{2\pi}{l}$. k_l by its nature is greater than ξ, and in present study it was typically one order greater: tens of microns.

The relatively low density of the vortex gas leaves many single vortices out of the interaction, preventing them from joining the fractal structures and participating in the cascade. The numerical IKE spectra are dominated by these single vortices with a characteristic -1 slope. Removing the single vortices while keeping the vortex clusters allows to observe the $-5/3$ IKE spectrum over a larger scale for all stirring strategies. The usage of Brownian stirrers gives the most extended $-5/3$ region on IKE spectrum after vortex clusters detection procedure. Fitting confirms that the expected scaling falls within the bounds of the confidence interval. One can explicitly extract a non-integer (fractal) dimension of the vortex clusters at the same scales.

It was demonstrated that the observed $-5/3$ is a result of the energy redistribution during the initial moments of stirring. The energy is injected at relatively small scales and transferred to the larger scales (smaller wave vectors). The analysis of the time dependence of the energy stored in large-scale and small-scale structures supports the hypothesis of the inverse energy cascade.

To conclude, the direct observation (using the angle-resolved luminescence detection) of the $-5/3$ cascade in the energy spectrum still remains a challenging task for polariton quantum fluids. It might require single-shot time-resolved measurement of the amplitude and phase of the wave function, followed by the clustering procedure. Still, among the different considered stirring procedures the Brownian stirrers are preferable. Time-dependent studies should also allow to observe the energy redistribution during the formation of the cascade.

Bibliography

[1] L. D. Landau and E. M. Lifshitz, *Course of theoretical physics*. Elsevier, 2013.

[2] A. Obukhov, "Spectral energy distribution in a turbulent flow," *Izv. Akad. Nauk. SSSR. Ser. Geogr. i. Geofiz*, vol. 5, pp. 453–466, 1941.

[3] A. Oboukhov, "On the distribution of energy in the spectrum of turbulent flow," *Dokl. Akad. Sci. Nauk SSSR A*, vol. 32, pp. 22–24, 1941.

[4] A. N. Kolmogorov, "Dissipation of energy in locally isotropic turbulence," in *Akademiia Nauk SSSR Doklady*, vol. 32, p. 16, 1941.

[5] A. N. Kolmogorov, "The local structure of turbulence in incompressible viscous fluid for very large reynolds numbers," in *Dokl. Akad. Nauk SSSR*, vol. 30, pp. 299–303, 1941.

[6] A. N. Kolmogorov, "The local structure of turbulence in incompressible viscous fluid for very large reynolds numbers," *Proceedings of the Royal Society of London. Series A: Mathematical and Physical Sciences*, vol. 434, no. 1890, pp. 9–13, 1991.

[7] L. F. Richardson, *Weather prediction by numerical process*. Cambridge university press, 2007.

[8] O. Regev, O. M. Umurhan, and P. A. Yecko, *Modern Fluid Dynamics for Physics and Astrophysics*. Springer, 2016.

[9] R. H. Kraichnan, "Inertial ranges in two-dimensional turbulence," *The Physics of Fluids*, vol. 10, no. 7, pp. 1417–1423, 1967.

[10] T.-L. Horng, C.-H. Hsueh, S.-W. Su, Y.-M. Kao, and S.-C. Gou, "Two-dimensional quantum turbulence in a nonuniform bose-einstein condensate," *Phys. Rev. A*, vol. 80, p. 023618, Aug 2009.

[11] M. Tsubota, K. Fujimoto, and S. Yui, "Numerical studies of quantum turbulence," *Journal of Low Temperature Physics*, vol. 188, no. 5-6, pp. 119–189, 2017.

[12] W. Vinen, "Mutual friction in a heat current in liquid helium ii i. experiments on steady heat currents," *Proc. R. Soc. Lond. A*, vol. 240, no. 1220, pp. 114–127, 1957.

[13] L. Skrbek, "Quantum turbulence," in *Journal of Physics: Conference Series*, vol. 318, p. 012004, IOP Publishing, 2011.

[14] C. F. Barenghi, L. Skrbek, and K. R. Sreenivasan, "Introduction to quantum turbulence," *Proceedings of the National Academy of Sciences*, vol. 111, no. Supplement 1, pp. 4647–4652, 2014.

[15] M. Tsubota, M. Kobayashi, and H. Takeuchi, "Quantum hydrodynamics," *Physics Reports*, vol. 522, no. 3, pp. 191–238, 2013.

[16] A. Allen, N. Parker, N. Proukakis, and C. Barenghi, "Quantum turbulence in atomic bose-einstein condensates," in *Journal of Physics: Conference Series*, vol. 544, p. 012023, IOP Publishing, 2014.

[17] G. Stagg, A. Allen, N. Parker, and C. Barenghi, "Generation and decay of two-dimensional quantum turbulence in a trapped bose-einstein condensate," *Physical Review A*, vol. 91, no. 1, p. 013612, 2015.

[18] A. C. White, B. P. Anderson, and V. S. Bagnato, "Vortices and turbulence in trapped atomic condensates," *Proceedings of the National Academy of Sciences*, vol. 111, no. Supplement 1, pp. 4719–4726, 2014.

[19] N. Navon, A. L. Gaunt, R. P. Smith, and Z. Hadzibabic, "Emergence of a turbulent cascade in a quantum gas," *Nature*, vol. 539, p. 72, 2016.

[20] A. Alexakis and L. Biferale, "Cascades and transitions in turbulent flows," *Physics Reports*, vol. 767-769, pp. 1 – 101, 2018. Cascades and transitions in turbulent flows.

[21] M. T. Reeves, T. P. Billam, B. P. Anderson, and A. S. Bradley, "Inverse energy cascade in forced two-dimensional quantum turbulence," *Physical review letters*, vol. 110, no. 10, p. 104501, 2013.

[22] R. Numasato, M. Tsubota, and V. S. L'vov, "Direct energy cascade in two-dimensional compressible quantum turbulence," *Phys. Rev. A*, vol. 81, p. 063630, Jun 2010.

[23] M. T. Reeves, T. P. Billam, X. Yu, and A. S. Bradley, "Enstrophy cascade in decaying two-dimensional quantum turbulence," *Physical review letters*, vol. 119, no. 18, p. 184502, 2017.

[24] T. Simula, M. J. Davis, and K. Helmerson, "Emergence of order from turbulence in an isolated planar superfluid," *Physical review letters*, vol. 113, no. 16, p. 165302, 2014.

[25] J. H. Kim, W. J. Kwon, and Y. Shin, "Role of thermal friction in relaxation of turbulent bose-einstein condensates," *Phys. Rev. A*, vol. 94, p. 033612, Sep 2016.

[26] A. J. Groszek, M. J. Davis, D. M. Paganin, K. Helmerson, and T. P. Simula, "Vortex thermometry for turbulent two-dimensional fluids," *Physical review letters*, vol. 120, no. 3, p. 034504, 2018.

[27] A. J. Groszek, M. J. Davis, and T. P. Simula, "Decaying quantum turbulence in a two-dimensional bose-einstein condensate at finite temperature," *arXiv preprint arXiv:1903.05528*, 2019.

[28] G. Gauthier, M. T. Reeves, X. Yu, A. S. Bradley, M. A. Baker, T. A. Bell, H. Rubinsztein-Dunlop, M. J. Davis, and T. W. Neely, "Giant vortex clusters in a two-dimensional quantum fluid," *Science*, vol. 364, no. 6447, pp. 1264–1267, 2019.

[29] S. P. Johnstone, A. J. Groszek, P. T. Starkey, C. J. Billington, T. P. Simula, and K. Helmerson, "Evolution of large-scale flow from turbulence in a two-dimensional superfluid," *Science*, vol. 364, no. 6447, pp. 1267–1271, 2019.

[30] N. Bogoliubov, "On the theory of superfluidity," *J. Phys*, vol. 11, no. 1, p. 23, 1947.

[31] E. P. Gross, "Structure of a quantized vortex in boson systems," *Il Nuovo Cimento (1955-1965)*, vol. 20, no. 3, pp. 454–477, 1961.

[32] M. Reeves, B. Anderson, and A. Bradley, "Classical and quantum regimes of two-dimensional turbulence in trapped bose-einstein condensates," *Physical Review A*, vol. 86, no. 5, p. 053621, 2012.

[33] A. Skaugen and L. Angheluta, "Vortex clustering and universal scaling laws in two-dimensional quantum turbulence," *Physical Review E*, vol. 93, no. 3, p. 032106, 2016.

[34] A. S. Bradley and B. P. Anderson, "Energy spectra of vortex distributions in two-dimensional quantum turbulence," *Physical Review X*, vol. 2, no. 4, p. 041001, 2012.

[35] H. Flayac, G. Pavlovic, M. Kaliteevski, and I. Shelykh, "Electric generation of vortices in polariton superfluids," *Physical Review B*, vol. 85, no. 7, p. 075312, 2012.

[36] S. Pigeon and A. Bramati, "Sustained propagation and control of topological excitations in polariton superfluid," *New Journal of Physics*, vol. 19, no. 9, p. 095004, 2017.

[37] E. Zaremba, A. Griffin, and T. Nikuni, "Two-fluid hydrodynamics for a trapped weakly interacting bose gas," *Phys. Rev. A*, vol. 57, pp. 4695–4698, Jun 1998.

[38] M. Kobayashi and M. Tsubota, "Dissipation of gross-pitaevskii turbulence coupled with thermal excitations," *Journal of Low Temperature Physics*, vol. 148, pp. 275–279, Aug 2007.

[39] L. P. Pitaevskii, "Properties of the spectrum of elementary excitations near the disintegration threshold of the excitations," *Sov. Phys. JETP*, vol. 35, p. 282, 1959.

[40] I. Carusotto and C. Ciuti, "Quantum fluids of light," *Rev. Mod. Phys.*, vol. 85, pp. 299–366, Feb 2013.

[41] X. Yu and A. S. Bradley, "Emergent non-eulerian hydrodynamics of quantum vortices in two dimensions," *Phys. Rev. Lett.*, vol. 119, p. 185301, Oct 2017.

[42] R. N. Valani, A. J. Groszek, and T. P. Simula, "Einstein–bose condensation of onsager vortices," *New Journal of Physics*, vol. 20, no. 5, p. 053038, 2018.

[43] J. Kasprzak, D. D. Solnyshkov, R. André, L. S. Dang, and G. Malpuech, "Formation of an exciton polariton condensate: Thermodynamic versus kinetic regimes," *Phys. Rev. Lett.*, vol. 101, p. 146404, Oct 2008.

[44] E. Wertz, L. Ferrier, D. D. Solnyshkov, P. Senellart, D. Bajoni, A. Miard, A. Lemaître, G. Malpuech, and J. Bloch, "Spontaneous formation of a polariton condensate in a planar gaas microcavity," *Applied Physics Letters*, vol. 95, no. 5, p. 051108, 2009.

[45] J. Levrat, R. Butté, E. Feltin, J.-F. m. c. Carlin, N. Grandjean, D. Solnyshkov, and G. Malpuech, "Condensation phase diagram of cavity polaritons in gan-based microcavities: Experiment and theory," *Phys. Rev. B*, vol. 81, p. 125305, Mar 2010.

[46] F. Li, L. Orosz, O. Kamoun, S. Bouchoule, C. Brimont, P. Disseix, T. Guillet, X. Lafosse, M. Leroux, J. Leymarie, M. Mexis, M. Mihailovic, G. Patriarche, F. Réveret, D. Solnyshkov, J. Zuniga-Perez, and G. Malpuech, "From excitonic to photonic polariton condensate in a zno-based microcavity," *Phys. Rev. Lett.*, vol. 110, p. 196406, May 2013.

[47] D. D. Solnyshkov, H. Terças, K. Dini, and G. Malpuech, "Hybrid boltzmann˘gross-pitaevskii theory of bose-einstein condensation and superfluidity in open driven-dissipative systems," *Phys. Rev. A*, vol. 89, p. 033626, Mar 2014.

[48] A. Baas, J. P. Karr, H. Eleuch, and E. Giacobino, "Optical bistability in semiconductor microcavities," *Phys. Rev. A*, vol. 69, p. 023809, Feb 2004.

[49] M. Wouters and I. Carusotto, "Excitations in a nonequilibrium bose-einstein condensate of exciton polaritons," *Phys. Rev. Lett.*, vol. 99, p. 140402, Oct 2007.

[50] J. Keeling and N. G. Berloff, "Spontaneous rotating vortex lattices in a pumped decaying condensate," *Phys. Rev. Lett.*, vol. 100, p. 250401, Jun 2008.

[51] M. Wouters and I. Carusotto, "Superfluidity and critical velocities in nonequilibrium bose-einstein condensates," *Phys. Rev. Lett.*, vol. 105, p. 020602, Jul 2010.

[52] M. Wouters, T. C. H. Liew, and V. Savona, "Energy relaxation in one-dimensional polariton condensates," *Phys. Rev. B*, vol. 82, p. 245315, Dec 2010.

[53] P.-E. Larré, N. Pavloff, and A. M. Kamchatnov, "Wave pattern induced by a localized obstacle in the flow of a one-dimensional polariton condensate," *Phys. Rev. B*, vol. 86, p. 165304, Oct 2012.

[54] A. Chiocchetta and I. Carusotto, "Non-equilibrium quasi-condensates in reduced dimensions," *EPL (Europhysics Letters)*, vol. 102, p. 67007, jun 2013.

[55] E. Altman, L. M. Sieberer, L. Chen, S. Diehl, and J. Toner, "Two-dimensional superfluidity of exciton polaritons requires strong anisotropy," *Phys. Rev. X*, vol. 5, p. 011017, Feb 2015.

[56] F. Baboux, D. D. Bernardis, V. Goblot, V. N. Gladilin, C. Gomez, E. Galopin, L. L. Gratiet, A. Lemaître, I. Sagnes, I. Carusotto, M. Wouters, A. Amo, and J. Bloch, "Unstable and stable regimes of polariton condensation," *Optica*, vol. 5, pp. 1163–1170, Oct 2018.

[57] L. Ferrier, E. Wertz, R. Johne, D. D. Solnyshkov, P. Senellart, I. Sagnes, A. Lemaître, G. Malpuech, and J. Bloch, "Interactions in confined polariton condensates," *Physical Review Letters*, vol. 106, no. 12, p. 126401, 2011.

[58] D. Bajoni, P. Senellart, E. Wertz, I. Sagnes, A. Miard, A. Lemaître, and J. Bloch, "Polariton laser using single micropillar GaAs−GaAlAs semiconductor cavities," *Phys. Rev. Lett.*, vol. 100, p. 047401, Jan 2008.

[59] D. Caputo, D. Ballarini, G. Dagvadorj, C. S. Muñoz, M. De Giorgi, L. Dominici, K. West, L. N. Pfeiffer, G. Gigli, F. P. Laussy, *et al.*, "Topological order and thermal equilibrium in polariton condensates," *Nature Materials*, vol. 17, no. 2, p. 145, 2018.

[60] G. Boffetta, A. Celani, and M. Vergassola, "Inverse energy cascade in two-dimensional turbulence: Deviations from gaussian behavior," *Phys. Rev. E*, vol. 61, pp. R29–R32, Jan 2000.

[61] C. A. Jones and P. H. Roberts, "Motions in a bose condensate. IV. axisymmetric solitary waves," *Journal of Physics A: Mathematical and General*, vol. 15, pp. 2599–2619, aug 1982.

[62] L. Pitaevskii and S. Stringari, *Bose-Einstein Condensation*. Oxford Science Publications - International Series of Monographs on Physics 116, 2003.

[63] H. Salman and D. Maestrini, "Long-range ordering of topological excitations in a two-dimensional superfluid far from equilibrium," *Physical Review A*, vol. 94, no. 4, p. 043642, 2016.

[64] D. Sanvitto, F. M. Marchetti, M. H. Szymanska, G. Tosi, M. Baudisch, F. P. Laussy, D. N. Krizhanovskii, M. S. Skolnick, L. Marrucci, A. Lemaitre, J. Bloch, C. Tejedor, and L. Vina, "Persistent currents and quantized vortices in a polariton superfluid," *Nature Physics*, vol. 6, p. 527, 2010.

[65] V. G. Sala, D. D. Solnyshkov, I. Carusotto, T. Jacqmin, A. Lemaître, H. Terças, A. Nalitov, M. Abbarchi, E. Galopin, I. Sagnes, J. Bloch, G. Malpuech, and A. Amo, "Spin-orbit coupling for photons and polaritons in microstructures," *Phys. Rev. X*, vol. 5, p. 011034, Mar 2015.

[66] G. Kowal and A. Lazarian, "Velocity field of compressible magnetohydrodynamic turbulence: wavelet decomposition and mode scalings," *The Astrophysical Journal*, vol. 720, no. 1, p. 742, 2010.

[67] A. Clauset, C. Shalizi, and M. Newman, "Power-law distributions in empirical data," *SIAM Review*, vol. 51, no. 4, pp. 661–703, 2009.

[68] E. A. Kuznetsov and S. K. Turitsyn, "Instability and collapse of solitons in media with a defocusing nonlinearity," *Sov. Phys. JETP*, vol. 67, p. 1583, 1988.

Chapter 4

Modulational instability of solitons and vortex street formation in the quantum fluids of cavity exciton-polaritons

Contents

4.1 Introduction

As it was outlined in the introductory chapters, the Bose-Einstein condensate is a new state of matter which gives the astonishing possibility of observation of quantum phenomena, like the existence of the wave function, on macroscopic scales. And a particular type of BEC implementation is the one based on exciton-polaritons in semiconductor microcavities [1]. These composite quasi-particles are semi-photons and semi-excitons existing in the regime of strong coupling [2]. From the photons, the polaritons inherit the full-optical control of excitation, as well as the possibility of optical detection. And due to the non-linear interactions of the excitonic component, the behavior of polariton Bose-Einstein condensates, and, more generally, of polaritons at high densities, resembles that of quantum fluids [3]. The polariton quantum fluids are a promising platform for lasing [4], topological physics [5, 6], and many other applications. Other direction of research on polariton quantum fluids, more fundamental, is the analog physics [7, 8] and practical implementation of various algorithms: both analog and quantum. For example, the polariton platform was used to implement the XY Hamiltonian by imprinting polariton condensate lattices and engineering the coupling strengths between the lattice sites [9]. Other remarkable proposed concept consisted in the control of polariton spatial propagation along the channels, resulting in the functioning of the "polariton neurons" [10]. Among other algorithms, a particularly attractive field is that of the finding and research of the physical systems possessing the properties of maze solving [11, 12, 13, 14, 15, 16]. It was also outlined that the spatio-temporal dynamics of polariton quantum fluids obeys the Gross-Pitaevskii equation [17], the version of the Schrödinger equation with non-linear interaction term and with additional possibility to phenomenologically take into account the finite lifetime of polaritons, non-resonant or quasi-resonant pumping regimes, and other specificities of polaritons in semiconductor microcavities, like the effects of various polarizations. The conservative Gross-Pitaevskii equation possesses such typical solutions as 0D quantum vortices and 1D solitons [18, 19]. These solutions have a form of density dip (point-like and line-like, respectively) accompanied with strong fluxes corresponding to abrupt phase alterations of the order of π. These phase patterns (especially for the vortices associated with a point of diverging circulation) appear to be very stable due to their topological nature and, as a result, provide the stability to the corresponding solutions of GPE overall. Even in the driven-dissipative polariton systems, one has successfully detected both vortices [20, 21, 22, 23] and solitons.

A bright example of the latter, which revealed the potential of polariton-based systems, is the observation of oblique dark solitons [24, 25, 26], which form when a supersonic quantum fluid hits a defect (initially proposed in 2006 [27] for atomic BECs). The 2D solitons forming behind the defect remained stable because the transverse "snake instability"[28, 29], making 2D solitons normally unstable, was carried away by the supersonic flow, making the soliton effectively 1D [30, 31]. Such supersonic flow is energetically unstable, but polariton flows were efficiently decoupled from thermal relaxation [32, 33], which made possible the observation of oblique dark solitons [25, 26]. Another configurations allowed observing solitons bonded into the soliton molecules [34, 35] and thus being quasi parallel for long distances. An interesting regime occurs if the fluid velocity is decreased just below the speed of sound. In such a case, the subsonic flow still interacts with the defect exhibiting a local acceleration. This leads to the formation of quantum vortex

streets composed of vortex-antivortex pairs. This quantum version of von Karman vortex streets can be understood as a decay of the oblique solitons via the snake instability, when the stabilization by the supersonic flow is lost.

The creation of vortex-antivortex pairs has been reported in time-resolved pulsed experiments, both in polaritons [36, 37] and atomic quantum fluids [38]. Similar proposals were made for non-resonantly pumped polaritons [39, 40]. However, the study of the snake instability dynamics leading to quantum vortex streets requires both *cw* excitation and time resolution, and it remained elusive so far. In a recent theoretical work, it was proposed to improve this scheme by sustaining the propagating flow against radiative decay by using a support laser covering the whole sample [41]. Interestingly, this configuration demonstrates original density-phase defects. This pump-support scheme is not limited to the study of the flow scattering on defects, but can be used in a more general frame to create and study a large variety of topological defects [42, 43, 44]. Topological defects in the driven-dissipative case can be stationary only when the support laser intensity falls in the bistability loop of the non-linear system [45, 46, 47, 41], where the density can be either low or high, depending on the laser absorption. Stationary phase defects exist in low-density regions or within the bistability hysteresis loop, where the phase is not fixed, because most particles are not directly injected by the laser but diffuse from higher-density regions. The control of the spatial distribution of intensity and phase allows to realize various confining potentials, such as 1D channels, 0D traps [20], or circuits made by the combination of both.

The present chapter is devoted to theoretical study of snake (modulational) instability in polariton quantum fluids and also proposes a scheme of a practical realization of the polariton-based maze solver circuit. Confining the soliton pair along the axis of a channel with the walls at high polariton density under laser irradiation (pump) resulted in fixing the solitons at some stage of their decay to the chain of vortex pairs. The finite lifetime of polaritons in the channel was overcome by the weaker support, falling within or slightly lower the bistability hysteresis loop. Simultaneously tuning the values of pump and support allowed to control the wave vector of modulational instability and even its symmetry. Moreover, this scheme demonstrated enough flexibility to be used in the field of algorithm implementation, developing the general ideas of "polariton neurons". By shaping the channels in the form of a given maze and properly tuning the intensity of the support beam, one can obtain a solution of this maze with the solitons tracing the desired path. This solution is based on the well-known and perfomant algorithm of dead end filling, which is physically realized by the effect of soliton repulsion from the dead ends of closed channels. Prospectively, the proposed scheme can be verified experimentally with the help of flexible and simple to implement spatial light modulator (SLM) engineering of a laser profile.

The chapter is organized as follows. It contains 3 main sections and a concluding section. The first of them will describe the peculiarities of motion of the domain wall between the spatial domains at upper and lower bistability branches in the region of laser intensities close to bistability hystheresis loop. Next section studies the behavior of the soliton pair confined in the corridor with the walls "made" of high-density regions under intensive laser irradiation including the phenomenon of developing the modulational instability in such system. Finally, the maze-solving property is studied, including the parameters necessary for maze solving, size scaling of a scheme, robustness with respect

to the disorder in a cavity, topology of the maze.

4.2 Domain wall between high and low density regions in bistable regime

4.2.1 Pump/support scheme

The topological defects in quantum fluids like solitons and quantum vortices imply the abrupt variation of the wave function phase and amplitude (straightly connected with polariton density). Therefore, it is challenging to obtain such topological defects in experiments with cw microcavity irradiation above the region of bistability: the phase becomes pinned to the phase of a laser and high density is expected in all irradiated area. However this restriction can be avoided if one returns to the laser power lying within the hysteresis loop on the bistability curve. Indeed, within the bistable hysteresis cycle, two regions are available for the system, respectively at high and low polariton density and also with opposite phase. In the high-density regions above the bistability regime, the phase is fixed by the resonant laser, as mentioned above. On the contrary, the regions of the bistability regime can have an arbitrary phase and a density from nearly zero to density defined by the relation $gn \approx \hbar\omega_0$, which enables the existence of a rich variety of topological defects, while the radiative decay of the polaritons is compensated, allowing long propagation distances in cw experiment.

The configuration studied in this chapter proposes the further development of the so called "pump/support" scheme, proposed in [41] for sustaining the propagation of topological defects in dissipative polariton quantum fluid (see Fig. 4.1). In such scheme, a strong localized pump drives the system to the upper bistability branch. This pump is surrounded by a weaker support beam with the intensity falling within a bistability loop. This condition allows to overcome the polariton decay while avoiding the phase fixing.

Numerous results in the chapter will be obtained from numerical simulations. The resonantly pumped microcavity is modelled by the standard driven-dissipative Gross-Pitaevskii equation, noteworthy, formally equivalent to the Lugiato-Lefever equation [48]. The polarization degree of freedom, the non-parabolicity of the polariton dispersion, and any thermal effects [49, 50] are neglected. The equation to be simulated reads:

$$i\hbar\frac{\partial\psi}{\partial t} = \left[-\frac{\hbar^2\nabla^2}{2m} - i\Gamma + g\left|\psi\right|^2\right]\psi + (S + P(\mathbf{r}))e^{-i\omega_0 t}, \tag{4.1}$$

where $\Gamma = \hbar/(2\tau)$ is the polariton decay rate ($\tau = 15$ ps), $m = 8\times10^{-5}m_0$ is the polariton mass (m_0 is the free electron mass), $g = 5$ μeVμm^2 is the polariton-polariton interaction constant. The detuning between the ground state and the pump laser is $\omega_0 = 0.14$ meV$/\hbar$. The support S and the pump $P(\mathbf{r})$ are at normal incidence (zero wave vector). The terms of pump and support are written explicitly, which stresses that pump can be spatially controlled by designation $P(\mathbf{r})$. The spatial step size was in most configurations equal to 1 micrometer. The time step was 0.01 ps providing the best compromise between calculation speed and precision. Laser detuning was taken as 14 μeV as a value typical for the experiments with the cavity used e.g. in Ref. [35]. The presented simulations

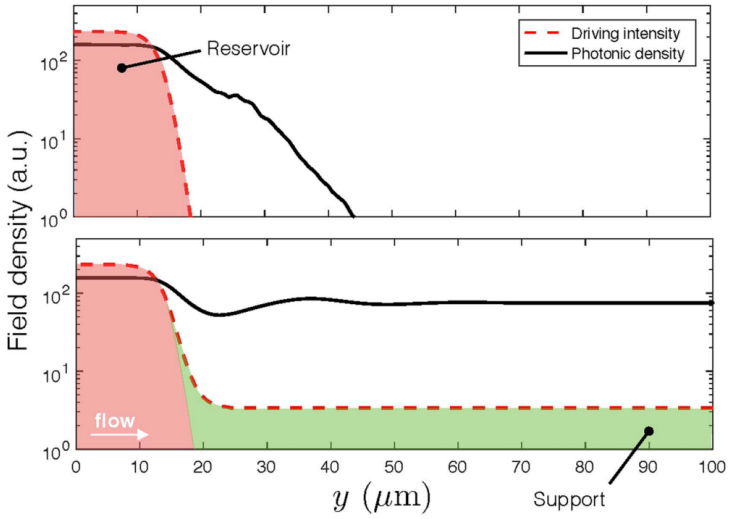

Figure 4.1: The sustained quantum fluid propagation in the "pump/support" scheme. Adopted from Ref. [41]. The intensive laser pump beam creates the high-density reservoir from which the polaritons can propagate at long distances thanks to the support beam protecting from the decay.

are in general devoted to design the experiments, that can be rapidly performed with the same sample and with the usage of SLM in the group in LKB headed by Prof. A. Bramati.

4.2.2 Domain wall motion

First, the spatially homogeneous laser pumping profile (support only) is considered. The bistability loop obtained for the employed parameters is shown in Fig. 4.2(a). Green curve corresponds to the path upwards from zero laser intensity and red curve is for the descending path from high power to zero.

Next, a half-space pump ($x < 30$ μm) locally switching the system to the higher branch of the bistability loop is added, whereas the other half-space remains on the lower branch, which is allowed by the support. The use of a spatially inhomogeneous pump $P(\mathbf{r})$ allows to control the pumping intensity in the high- and low-density regions independently.

Figure 4.2(b) shows the two regions of high and low density separated by a domain wall (DW). The region under the pump shows a large intensity and a fixed phase. The intensity at the DW decays within one healing length $\xi = \hbar/\sqrt{2gnm}$ (n is the density) and then exhibits small periodic oscillations of intensity. These oscillations are due to the interference between the polaritons coming from the high-density region (and thus gaining a phase) and the polaritons that are created locally by the support. The DW is stable against the development of instabilities along Y, but can propagate along X. Such DW propagation has been previously considered for polaritons [10, 51] and in general for switching waves in optics [52, 53, 54] and beyond. Starting from this spatial profile depicted in Fig. 4.2(b), the domain wall can move in two directions along the X axis: either to the left ($S < S_c$, contracting the region at upper bistability branch) or to the right ($S > S_c$, expanding the region at upper bistability branch). The velocity v of the DW motion is an important parameter of the considered problem and it was computed

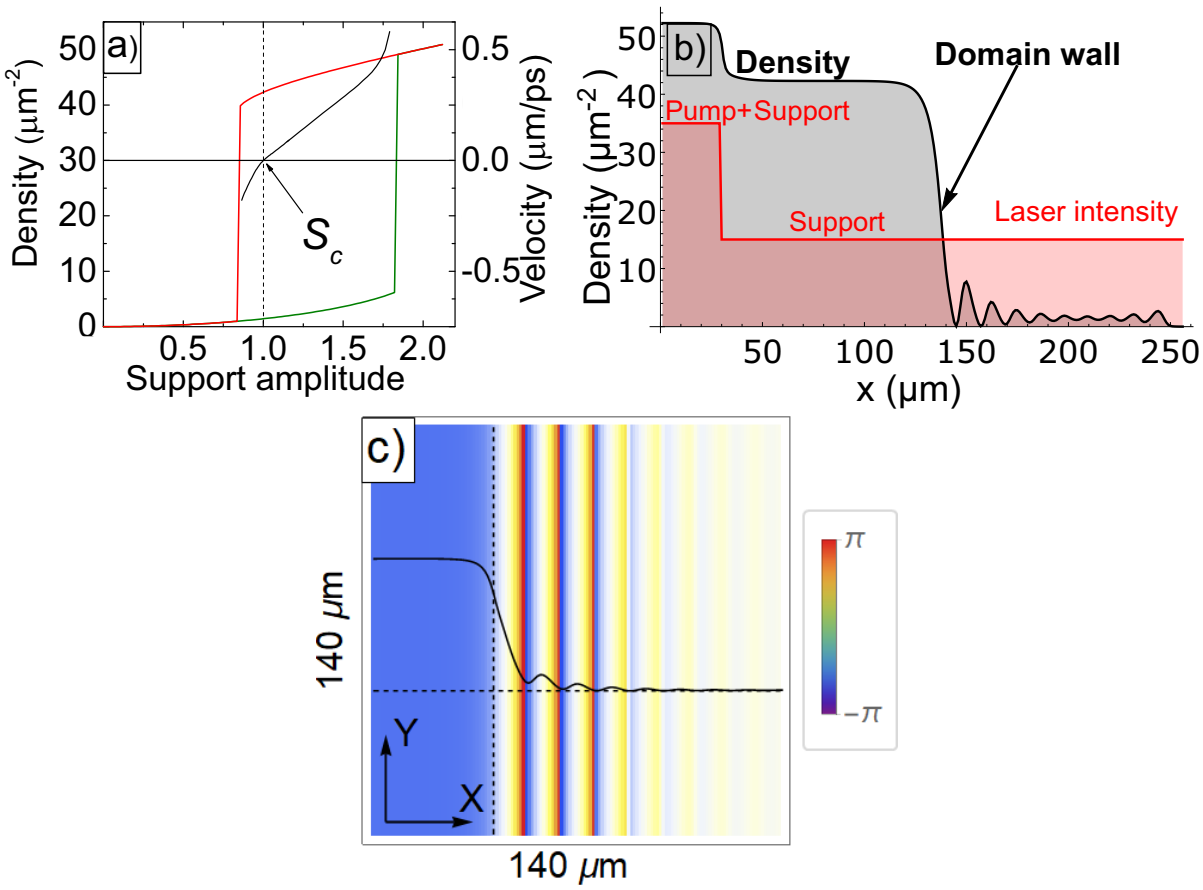

Figure 4.2: a) Polariton bistability: density as a function of the pump (red, green); DW velocity (black, right Y axis). b) A single high-density region generated by a pump (left), with support present everywhere: condensate density (black curve) combined with the profile of laser intensity (red curve). Starting from this spatial profile, the domain wall can move either to the left ($S < S_c$) or to the right ($S > S_c$). c) "Top view" 2D plot of panel b) with the phase pattern of the domain wall combined with the polariton density plot (black curve).

numerically for actual parameters as a function of support intensity. The numerical results are shown in Fig. 4.2(a) (black curve, with the background of the bistability loop). Reasonably, the area where the DW velocity is meaningful lies within the left and right limits of the bistability loop. At the intensities out of the loop, the switching happens not as a DW motion, but simultaneously in all space.

4.2.3 Derivation critical support value of domain wall stability

The behavior of a DW can be explained on the basis of so-called "Maxwell construction" for the phase transitions between vapor and liquid in thermodynamics [55]. The behavior of bistable systems and, in particular, spatially inhomogeneous solutions present in such systems were a subject of studies for a long time. An overview on optical systems can be found in Ref. [52].

One should start by looking for a stationary spatially inhomogeneous solution where a part of the system is at the upper bistability branch, whereas another part is at the lower bistability branch. These two parts are separated by a domain wall (or switching wall). This problem can be solved analytically for negligibly small dissipation Γ (as compared with the laser detuning $\delta = \hbar\omega_0$), and then the solution can be generalized to non-zero Γ.

The stationary driven-dissipative Gross-Pitaevskii equation that needs to be satisfied by the wave function reads:

$$\left(-\hbar\omega_0 - \frac{\hbar^2}{2m}\Delta + g|\psi_0|^2 - i\Gamma_0\right)\psi_0 + S = 0, \tag{4.2}$$

where one will neglect the term Γ at first. Once it is neglected, the wave function ψ and the pumping (the support S to be more precise) can be assumed to take only real values without loss of generality (since all coefficients are real). The equation (4.2) can therefore be rewritten as

$$m_0\frac{d^2x}{dt^2} = F(x), \tag{4.3}$$

which is a Newton's equation of motion for a material point ($x = \psi$) with a mass $m_0 = \hbar^2/2m$ under the effect of a position-dependent "force"

$$F(x) = gx^3 - \delta x + S, \tag{4.4}$$

to which one may attribute a "potential"

$$U(x) = -\int F(x)\ dx = -\frac{gx^4}{4} + \frac{\delta x^2}{2} - Sx. \tag{4.5}$$

The two maxima of this potential located at the coordinates x_1 and x_3 correspond to the two stable domains (high density and low density), while the minimum located at x_2 corresponds to the inaccessible part of the bistability curve. The system is stationary only if the values of the effective potentials at the two maxima are exactly the same:

$$U(x_1) = U(x_3), \tag{4.6}$$

otherwise the domain wall starts to propagate. Indeed, a material point should start its motion at one maximum and finish at the other maximum, and for this the two maxima have to be at the same potential height. The points x_1 and x_3, corresponding to the extrema of $U(x)$, can be found analytically from the cubic equation $F(x) = 0$, and the condition (4.6) can be rewritten as

$$\int_{x_1}^{x_3} F(x)\ dx = 0, \tag{4.7}$$

corresponding to the Maxwell construction in thermodynamics [55]. Solving this equation analytically for the unknown S gives finally:

$$S_c = \frac{2\delta^{3/2}}{3\sqrt{3}g^{1/2}}, \tag{4.8}$$

and the ratio with respect to the pumping required for bistability $S_{min} = \Gamma_0\sqrt{\hbar\omega/g}$ is given by

$$\frac{S_c}{S_{min}} = \frac{2}{3\sqrt{3}}\frac{\delta}{\Gamma}. \tag{4.9}$$

A more precise result can be obtained only numerically, which will be demonstrated below. But still some analytical reasoning helps to obtain the final results. For non-negligible Γ, all terms in the equation (4.2) become comparable. The real terms (the kinetic and the interaction energy, the detuning) are of the order of $\delta = \hbar\omega_0$, while the only imaginary term is Γ (imaginary part of kinetic energy is small with respect to Γ). Thus, the expression for the critical pumping S_c at Γ comparable with $\hbar\omega_0$ can be sought by replacing of the first three terms in (4.2) by $\hbar\omega_0$ with some coefficient:

$$\left(C_1\hbar\omega_0 - i\Gamma_0\right)\psi_0 + S = 0. \tag{4.10}$$

Together with assumption $\psi \approx \sqrt{\hbar\omega_0/g}$ one can write

$$S_c = C_2\sqrt{\frac{\hbar\omega_0}{g}}\sqrt{\left(C_1\hbar\omega_0\right)^2 + \Gamma^2}. \tag{4.11}$$

These coefficients can be found from numerical simulations by the small variation of parameters $\omega_0 \to \omega_0 + \Delta\omega_0$, $\Gamma \to \Gamma + \Delta\Gamma$, and $g \to g + \Delta g$ near some "reference" values, which allows obtaining the coefficients in the Taylor expansion:

$$\frac{S_c(\omega_0 + \Delta\omega_0, \Gamma + \Delta\Gamma, g + \Delta g)}{S_c(\omega_0, \Gamma, g)} = 1 + c_\omega\frac{\Delta\omega_0}{\omega_0} + c_\Gamma\frac{\Delta\Gamma}{\Gamma} + c_g\frac{\Delta g}{g}. \tag{4.12}$$

The coefficients are $c_\omega \approx 0.75$, $c_\Gamma \approx 0.75$, $c_g = -0.5$. Fig. 4.3 shows the result of simulations for S_c as a function of $\Delta\omega_0/\omega_0$.

As a net result, one obtains

$$S_c = \sqrt{\frac{\hbar\omega_0}{g}}\sqrt{\left(\frac{3\hbar\omega_0}{32}\right)^2 + \Gamma^2} \tag{4.13}$$

One sees that this equation has the same Taylor expansion as Eq. (4.12) for actual values of system parameters.

4.2.4 Derivation the velocity of domain wall

For $S \neq S_c$, one of the domains becomes more favorable than the other, and the domain wall starts to propagate. Assuming that the density changes linearly with the position across the domain wall (which is valid in the vicinity of the inflection point of this wall), one can write the following expression for the speed of the wall:

$$v = \frac{\partial n}{\partial t}\frac{\Delta x}{\Delta n}, \tag{4.14}$$

where Δx is the width of the domain wall and Δn is the difference of the densities in the high and low density regions.

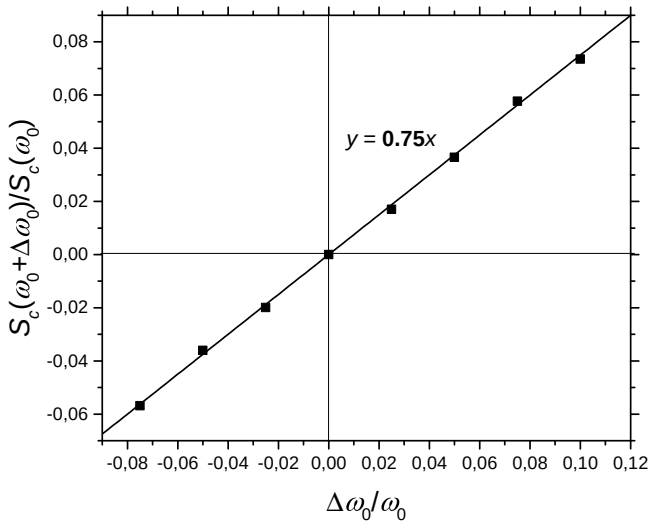

Figure 4.3: Critical support S_c as function of detuning at low values of $\Delta\omega_0/\omega_0$. The results obtained by GPE simulation of DW motion.

To find the derivative $\partial n/\partial t$, one should define n_0 as the density at the inflection point which corresponds to S_c. The only contribution into $\partial\psi/\partial t$ at $S \neq S_c$ can come from the difference $S-S_c$ (all other terms in the time-dependent driven-dissipative Gross-Pitaevskii equation cancel):

$$\frac{\partial\psi}{\partial t} = \frac{S - S_c}{i\hbar}, \tag{4.15}$$

which allows to write the solution

$$\psi(t) = \frac{S - S_c}{i\hbar}t + \sqrt{n_0}e^{i\phi_0}. \tag{4.16}$$

This expression strongly depends on the phase ϕ_0 of the wave function at the inflection point (with respect to the phase of the pump). In a homogeneous system, the phase is given by $\tan\phi = -\Gamma/(gn - \hbar\omega_0)$. In the low-density region, $\phi \to 0$, whereas in the high-density region $\phi \to \pi/2$ just above the threshold density $gn \approx \hbar\omega_0$. It is reasonably to assume that ϕ_0 takes an intermediate value $\phi_0 = \pi/4$, and one can also assume that it changes linearly with $S-S_c$ for small deviations from S_c, in which case the time derivative of the density can be found as:

$$\frac{\partial n}{\partial t} = \frac{\partial}{\partial t}|\psi(t)|^2 \approx 2\sqrt{n_0}\frac{S - S_c}{\hbar}\frac{1}{\sqrt{2}}\left(1 - \chi\frac{S - S_c}{S_c}\right). \tag{4.17}$$

For $S \approx S_c$, the second-order correction can be neglected, but it starts to become important for larger deviation of the pumping, creating an important difference between the speed of the wall for the cases of shrinking or expanding high-density domain.

In the simplest case, the speed can be found as

$$v = \sqrt{2}\sqrt{n_0}\frac{S - S_c}{\hbar}\frac{\Delta x}{\Delta n} \tag{4.18}$$

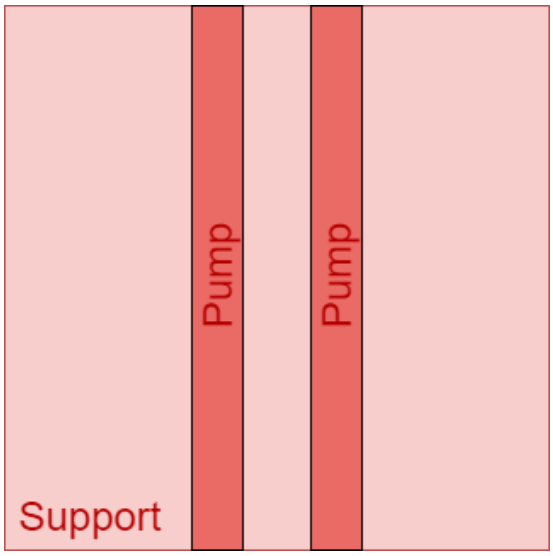

Figure 4.4: Scheme of laser profile shaping the corridor.

By estimating $\sqrt{\Delta n} \approx \sqrt{n_0} \approx S_c/\Gamma$ and taking $\Delta x = \sqrt{2}\xi$ one rewrites Eq. (4.18) as

$$v \sim 2\frac{S - S_c}{S_c}\frac{\xi}{\tau} \tag{4.19}$$

The expression (4.19) for the values used in numerical simulations gives $v = 12$ μm/ns, very close to the numerical value of 30 μm/ns for $(S - S_c)/S_c = 0.05$.

4.3 Solitons in the corridor

Next, it is instructively to consider a second high-density region with its boundary parallel to the first one, defining an all-optically controlled confining potential. Similar configuration, but without the support beam, has been studied in [56]. Fig. 4.4 sketches the spatial structure of laser profile for such situation.

One should start by the simplest case, namely by considering high density regions with the same phase and a fixed channel (corridor) width $L = 24$ μm ($\sim 13\xi$ of the high density region). Fig. 4.6 is computed at $S = 0.25S_c$ and $P = 1.25S_c$. The left panel presents the stationary intensity distribution with 2 dark solitons in the channel. The system is effectively 1D, since it is translationally invariant along Y (periodic boundary conditions). Single dark soliton is an anti-symmetric state with a π phase shift. The phase constraints imposed by the high-density regions therefore only allow an even number of solitons. Other possible explanation is that the in the case of the polaritons going from the walls to the center of the corridor, they accumulate the same phase and thus the interference in the center of the corridor is obligatory constructive giving a maximum of the density. Away from the center, the interference is destructive, favoring the density dips, consistent with the natural structure of solitons. These soliton multiplets are however unstable with respect to the development of instability along Y for a large range of parameters.

The 2D modulational instabilities in the numerical simulations can be triggered by any noise or fluctuations breaking the translational symmetry along the Y-axis. Here, a

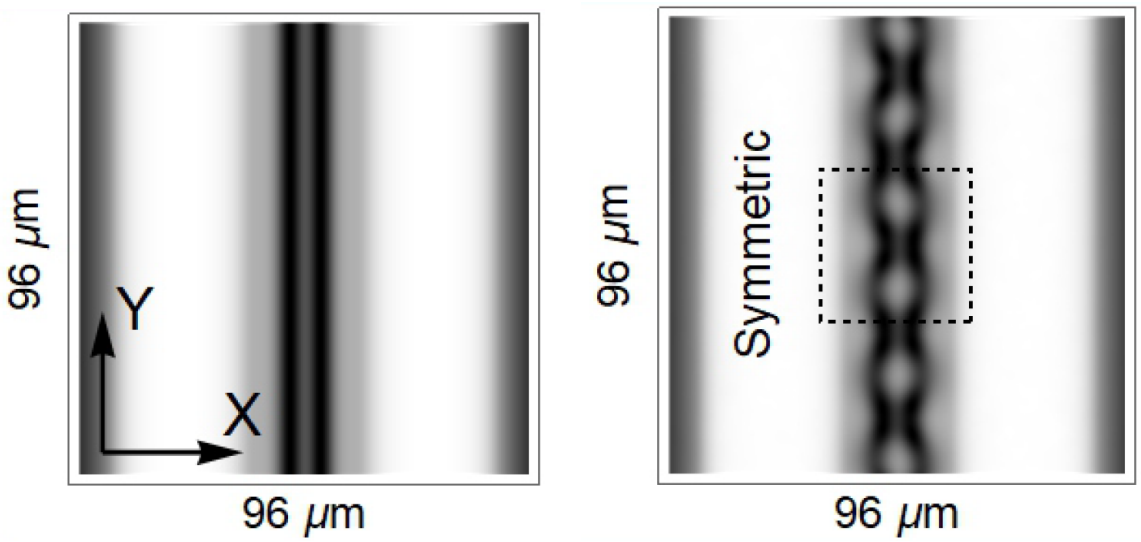

Figure 4.5: Left panel shows the initial density profile in the corridor. The problem is effectively 1D, no gradients and fluxes along the Y axis are present. After adding some disorder, the instability begins developing and finally becomes frozen in the state shown in the right panel.

weak Gaussian disorder with a correlation length of 2 μm and an amplitude $\gamma = 0.01$ meV is considered. The right panel of Fig. 4.5 shows the frozen snake instability developed from the state shown in the left panel. In practice, instability can be switched by the weakest disorder comparable with machine precision and much smaller e.g. than 1 μm in size defect of μeV amplitude situated somewhere in the corridor. For obtaining the left panel, no disorder was plugged.

4.3.1 Stability of driven-dissipative solitons in 2D

The soliton stability in the 2D driven-dissipative configuration can be analyzed using the Bogoliubov-de Gennes equations for weak excitations of the quantum fluid in the very similar manner as for the case of conservative system, which was considered in Chapter 2. Let ψ be the non-trivial solitonic solution of the driven-dissipative Gross-Pitaevskii equation written on the polariton basis:

$$i\hbar\frac{\partial\psi}{\partial t} = -\frac{\hbar^2}{2m}\Delta\psi + g|\psi|^2\psi - i\Gamma\psi + P(x,y)e^{-i\omega_0 t}. \tag{4.20}$$

Next, one can write $\psi = \psi_0(x,y)e^{-i\omega_0 t}$, and the perturbed solution is $\psi_0(x,y) + A(x)e^{i(k_y y-\omega t)} + B^*(x)e^{-i(k_y y-\omega t)}$, where ω is the perturbation frequency relative to the laser frequency ω_0 and $\psi_0(x,y)$ is the solution of the stationary equation

$$\hbar\omega_0\psi_0 = -\frac{\hbar^2}{2m}\Delta\psi_0 + g|\psi_0|^2\psi_0 - i\Gamma\psi_0 + P, \tag{4.21}$$

given in fact in the left panel of Fig. 4.5 or in the left column of Fig. 4.6). As is seen from the ansatz, if the excitiation frequency has a positive imaginary part, the amplitude of

such excitation will grow in time. Linearizing (4.20), one can obtain the Bogoliubov-de Gennes equations for coefficients A and B:

$$\begin{pmatrix} L(x,k_y)-\hbar\omega & g\psi_0^2 \\ g\psi_0^{*2} & L(x,k_y)+\hbar\omega \end{pmatrix} \begin{pmatrix} A \\ B \end{pmatrix} = \begin{pmatrix} 0 \\ 0 \end{pmatrix}, \tag{4.22}$$

where one is interested in the bogolon states confined along the X direction by the walls of the corridor. The definition

$$L(x,k_y) = -\frac{\hbar^2}{2m}\left(\frac{\partial^2}{\partial x^2} - k_y^2\right) + 2g|\psi_0|^2 - i\Gamma - \hbar\omega_0 \tag{4.23}$$

is used. The translational invariance along Y allowed to replace $-\nabla^2 \to k_y^2 - \partial^2/\partial x^2$, where k_y is the wave vector of perturbations.

One sees that with respect to conservative system, the chemical potential μ is replaced by the laser frequency in the driven-dissipative case [57, 58]. The main yield obtained from the Bogoliubov-de Gennes equations is the dependencies of the highest in $\Im\omega(k_y)$ between all modes at each value of k_y.

The value of the *maximal instability wave vector for a single soliton* can be estimated from very general reasoning. For a single state quantized in a potential trap formed by the profile of a single dark soliton, its energy (which is not yet the bogolon frequency) can be estimated as [18]:

$$-\frac{\hbar^2}{2m}\frac{\partial^2 A}{\partial x^2} + g|\psi_0|^2 A - \hbar\omega_0 A \approx -\frac{\hbar\omega_0}{2}A, \tag{4.24}$$

which supposes that the system is above the bistability threshold and that the soliton is almost dark. The diagonalization of the matrix (4.22) thus gives an equation

$$\left(\frac{\hbar^2 k_y^2}{2m} + g|\psi_0|^2 - i\Gamma - \frac{\hbar\omega_0}{2}\right)^2 - g^2|\psi_0|^4 = \hbar^2\omega^2, \tag{4.25}$$

which allows to estimate the value of the imaginary part of ω. Indeed, it is supposed that $\Gamma \ll \hbar\omega_0$, the solution for ω becomes imaginary if the real part of (4.25) is negative. Maximal imaginary part is achieved if the first square is zero and the second square is maximized, which is obtained at a point x_0 where $g|\psi_0(x_0)|^2 = \hbar\omega_0/2$, determining the maximal possible positive imaginary part of $\hbar\omega$ as

$$\Gamma_{max} = \frac{\hbar\omega_0}{2} - \Gamma. \tag{4.26}$$

In this case, the soliton is clearly always unstable, because the negative contribution to the imaginary part is much smaller than the positive one, as required for the bistability. One can conclude that 2D solitons in the driven-dissipative configuration remain unstable with respect to small perturbations, at least if they are obtained at the upper bistability branch.

This also provides a criterion for the maximal wavevector k_y of the unstable region:

$$k_y^* = \sqrt{\frac{m\omega_0}{\hbar}}. \tag{4.27}$$

which is allowed at a different point x_1, where $g|\psi_0(x_1)|^2 \approx 0$. At the upper part of the bistability curve, where $\hbar\omega_0 = gn$, this expression can be linked with the inverse of the healing length of the quantum fluid ξ:

$$k_y^* = \frac{1}{\xi\sqrt{2}}. \tag{4.28}$$

Between various solutions (eigenstates) of Eq. (4.22) the effect of *mode competition* takes place. The profile of ψ_0 acts in some sense as a potential profile for the bogolon wave function within the Schrödinger equation. If several quantized states are present in the trap with the energies E_n, the highest energy state forms the bogolon with the highest imaginary part. Indeed, the imaginary part of ω from the simplified equation

$$\hbar^2\omega^2 = \left(g|\psi_0(x)|^2 - E_n\right)^2 - g^2|\psi_0(x)|^4 \tag{4.29}$$

is due to the second term, which is negative. The minimal value of the first term is zero. It is achieved when $g|\psi_0(x)|^2 = E_n$, which determines the value of $g|\psi_0(x)|^2$, and the imaginary part is therefore simply

$$\Im(\hbar\omega) = E_n \tag{4.30}$$

measured from the energy of the bare states. Thus the conclusion on the mode competition in the trap is therefore that the highest mode in the trap always wins (developing first the instability), as soon as it is sufficiently well localized in it. A more exact result was obtained by numerical solution.

The lowest energy mode in the double-well potential formed by the soliton pair is a symmetric bound state, whereas the highest mode is an anti-symmetric anti-bound state (like bonding and antibonding orbitals in the molecules). However, the symmetry of the patterns is normally inversed (it will be seen in the 3$^{\text{rd}}$ column of Fig. 4.6), because each soliton is anti-symmetric by itself (π phase jump). An antisymmetric superposition of solitons is therefore a symmetric function, which gives rise to the symmetric pattern observed in the 2nd line of Fig. 4.6.

4.3.2 Phase diagram versus Pump and Support

The behavior (to be precise, stability and parity) of the system of solitons in the channel depends on the values of pump P and support S. Therefore, it is instructive to investigate the system varying these parameters. Some typical situations are given in Fig. 4.6. The parameters are $S = 0.25S_c$ and three different values of P are taken. The first column of Fig. 4.6 shows the initial states with straight unperturbed solitons (effectively 1D problem). The second column of Fig. 4.6 shows the highest imaginary part of the energy of the weak excitations versus their longitudinal wave vector k_y, obtained from the Bogoliubov-de Gennes equations, details on which were given in the previous subsection. The winning mode and the corresponding wave vector are shown with an arrow. The third column shows the developed and static in time frozen snake instability pattern consisting of vortex-antivortex pairs. The fourth column gives the magnification on the cores of the vortices plotted in third column and presents their phase patterns.

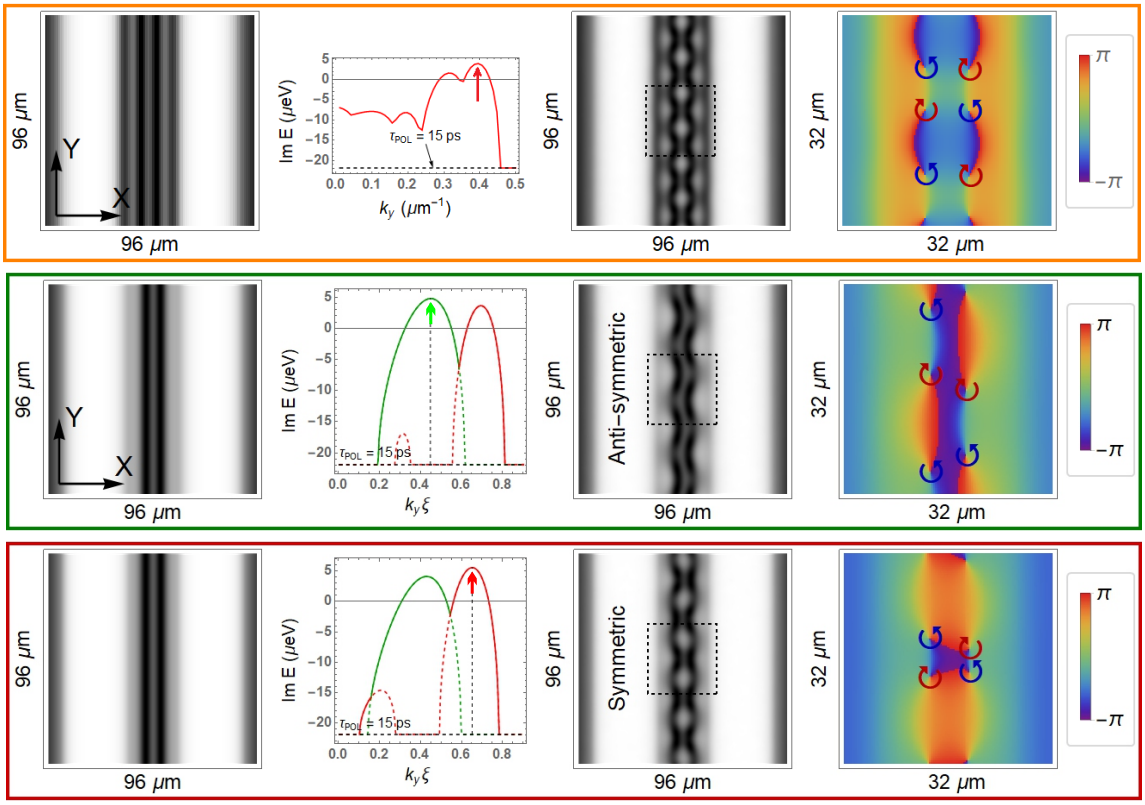

Figure 4.6: Modulational instability of guided solitons. $L = 25$ μm. $S = 0.25S_c$, $P = 0.4, 1.25, 2S_c$ (top, center, bottom rows, respectively). Columns: 1) stationary solution with even number of solitons between the high-density walls. 2) imaginary part of the energy of weak excitations of the stationary solution from the 1st column as a function of k_y. 3,4): stationary solution after the development of the modulational instability (density in 3rd column and magnification with the phase in 4th column) in the presence of weak disorder.

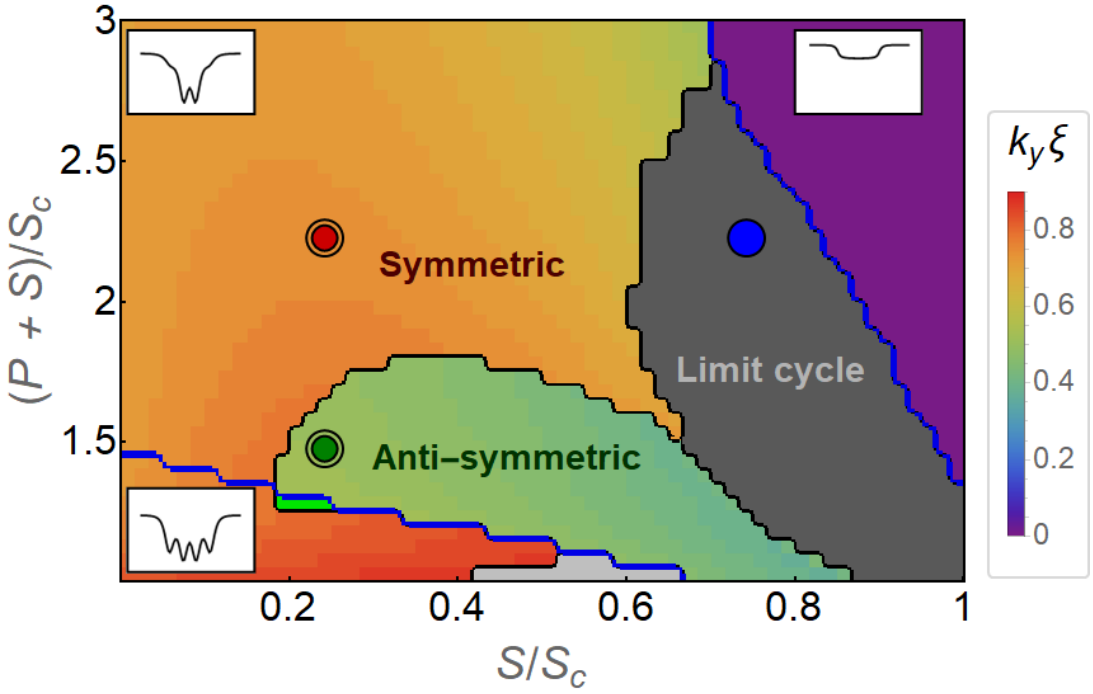

Figure 4.7: Phase diagram versus support S and pump P. The color shows the maximal instability wave vector k_y^* for each pair $(S, P + S)$. Green tones are for long period antisymmetric excitations (snakes, smaller wave vector) and orange/red tones are for symmetric excitations with shorter period. Lower left corner separated by the blue curve corresponds to the 4-soliton initial state. Dark gray area is for oscillating in time solitons and violet is for high density in channels (no solitons). Colored dots correspond to the panels in the boxes of the same color in Fig. 4.6. Blue dot is for maze pathfinding regime. The insets show the transverse profiles of unperturbed density in the channel.

Figure 4.7 shows a phase diagram obtained from the Bogoliubov-de Gennes equations-based stability analysis versus pump and support intensities (with constant L and $\hbar\omega_0$). The phase in the upper right corner (purple) corresponds to high density in the channel (no solitons or vortices). It occurs for support values typically smaller than S_c, because of the particle flow coming from the two DWs instead of one. This regime is qualitatively similar with the one of the polariton neuron picture [10]. The dark grey region corresponds to a non-stationary steady state (limit cycle), at least in the conditions of the conducted simulations, namely without energy relaxation and for sufficiently low disorder. This phase shows a pair of breathing solitons oscillating in time. The small light-grey domain corresponds to a lattice of four stable solitons. This occurs for small P and large S, so weak transverse flows which favours the soliton lattice stability. In this phase the maximal imaginary part of bogolon frequency is negative for all values of k_y. The next phase located at the bottom left corner corresponds to the collapse of 4 solitons into a symmetric pair of vortex chains (see upper row of Fig. 4.6). The two next phases located above the blue line correspond to the collapse of 2 solitons into symmetric and anti-symmetric vortex chains respectively (as in bottom and center rows of Fig. 4.6). A tiny domain (lime-green) exhibits the collapse of 4 solitons into an anti-symmetric pair of vortex chains. The false color scale of the figure shows the maximal instability wave vector k_y^* (except for the non-stationary (limit cycle) and stable phases). The anti-symmetric solutions have an approximately twice larger period than the symmetric ones. The k_y^* gradient within a given phase is relatively small, which means that the patterns visibility should not be strongly affected by pump/support intensity fluctuations in a real experiment. Disorder broadens the transitions between the phases, but the core regions remain well defined, see next subsection for details.

The precise realization of the disorder determines the positioning (in fact due to the pinning) of the pattern along Y, but does not affect the shape (parity and wave vector k_y), at least if the disorder amplitude is sufficiently small: $\gamma \ll \hbar\omega_0$. Additional simulations shown in the corresponding subsection confirm that these stationary patterns are accessible considering realistic disorder parameters up to 0.1 meV. In all cases, the solitons break into two vortex anti-vortex chains, which can be seen as stationary vortex streets. 2D analysis confirms the stability of the final patterns. It means that the snake instability develops, but is then frozen by the presence of the confining potential.

4.3.3 Effects of disorder on phase diagram

Disorder can lead to the vanishing of all the interesting effects by destroying solitons and vortex pairs, but it is always present in the real samples and, moreover, the disorder is the thing that switches on the instability by the breaking of the translational invariance in the direction along the channel. In the absence of disorder, no transformation from solitons to vortex street occurs in the simulations. In experiments, the patterns arising from the development of the instability are affected in space by the pinning induced by the disorder [59].

When disorder is present, the patterns are not as regular as in a quasi-ideal case, which complicates the analysis of the obtained states. One can nevertheless discriminate a symmetric and an anti-symmetric pattern using the standard deviation of the X coordinate

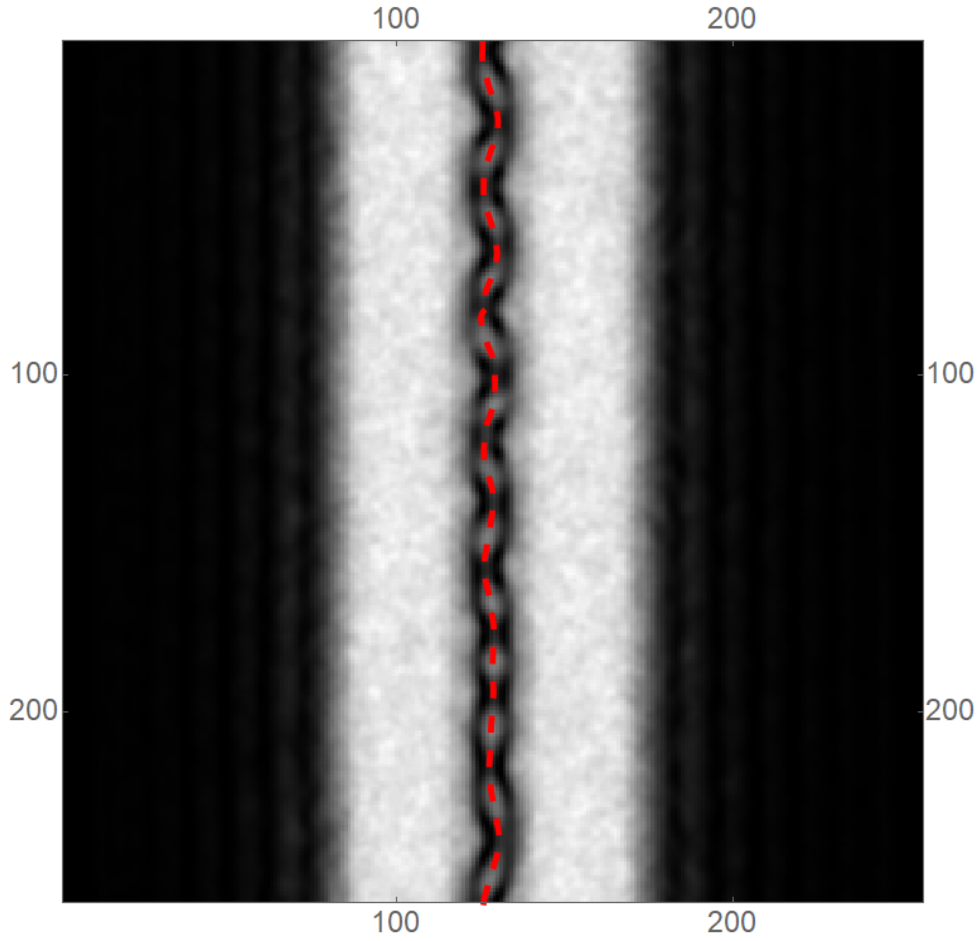

Figure 4.8: Tracing of the center $X_c(y)$ for the central left inset of Fig. S8. The concurrence of the symmetric and anti-symmetric modes is well visible and affected by spatial realization of a disorder with dominating of the wave vectors from various ranges.

of the solitons mass center $X_c(y)$. This deviation reads $\langle \Delta^2 \rangle = \left\langle (X_c(y) - \langle X_c(y) \rangle_y)^2 \right\rangle_y$, where $\langle \rangle_y$ means averaging over the Y coordinate (vertical axis). For symmetric patterns, the center is nearly aligned vertically, while for the anti-symmetric patterns the center undergoes sinusoidal trajectory and thus the deviation is larger, see Fig. 4.8. Computing or measuring experimentally this quantity allows to clearly distinguish different phases, as shown in the insets of Fig. 4.9.

Large disorder should lead to a smoothing of the phase diagram. To test the robustness of the phases obtained based on the Bogoliubov-de Gennes equations discussed in previous subsection with respect to the disorder, an alternative phase diagram (Fig. 4.9) where the disorder amplitude is 0.1 meV (as compared with 0.01 meV in the previous one) was plotted. The limit cycle with oscillating solitons can still persist in the presence of disorder. This motion results in their broadening and "shallowing", as clearly seen in the right inset of Fig. 4.9. Importantly, the disorder can also suppress the motion of the solitons and thus the limit cycle phase region becomes much smaller with stronger disorder. This diagram was calculated with newly randomly generated noise for each pair (S, P), which enhances the sampling.

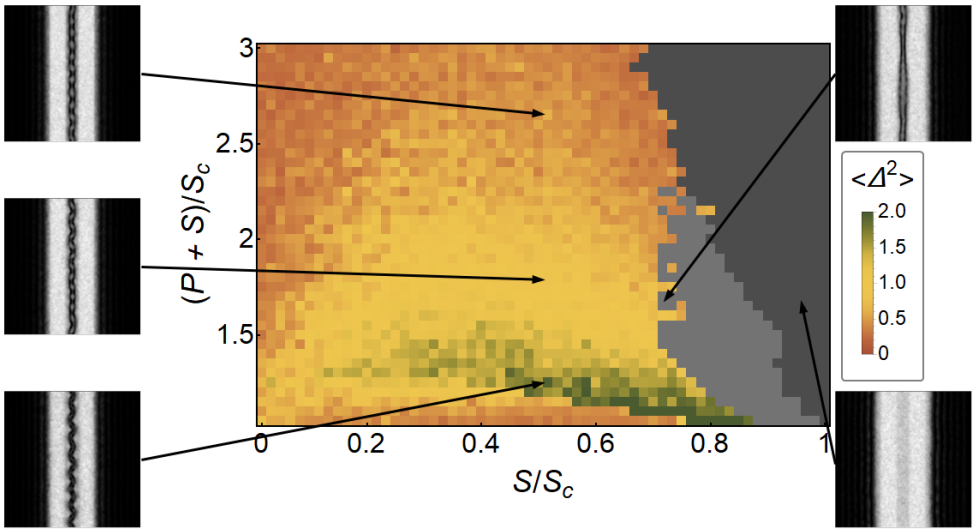

Figure 4.9: Phase diagram obtained by simulations with disorder. Color shows the standard deviation of center between the solitons $X_c(y)$. Light gray area corresponds to limit cycle phase with no solution stationary in time. Dark gray shows the no-soliton phase with the full filling of the channel with polaritons.

Within the same disorder-based technique (not based on the Bogoliubov-de Gennes equations) the case of the corridor walls situated closer to each other was considered. Fig. 4.10 shows the phase diagram for the corridor of lower size (16 μm). One sees that the region, where the frozen modulational instability exists, is sufficiently contracted with respect to wide corridor (gray and blue areas correspond to a filled channel or a stable system).

4.3.4 Solitons under π phase shift

In previous subsections, the results obtained when the phase of the pumping laser is homogeneous in space, and only the density profile is varying (allowing to obtain the high-density walls), were shown. Another interesting possibility offered by this driven-dissipative system is to tune the relative phase of the pump between the walls, which is a generalization of Ref. [60] to 2D. In this subsection, the additional results concerning the formation of solitons and their stability for a π phase difference between the pump at the walls will be presented. In this case, no support is used (otherwise it would exhibit different interference with the two pumping lasers of different phase). In such a case, an odd number of solitons forms, decaying into the same number of chains of vortex-antivortex pairs.

Figure 4.11 shows the results obtained in this configuration, with top and bottom rows corresponding to two different values of the pump P. The first column shows the spatial density profile with 3 or 1 solitons, depending on the distance available for them because of the pump-induced broadening of the walls. The second column shows the imaginary part of the energy obtained from the Bogoliubov-de Gennes analysis as described above. Both curves exhibit a maximum with positive imaginary part, confirming the existence of modulational instability. The final stage of the development of this instability is shown

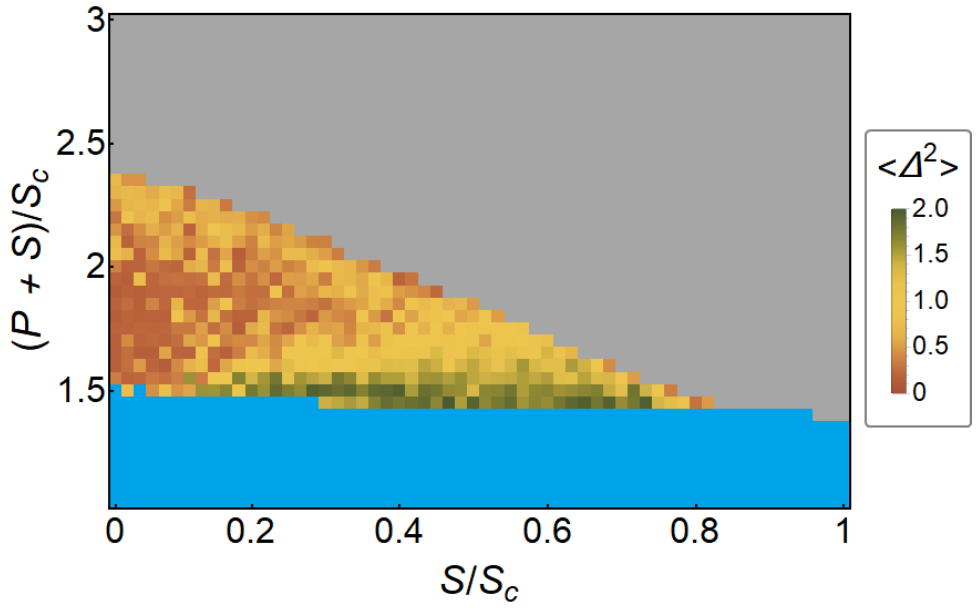

Figure 4.10: Phase diagram obtained by simulations with disorder for the corridor of 16 μm width.

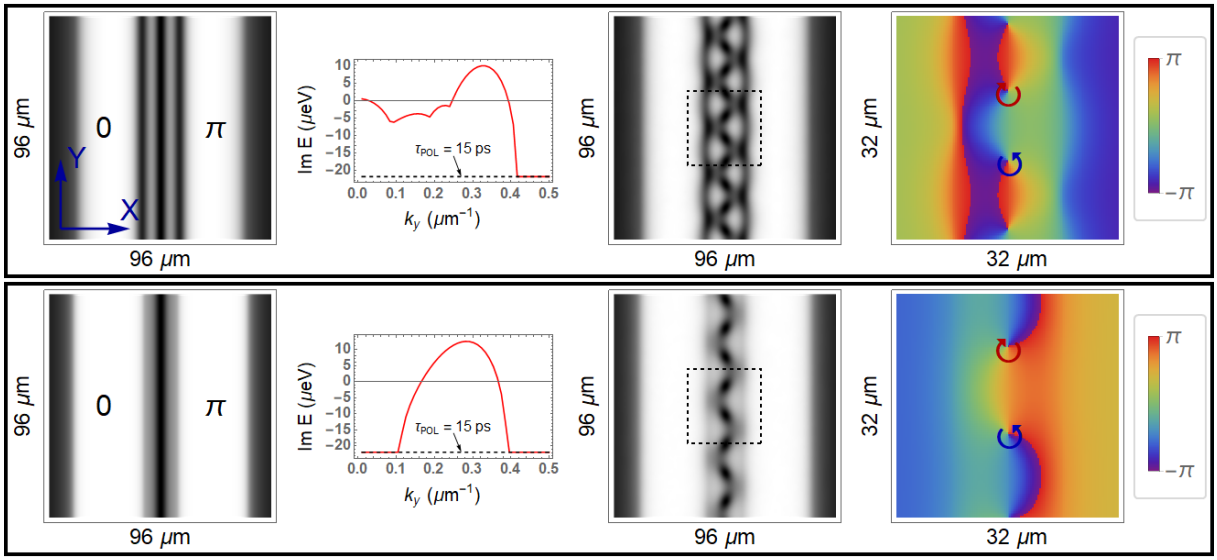

Figure 4.11: Modulational instability of guided solitons with a π phase shift between the walls. $L = 15$ μm, $P = 0.8, 1.2S_c$. (top, bottom). Columns: 1) stationary solution with even number of solitons between the high-density walls. 2) imaginary part of the energy of weak excitations of the stationary solution from the 1st column as a function of k_y. 3,4): stationary solution after the development of the modulational instability (density, phase) in the presence of weak disorder.

in the 3rd column: it exhibits either 3 vortex chains or a single vortex chain. Finally, the phase distribution shown in the 4th column confirms the formation of vortices and anti-vortices evidenced by the density shown in the 3rd column.

4.4 Maze solving property

4.4.1 Soliton head in a maze as a domain wall

In previous sections of the chapter (in contrast with present section) a system infinite in the Y direction (implemented by periodic boundary conditions) was considered. The geometry that is addressed now is a 2D maze of 1D channels [Fig. 4.12(a,b)]. For a proper value of (S, P), immediately after the jump of the walls on the upper branch, the maze is filled with solitons. However, the dead ends represent a configuration different from that of Fig. 4.5 and Fig. 4.6: the heads of the vortex streets start to withdraw. Fig 4.12(a) shows the intensity distribution 20 ps after driving pump and support are switched on (blue circle in Fig. 4.7 in the non-stationary/limit cycle phase). The heads are moving in the directions symbolized by the arrows. Fig 4.12(b) shows the final intensity distribution ($t = 1$ ns), where the street only connects the two exits of the maze. A zoom on the vortex street head is shown in Fig. 4.12(c).

This head is also a domain wall, but the conditions for its motion are different from the lateral DW in an open 1D channel that were considered previously. Indeed, the motion of the head-DW along X is facilitated by the confinement and the flow along Y coming from the two lateral walls. When the head-DW arrives at a cross-roads, an open 1D channel geometry is restored and the DW stops. Fig. 4.12(d) shows the critical support intensity for the motion of the two types of DW (dead and open ends correspond to blue and red colors, respectively). Both decrease when the corridor becomes narrower, tending to zero for $L \approx 14$ μm. This is the minimal width of a finite quantum well (of 0.14 meV depth, given by the laser detuning), where the two-node state can exist for such particle mass.

As expected, there is a substantial support range where the head-DW propagates, whereas an open 1D corridor remains stable. Within this range, this configuration represents an optical maze solver. The head-DW motion can be affected by disorder, but being an extended object, it is less sensitive than vortices which easily pin on defects [22]. Numerical simulations show that disorder trapping can be avoided by working at higher detunings $\hbar\omega_0 > 3\gamma$ and, if necessary, shorter lifetimes, making the effects observable in realistic systems.

As mentioned above, this soliton "head" can be considered as a vertical domain wall between the domains. This wall is between a high-density region (the wall limiting the dead end) and a low-density region (the region with solitons). There are now 3 domain walls in the system: two of them (horizontal) are opposite to each other, whereas one (vertical, see Fig. 4.13) can propagate, depending on the conditions. The extra kinetic energy appearing because of the variation of the wavefunction in the transverse direction (vertical), absent in the infinite system (for a very large channel), changes the conditions of the local bistability loop. The flows toward the low density region are also larger and both effects together (kinetic energy and flows) make the low-density regime impossible for the same parameters for which it was possible in the infinite system. The domain

wall starts to propagate, leading to the expansion of the high-density region, erasing progressively the solitons in the channel.

Figure 4.14 plots the velocity of the "soliton head" (blue line) as a function of the Support in the 24 μm channel for the same value of the pump which was used in the maze solving regime (see Fig. 3). One sees a behavior very similar to the "pure" domain wall from Fig.4.2 (replotted as a black line), but shifted to much smaller values of S. This shift is due to the confinement of the domain wall in the transverse direction (vertical) and to the extra flows from the walls of the channel (shown in Fig. 4(c) of the main text).

To elucidate the contribution of these two effects, one can use an additional phase diagram (Fig. 4.16), showing for a single channel having a dead end the boundary between the two cases (solitons or high density in the channel) versus the channel width L and the support amplitude S. The boundary between the two cases in shown in Fig. 4(d) of the main text. It is well described by an inverse square function with a single-parameter fit:

$$\frac{S}{S_c} = 1 - \frac{L_0^2}{L^2} \tag{4.31}$$

giving $L_0 = 13.9 \pm 0.1$ μm. This is the narrowest channel width where a pair of solitons can exist without support. The inverse square dependence is typical for a quantity depending on the confinement energy, and the value of $L \approx 14$ μm corresponds to the minimal width of a finite quantum well (with its depth of 0.14 meV given by the laser detuning) where the two-node state can be confined for such particle mass (accounting for the finite broadening due to the lifetime). For a wider channel, the kinetic energy of the two-node state is lower, and the support and the flows shift it upwards via the interactions. The inverse square law holds well up to $L = 30$ μm, which is larger than the channel width used for the main phase diagram (24 μm). For even larger channels, the dependence becomes more complicated, because the low-density solution can contain more than 2 solitons, depending on L. The detailed study of this dependence is beyond the scope of the present work.

Noteworthy, Fig. 4.12 (d) plots the threshold support intensity versus the channel width for an open-end system, which exhibits higher values than for the dead end case as previously explained. Interestingly, the provided simulations show that in a large open-end channel the threshold support can even be larger than S_c. Indeed, in such case the lateral walls start to propagate towards the center where a 4-soliton structure forms. This structure is quite stable and produces a quantum pressure, which counteracts the pressure of the interactions and blocks the motion of the walls even if S is slightly larger than S_c. One should take into account that the fact that the threshold for the open end channels is higher than for a dead end channel, is what allows the head domain wall to withdraw from from the dead ends, but to stop at the crossroads, and therefore the maze solving process.

It is possible to plot the phase diagram (in the same Pump and Support coordinates as in Fig. 4.7) that indicates the situation of the successful or not maze solving. Fig. 4.15 shows the relevant data. One sees that the region where the maze is successfully solved, indeed well corresponds to the domain of the limit-cycle regime from Fig. 4.7 and Fig. 4.9.

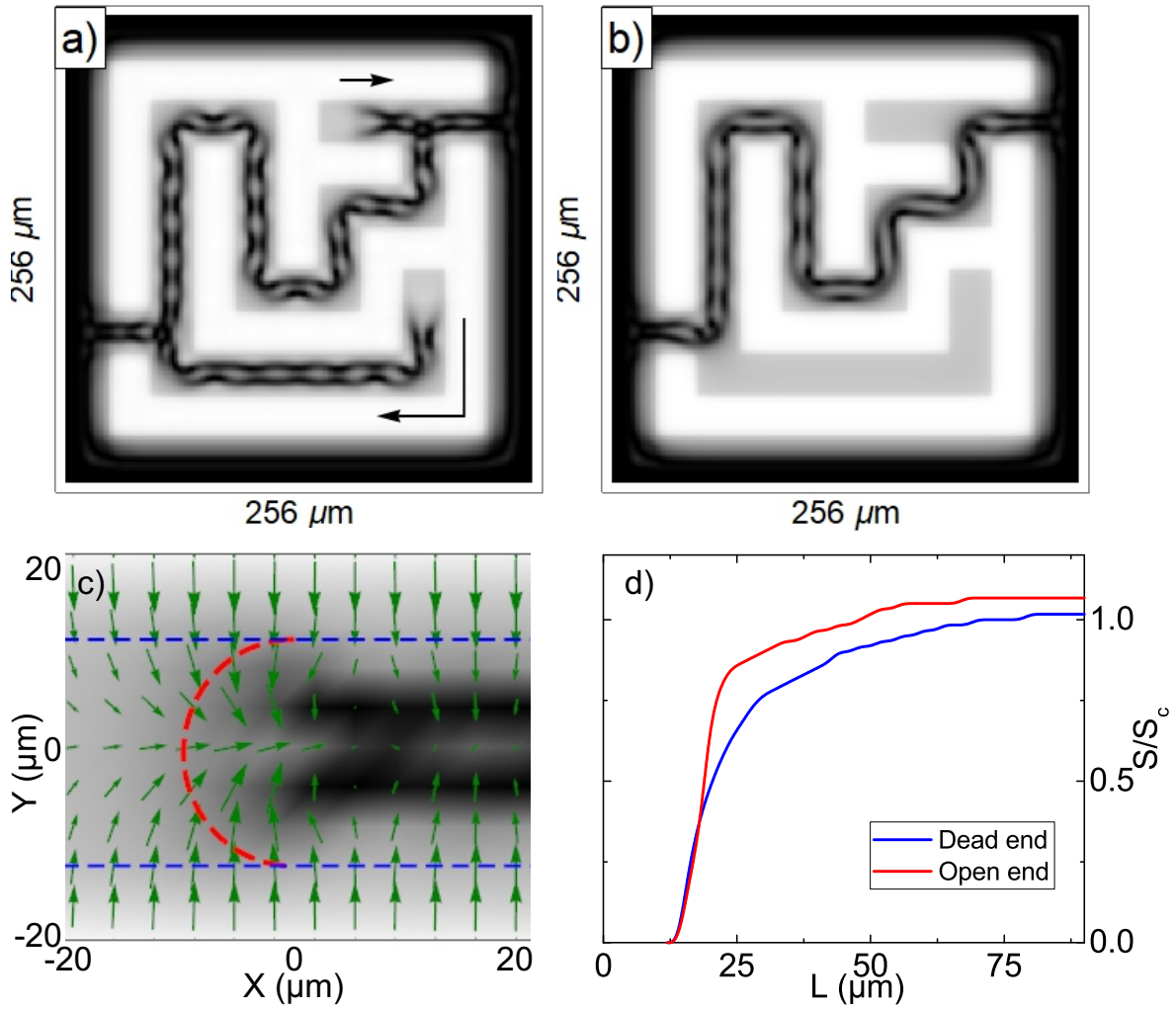

Figure 4.12: Maze solving: a) initial moments: soliton heads repelled from dead ends; b) shows the stationary final distribution (maze solved); c) DW repelled from the dead end: confinement and particle flows; d) Support threshold vs channel width for dead end (blue) and open end (red).

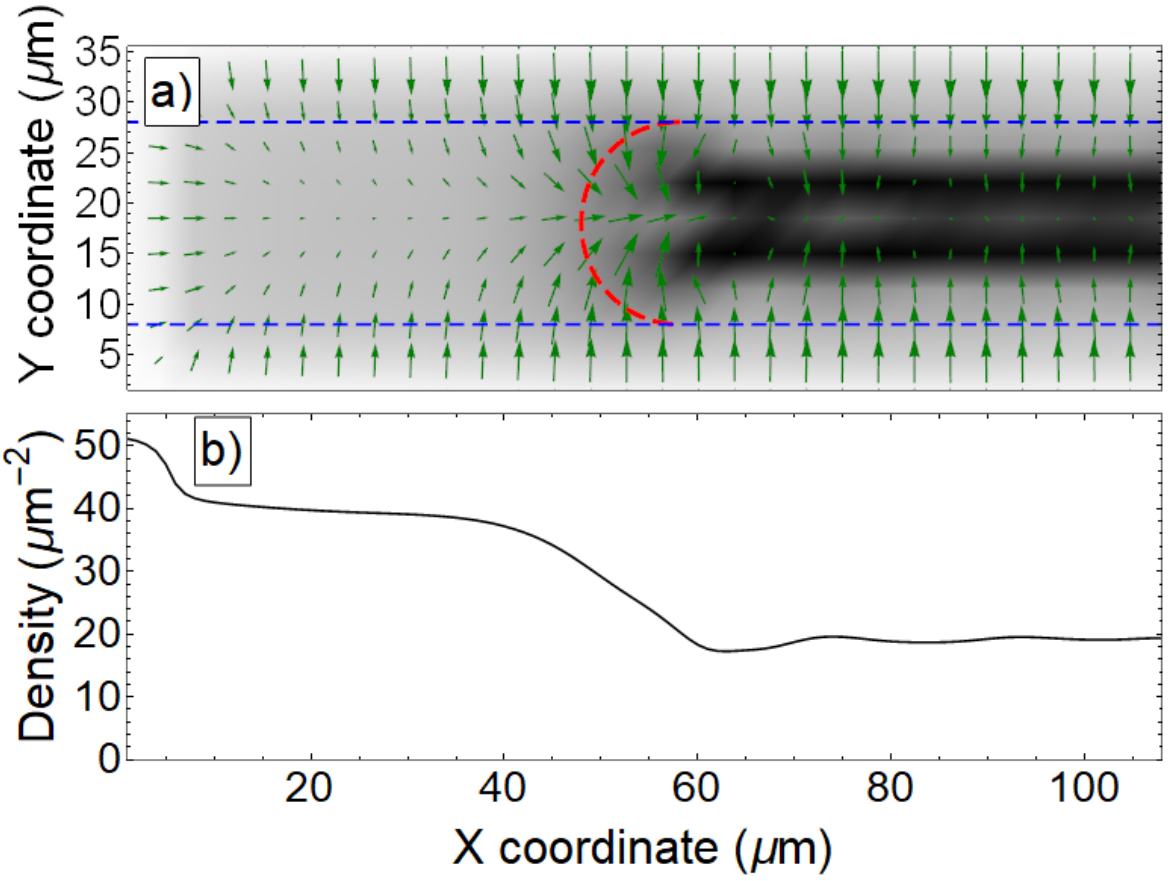

Figure 4.13: "Head of a soliton" at higher horizontal scale. Panel a). 2D map of polariton density together with the fluxes in the the quantum fluid. The corridor dead end is visible from 50 to approx. 60 micrometers on the left. Red dashed semi-circle sketches the domain wall curved profile. Panel b). Profile of polarion density averaged over Y direction (between the blue dashed horizontal lines). The domain wall corresponding to "soliton head" is clearly visible as abrupt jump of the mean density in the corridor from 40 to 60 micrometers.

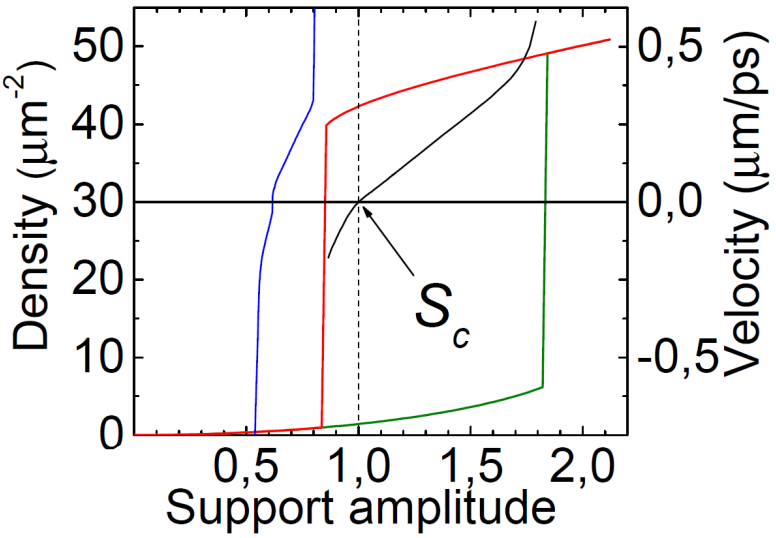

Figure 4.14: Velocity of DW in the 24 μm channel (blue curve) together with free DW velocity. Maze solving regime is realized in the velocity range from 0 to $\approx 0.2\mu$m/ps. The bistability curve of a homogeneous system is plotted for a reference.

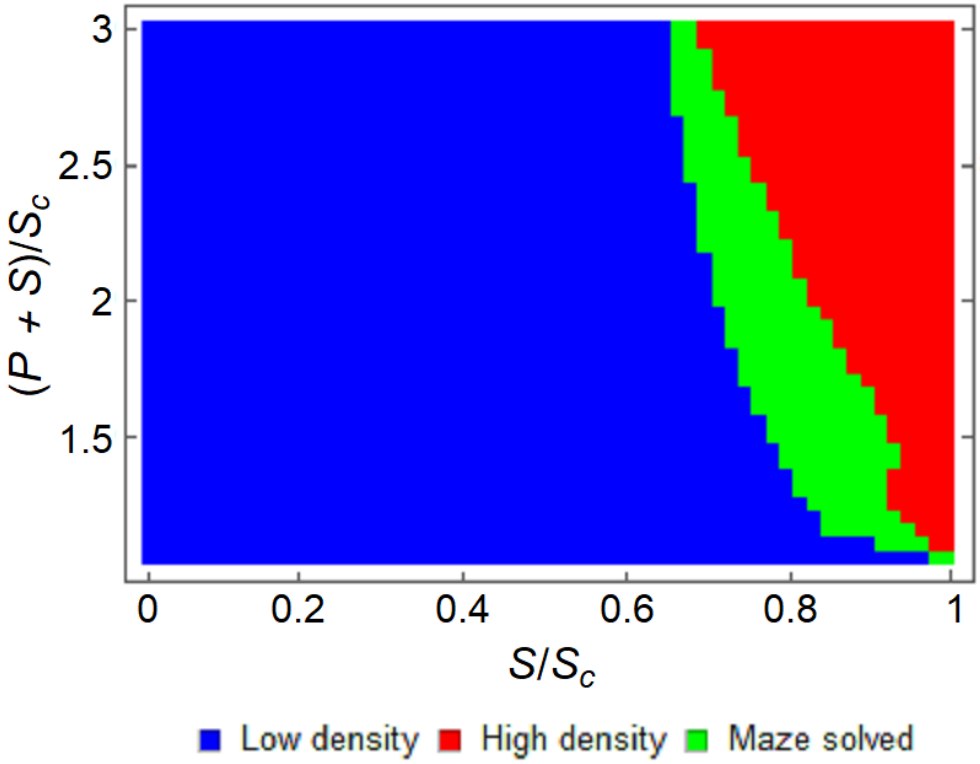

Figure 4.15: Phase diagram of maze solving. The legend corresponds to the situation (in fact the density) in the corridor, the walls are always at upper bistability branch.

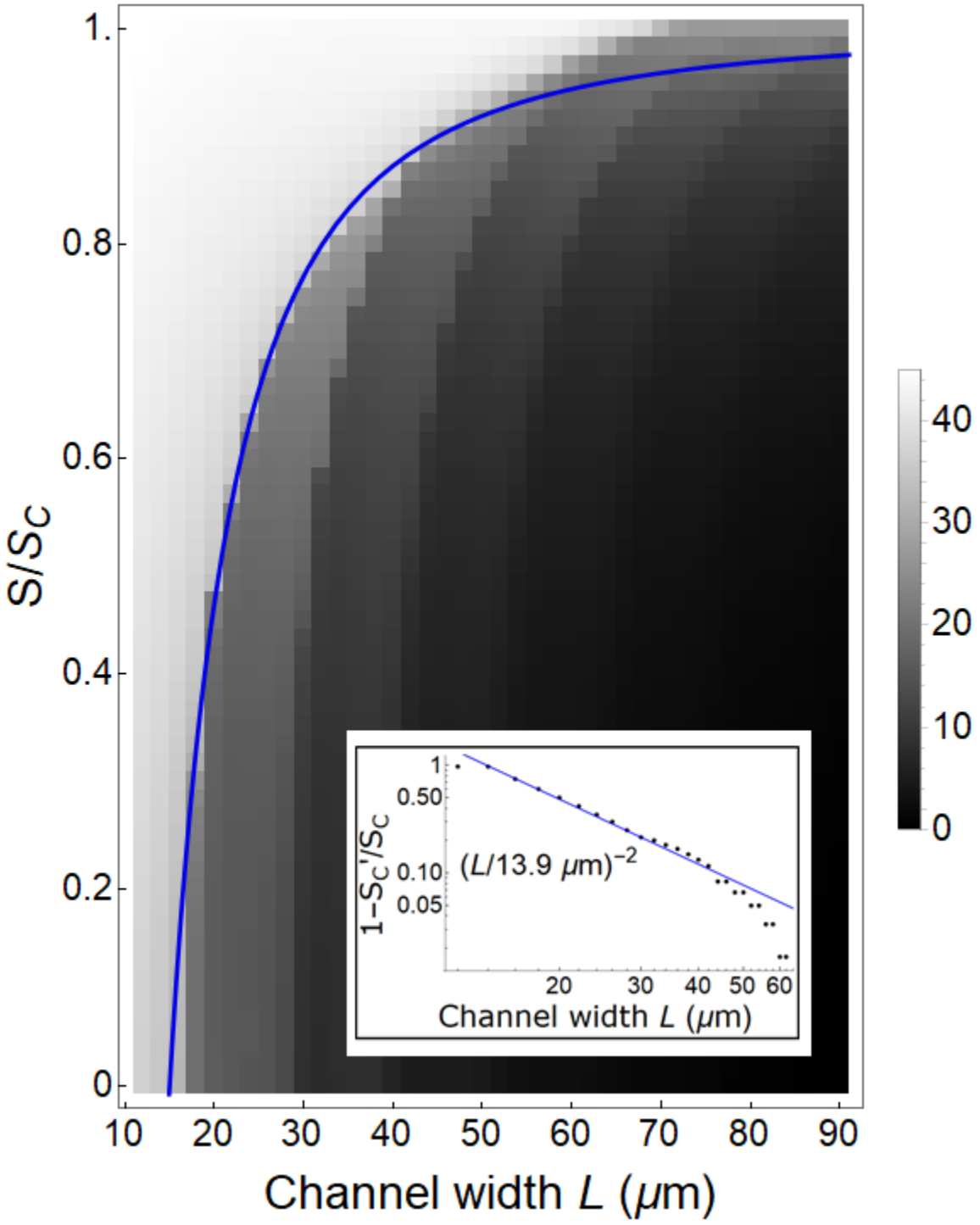

Figure 4.16: Mean polariton density in the corridor as a function of corridor width and support level S. Light grey area in upper left corner corresponds to full filling the corridor with polaritons (repulsion of a dead end). Blue curve shows the inverse square fit $S/S_c = 1 - L_0^2/L^2$. The extracted values of $1 - S/S_c$ and their fit for $L < 30$ μm in log-log scale are shown in the inset.

Figure 4.17: The maze of differing topology that can be solved by the proposed analog algorithm. The common feature of the topologies is the path connecting the extensive low density regions (regions far from the walls of pump).

4.4.2 Different maze topologies, size scaling, disorder effects, speed of the maze solving

The main property of the vortex street repelled from the dead end is thus to connect the areas with low density from which the repulsion does not take place. Thus one can change the *topology* of the maze and also to obtain it solved. E.g. one can implement the topology with the extensive enough central region, a path from which should be found to the exterior of the maze. Fig. 4.17 shows the example of such a maze successfully solved. Also, one can sufficiently increase the linear size of the maze without losing the maze-solving property. Fig. 4.18 shows the solution of a maze of 1000 μm in size. Practically, the size of the maze that can be solved is limited by the coherence length of the quantum fluid and by the possibilities of the optics of the experimental setup to properly focus and maintain the homogeneous spatial profile of the laser.

In presence of a larger (an more realistic for numerous samples) *disorder* the detuning has to be increased to overcome its effect. Fig. 4.19 is computed for a disorder of 0.1 meV and justifies that the maze solving property remains in such conditions. To avoid disorder disturbance, all parameters (detuning, lifetime, pump and support intensity) were modified, in order for the kinetic and interaction energies to be at least 3 times larger than the disorder amplitude. One should note that the used parameters are perfectly

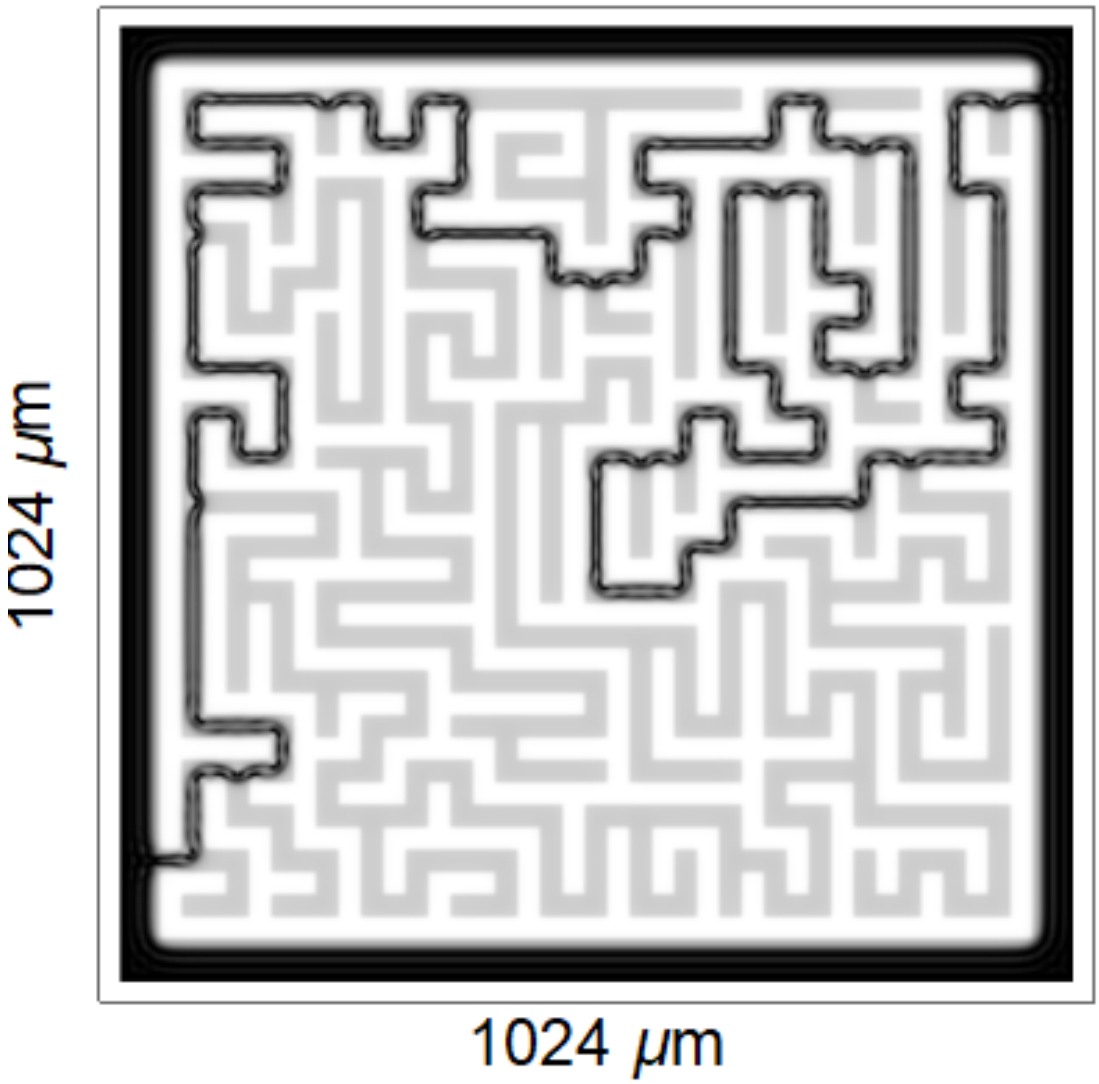

Figure 4.18: Scaling of the maze solving scheme up to 1024 μm size of the maze.

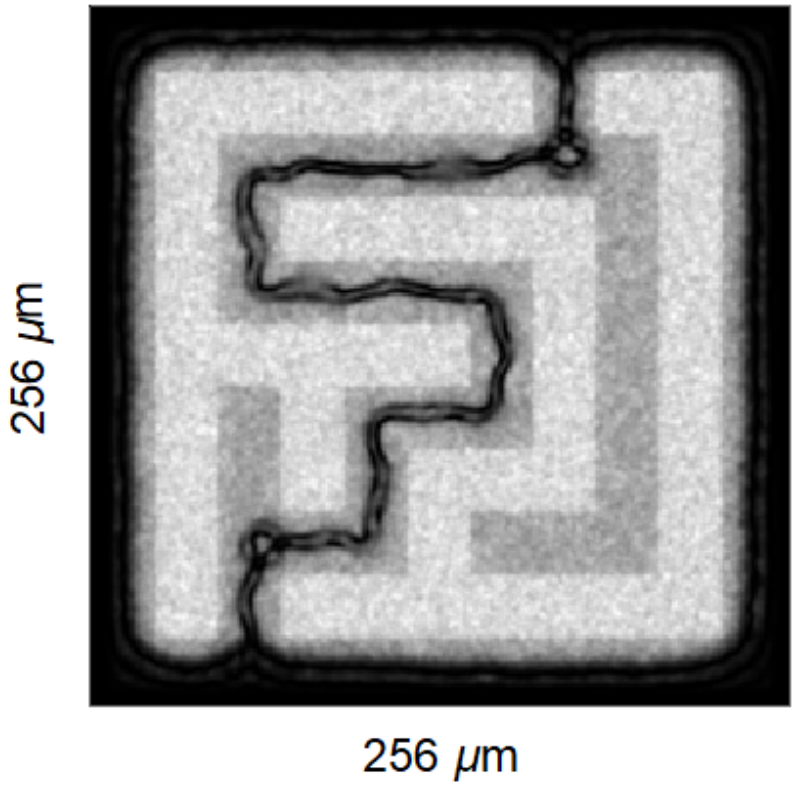

Figure 4.19: The maze solved at disorder of 0.1 meV. The other parameters have been increased with respect to the one used in the main text, namely detuning 3.2 times larger (0.45 meV), lifetime 3.2 times smaller (4.7 ps), and laser intensity 7 times larger, support $S \approx 5S_c$ and channel walls $P + S \approx 16S_c$.

accessible experimentally. As one can see, the maze remains well defined and is solved, despite the disorder value.

The *solving time* is determined by the velocity v of the head-DW, see Fig. 4.14. In the worst case, the length of the dead end is NL, where N is the number of cells in the maze (or vertices in the graph) and L is the width of a channel. If Z is the overall system size, the maximal number of cells is $N = Z^2/L^2$. The solving time is therefore $t = NL/v$. The best among the other maze solving (pathfinding) algorithms [61] such as the Depth-First Search also exhibit the worst-case complexity of $O(N)$, but the practical advantage of the present analog implementation is the small value of the prefactor $L/v \sim 0.5$ ns: the high velocity v reduces the solving time, allowing such an analog maze solver to outperform a modern PC which needs hundreds of clock ticks to check a single cell.

4.5 Conclusions

To conclude, in this chapter I have shown that the modulational instability can be controlled and stabilized in a driven-dissipative polariton system allowing the on-demand formation of soliton molecules and vortex streets exhibiting a particularly rich phase diagram for various levels of pump and support laser beams. The symmetric and anti-symmetric phases exist for various values of these parameters. The development of instability was analyzed both with the Bogiliubov-de Gennes equation (linearization of stationary GPE) and using the complete simulation of DDGPE in presence of the disorder that in fact switches on the development of the bistability. In some regimes the limit-cycle behavior take place.

The non-stationary regimes can be used for fast analog maze solving. The demonstrated property of all-optical maze solving is important for the large interdisciplinary field of analog graph solving algorithms.

Bibliography

[1] J. Kasprzak, M. Richard, S. Kundermann, A. Baas, P. Jeambrun, J. Keeling, F. Marchetti, M. Szymańska, R. Andre, J. Staehli, *et al.*, "Bose–einstein condensation of exciton polaritons," *Nature*, vol. 443, no. 7110, p. 409, 2006.

[2] A. Kavokin and G. Malpuech, *Cavity polaritons*, vol. 32. Elsevier, 2003.

[3] I. Carusotto and C. Ciuti, "Quantum fluids of light," *Rev. Mod. Phys.*, vol. 85, pp. 299–366, Feb 2013.

[4] D. Bajoni, P. Senellart, E. Wertz, I. Sagnes, A. Miard, A. Lemaître, and J. Bloch, "Polariton laser using single micropillar gaas- gaalas semiconductor cavities," *Physical review letters*, vol. 100, no. 4, p. 047401, 2008.

[5] T. Ozawa, H. M. Price, A. Amo, N. Goldman, M. Hafezi, L. Lu, M. C. Rechtsman, D. Schuster, J. Simon, O. Zilberberg, *et al.*, "Topological photonics," *Reviews of Modern Physics*, vol. 91, no. 1, p. 015006, 2019.

[6] A. Gianfrate, O. Bleu, L. Dominici, V. Ardizzone, M. De Giorgi, D. Ballarini, G. Lerario, K. West, L. Pfeiffer, D. Solnyshkov, *et al.*, "Measurement of the quantum geometric tensor and of the anomalous hall drift," *Nature*, vol. 578, no. 7795, pp. 381–385, 2020.

[7] D. Solnyshkov, H. Flayac, and G. Malpuech, "Black holes and wormholes in spinor polariton condensates," *Physical Review B*, vol. 84, no. 23, p. 233405, 2011.

[8] D. Solnyshkov, C. Leblanc, S. Koniakhin, O. Bleu, and G. Malpuech, "Quantum analogue of a kerr black hole and the penrose effect in a bose-einstein condensate," *Physical Review B*, vol. 99, no. 21, p. 214511, 2019.

[9] N. G. Berloff, M. Silva, K. Kalinin, A. Askitopoulos, J. D. Topfer, P. Cilibrizzi, W. Langbein, and P. G. Lagoudakis, "Realizing the classical XY hamiltonian in polariton simulators," *Nature Materials*, vol. 16, p. 1120, 2017.

[10] T. C. H. Liew, A. V. Kavokin, and I. A. Shelykh, "Optical circuits based on polariton neurons in semiconductor microcavities," *Phys. Rev. Lett.*, vol. 101, p. 016402, Jul 2008.

[11] C. Shannon, "Presentation of a maze solving machine," in *Trans. 8th Conf. Cybernetics*, p. 169, 1951.

[12] O. Steinbock, A. Toth, and K. Showalter, "Navigating complex labyrinths - optimal paths from chemical waves," *Science*, vol. 267, pp. 868–871, FEB 10 1995.

[13] F. Caruso, A. Crespi, A. G. Ciriolo, F. Sciarrino, and R. Osellame, "Fast escape of a quantum walker from an integrated photonic maze," *Nature Comm.*, vol. 7, JUN 2016.

[14] A. Nair, K. Raghunandan, V. Yaswant, S. S. Pillai, and S. Sambandan, "Maze solving automatons for self-healing of open interconnects: Modular add-on for circuit boards," *Applied Physics Letters*, vol. 106, no. 12, p. 123103, 2015.

[15] J. Chao, J. Wang, F. Wang, X. Ouyang, E. Kopperger, H. Liu, Q. Li, J. Shi, L. Wang, J. Hu, L. Wang, W. Huang, F. C. Simmel, and C. Fan, "Solving mazes with single-molecule DNA navigators," *NATURE MATERIALS*, vol. 18, pp. 273+, MAR 2019.

[16] A. Adamatzky, A. Chiolerio, and K. Szacilowski, "Liquid metal droplet solves maze," *SOFT MATTER*, vol. 16, pp. 1455–1462, FEB 14 2020.

[17] N. Bogoliubov, "On the theory of superfluidity," *J. Phys*, vol. 11, no. 1, p. 23, 1947.

[18] L. Pitaevskii and S. Stringari, *Bose-Einstein Condensation*. Oxford Science Publications - International Series of Monographs on Physics 116, 2003.

[19] E. P. Gross, "Structure of a quantized vortex in boson systems," *Il Nuovo Cimento (1955-1965)*, vol. 20, no. 3, pp. 454–477, 1961.

[20] R. Hivet, E. Cancellieri, T. Boulier, D. Ballarini, D. Sanvitto, F. M. Marchetti, M. H. Szymanska, C. Ciuti, E. Giacobino, and A. Bramati, "Interaction-shaped vortex-antivortex lattices in polariton fluids," *Phys. Rev. B*, vol. 89, p. 134501, Apr 2014.

[21] T. Boulier, H. Terças, D. Solnyshkov, Q. Glorieux, E. Giacobino, G. Malpuech, and A. Bramati, "Vortex chain in a resonantly pumped polariton superfluid," *Scientific reports*, vol. 5, p. 9230, 2015.

[22] K. G. Lagoudakis, T. Ostatnický, A. V. Kavokin, Y. G. Rubo, R. André, and B. Deveaud-Plédran, "Observation of half-quantum vortices in an exciton-polariton condensate," *Science*, vol. 326, no. 5955, pp. 974–976, 2009.

[23] K. G. Lagoudakis, M. Wouters, M. Richard, A. Baas, I. Carusotto, R. André, L. S. Dang, and B. Deveaud-Plédran, "Quantized vortices in an exciton–polariton condensate," *Nature physics*, vol. 4, no. 9, pp. 706–710, 2008.

[24] S. Pigeon, I. Carusotto, and C. Ciuti, "Hydrodynamic nucleation of vortices and solitons in a resonantly excited polariton superfluid," *Phys. Rev. B*, vol. 83, p. 144513, Apr 2011.

[25] A. Amo, S. Pigeon, D. Sanvitto, V. Sala, R. Hivet, I. Carusotto, F. Pisanello, G. Leménager, R. Houdré, E. Giacobino, *et al.*, "Polariton superfluids reveal quantum hydrodynamic solitons," *Science*, vol. 332, no. 6034, pp. 1167–1170, 2011.

[26] R. Hivet, H. Flayac, D. D. Solnyshkov, D. Tanese, T. Boulier, D. Andreoli, E. Giacobino, J. Bloch, A. Bramati, G. Malpuech, and A. Amo, "Half-solitons in a polariton quantum fluid behave like magnetic monopoles," *Nat Phys*, vol. 8, pp. 724–728, oct 2012.

[27] G. A. El, A. Gammal, and A. M. Kamchatnov, "Oblique dark solitons in supersonic flow of a bose-einstein condensate," *Phys. Rev. Lett.*, vol. 97, p. 180405, Nov 2006.

[28] Y. S. Kivshar and D. E. Pelinovsky, "Self-focusing and transverse instabilities of solitary waves," *Physics Reports*, vol. 331, no. 4, pp. 117 – 195, 2000.

[29] Z. Dutton, M. Budde, C. Slowe, and L. V. Hau, "Observation of quantum shock waves created with ultra- compressed slow light pulses in a bose-einstein condensate," *Science*, vol. 293, no. 5530, pp. 663–668, 2001.

[30] A. M. Kamchatnov and L. P. Pitaevskii, "Stabilization of solitons generated by a supersonic flow of bose-einstein condensate past an obstacle," *Phys. Rev. Lett.*, vol. 100, p. 160402, Apr 2008.

[31] P. M. Walker, L. Tinkler, B. Royall, D. V. Skryabin, I. Farrer, D. A. Ritchie, M. S. Skolnick, and D. N. Krizhanovskii, "Dark solitons in high velocity waveguide polariton fluids," *Phys. Rev. Lett.*, vol. 119, p. 097403, Aug 2017.

[32] E. Wertz, L. Ferrier, D. Solnyshkov, R. Johne, D. Sanvitto, A. Lemaître, I. Sagnes, R. Grousson, A. V. Kavokin, P. Senellart, *et al.*, "Spontaneous formation and optical manipulation of extended polariton condensates," *Nature physics*, vol. 6, no. 11, p. 860, 2010.

[33] E. Wertz, A. Amo, D. D. Solnyshkov, L. Ferrier, T. C. H. Liew, D. Sanvitto, P. Senellart, I. Sagnes, A. Lemaître, A. V. Kavokin, G. Malpuech, and J. Bloch, "Propagation and amplification dynamics of 1d polariton condensates," *Phys. Rev. Lett.*, vol. 109, p. 216404, Nov 2012.

[34] G. Lerario, S. V. Koniakhin, A. Maître, D. Solnyshkov, A. Zilio, Q. Glorieux, G. Malpuech, E. Giacobino, S. Pigeon, and A. Bramati, "Parallel dark soliton pair in a bistable 2d exciton-polariton superfluid," *arXiv preprint arXiv:2003.11408*, 2020.

[35] A. Maître, G. Lerario, A. Medeiros, F. Claude, Q. Glorieux, E. Giacobino, S. Pigeon, and A. Bramati, "Dark-soliton molecules in an exciton-polariton superfluid," *arXiv preprint arXiv:2001.10653*, 2020.

[36] D. Sanvitto, S. Pigeon, A. Amo, D. Ballarini, M. De Giorgi, I. Carusotto, R. Hivet, F. Pisanello, V. Sala, P. Guimaraes, *et al.*, "All-optical control of the quantum flow of a polariton condensate," *Nature Photonics*, vol. 5, no. 10, p. 610, 2011.

[37] G. Nardin, G. Grosso, Y. Léger, B. Pi¸etka, F. Morier-Genoud, and B. Deveaud-Plédran, "Hydrodynamic nucleation of quantized vortex pairs in a polariton quantum fluid," *Nature Physics*, vol. 7, no. 8, p. 635, 2011.

[38] W. J. Kwon, J. H. Kim, S. W. Seo, and Y. Shin, "Observation of von kármán vortex street in an atomic superfluid gas," *Phys. Rev. Lett.*, vol. 117, p. 245301, Dec 2016.

[39] L. A. Smirnov, D. A. Smirnova, E. A. Ostrovskaya, and Y. S. Kivshar, "Dynamics and stability of dark solitons in exciton-polariton condensates," *Phys. Rev. B*, vol. 89, p. 235310, Jun 2014.

[40] T. C. H. Liew, O. A. Egorov, M. Matuszewski, O. Kyriienko, X. Ma, and E. A. Ostrovskaya, "Instability-induced formation and nonequilibrium dynamics of phase defects in polariton condensates," *Phys. Rev. B*, vol. 91, p. 085413, Feb 2015.

[41] S. Pigeon and A. Bramati, "Sustained propagation and control of topological excitations in polariton superfluid," *New Journal of Physics*, vol. 19, no. 9, p. 095004, 2017.

[42] M. Sich, D. N. Krizhanovskii, M. S. Skolnick, A. V. Gorbach, R. Hartley, D. V. Skryabin, E. A. Cerda-Mendez, K. Biermann, R. Hey, and P. V. Santos, "Observation of bright polariton solitons in a semiconductor microcavity," *Nature Photonics*, vol. 6, pp. 50–55, JAN 2012.

[43] H. Tercas, D. D. Solnyshkov, and G. Malpuech, "High-speed dc transport of emergent monopoles in spinor photonic fluids," *Phys. Rev. Lett.*, vol. 113, p. 036403, Jul 2014.

[44] M. Sich, J. K. Chana, O. A. Egorov, H. Sigurdsson, I. A. Shelykh, D. V. Skryabin, P. M. Walker, E. Clarke, B. Royall, M. S. Skolnick, and D. N. Krizhanovskii, "Transition from propagating polariton solitons to a standing wave condensate induced by interactions," *Phys. Rev. Lett.*, vol. 120, p. 167402, Apr 2018.

[45] A. Baas, J. P. Karr, H. Eleuch, and E. Giacobino, "Optical bistability in semiconductor microcavities," *Phys. Rev. A*, vol. 69, p. 023809, Feb 2004.

[46] A. V. Yulin, O. A. Egorov, F. Lederer, and D. V. Skryabin, "Dark polariton solitons in semiconductor microcavities," *Phys. Rev. A*, vol. 78, p. 061801, Dec 2008.

[47] W. Zhang and Y. Rao, "Coupled polariton solitons in semiconductor microcavities with a double-well potential," *Chaos, Solitons, and Fractals*, vol. 45, no. 4, pp. 373 – 377, 2012.

[48] L. A. Lugiato and R. Lefever, "Spatial dissipative structures in passive optical systems," *Phys. Rev. Lett.*, vol. 58, p. 2209, May 1987.

[49] D. V. Vishnevsky, D. D. Solnyshkov, N. A. Gippius, and G. Malpuech, "Multistability of cavity exciton polaritons affected by the thermally generated exciton reservoir," *Phys. Rev. B*, vol. 85, p. 155328, Apr 2012.

[50] P. Stepanov, I. Amelio, J.-G. Rousset, J. Bloch, A. Amo, A. Minguzzi, I. Carusotto, and M. Richard, "Two-components nature of the excitations in a polariton superfluid," *arXiv:1810.12570*, 2018.

[51] A. Amo, S. Pigeon, C. Adrados, R. Houdré, E. Giacobino, C. Ciuti, and A. Bramati, "Light engineering of the polariton landscape in semiconductor microcavities," *Phys. Rev. B*, vol. 82, p. 081301, Aug 2010.

[52] N. N. Rozanov, *Spatial Hysteresis and Optical Patterns.* Springer, Berlin, 2002.

[53] I. Ganne, G. Slekys, I. Sagnes, and R. Kuszelewicz, "Optical switching waves in iii-v semiconductor microresonators," *Phys. Rev. B*, vol. 63, p. 075318, Feb 2001.

[54] V. Odent, E. Louvergneaux, M. Clerc, and I. Andrade-Silva, "Optical wall dynamics induced by coexistence of monostable and bistable spatial regions," *Physical Review E*, vol. 94, no. 5, p. 052220, 2016.

[55] J. C. Maxwell, "On the dynamical evidence of the molecular constitution of bodies," *Nature*, vol. 11, p. 357, 1875.

[56] T. Aioi, T. Kadokura, and H. Saito, "Dissipative structures of quantized vortices in a coherently pumped polariton superfluid," *Phys. Rev. B*, vol. 87, p. 205312, May 2013.

[57] I. Carusotto and C. Ciuti, "Probing microcavity polariton superfluidity through resonant rayleigh scattering," *Physical review letters*, vol. 93, no. 16, p. 166401, 2004.

[58] D. Solnyshkov, I. Shelykh, N. Gippius, A. Kavokin, and G. Malpuech, "Dispersion of interacting spinor cavity polaritons out of thermal equilibrium," *Physical Review B*, vol. 77, no. 4, p. 045314, 2008.

[59] F. Manni, T. C. H. Liew, K. G. Lagoudakis, C. Ouellet-Plamondon, R. André, V. Savona, and B. Deveaud, "Spontaneous self-ordered states of vortex-antivortex pairs in a polariton condensate," *Phys. Rev. B*, vol. 88, p. 201303, Nov 2013.

[60] V. Goblot, H. S. Nguyen, I. Carusotto, E. Galopin, A. Lemaître, I. Sagnes, A. Amo, and J. Bloch, "Phase-controlled bistability of a dark soliton train in a polariton fluid," *Phys. Rev. Lett.*, vol. 117, p. 217401, Nov 2016.

[61] S. Even, *Graph Algorithms*. Cambridge University Press, 2011.

Conclusions and perspectives

In the series of works on which this thesis is based, the phenomena related with real-space topological defects (excitations) in exciton-polariton quantum fluids were studied. These defects are quantum vortices and solitons.

Chapter 3 is devoted to the studies of quantum turbulence, arising in 2D as a complex stochastic behavior of quantum vortices. First, the essential analysis tools were introduced: numerical solution of the Gross-Pitaevskii equation, calculation of the incompressible kinetic energy (IKE) spectrum based on the Fourier transformation and its semi-analytical calculation via the positions of vortices, the procedure of vortex cluster separation. Using these tools, the following data was obtained: IKE spectra for various quantum fluid stirring (excitation) methods, the separated contributions to IKE from clustered vortices, power laws of these IKE, fractal dimensions of the structures formed of clustered vortices, energy transfer rate between various size scales while exciting the quantum fluid. It was shown that the polariton condensates are particularly suitable for the possible observation of scaling on sufficiently large scales. The shape of raw energy spectra was shown to depend on the procedure of condensate excitation (stirring), but the energy spectra of clustered vortices always exhibited the -5/3 power law. In the optimal case, the cascade was observed over almost 2 decades.

In *Chapter 4* the modulational instability of solitons in exciton-polariton quantum fluids in the bistable regime was studied. First, the peculiarities of motion of the domain wall between the spatial domains at upper and lower bistability branches in the region of laser intensities close to bistability hystheresis loop were described. Next, the soliton pair confined in the channel with the walls "made" of high-density regions under intensive laser irradiation including the phenomenon of developing the modulational instability in such system was studied. By the means of the numerical simulations of GPE and the Bogoliubov-de Gennes equations, the formation of symmetric and anti-symmetric quantum vortex streets was observed for various intensities of laser and the corresponding phase diagram was plotted. Finally, the maze-solving property in such bistable system, was demonstrated. The parameters of the system were taken close to ones of the cavity that is used in LKB, UPMC (Paris), to give the straight possibility of the verification of the obtained theoretical results. Thus, the perspective of the present research is a work in close collaboration with experimental team, giving advises and support in order to obtain the most favorable regimes in practice. To better reproduce the experimental results, the usage of calculation in exction-photon basis will be possibly required, instead of the single-component case. The first obtained experimental results (which were obtained when this thesis was being written) are already very encouraging and promising.

The direction of quantum turbulence also appeals for further studies. Most of the

results in Chapter 3 were obtained in the idealized conservative case: infinite polariton lifetime, no pumping whether quasi-resonant or off-resonant, no disorder and cavity impurities. One can aim to develop an ultimately realistic experimental scheme for observation of quantum turbulence in the BECs/quantum fluids based on exciton-polaritons, which is very challenging. Such parameters as polariton lifetimes, energy and spatial profile and the regime (quasi-resonant or non-resonant) of pumping, can be analyzed by the means of Gross-Pitaevskii equation with parameters most suitable to observe the turbulence. One can use the quasi-resonant pumping scheme (close to the one used in Chapter 4) and play with the bistability hysteresis loop or consider the off-resonant pumping with the stimulated scattering from the reservoir. Other question to be solved is about the method to excite ("stir") the quantum fluid, in another words to inject the kinetic energy and to create the complex stochastic fluxes, with experimentally accessible parameters of the stirrers. Finally, one can extend the consideration to the spinor quantum fluids, when each of the spinor components corresponds to a specific polarization, and these components are coupled by the off-diagonal spin-orbit coupling Hamiltonian terms (e.g. TE-TM splitting). As a result, the mutual transfer of angular momentum between the components accompanied with vortex creation will take place. Fixation of the vortices after a period of free turbulent motion (which gives the possibility to examine them in cw experiment) can be realized via the so called effect of vortex pinning, when the vortex center overlaps with the density dip created by the switched on point-like potential barrier. The scheme of vortex pinning by the optically created pinning potential is also of high interest.

Publications

- **S. V. Koniakhin**, O. Bleu, G. Malpuech, and D. Solnyshkov, "2D quantum turbulence in a polariton quantum fluid," *Chaos, Solitons & Fractals*, vol. 132, p. 109574, 2020.
- **S. V. Koniakhin**, O. Bleu, D. D. Stupin, S. Pigeon, A. Maitre, F. Claude, G. Lerario, Q. Glorieux, A. Bramati, D. Solnyshkov, and G. Malpuech, "Stationary quantum vortex street in a driven-dissipative quantum fluid of light," *Phys. Rev. Lett.*, vol. 123, p. 215301, 2019.
- D. D. Solnyshkov, C. Leblanc, **S. V. Koniakhin**, O. Bleu, and G. Malpuech, "Quantum analogue of a Kerr black hole and the Penrose effect in a Bose-Einstein condensate," *Phys. Rev. B*, vol. 99, p. 214511, Jun 2019.
- Z. Zhang, F. Li, G. Malpuech, Y. Zhang, O. Bleu, **S. V. Koniakhin**, C. Li, Y. Zhang, M. Xiao, and D. D. Solnyshkov, "Particlelike behavior of topological defects in linear wave packets in photonic graphene," *Phys. Rev. Lett.*, vol. 122, p. 233905, Jun 2019.

Preprints:

- G. Lerario, **S. V. Koniakhin**, A. Maître, D. Solnyshkov, A. Zilio, Q. Glorieux, G. Malpuech, E. Giacobino, S. Pigeon, and A. Bramati, "Parallel dark soliton pair in a bistable 2D exciton-polariton superfluid," *arXiv preprint arXiv:2003.11408*, 2020

In preparation:

- F. Claude, **S. V. Koniakhin**, A. Maître, S. Pigeon, G. Lerario, D. D. Stupin, Q. Glorieux, E. Giacobino, D. Solnyshkov, G. Malpuech, and A. Bramati, "Frozen snake instabilities in a polariton superfluid," 2020

Conferences

- S. V. Koniankin, "Complex behavior of topological excitations in polariton quantum fluids," in *Le 25ème Congrès Général de la Société Française de Physique*, Nantes, 8-12 July 2019. Oral talk
- S. V. Koniankin, "Snake instability control and stationary quantum vortex street in a driven-dissipative quantum fluid of light," in *International Conference on Optics of Excitons in Confined Systems*, St. Petersburg, Russia, 16-20 September 2019. Oral talk
- S. V. Koniankin, "Quantum turbulence in exciton-polatiron quantum fluids," in *20th International Conference on Physics of Light-Matter Coupling in Nanostructures*, Moscow, Russia, 1-7 July 2019. Poster
- S. V. Koniankin, "Analog Kerr black hole and Penrose effect in a Bose-Einstein condensate," in *Chiral modes in optics and electronics of 2D systems*, Aussois, 26-28 Novembre 2018. Poster

Dynamics of topological defects in exciton-polariton quantum fluids

Abstract: The Bose-Einstein condensate is a new state of matter which gives the astonishing possibility of observation of quantum phenomena, like the existence of the wave function on macroscopic scales. Present research is devoted to the particular type of BECs based on excitons-polaritons in semiconductor microcavities. Due to non-linear interactions, the behavior of Bose-Einstein condensates, and more general of polaritons at high densities, resembles that of classical fluids. Better comprehension of these similarities is one of the goals of ANR "Quantum fluids of light" project, within which present research was conducted. The first two chapters of the manuscript provide the necessary introduction to the physics of excitons-polaritons and properties of polariton condensates (including the topological defects: vortices and solitons), respectively.

In classical fluids, the solitons are solitary waves propagating over long distances without deformation and similar situation is actual for 1D quantum fluids. However, in 2D case the solitons undergo the so-called "snake instability" and transform to the chains of vortex-antivortex pairs, which is a principal obstacle to study this phenomenon in polariton quantum fluids especially in CW experiments. In the next chapter, the simple to implement by the means of spatial light modulator configuration that allows avoiding this restriction was proposed and extensively studied. The configuration is a narrow 1D channel with the walls of high condensate density at upper bistability branch created by intensive laser radiation. It was shown that in such channels dark solitons appear parallel to the channel axis by odd (1-3) or even (2-4) number in order to accommodate the phase constraint induced between the walls. According to the Bogoliubov-de Gennes analysis, these soliton molecules are typically unstable and trigged by the disorder evolve toward stationary symmetric or anti-symmetric arrays of vortex streets. Also the soliton head repulsion from the corridor dead-end was demonstrated, giving a straight possibility to experimentally implement maze solving procedure by dead-end stroking algorithm.

As for quantum turbulence, the possibility of observing the energy transfer from small spatial scales to large ones (reverse energy cascade) and the formation of fractal structures composed of quantum vortices in polaritonic condensates were demonstrated. The region of Kolmogorov -5/3 power law in the spectrum of incompressible kinetic energy coincides with the region of fractional Minkowski dimension of the structures of clustered vortices. However, for various condensate stirring methods, this power law becomes visible only after eliminating the contribution of single vortices and vortex dipoles. Thus, the experimental observation of the spectrum of such shape will be possible after full wave function reconstruction including both amplitude and phase, which justifies that polaritons are the promising platform for studying quantum turbulence.

Keywords: Photonics, exciton-polaritons, Bose-Einstein condensates, Gross-Pitaevskii equation, numerical simulations, Bogoliubov excitations, solitons, quantum vortices, quantum turbulence